

UNIVERSIDADE DE SÃO PAULO
INSTITUTO DE FÍSICA

Estruturas em larga escala em levantamentos fotométricos e espectroscópicos

Hugo Orlando Camacho Chavez

Orientador: Prof. Dr. Marcos Vinicius Borges Teixeira Lima

Tese apresentada ao Instituto de Física da Universidade de São Paulo
para a obtenção do título de Doutor em Ciências.

Banca Examinadora:

Prof. Dr. Marcos Vinicius Borges Teixeira Lima (IF-USP)

Prof. Dr. Luis Raul Weber Abramo (IF-USP)

Prof. Dr. Laerte Sodré Jr. (IAG-USP)

Prof. Dr. Eduardo Serra Cypriano (IAG-USP)

Prof. Dr. Miguel Boavista Quartin (IF-UFRJ)

São Paulo
2019

FICHA CATALOGRÁFICA
Preparada pelo Serviço de Biblioteca e Informação
do Instituto de Física da Universidade de São Paulo

Camacho Chavez, Hugo Orlando

Estruturas em larga escala em levantamentos fotométricos e espectroscópicos. São Paulo, 2019.

Tese (Doutorado) – Universidade de São Paulo. Instituto de Física.
Depto. de Física Matemática

Orientador: Prof. Dr. Marcos Vinicius Borges Teixeira Lima
Área de Concentração: Cosmologia.

Unitermos: 1. Cosmologia; 2. Astronomia; 3. Estrutura do universo.

USP/IF/SBI-029/2019

UNIVERSITY OF SÃO PAULO
INSTITUTE OF PHYSICS

Large Scale Structures in photometric and spectroscopic surveys

Hugo Orlando Camacho Chavez

Advisor: Prof. Dr. Marcos Vinicius Borges Teixeira Lima

Thesis submitted to the Institute of Physics of the University of São Paulo in partial fulfillment of the requirements for the degree of Ph.D. in Physics.

Examination board:

Prof. Dr. Marcos Vinicius Borges Teixeira Lima (IF-USP)

Prof. Dr. Luis Raul Weber Abramo (IF-USP)

Prof. Dr. Laerte Sodré Jr. (IAG-USP)

Prof. Dr. Eduardo Serra Cypriano (IAG-USP)

Prof. Dr. Miguel Boavista Quartin (IF-UFRJ)

São Paulo
2019

Resumo

A dinâmica da formação de estruturas em larga escala no universo, assim como a matéria escura, a energia escura, a expansão acelerada do universo e suas inter-relações permanecem atualmente como grandes desafios da cosmologia moderna e tem motivado numerosos estudos na última década. Em particular, a compreensão da aceleração cósmica prenuncia implicações importantes que podem revolucionar as teorias da cosmologia, gravitação e física de partículas elementares, entre outras. Testes cosmológicos complementares em grandes levantamentos de galáxias óticas e espectroscópicos, como o DES e o eBOSS representam uma abordagem poderosa para estes problemas e, ao mesmo tempo, oferecem novos desafios práticos e teóricos para extrair a informação contida nos dados. Neste trabalho, apresentamos análises da estrutura de larga escala do universo no contexto de dois levantamentos de galáxias, o DES e o eBOSS, medindo o sinal de aglomeração de traçadores para a distribuição de matéria usando diferentes abordagens para sua função de correlação de dois pontos e espectro de potências. No contexto do BOSS-eBOSS, apresentamos contribuições para algumas das primeiras análises do sinal de clustering no espaço de configuração de ELGs e LRGs com dados tempranos do eBOSS e sua interpretação e comparação com dados anteriores e modelos teóricos. No contexto do DES, apresentamos medições do espectro de potência angular de galáxias usando dados do primeiro ano (Y1) de observações e utilizamos estas medidas para estudar o sinal de BAO no espaço harmônico. Este trabalho faz parte do esforço do DES para a análise do sinal de BAO em dados Y1.

Palavras chave: Cosmologia, Astronomia, Estrutura do universo.

Abstract

The dynamics of formation of the observed large-scale structures, along with dark matter, dark energy, the accelerated expansion of the universe and their inter-connections remain as some of the biggest puzzles of modern cosmology and have been extensively investigated over the last years. In particular, understanding the nature of cosmic acceleration foresees important implications for Cosmology, Gravitation and Particle Physics, among others. Complementary cosmological probes from large photometric and spectroscopic galaxy surveys, such as DES and eBOSS, represent a powerful approach to these problems, while simultaneously offering new practical and theoretical challenges for exploiting the information contained in observed data. In this work, we present three analyses of the large scale structure of the universe in the context of two galaxy surveys, the DES and the eBOSS, by measuring clustering signal of tracers for the matter distribution using different approaches to their two-point correlation function and power spectrum. In the context of BOSS-eBOSS, we present contributions to some of the first analyses of the clustering signal in configuration space of ELGs and LRGs with early eBOSS data and their interpretation and comparison with previous data and theoretical models. In the context of DES, we present measurements of the galaxy angular power spectrum of galaxies using data from the first year of observations and use these measurements to search for the BAO feature in harmonic space. This work is part of the DES effort for the analysis of the BAO feature in Y1 data.

Keywords: Cosmology, Astronomy, Structure of the universe.

Acknowledgements

First and foremost I would like to thank my advisor, Marcos Lima, for all his help, support and constant encouragement without which this work truly would not have been possible.

During the development of this work, I was fortunate to interact and learn from many people, without whom the results presented here would not have been possible. I thank all the Brazilian DES-LSS working group, in particular, Aurelio Carnero and Fernando de Simoni. I also thank all the DES-LSS working group, in particular, its conveners during 2018, Ashley Ross and Martin Crocce. It has been an incredible experience to be part of such a highly qualified team. I also want to thank all the people with whom I collaborated on the results presented here, in particular, Stephanie Jouvel, Zhongxu Zhai, Kwan Chuen-Chan, and Santiago Avila.

I want to thank everyone in the Cosmology group at DFMA/IF/USP and IFT/UNESP, for providing the best work environment and for the valuable discussions on seminars and classes and outside them. In particular, I thank Michel Agüena for his constant and enjoyable collaboration and friendship, and Felipe Oliveira and Vinicius Busti for their friendship and valuable teachings. I thank Nickolas Kokron, Fabien Lacasa and Rogerio Rosenfeld, for introducing all of us to the PCL/MASTER estimator of C_ℓ 's and their powerful and valuable insights on cosmology and astrophysics. I also thank Rodrigo Voivodic, Leonardo Duarte, Henrique Xavier, Leandro Beraldo, Carolina Queiroz, Henrique Rubira, Caroline Guandalin, Renan Boschetti, and many others who kindly shared directly and indirectly their time and knowledge with me. I learned a lot from all of you.

I also kindly thank the members of my defense committee for multiple suggestions that helped improve the manuscript substantially.

I thank the Laboratorio Inter-Institucional de e-Astronomia (LIIneA) for providing me with the incredible opportunity of being an active member of collaborations such as eBOSS, DES and LSST. I thank the LIIneA staff, specially Rosane, who kindly helped me on everything related to travels and Rio de Janeiro and all the IT team. Without their dedication, this work

certainly would not be a reality.

I am very grateful to Leonardo Castañeda for introducing me to Cosmology and for his valuable teachings and friendship and to all my friends of the Gravitation and Cosmology group at Universidad Nacional de Colombia. In particular I thank my old friend Sergio Rodriguez for his constant encouragement and valuable friendship through all these years.

I thank my friends, who have never stopped believing in me and kindly supporting me in all my projects, Oscar Lopez (RIP), Diego Fabra, Raissa Oblitas, Yuber Perez, Antonio Sanchez, Cristian Duitama, Leonardo Gil, Jonathan Mancilla, Ramiro Beltran, Andrés Manrique. I am very grateful for all your teachings.

Nobody has been more important to me in the development of this work than the members of my family. I want to thank my parents, my brother and my grandparents, whose love, guidance and teachings are always with me. I wish to thank Carol, for her loving and supportive partnership through all this journey and for always providing inspiration and motivation.

This work would not have been possible without the financial support of CNPq under grant 141935/2014-6 and through the INCT-eUniverse under grant 381570/2018-5. This work has made use of the computing facilities of the Laboratory of Astroinformatics (IAG/USP, NAT/Unicsul), whose purchase was made possible by the Brazilian agency FAPESP (grant 2009/54006-4) and the INCT-A.

Contents

Acknowledgements	vii
1 Introduction	1
1.1 Cosmological motivations	1
1.2 Large scale structure	4
1.3 Galaxy surveys	5
1.3.1 The extended Baryon Oscillation Spectroscopic Survey	6
1.3.2 The Dark Energy Survey	7
1.4 Thesis outline	8
2 Theoretical framework	9
2.1 Background cosmology	9
2.1.1 Metric	10
2.1.2 Redshift	12
2.1.3 Einstein equations and Friedmann equations	13
2.1.4 Density parameters	14
2.1.5 Distances	16
2.2 Cosmological perturbation theory	17
2.2.1 Linear growth evolution of matter	20
2.2.2 Nonlinear evolution	22
2.3 Halo-galaxy connection	32
2.3.1 The halo model	32
2.3.2 Halo occupation distribution	36
2.4 Galaxy clustering observables	37
2.4.1 Galaxy correlation function	38
2.4.2 Correlation function and power spectrum	43
2.4.3 Angular clustering	47
2.4.4 Galaxy bias	50
2.4.5 Redshift space distortions	51
2.4.6 Projected correlation function	57
2.4.7 Covariance matrices	60

2.4.8	Baryon acoustic oscillations	66
3	ELG clustering at eBOSS and DES	75
3.1	eBOSS ELG sample from DES photometry	76
3.2	eBOSS ELGs clustering properties	77
3.2.1	Random fields	79
3.2.2	Two-point spatial correlation function	82
3.2.3	Galaxy bias	88
3.3	Discussion	91
4	LRG clustering at eBOSS	95
4.1	The eBOSS-BOSS LRG sample	95
4.2	LRG clustering measurements	97
4.3	Discussion	102
5	DES Y1 angular power spectrum BAO	105
5.1	Theory	107
5.1.1	APS template	108
5.2	DES Y1 BAO galaxy sample	109
5.2.1	Pixelized map generation	112
5.3	DES mock simulations	113
5.4	Angular power spectrum measurement in cut sky	113
5.5	Tests of methodology on mocks	115
5.5.1	Measurements of the APS	115
5.5.2	Covariance matrix	115
5.5.3	Parameter estimation	118
5.5.4	Robustness tests	121
5.6	BAO in DES Y1 data	129
5.7	Discussion	136
6	Conclusion and outlook	143
	Appendices	153
A	Alternative metrics	153
B	Cosmological perturbations	157
B.1	Background geometry	157
B.2	Perturbation theory and the gauge problem	158
B.2.1	Taylor expansion of a tensor field	160
B.2.2	Gauge transformations and gauge invariance	161
B.3	First order perturbations	164

<i>CONTENTS</i>	xi
B.3.1 Scalar–vector–tensor decomposition	164
B.3.2 Metric perturbations	165
B.3.3 First order scalar perturbations	166
B.3.4 Matter–energy perturbations	169
B.3.5 First order Einstein field equations	171
C Sound horizon	173
D Two-point functions on the sphere	175
E Hankel transforms and FFTlog	177
Bibliography	181

Chapter 1

Introduction

1.1 Cosmological motivations

In recent years Cosmology has entered a “golden age”. There are two fundamental reasons for this: (i) our knowledge about the universe appears to be consolidating along with all observational data that seem to converge consistently into a standard cosmological model, a *concordance model*, and (ii) on top of this consolidation, cosmology faces many fascinating theoretical and practical/observational challenges. Theoretical challenges are mostly related to the physical nature of the constituents of the concordance model, from which the nature of dark matter and dark energy or cosmic acceleration are among the most renowned. Practical challenges are mainly related to the variety of observational probes proposed, their proper interpretation, their consistent combination and the necessity of dealing with large amounts of data that are expected from current and upcoming observations.

The possible causes of cosmic acceleration and their fundamental implications have inspired ambitious observational efforts for measuring the universe expansion history, with hopes of revealing its origin. The report of the Dark Energy Task Force (DETF; Albrecht et al., 2006) represented a major effort in defining the problem, categorizing the observational approaches and providing a quantitative framework for comparing their capabilities. The DETF categorized on-going experiments as “Stage I”, discovery experiments as “Stage II”, and the next generation experiments as “Stage III”. Finally, the DETF looked forward to a generation of more capable (and more expensive) “Stage IV” efforts that might begin observations around the second half of the coming decade. The DETF focused on four cosmological observables: Type-Ia supernovae (SNIa); clusters of galaxies; clustering of galaxies and baryon acoustic oscillations (BAO); and weak gravitational lensing. Except

for SNIa, which maps the expansion history directly, all these techniques are fundamentally related to the large-scale structure (LSS) of the universe, whose study is, therefore, the natural path for investigating most of the theoretical challenges of cosmology.

For cosmic acceleration, the so-called dark energy controls the expansion history of the universe, which in turn affects structure formation and defines observational properties of astrophysical objects such as galaxies cataloged by their angular positions and redshifts. The relation between redshift and physical distances depends on the expansion rate and the spatial geometry of the universe. Besides that, the expansion rate works as a dragging force that slows down the gravitational evolution of cosmic structure. Therefore, by measuring distances and growth of cosmic structures, one can constrain the properties of dark energy or any other explanation for the accelerated expansion. In this context, modern galaxy surveys have become fundamental in advancing our understanding of the universe (see section 1.3).

During the last decade of the last century, a major discovery was made in Cosmology: the scientific community reached the conclusion that dark matter and ordinary matter were insufficient to describe a variety of cosmological observations within the framework of the standard cosmological model accurately just depicted above, i.e. a RW metric describing the spacetime symmetries and the validity of General Relativity (GR) on cosmological scales (see Chap. 2). The distance-redshift relation derived from luminosity measurements of type Ia supernovae revealed that in the context of the standard model about 73% of the total energy density in the universe comes from an additional component, which causes the universe not only to expand but to do it in an accelerated way (Riess et al., 1998; Perlmutter et al., 1999). More recent results for the observational evidence of the energy/matter content of the universe come from measurements of the temperature fluctuations in the cosmic microwave background (CMB) radiation as determined by the *Planck mission* (Planck Collaboration et al., 2013). These results have been shown to be consistent with the so-called Λ CDM concordance model of cosmology, consisting of a nearly spatially flat universe, determined to an accuracy of better than a percent, dominated by two unknown components, the *dark matter* and *dark energy*, with 26.8% and 68.3% of the total energy content in the universe respectively, and with only 4.9% of ordinary matter, i.e. baryons (see Planck Collaboration et al., 2013, for a more detailed discussion).

The nature of dark matter and dark energy or the accelerated expansion of the universe constitute two of the most important open problems in Physics today. The most basic model of dark energy (DE) describes it as

a *cosmological constant* Λ , for which density and pressure are constant and related by the equation of state parameter $w = p/\rho = -1$. A large number of alternative models has been explored in recent years. They are mostly separated into two groups: (a) models in which DE is, in fact, a gravitational source in the context of GR, and then is modeled as an evolving field, like e.g., *quintessence* (see, e.g., Amendola & Tsujikawa, 2010; Peebles & Ratra, 2003; Copeland et al., 2006, for a detailed review), and (b) models in which the theoretical basis of gravitational phenomena is proposed to be changed, i.e., the equations of GR are modified in order to describe the acceleration as a dynamical (gravitational) effect (see, e.g. Amendola & Tsujikawa, 2010; Tsujikawa, 2010, for a detailed review).

This scenario is quite rich from the theoretical perspective since there are multiple alternative explanations for cosmic acceleration, including several models of dark energy and modified gravity. As an example, let us mention a powerful mathematical result at the heart of our modern theory for the gravitational interaction, GR, namely, the Lovelock Theorem (see, e.g. §2 of Clifton et al., 2012, and references therein). The Lovelock theorem states that the Einstein tensor, up to a constant multiplying the metric tensor, is the only possible form for Euler-Lagrange equations of motion (EOM) for a theory i) whose EOM come from an action principle, ii) that considers the metric as the only dynamic field, iii) with EOM up to second-order derivatives and iv) in four dimensions. The profound implication of this mathematical statement is that in order to describe the gravitational interaction with a model different from GR, we must give up at least one of the conditions above.

From the observational side, two significant sensitivity windows have been, and will continue to be, explored: i) the expansion history and ii) the growth of structures in the universe. Different probes have been designed to optimize the sensitivity on each of those.

For the expansion history, one pursues the reconstruction of the evolution of the background geometry through cosmic time via the establishment of a distance-redshift relation. These include BAO and SNIa. We can think of BAO as a *standard ruler* method, in which a given known scale is observed at different distances from the observer. The distance sound waves could travel on the primordial fluid of photons and baryons¹ sets this very convenient scale, as it can be robustly predicted theoretically. After decoupling, the BAO scale is imprinted in both photons and baryons and can be observed on

¹Hereafter we adopt the astronomical convention of calling *baryons* all known massive particle species in the standard model, in contrast to the more detailed definition in particle physics based on quantum statistics. Dark matter is not included in this definition.

the sea of decoupled photons probed through their temperature correlations in the sky, and on the matter distribution at low redshifts.

Meanwhile, SNIa can be understood as a *standard candle* method, in which the brightness of exploding stars with known luminosity are observed, and the redshift of the host galaxy is measured. SNIa's are convenient sources for this purpose, as their luminosity can be standardized from their light curves. By measuring sources at multiple redshifts, one has direct access to the universe geometry and can then reconstruct the expansion history.

For the growth of structures, the idea is somewhat different. In this case, one looks for the late-time local evolution of matter around evolved gravitational potential wells. One convenient way to track this evolution is by looking at the so-called *Redshift Space Distortions* (RSD). Schematically, the distribution of luminous sources appears different when looked along and perpendicular to the line of sight (or on the plane of the sky). The physical reason for that is that for the radial positions we measure redshifts. Despite possible intrinsic errors on their determination, redshifts contain not only information about distances but also about velocities via, e.g., the Doppler effect. On top of that, at late times, luminous sources should be falling into gravitational potential wells, so the information of the infall velocities – directly related to the origin and evolution of the potential wells and then to the growth of structures – should be imprinted on its measured redshift.

One useful approach to cosmic acceleration can be then to try to answer consistency questions that bring light to its nature. Some examples are: i) Do measurements of the expansion history and growth of structure agree? ii) Do data from the early and late universe agree, in the sense of being well described by the same model parameters? iii) Also, directly related to cosmic acceleration, does the dark energy density evolve with the expansion, or is it well described by a cosmological constant?

1.2 Large scale structure

The large-scale distribution of galaxies contains information about the cosmological model that best describes our universe (e.g., Dodelson, 2003; Lyth & Liddle, 2009). After the great success of maps of the cosmic microwave background (CMB) in providing cosmological information, large galaxy surveys have become one of the major contributors to our understanding of gravity and the ingredients that make up the cosmos. They provide evidence for the consistency of our description for the evolution of the universe from the early CMB epoch to present times.

The distribution of galaxies in the universe carries cosmological informa-

tion that was imprinted from the era when baryons and photons were tightly coupled. The so-called BAO feature results from processes that occur up to the baryon drag epoch, and are sensitive in particular to the sound horizon at decoupling.

It is possible to quantify the distribution of galaxies by measuring their 2-point correlation function. One can measure either the three-dimensional 2-point galaxy correlation function in configuration space or its Fourier transform, the power spectrum. In principle, both quantities carry the same information, but in practice, they may have different sensitivities to the estimation of cosmological parameters due to, among other effects, different covariance matrices, different responses to systematic effects, etc. For instance, Gaussian covariance matrices for the power spectrum are diagonal in the full-sky case, whereas for the spatial correlation function significant correlations are expected. Hence performing measurements in both configuration and Fourier space serves as a consistency check, and may also provide complementary information to tame some of the observational issues.

In galaxy surveys where redshifts are not precisely measured, as is the case of photometric surveys where one can only compute photometric redshifts (photo- z), one considers the projected galaxy distribution into redshift bins. In this case what is measured is the angular correlation function (ACF, denoted by $w(\theta)$) or the angular power spectrum (APS, denoted by C_ℓ). Correlations of higher order carry information, e.g. about the Gaussian nature of the density field at present or at early times.

1.3 Galaxy surveys

From the photometric side, several observational survey programs are underway, e.g. the Dark Energy Survey² (DES; Flaugher, 2005), the KiDS³ and the HSC⁴. These experiments are designed to provide imaging in the optical and near infra-red, with sufficient depth, for wide areas and with high quality to enable competitive cosmological constraints from the universe's large-scale structure at $z < 2$.

Meanwhile future surveys such as LSST⁵, Euclid⁶ and WFIRST⁷ will enable order-of-magnitude improvements on cosmological constraints if sys-

²<https://www.darkenergysurvey.org>

³<http://kids.strw.leidenuniv.nl>

⁴<http://www.subarutelescope.org/Projects/HSC>

⁵<http://www.lsst.org>

⁶<http://sci.esa.int/science-e/www/area/index.cfm?fareaid=102>

⁷<http://wfirst.gsfc.nasa.gov>

tematic uncertainties can be sufficiently controlled.

From the spectroscopic side, motivated by the success of the Baryon Oscillation Spectroscopic Survey (BOSS; Gunn et al., 2006), the extended-Baryon Oscillation Spectroscopic Survey⁸ (eBOSS; Dawson et al., 2016) is underway, designed as a six-year program to explore a larger volume and higher redshifts of the universe. Its primary scientific goal has been to provide high-precision measurements of the BAO scale and RSDs in the redshift range $0.6 < z < 2.0$ (Zhao et al., 2016).

Likewise, future galaxy spectroscopic surveys such as the ground-based Dark Energy Spectroscopic Instrument⁹ (DESI; DESI Collaboration et al., 2016a,b), and space missions such as Euclid¹⁰ (Amendola et al., 2013) will extensively probe the intermediate redshift range $1 \leq z \leq 2$, providing cosmological measurements with unprecedented precision in the next decade.

In this thesis, we perform clustering measurements of galaxies from the SDSS and the DES. These measurements are combined with theoretical predictions using statistical tools in order to study the bias of SDSS galaxies and to extract the cosmological BAO feature of DES galaxies. Next, we provide a quick description of these surveys.

1.3.1 The extended Baryon Oscillation Spectroscopic Survey

The extended Baryon Oscillation Spectroscopic Survey (eBOSS) is part of the fourth stage of the Sloan Digital Sky Survey (SDSS-IV), a multi-spectral imaging and spectroscopic redshift survey using a dedicated 2.5-meter wide-angle optical telescope at Apache Point Observatory in New Mexico. Motivated by the success of his predecessor, BOSS, eBOSS has explored a larger volume and higher redshift of the universe. Operating from July 2014 to February 2019, the primary scientific goal of eBOSS is to probe the expansion history and growth of structures at the time where the transition from deceleration to acceleration occur providing the first high precision measurements of baryon acoustic oscillations (BAO) and redshift space distortions (RSD) over the range $0.6 < z < 2.5$. In order to do this, eBOSS is expected to catalogue 300000 luminous red galaxies over 6000 deg^2 and $0.6 < z < 1.0$, 175000 emission line galaxies over 1000 deg^2 and $0.6 < z < 1.1$ and 500000 quasars over 6000 deg^2 and $0.8 < z < 2.5$.

⁸<http://www.sdss.org/surveys/eboss/>

⁹<https://www.desi.lbl.gov/>

¹⁰<https://www.cosmos.esa.int/web/euclid/>

1.3.2 The Dark Energy Survey

The Dark Energy Survey (DES) is a new generation galaxy survey designed to study the late cosmic acceleration of the universe through the dynamics of the expansion and the growth of structures at large scales. The DES is a collaboration of over a hundred researchers from the USA, UK, Spain, Germany, Switzerland, and Brazil. The main innovation in the project is the development of the Dark Energy Camera (DECam), a new optical CCD camera of 520 megapixels and 2.2 deg of field of view, which has been placed at the Blanco 4-meter telescope located at Cerro Tololo Inter-American Observatory (CTIO) in Chile and saw its first light in September 2012. For over five years it used 30% of the telescope available time to carry out a wide-area survey and reach redshifts $0.2 \leq z \leq 1.3 - 2$ with a depth of ~ 24 in magnitude in SDSS broad bands, $g = 24.6$, $r = 24.1$, $i = 24.3$ and $z = 23.9$ over 5000 deg^2 in the southern galactic sky.

The main scientific goal of the DES is to determine if cosmic acceleration can be modeled by a pure cosmological constant or if its energy density evolves in time. For that, the DES has detected ~ 10000 optical galaxy clusters and has measured shapes, redshifts, and positions of ~ 100 millions of galaxies. It will obtain cosmological information about the physical nature of dark energy via four different methods (cosmological observables): i) counts and spatial distribution of galaxy clusters with $0.2 \leq z \leq 1.3$, ii) the evolution of the angular clustering of galaxies, iii) weak lensing tomography up to $z \sim 1$ and iv) distances and luminosities of SNIa in $0.3 \leq z \leq 0.8$. Combining for the first time the purely cosmographic SNIa and BAO measurements with the growth-sensitive weak lensing and galaxy clustering measurements, the DES will independently place strong constraints on the nature of dark energy. While observations and data analyses proceed by different working groups in the collaboration, simulations are also performed to validate analysis tools and forecast results with higher confidence.

The DES has ended data collection in January 2019. There is the first set of data taken on the Science Verification (SV) season covering a small area on the sky, 150 deg^2 , to the full depth. All the scientific projects from the DES collaboration on SV data have been completed, and there is a public release of the SV data. The first year (Y1) season of observations, covers 1500 deg^2 to about 40% of the final depth. Almost all of the DES collaboration scientific projects have been completed, and there is also a public release of data. As of early 2019, the collaboration is under the process of analyzing the data taken from the third year season (Y3), in which the full area of 5000 deg^2 was covered to about 50% of the depth. A release of cosmological results for Y3 is expected after the northern summer of the present year,

2019. The final seasons Y4 and Y5 data have already been collected, and the process of vetting catalogs is underway.

1.4 Thesis outline

In this thesis, we make use of spectroscopic data from eBOSS and photometric data from the DES to study clustering properties of multiple galaxy types and extract astrophysical (bias) and also cosmological information (BAO feature in their angular spectrum).

We start in Chap. 2, providing a theoretical framework of our work. We discuss background cosmology and both linear and non-linear perturbations around this background. We consider non-linear effects from Perturbation Theory (standard and renormalized) as well as the Halo Model, pointing out connections with recent analyses for extracting the BAO feature from two-point statistics of galaxy positions. We also describe the underlying formalism necessary to predict LSS observables such as correlations and spectra, as well as their covariances.

In Chap. 3, we study the clustering of Emission-Line Galaxies (ELG's) from joint measurements of eBOSS and DES. We characterize the bias of this sample, showing that it agrees with previous measurements of this galaxy population. This work showcased an interesting synergy between a spectroscopic and a photometric survey when defining a galaxy sample and measuring their clustering properties.

In Chap. 4, we study clustering measurements of Luminous Red Galaxies (LRG's) from eBOSS. We again measured the clustering properties of this sample and estimated its bias. An agreement is found when comparing bias estimated directly from two-point statistics and the prediction from a fitted Halo Occupation Distribution (HOD). This work was the very first scientific result from eBOSS and paved the way for later cosmological analyses.

In Chap. 5, We present the major contribution of this thesis, a study of the clustering properties of a sample of luminous galaxies from DES. We used these clustering measurements to detect the BAO feature in the angular power spectrum of DES galaxies. This result was also combined with other probes to constrain cosmological parameters.

Finally, in Chap. 6, We present our conclusions. We also outline research directions and future perspectives.

Chapter 2

Theoretical framework

This chapter presents the basic formalism used in the remaining of the thesis. We start discussing the standard model for the background cosmology and proceed to describe standard perturbation theory and its linear realization. Next, we discuss the nonlinear evolution of perturbations on Renormalized Perturbation Theory (RPT) and Halo Model frameworks. We then briefly review the theoretical basis for modeling multiple two-point statistics of dark matter tracers (e.g., galaxies) and their interpretation. We conclude with a discussion of modern analysis methods for extracting the BAO feature from the distribution of tracers of the matter field at low redshifts.

All the theoretical predictions presented here assume the an FLRW model with a cosmological constant, Λ CDM with parameters fixed by the Planck 2018 best fit (Plik best fit column in Planck Collaboration et al., 2018, Table 1).

2.1 Background cosmology

The universe is observed to be isotropic relative to us to a high degree of confidence, once we i) average over large enough scales, considerably larger than the typical scales of clusters of galaxies, and ii) allow for an observer peculiar velocity relative to the average motion of matter in the universe. In practice, this velocity is treated as relative to the cosmic microwave background (CMB) radiation. In other words, on cosmologically observable scales, no particular direction can be stated to be preferred over others. One ends up with two possibilities: a) either the universe is spatially homogeneous, and as a specific observer we are on a typical place as the universe is isotropic for any typical observer, or b) the universe is spatially inhomogeneous, and we are near a distinguished place with respect to which the universe looks isotropic.

The common choice of the modern scientific community is the former one. It is commonly interpreted as the *Copernican principle*, i.e., the assumption that we are not at a privileged position in the universe (Weinberg, 1972; Peter & Uzan, 2013).

The Copernican principle along with the observed isotropy are sufficient conditions for the global spatial homogeneity of the universe (Peter & Uzan, 2013). The modern standard cosmological model is therefore based on the assumption that the universe is *spatially homogeneous and isotropic*. This assumption is called the *cosmological principle*. Spatial homogeneity implies the existence of a one-parameter family of space-like hypersurfaces Σ_t (surfaces of homogeneity), foliating the spacetime, in which the Copernican principle is valid, and therefore every point is equivalent. On the other hand, spatial isotropy implies the existence of a congruence of time-like worldlines with tangent vector u^{a1} defining the four-velocity of the so-called *isotropic observers*, such that it is impossible to construct a preferred tangent vector perpendicular to u^a .

The four-velocity of isotropic observers, u^a , and the homogeneity hypersurfaces Σ_t should be perpendicular. Otherwise, the universe would have a privileged spatial direction, violating isotropy. As three-dimensional subspaces, the Σ_t surfaces, are *maximally symmetric*, and consequently are spaces of constant curvature (Weinberg, 1972; Peter & Uzan, 2013). The isotropic observers acquire the property that for each time, they observe a maximally symmetric 3D space, which is why they are also called *fundamental observers*.

2.1.1 Metric

One can then define a coordinate time t , the *cosmic time*, as the proper time measured by the fundamental observers, $dt = dx^a u_a$ in terms of which the spacetime metric can be written as

$$g_{ab} = u_a u_b + \hat{\gamma}_{ab}(t), \quad (2.1)$$

where for each value of t , $\hat{\gamma}_{ab}(t)$ determines the metric of the constant time hypersurfaces Σ_t . Since these hypersurfaces should be of constant curvature for each cosmic time instant, one can choose comoving spatial coordinates (x^i) to separate the time dependence and write the spacetime metric tensor

¹Throughout this work the index convention is such that spacetime and spatial indices with respect to a general basis are denoted by $a, b, \dots = 0, 1, 2, 3$ and $\alpha, \beta, \dots = 1, 2, 3$ respectively, while spacetime and spatial indices in a coordinate basis are $\mu, \nu, \dots = 0, 1, 2, 3$ and $i, j, \dots = 1, 2, 3$, respectively.

as

$$\bar{g} = -dt \otimes dt + a^2(t) \gamma_{ij} dx^i \otimes dx^j, \quad (2.2)$$

where the function $a(t)$, giving the time evolution of the hypersurfaces Σ_t , is the cosmic *scale factor*, determining how physical spatial scales change with time and relate to the comoving scales. The spatial metric of components γ_{ij} in comoving coordinates defines generic 3D spaces of constant curvature. A spacetime metric with the form of Eq. (2.2) and the above characteristics is known as a *Robertson-Walker metric* (RW).

It is useful to introduce the *conformal time* η by the relation $ad\eta = dt$, in terms of which the RW metric (2.2) reads

$$\bar{g} = a^2(\eta) [-d\eta \otimes d\eta + \gamma_{ij} dx^i \otimes dx^j]. \quad (2.3)$$

Given the metric $\bar{g} = g_{\mu\nu}$, the 4-dimensional spacetime line element is given by

$$ds^2 = g_{\mu\nu} dx^\mu dx^\nu = -dt^2 + a^2(t) \gamma_{ij} dx^i dx^j, \quad (2.4)$$

$$= a^2(t) [-d\eta^2 + \gamma_{ij} dx^i dx^j], \quad (2.5)$$

For the constant time hypersurfaces one can choose spherical coordinates $x^i = (r, \theta, \varphi)$, where r is a *comoving* radial coordinate and (θ, φ) are the usual polar and azimuthal angles of spherical coordinates on the unit sphere \mathbb{S}_2 . The components of the spatial metric for this coordinate choice are given in the (comoving) spatial line element as

$$d\ell^2 = \gamma_{ij} dx^i dx^j = dr^2 + f_K^2(r) d\Omega^2, \quad (2.6)$$

where the angular part of the line element is given by

$$d\Omega^2 = d\theta^2 + \sin^2(\theta) d\varphi^2. \quad (2.7)$$

The function $D_A = f_K(r)$ defines the *comoving* angular diameter distance and depends on the sign of the curvature parameter K as

$$D_A = f_K(r) = \begin{cases} (-K)^{-1/2} \sinh(\sqrt{-K}r) & K < 0, \\ r & K = 0, \\ K^{-1/2} \sin(\sqrt{K}r) & K > 0. \end{cases} \quad (2.8)$$

Here $K^{-1/2}$ represents the curvature radius in each case, which is imaginary for negative curvature and infinite for zero curvature.

We can also replace r by $D_A = f_K(r)$ as the spatial coordinate. In terms of $x^i = (D_A, \theta, \varphi)$, the spatial metric reads

$$d\ell^2 = \gamma_{ij} dx^i dx^j = \frac{dD_A^2}{1 - KD_A^2} + D_A^2 d\Omega^2. \quad (2.9)$$

From Eqs. (2.8) one can see that the spatial metric γ_{ij} for the $K \neq 0$ cases reduces to the flat case when $r|K|^{1/2} \rightarrow 0$, i.e. for scales much smaller than the curvature radius $|K|^{-1/2}$.

Fundamental observers move on lines defined by constant comoving coordinates, i.e. $x^i = \text{const.}$, so their four-velocity components are $u^\mu = dx^\mu/dt = \delta_0^\mu$ on coordinates $x^\mu = (t, x^i)$ and consequently $u^\nu = a^{-1}\delta_0^\nu$ on coordinates $x^\nu = (\eta, x^i)$.

In Appendix A we provide further discussion on alternative coordinates, metrics and curvature definitions.

2.1.2 Redshift

The *redshift* z of a source at emission (e), as measured by an observer (o), is defined in terms of the wavelength λ of light,

$$z = \frac{\lambda_o - \lambda_e}{\lambda_e}. \quad (2.10)$$

On astrophysical observations, measurements of redshifts are commonly performed by identifying absorption or emission lines for particular elements in object's spectra and comparing them with known (laboratory) ones for the same elements at rest. This implicitly assumes that atomic physics does not change over cosmological scales. For the RW geometry, a cosmological redshift can be introduced as a pure gravitational effect related to the scale factor by (Weinberg, 1972)

$$1 + z = \frac{a(t_o)}{a(t_e)}. \quad (2.11)$$

In a simplified way, we can understand Eq. (2.11) as the effect on observed spectra due to the evolution of distance measurements in the universe. As $a(t)$ is a free function, in order for the RW metric to be a solution of the EFE for particular matter-energy content, it is useful to rescale it such that $a(z = 0) = 1$, i.e., since $z = 0$ should be equivalent to the present time, we fix the scale factor to be unity today.

2.1.3 Einstein equations and Friedmann equations

In order to specify a cosmological model, besides the spacetime geometry, one needs a suitable matter/energy content and a gravitational theory or a specification of the interaction of the geometry and the matter/energy content (Ellis & van Elst, 1999). Modern Cosmology assumes the latter through Einstein's relativistic gravitational field equations (EFE) given by

$$G_{ab} := R_{ab} - \frac{1}{2}Rg_{ab} = \kappa T_{ab} - \Lambda g_{ab}, \quad (2.12)$$

where G_{ab} and R_{ab} are the components (on a general basis) of the Einstein and Ricci tensors, respectively, R is the Ricci (or curvature) scalar, $\kappa := 8\pi G_N^2$, T_{ab} are the components of the energy-momentum tensor and Λ is the cosmological constant, a spacetime constant in the sense that its covariant derivative is null, i.e., $\nabla_a \Lambda = 0$. The EFE also guarantee the local conservation of energy and momentum, as the twice-contracted Bianchi identities, $\nabla_a G^{ab} = 0$, imply $\nabla_a T^{ab} = 0$ (Weinberg, 1972).

Any cosmological model with a RW geometry and some suitably specified matter/energy content determining the dynamical evolution according to General Relativity via the EFE Eqs. (2.12) is called a *Friedmann-Lemaître-Robertson-Walker* model (FLRW). In this work, only FLRW cosmological models are considered. On any FLRW model, as a consequence of the cosmological principle, the only non-zero energy/momentum variables are the energy density ρ and the isotropic pressure p . It is important to note that there are neither vectors nor tensors non-zero energy-momentum degrees of freedom. Furthermore, these scalar fields are all functions of time alone, because of the assumptions of homogeneity and isotropy. Thus, fundamental observers on FLRW models measure an energy-momentum tensor, irrespective of the chosen time coordinate, cosmic or conformal, of the form

$$T_\mu{}^\nu = T_{\mu\sigma}g^{\sigma\nu} = \begin{bmatrix} -\rho & 0 & 0 & 0 \\ 0 & p & 0 & 0 \\ 0 & 0 & p & 0 \\ 0 & 0 & 0 & p \end{bmatrix}. \quad (2.13)$$

In other words, FLRW universe models are made up of energy-matter contents that give rise to an effective perfect fluid energy-momentum tensor. From the 10 components of T_{ab} , only the two scalar ones are non-zero.

The equations governing the dynamics of FLRW universe models can be obtained considering the EFE Eqs. (2.12), for the RW geometry in Eq. (2.3)

²Throughout this work natural units are assumed $c = \hbar = k_B = 1$. Then the gravitational constant in EFE reads $\kappa = 8\pi G_N$, where G_N is Newton's gravitational constant.

with the energy-momentum tensor given by Eq. (2.13). In terms of the conformal time η the EFE equations are³

$$\left(\frac{a'}{a}\right)^2 + K = \frac{\kappa}{3}a^2\rho + \frac{a^2\Lambda}{3}, \quad (2.14a)$$

$$2\left(\frac{a''}{a}\right) + \left(\frac{a'}{a}\right)^2 + K = -\kappa a^2 p + a^2\Lambda; \quad (2.14b)$$

and in terms of the cosmic time are

$$\left(\frac{\dot{a}}{a}\right)^2 + \frac{K}{a^2} = \frac{\kappa}{3}\rho + \frac{\Lambda}{3}, \quad (2.15a)$$

$$2\frac{\ddot{a}}{a} + \left(\frac{\dot{a}}{a}\right)^2 + \frac{K}{a^2} = -\kappa p + \Lambda. \quad (2.15b)$$

The local conservation of energy/momentum is contained on the systems of Eqs. (2.14) and (2.15) because of the Bianchi identities and can be expressed by

$$\rho' + 3\frac{a'}{a}(\rho + p) = 0 \quad \text{and} \quad \dot{\rho} + 3\frac{\dot{a}}{a}(\rho + p) = 0, \quad (2.16)$$

in conformal and cosmic time respectively.

The systems of Eqs. (2.14) or (2.15) are known as the *Friedmann equations* and relate the rate of expansion/contraction of the universe with its matter/energy content and its spatial curvature. On the other hand, Eqs. (2.16) describe the energy conservation in the universe.

When $a \neq 0$, Eq. (2.15b) is easily readable from Eq. (2.15a) and the last equation in Eq. (2.16). Therefore, the Friedmann equation Eq. (2.15a) and the conservation equation Eq. (2.16) are enough to describe the expansion.

2.1.4 Density parameters

It is useful and also a common practice in the literature to write the Friedmann equations in adimensional form. Therefore, *dimensionless density parameters* are introduced as

$$\Omega_i(\eta) = \frac{\rho_i(\eta)}{\rho_{\text{crit}}}, \quad \Omega_\Lambda = \frac{\Lambda}{3H^2}, \quad (2.17)$$

where $\rho_{\text{crit}} := 3H^2/\kappa$ is the *critical density*, corresponding to the evolution that the energy density would have in the exact case of a spatially flat universe, with $H := \dot{a}/a$ the *Hubble parameter*. A density-like parameter for

³Throughout this work the prime symbol ' denotes derivative with respect to conformal time η and the dot ' with respect to cosmic time t .

curvature can also be introduced as $\Omega_K(\eta) = -K/a^2 H^2$ in terms of which the Friedmann equation (2.15a) becomes

$$\Omega + \Omega_\Lambda + \Omega_K = 1. \quad (2.18)$$

The density parameter Ω here represents the contribution to the energy density of all matter-energy fields present, i.e. baryons, cold dark matter (CDM), radiation, neutrinos, etc., but not the cosmological constant. It is useful to separate the radiation and matter contributions, $\Omega = \Omega_m + \Omega_r$, because of their different evolutions. We can further split matter into CDM and baryons as $\Omega_m = \Omega_c + \Omega_b$. The conservation Eq. (2.16) is easily solved for perfect fluids with equation of state (EOS) $w = p/\rho = \text{constant}$. For species i , one finds⁴

$$\rho_i(a) = \rho_{i0} a^{-3(1+w_i)} = \Omega_i(a) \rho_{\text{crit}}(a) \quad (2.19)$$

Taking into account that for pressureless matter $w = 0$ and for radiation $w = 1/3$, the Friedmann equation can be written in adimensional form as

$$\begin{aligned} E^2(a) &:= \frac{H^2(a)}{H_0^2} = \Omega_{m0} a^{-3} + \Omega_{r0} a^{-4} + \Omega_K a^{-2} + \Omega_{\text{DE}0} a^{-3(1+w)}, \\ E^2(z) &= \Omega_{m0}(1+z)^3 + \Omega_{r0}(1+z)^4 + \Omega_K(1+z)^2 + \Omega_{\text{DE}0}(1+z)^{3(1+w)}, \end{aligned} \quad (2.20)$$

where to simplify we are writing $\Omega_K = \Omega_{K0} = -K/H_0^2$, and we introduced a constant *equation of state* parameter for dark energy (DE) $w = p_{\text{DE}}/\rho_{\text{DE}}$. We also defined the time-dependent function $E(z)$ as the Hubble parameter normalized by its value today, and we used Eq. (2.11) choosing $a_0 = 1$.

When DE is assumed to be a cosmological constant, we replace Ω_{DE} by Ω_Λ , and set $\rho_{\text{DE}}(z) = \rho_{\text{DE}0}$; otherwise, it is described by the energy density ρ_{DE} and may change with time. Finally, it is also a common practice in the literature to describe the Hubble parameter evolution with the dimensionless variable h defined via

$$H_0 = 100h \frac{\text{Km/s}}{\text{Mpc}}. \quad (2.21)$$

Frequently we make use of the distance scale

$$\frac{c}{H_0} = \frac{2.997 \times 10^5 \text{ Km/s}}{100 \text{ Km/s (Mpc/h)}^{-1}} = 2997 \text{ Mpc/h} \quad (2.22)$$

and carry h along within distance or mass units.

⁴Throughout this work, quantities indexed by a 0 are defined to be evaluated today.

2.1.5 Distances

There are many ways of characterizing distance measurements between two points in the RW metric. For instance, since photons move on null geodesics ($ds^2 = 0$), we may consider the radial trajectory ($d^2\Omega = 0$) of photons. This defines the *line-of-sight* or *radial comoving distance* of an object at redshift z to us at $z = 0$, which is given by the *distance-redshift* relation

$$r(z) = \int_0^r dr' = \int_t^{t_0} \frac{dt'}{a(t')} = \int_0^z \frac{dz'}{H(z')} = D_{\text{H}0} \int_0^z \frac{dz'}{E(z')}, \quad (2.23)$$

where we used $da/dt = aH(a)$ and $a = (1+z)^{-1}$ above. Recall $E(z) = H(z)/H_0$ describes the expansion history according to the Friedmann Eq. (2.20) and we introduced the *Hubble distance*,

$$D_{\text{H}}(z) = \frac{c}{H(z)}, \quad D_{\text{H}0} = \frac{c}{H_0} \sim 2997 h^{-1} \text{ Mpc}. \quad (2.24)$$

One can say that the radial comoving distance $r(z)$ is the key distance measure in cosmology/cosmography, as all other relevant cosmological distance measures can be expressed in terms of this definition (for a review on distance measures, see, e.g. Hogg, 1999).

The ratio of an object's *comoving* transverse size to its angular size in radians is a very convenient astronomical distance, called *comoving* angular diameter distance D_{A} . Directly from the angular piece of the RW metric ($dr = 0$) and Eq. (2.8), we can see that $D_{\text{A}}(z) = f_{\text{K}}(r)$, or in terms of r , $D_{\text{H}0}$ and $\Omega_{\text{K}} = -K/H_0^2$

$$D_{\text{A}} = f_{\text{K}}(r) = \begin{cases} D_{\text{H}0} \Omega_{\text{K}}^{-1/2} \sinh\left(\Omega_{\text{K}}^{1/2} r/D_{\text{H}0}\right) & K > 0 \\ r & K = 0 \\ D_{\text{H}0} |\Omega_{\text{K}}|^{-1/2} \sinh\left(|\Omega_{\text{K}}|^{1/2} r/D_{\text{H}0}\right) & K < 0 \end{cases} \quad (2.25)$$

Finally, the *comoving volume* element, dV_{C} , is the volume measure in which number densities of non-evolving objects at each constant time hypersurface remain invariant. For a solid angle element, $d^2\Omega = \sin\theta d\theta d\phi$, the associated comoving volume element is given by

$$dV_{\text{C}} = (D_{\text{A}}^2 d^2\Omega) dr = D_{\text{H}0} \frac{D_{\text{A}}^2}{E(z)} d^2\Omega dz = D_{\text{V}}^3 d^2\Omega dz, \quad (2.26)$$

where on the last equality we introduced an effective *comoving volume distance*, D_{V} , combining comoving angular and radial distances in RW geometries.

For all *comoving* quantities defined above, one can trivially obtain *physical* quantities by multiplication of the scale factor $a = (1+z)^{-1}$.

2.2 Cosmological perturbation theory

In GR, in principle we have to solve ten coupled nonlinear partial differential equations for the metric tensor in terms of the gravity sources represented in the energy-momentum tensor: the EFE Eq. (2.12). This is only from the purely gravitational side. In cosmology, we also need to consider the evolution of species and their couplings. This is commonly done in the context of kinetic theory, so one formally needs to solve the coupled perturbed Boltzmann equations. The idea of perturbation theory (PT) is to reformulate (e.g., linearizing) the problem as an infinite hierarchy of linear differential equations for deviations of the metric with respect to a known solution of the EFE that defines the *background solution* of the system considered. In this way, one translates the difficulty from nonlinearity to the infinite number of equations (see, e.g., Wald, 1984, §7.5). The key assumption of the perturbative scheme is, as common practice in Physics, that one can truncate the problem at a finite order and obtain an approximate solution to the original system that is accurate enough for purposes of comparing theory predictions to observations.

The cosmological principle allows for relatively oversimplified background solutions of the EFE Eq. (2.12) as we saw above. Physical reality is far more complicated, as the distribution of matter is not exactly homogeneous on all scales. On small scales, below around 100 Mpc, one observes a vast variety of structures such as *walls* and *filaments* of matter, galaxy clusters, and galaxies. Besides, given the nonlinear nature of the EFE, it is a challenging task to solve them precisely for more complicated spacetime models. Thus, in order to obtain realistic models to compare with observations, one needs to consider approximations, aiming to obtain *almost-FLRW* models representing a universe that is FLRW-like on large scales, but allowing for generic inhomogeneities on small scales.

One major problem in studying such perturbed models is the *gauge problem*, related to the arbitrariness on the identification of perturbed and unperturbed (background) physical degrees of freedom (see, e.g. §5.2 in Peter & Uzan, 2013; Bardeen, 1980; Ma & Bertschinger, 1995; Bruni et al., 1997, for detailed discussions). Such identification depends on the choice of the coordinate system and thus on the specific spacetime observer. Consequently, the dynamical equations written in terms of perturbation variables have as solutions both *physical modes* and *gauge modes*, the latter corresponding to variations of gauge choice, i.e., a choice of the coordinate system used, rather than a physical variation of the corresponding background quantity. A way to overcome this problem is to identify proper *gauge-invariant* modes describing the physical degrees of freedom on the perturbative quantities, i.e.,

the actual physically observable quantities.

The fluctuations (perturbations) on the metric and the energy-momentum tensor of an FLRW model can be separated into three different modes: scalar-, vector- and tensor-like, the so-called *scalar, vector and tensor* (SVT) decomposition, which evolve independently in linear theory (Peter & Uzan, 2013). In this work, we will concentrate on scalar modes since they connect the metric perturbations to density, pressure, and velocity (see § B.3). Vector-like perturbations are damped by the cosmic expansion, and tensor modes are related to the propagation of gravitational waves. Our description here will focus mostly on linear scalar perturbations, although when comparing theory to observations, we must also consider nonlinear effects which propagate into linear scales. Linear (first order) scalar perturbations can be generally described by four functions for the metric and four for the energy-momentum tensor according to Eqs. (B.28) and (B.45) respectively.

The energy-momentum perturbations can be identified with the following physical quantities (for a detailed discussion, see § B.3.4): (a) the density contrast (fluctuation) at point \mathbf{x} and time η relative to the mean value $\rho(\eta)$,

$$\delta(\mathbf{x}, \eta) = \frac{\rho(\mathbf{x}, \eta)}{\rho(\eta)} - 1 \quad (2.27)$$

(b) the peculiar velocity, i.e., the intrinsic velocity of objects with respect to the comoving coordinates, $\mathbf{v}(\mathbf{x}, \eta)$ (c) the isotropic pressure perturbation $\delta p(\mathbf{x}, \eta) = p(\mathbf{x}, \eta) - \bar{p}(\eta)$, and (d) the anisotropic stress Π .

The solutions for these variables contain modes that depend on the choice of the coordinate system, i.e., on a *gauge* choice. Since scalar degrees of freedom of gauge transformations are characterized by two scalar fields, it is possible to choose a combination of the eight variables above and obtain six scalar *gauge invariant quantities* (see e.g. Bardeen, 1980; Ma & Bertschinger, 1995) and § B.3.3 and § B.3.4). Since in this work the interest is on the clustering of matter in the universe, the problem to consider is the evolution of the pressureless fluid (pure dust) describing the total content of matter in the universe, CDM plus baryonic, for which the energy-momentum tensor can be chosen as, $T_{ab} = u_a u_b \rho$, with u^a the fluid four-velocity and ρ the energy density. The scalar first order EFE in PT contains all the dynamics of the system. A detailed derivation of the gauge-invariant EOM to first order is presented in Appendix B.

On sufficiently large scales, the gravitational evolution of fluctuations in the total matter in the universe follows linear perturbation theory. In order to understand this linear evolution, let us introduce first-order perturbations to the metric tensor. For simplicity, let us follow the standard literature

and consider the *conformal Newtonian Gauge* in (η, x^i) coordinates. This is nothing but the general scalar gauge case, Eq. (B.28), fixing $B = E = 0$, leaving the metric non-vanishing components,

$$\delta g_{00} = -2\Phi, \quad (2.28a)$$

$$\delta g_{ij} = 2a^2 \gamma_{ij} \Psi, \quad (2.28b)$$

where Φ, Ψ are gravitational potentials representing first order scalar perturbations to the metric, and recall γ_{ij} is the spatial metric within the RW spacetime metric.⁵

Likewise, we may introduce perturbations to the energy-momentum tensor. In the same gauge and for a general species, (see discussion in § B.3.4), we can write

$$\delta T^0_0 = -\delta\rho, \quad (2.29a)$$

$$\delta T^0_i = (\bar{\rho} + \bar{p}) (D_i v), \quad (2.29b)$$

$$\delta T^i_j = \delta p \gamma^i_j + a^2 \delta \pi^i_j. \quad (2.29c)$$

where $\delta\rho, \delta p$ are first order perturbations to the density and pressure. Similarly v is the first order scalar mode of the velocity of fundamental observers, Eq. (B.42), under SVT decomposition (see § B.3.1), i.e, the field of peculiar velocities. Notice that here D^i represents the covariant derivative related to the spacial metric γ_{ij} , i.e., on the constant time hypersurfaces (for a flat universe ($K = 0$) $\gamma_{ij} = \delta_{ij}$ in cartesian coordinates and $D_i = \partial_i$). Finally $\delta \pi^i_j$ is the perturbation related to the so-called anisotropic stress.

The first order EFE, $\delta G^\mu_\nu = \kappa \delta T^\mu_\nu$, on the comoving Newtonian gauge therefore results in (see § B.3.5 for a more general and detailed discussion)

$$(\nabla^2 + 3K) \Psi - 3\mathcal{H} (\Psi' + \mathcal{H}\Phi) = a^2 \frac{\kappa}{2} \delta\rho, \quad (2.30a)$$

$$\Psi' + \mathcal{H}\Phi = -a^2 \frac{\kappa}{2} (\bar{\rho} + \bar{p}) v, \quad (2.30b)$$

$$\Phi'' + 2\mathcal{H}\Phi' - K\Phi + \mathcal{H}\Psi' + (2\mathcal{H}' + \mathcal{H}^2) \Psi = a^2 \frac{\kappa}{2} \delta p, \quad (2.30c)$$

$$\Phi - \Psi = a^2 \kappa \Pi, \quad (2.30d)$$

where Π is the scalar part of $\delta \pi^i_j$ according to Eq. (B.44). Note that the set of EFE's above formally contains the local conservation of the energy-momentum tensor $\nabla_\mu T^\mu_\nu = 0$ as long as Bianchi identities hold.

⁵We call the reader's attention to the convention adopted. On some textbooks the notation for the gravitational potentials is the opposite of the one adopted here.

This system fully describes the evolution of perturbations in the matter-energy content associated with gravitational perturbations around FLRW when coupled with the corresponding background solutions. One immediate conclusion from the last of the above equations is that for species having zero scalar anisotropic stress, $\Pi = 0$, the first order metric perturbations are equal, i.e., $\Psi = \Phi$ and we only need to consider one gravitational potential in the EOM.

2.2.1 Linear growth evolution of matter

Let us now specialize and simplify our discussion for cold-dark-matter (CDM), which is described by an energy-momentum tensor with zero pressure and anisotropic stress to all orders in PT. From the previous discussion and to first order, one then ends up with three independent linear scalar degrees of freedom: a gravitational potential $\Phi = \Psi$, the density fluctuation δ , and the scalar component of the peculiar velocity v . Their evolution is described by the three first equations in Eq. (2.30) (the fourth one sets $\Phi = \Psi$) which can be combined with the background equations in order to arrive at the system (for a more detailed and general discussion see § B.3)

$$\delta' + (\nabla^2 + 3K)v = 0, \quad (2.31a)$$

$$v' + \mathcal{H}v + \Phi = 0, \quad (2.31b)$$

$$(\nabla^2 + 3K)\Phi = a^2 \frac{\kappa}{2} \bar{\rho} \delta. \quad (2.31c)$$

This system of equations fully describes the problem for gauge invariant degrees of freedom in the context of GR. In Eq. (2.31) $\mathcal{H} = a'/a$ is the *conformal Hubble parameter*. Recall that primes denote derivatives with respect to the conformal time, δ , v and Φ denote the gauge-invariant density contrast, velocity potential, and gravitational potential and are gauge-invariant up to first order. Actually v denotes the longitudinal (the only scalar one) part of the velocity field, i.e., $v^i = D^i v$ (see Appendix B for details).

It is possible to eliminate the variables v and Φ to obtain an evolution equation for the gauge-invariant fluctuation in the matter density contrast δ :

$$\delta'' + \mathcal{H}\delta' - \frac{3H_0^2 \Omega_{m0}}{2a(\eta)} \delta = 0. \quad (2.32)$$

Note that, as long as the equations describe pressure-less matter, the background evolution is given by

$$\bar{\rho}(\eta) = \rho_{\text{crit}} \Omega_m(\eta) = \frac{3H_0^2}{\kappa} \Omega_m(\eta) = \frac{3H_0^2}{\kappa a^3(\eta)} \Omega_{m0}. \quad (2.33)$$

The equation for δ is separable in the time and spatial coordinates, so the solutions will be written as

$$\delta(\eta, x^i) = \delta(\eta_0, x^i) \frac{D(\eta)}{D(\eta_0)} = \delta_0(x^i) \frac{D(\eta)}{D(\eta_0)}, \quad (2.34)$$

Obviously we can normalize D to any arbitrary time. In this work, by convenience, the normalization is chosen with respect to the present time⁶. Therefore, the time-dependent part of the solution satisfies the equation

$$D'' + \mathcal{H}D' - \frac{3H_0^2\Omega_{m0}}{2a(\eta)}D = 0. \quad (2.35)$$

In Eq. (2.35) one has the freedom to change the time variable for the cosmic time, the scale factor, or the cosmic redshift depending on what is more convenient. The equations for these variables are then given by

$$\ddot{D} + 2H\dot{D} - \frac{3H_0^2\Omega_{m0}}{2a^3(t)}D = 0, \quad (2.36)$$

for the cosmic time,

$$\frac{d^2D}{da^2} + \left[\frac{3}{a} + \frac{d \ln E(a)}{da} \right] \frac{dD}{da} - \frac{3\Omega_{m0}}{2E(a)a^5}D = 0, \quad (2.37)$$

for the scale factor, where again $E(a)$ describes the expansion history according to the Friedmann Eq. (2.20), and

$$\frac{d^2D}{dz^2} + \left[\frac{1}{(1+z)} - \frac{d \ln E(z)}{dz} \right] \frac{dD}{dz} + \frac{3\Omega_{m0}(1+z)}{2E(z)}D = 0, \quad (2.38)$$

for the redshift.

The solutions for D depend on the background evolution via the Hubble parameter H . Solutions reduced to quadrature can only be obtained for very specific matter-energy contents and DE models. In general, the problem of finding the time evolution of matter fluctuations must be treated numerically, as is done in this work.

Consider now the evolution of the velocity field. Combining equations (2.31) with the solution for the matter fluctuations equation (2.34), one finds

$$v' + \mathcal{H}v = -\Phi = -\frac{3H_0^2\Omega_{m0}}{2a}G(\eta) (\nabla^2 + 3K)^{-1} \delta_0, \quad (2.39)$$

⁶Quantities with the subscript $_0$ denote evaluation at the present time.

where G denotes the growth factor normalized to its value today,

$$G(\eta) = D(\eta)/D(\eta_0). \quad (2.40)$$

The homogeneous solution of equation (2.39) is a decaying mode in time, $v_{\text{hom}} \propto a^{-2}$. An inhomogeneous solution can be obtained as

$$v = -\mathcal{H}Gf (\nabla^2 + 3K)^{-1} \delta_0 = -aHGf (\nabla^2 + 3K)^{-1} \delta_0, \quad (2.41)$$

where the function

$$f(\eta) := \frac{d \ln(G)}{d \ln(a)} = \frac{a}{G} \frac{dG}{da} = \frac{G'}{\mathcal{H}G} = \frac{\dot{G}}{HG}. \quad (2.42)$$

One may prove that Eq. (2.41) is actually a solution of the inhomogeneous equation, by separating variables to see that the spatial-dependent part goes as $(\nabla^2 + 3K)^{-1} \delta_0$ and the time-dependent part v_t satisfies

$$v_t' + \mathcal{H}v_t + \frac{3H_0^2 \Omega_{m0}}{2a} G(\eta) = 0, \quad (2.43)$$

so that, by comparing with the equation for the growth factor, Eq. (2.35), the solution can be written as $v_t = -G'(\eta) = -\mathcal{H}Gf$.

Up to now, we have been considering the general case of arbitrary spatial curvature for pedagogical purposes. From now on, we will set $K = 0$ as will be set for the analysis in subsequent chapters.

Peculiar velocities of galaxies from Eq. (2.41) induce RSD's in galaxy correlations. We will consider these effects in § 2.4.5 and incorporate them into predictions for galaxy correlations and spectra.

2.2.2 Nonlinear evolution

The linear theory described above cannot explain the vast complexity of structures observed below the typical scales of clusters of galaxies. Currently, there are three main approaches to tackle the issue of non-linearities for the dark matter scenario: perturbation theory, phenomenological models as the halo model and numerical modeling through, e.g. N-body simulations. In the present section, we will focus on the perturbative approach, and in the next section, we consider the halo model.

We will not discuss the use of N-body simulations, but there are multiple N-body codes and catalogs available for use (see, e.g. Klypin et al., 2016, and references therein). Approximate numerical methods for gravitational structure formation have appeared recently as a result of the increase

in computational requirements for full N-body simulations. Such methods have been designed mainly to produce approximate mock catalogs useful to approximate the complex covariance matrices of clustering statistics. Recently, Lippich et al. (2019); Colavincenzo et al. (2019) and Blot et al. (2019) classified the underlying algorithms in three main categories: i) predictive methods that follow the evolution of the linear density field deterministically: ICE-COLA (Izard et al., 2016), PEAK PATCH (Bond & Myers, 1996), and PINOCCHIO (Munari et al., 2017), ii) methods that require a calibration with N-body simulations: PATCHY (Kitaura et al., 2014) and HALOGEN (Avila et al., 2015), iii) and simpler recipes based on assumptions regarding the shape of the probability distribution function (PDF) of density fluctuations, e.g., lognormal (Xavier et al., 2016; Agrawal et al., 2017) and Gaussian density fields (Grieb et al., 2016). These references also present a performance comparison among these methods. For the work presented in Chap. 5, we made use of one method of the second category, namely, HALOGEN (Avila et al., 2015), which shows an excellent performance in reproducing two-point statistics covariance.

Perturbation theory, introduced in what follows, offers theoretical predictions with the advantage of being nearly free of fitting parameters in contrast to some degree of complexity from the numerical point of view. Less complex and consequently faster predictions for the clustering statistics have also been developed inspired by other theoretical models. For instance, Halofit (see e.g, Takahashi et al., 2012, and references therein) provides a fitting formulae for the nonlinear matter power spectrum inspired by the Halo Model⁷, parametrizing nonlinear effects as a combination of one- and two-halo terms fitted using numerical simulations.

On scales much smaller than the horizon and restricting the analysis to a spatially flat background, Newtonian physics can be used to sufficiently good approximation to describe the structure evolution (Peebles, 1980). The Newtonian equations for an ideal fluid of zero pressure in comoving coordinates are (see e.g., Peebles, 1980; Bernardeau et al., 2002),

$$\dot{\delta} + \frac{1}{a} \nabla \cdot [(1 + \delta) \mathbf{v}] = 0, \quad (2.44a)$$

$$\dot{\mathbf{v}} + H \mathbf{v} + \frac{1}{a} \mathbf{v} \cdot \nabla \mathbf{v} = -\frac{1}{a} \nabla \Phi, \quad (2.44b)$$

where $H = \dot{a}/a$ is the Hubble factor.

These are the *continuity* and *Euler equations* for the fluid, written in terms of the density fluctuation and comoving coordinates. In conjunction

⁷Introduced below in § 2.3.

with the Poisson equation (2.31c) in the spatially flat case,

$$\nabla^2\Phi = 4\pi G a^2 \bar{\rho}\delta \quad (2.45)$$

i.e., the standard *Poisson equation* for the Newtonian gravitational field in comoving coordinates, this system of equations fully specifies the dynamics of the fluid.

Linearizing the equations of motion (EOM), i.e considering only terms linear in δ and \mathbf{v} , the Newtonian EOM (2.44a) and (2.44b) become

$$\dot{\delta} + \frac{1}{a}\nabla \cdot \mathbf{v} = 0, \quad (2.46a)$$

$$\dot{\mathbf{v}} + H\mathbf{v} = -\frac{1}{a}\nabla\Phi. \quad (2.46b)$$

Thus, along with the Poisson Eq. (2.45), they are equivalent to the GR system for scalar perturbations in the spatially-flat case ($K = 0$), equations (2.31c). To see this explicitly, just make a change of variables $t \rightarrow \eta$ via $dt = a d\eta$ and introduce the velocity scalar potential v via $v_i = \partial_i v$.

In order to describe the fully nonlinear evolution, we must depart from the linear perturbation theory just discussed above. Given the difficulty to find exact solutions of the nonlinear dynamical Eqs. (2.44)–(2.45), a perturbative approach can be chosen. Our following discussion on the perturbative approach within the framework of spatial flatness and Newtonian description follows closely that of Bernardeau et al. (2002) and § 2.2 of Montesano (2011), to which we refer the reader for more details and discussion.

We begin by introducing the variable $\theta := \nabla \cdot \mathbf{v}$, the divergence of the peculiar velocity field. This variable is particularly useful because according to the SVT decomposition, for a spatially flat background $v_i = \partial_i v$, and therefore θ is nothing but the Laplacian of the scalar peculiar velocity potential, i.e.,

$$\theta = \nabla \cdot \mathbf{v} = \partial_i v^i = \partial_i \partial^i v = \nabla^2 v, \quad (2.47)$$

so that, by combining with the linear solution Eq. (2.41), we see that at the linear level it has the solution

$$\theta = -\mathcal{H}Gf\delta_0 = -aHGf\delta_0, \quad (2.48)$$

i.e., in the linear regime the spatial evolution of θ is given by the density contrast field of total matter today and its temporal evolution is the same of the scalar peculiar velocity potential, Eq. (2.41).

Thus, in terms of θ , one can take the Fourier transform of the full nonlinear continuity Eq. (2.44a) and obtain its representation in Fourier space

as

$$a\dot{\delta}(\mathbf{k}, t) + \theta(\mathbf{k}, t) = - \int d^3\mathbf{x} e^{i\mathbf{k}\cdot\mathbf{x}} \nabla \cdot (\mathbf{v}\delta)(\mathbf{x}, t). \quad (2.49)$$

One can then perform an integration by parts and write down the $\delta(\mathbf{k})$ and $\mathbf{v}(\mathbf{k})$ fields as Fourier integrals to obtain

$$a\dot{\delta}(\mathbf{k}, t) + \theta(\mathbf{k}, t) = - \int \frac{d^3\mathbf{k}_1}{(2\pi)^3} \int \frac{d^3\mathbf{k}_2}{(2\pi)^3} i\mathbf{k}\cdot\mathbf{v}(\mathbf{k}_1, t) \delta(\mathbf{k}_2, t) \int d^3\mathbf{x} e^{i\mathbf{x}\cdot(\mathbf{k}-\mathbf{k}_1-\mathbf{k}_2)}. \quad (2.50)$$

One now assumes the peculiar velocity field \mathbf{v} to be curl-free. This assumption was implicit in the SVT decomposition $v^i = D^i v$ in the context of relativistic perturbations as long as the transverse vectorial mode was not considered because we only consider scalar perturbations. In the Newtonian context, this assumption can be justified by noting that for a pressure-less ideal fluid, *linear* vorticity perturbations, that is, the transverse part of the peculiar velocity decays as a^{-1} (see § 2.3-2.4 in Bernardeau et al., 2002). The velocity then has only a divergence (scalar potential) part v , which in Fourier representation is expressed as $\mathbf{v}(\mathbf{k}) \propto \mathbf{k}$, so that on the last integral one can write

$$\mathbf{k} \cdot \mathbf{v}(\mathbf{k}_1, t) = \left[\mathbf{k} \cdot \hat{\mathbf{k}}_1 \right] \left[\hat{\mathbf{k}}_1 \cdot \mathbf{v}(\mathbf{k}_1, t) \right]. \quad (2.51)$$

Moreover, the \mathbf{x} -integral can be computed to give a Dirac delta function multiplied by $(2\pi)^3$ and thus one finally arrives to

$$a\dot{\delta}(\mathbf{k}, t) + \theta(\mathbf{k}, t) = - \int \frac{d^3\mathbf{k}_1}{(2\pi)^3} \int d^3\mathbf{k}_2 \delta_D(\mathbf{k}-\mathbf{k}_1-\mathbf{k}_2) \alpha(\mathbf{k}_1, \mathbf{k}_2) \theta(\mathbf{k}_1, t) \delta(\mathbf{k}_2, t), \quad (2.52)$$

with

$$\alpha(\mathbf{k}_1, \mathbf{k}_2) := \frac{(\mathbf{k}_1 + \mathbf{k}_2) \cdot \mathbf{k}_1}{k_1^2}. \quad (2.53)$$

In a way analogous to the calculation for the continuity equation, the Euler Eq. (2.44b) can be written in Fourier space, after combining it with the Poisson Eq. (2.45) as

$$a\dot{\theta}(\mathbf{k}, t) + \dot{a}\theta(\mathbf{k}, t) + \frac{3H_0\Omega_{m0}}{2a}\delta(\mathbf{k}, t) = - \int d^3\mathbf{x} e^{i\mathbf{k}\cdot\mathbf{x}} [\partial_i (v_j \partial_j) v_i](\mathbf{x}, t), \quad (2.54)$$

so that, integrating by parts and expanding the fields δ and \mathbf{v} in Fourier modes, the integral on the right-hand side becomes

$$- \int \frac{d^3\mathbf{k}_1}{(2\pi)^3} \int \frac{d^3\mathbf{k}_2}{(2\pi)^3} i\mathbf{k} \cdot \mathbf{v}(\mathbf{k}_1, t) [i\mathbf{k} \cdot \mathbf{v}(\mathbf{k}_2, t) + v(\mathbf{k}_2, t)] \int d^3\mathbf{x} e^{i\mathbf{x}\cdot(\mathbf{k}-\mathbf{k}_1-\mathbf{k}_2)}. \quad (2.55)$$

Then, neglecting the curl-part of the velocity field, as before, one arrives at

$$a\dot{\theta}(\mathbf{k}, t) + \dot{a}\theta(\mathbf{k}, t) + \frac{3H_0\Omega_{m0}}{2a}\delta(\mathbf{k}, t) = - \int \frac{d^3\mathbf{k}_1}{(2\pi)^3} \int d^3\mathbf{x} \delta_D(\mathbf{k} - \mathbf{k}_1 - \mathbf{k}_2) \\ \times \beta(\mathbf{k}_1, \mathbf{k}_2)\theta(\mathbf{k}_1, t)\theta(\mathbf{k}_2, t), \quad (2.56)$$

with

$$\beta(\mathbf{k}_1, \mathbf{k}_2) := \frac{|\mathbf{k}_1 + \mathbf{k}_2|^2 \mathbf{k}_1 \cdot \mathbf{k}_2}{2k_1^2 k_2^2}. \quad (2.57)$$

The last expression is obtained with the requirement that the integrand in Eq. (2.56) is symmetric in $\mathbf{k}_1, \mathbf{k}_2$.

The kernels α and β , Eqs. (2.53) and (2.57), respectively, describe the coupling between different Fourier modes of the fields δ and θ arising from the nonlinear terms in the fluid EOM motion (2.44a)-(2.45). In this sense, the evolution of both harmonic modes $\delta(\mathbf{k})$ and $\theta(\mathbf{k})$ at a given wave vector is determined by the mode-coupling of both fields at all pairs of wave vectors $(\mathbf{k}_1, \mathbf{k}_2)$ and these should have a sum equal to \mathbf{k} (as expressed by the Dirac delta on the equations) which is consistent with the requirement of spatial homogeneity.

Eqs. (2.44a)-(2.45) can be easily written for the conformal time η as

$$\delta'(\mathbf{k}, \eta) + \theta(\mathbf{k}, \eta) = - \int \frac{d^3\mathbf{k}_1}{(2\pi)^3} \int d^3\mathbf{k}_2 \delta_D(\mathbf{k} - \mathbf{k}_1 - \mathbf{k}_2) \\ \times \alpha(\mathbf{k}_1, \mathbf{k}_2)\theta(\mathbf{k}_1, \eta)\delta(\mathbf{k}_2, \eta), \quad (2.58a)$$

$$\theta'(\mathbf{k}, \eta) + \mathcal{H}\theta(\mathbf{k}, \eta) + \frac{3}{2}\mathcal{H}\Omega_{m0}\delta(\mathbf{k}, \eta) = - \int \frac{d^3\mathbf{k}_1}{(2\pi)^3} \int d^3\mathbf{k}_2 \delta_D(\mathbf{k} - \mathbf{k}_1 - \mathbf{k}_2) \\ \times \beta(\mathbf{k}_1, \mathbf{k}_2)\theta(\mathbf{k}_1, \eta)\theta(\mathbf{k}_2, \eta) \quad (2.58b)$$

This pair of equations are the basis of the cosmological *standard perturbation theory* (SPT). We begin by noting that for an Einstein-de Sitter (EdS) cosmological model ($\Omega_{m0} = 1$ and $\Omega_\Lambda = 0$), the Friedmann equation implies $a(\eta) \propto \eta^2$ and $\mathcal{H}(\eta) = 2/\eta$, while the linear growth Eq. (2.35) implies $G(\eta) = a$ and consequently $f(\eta) = 1$. In this case, Eqs. (2.58) can formally be solved with a perturbative expansion of the form⁸

$$\delta(\mathbf{k}, \eta) = \sum_{n=1}^{\infty} a^n(\eta)\delta_n(\mathbf{k}), \quad (2.59a)$$

$$\theta(\mathbf{k}, \eta) = -\mathcal{H} \sum_{n=1}^{\infty} a^n(\eta)\theta_n(\mathbf{k}). \quad (2.59b)$$

⁸We do not provide here a proof of this statement. However, the reader can (see e.g., Bernardeau et al., 2002, and references therein).

Note that these expansions are actually with respect to the linear density fields, as is desired in any perturbative scheme as long as the perturbative terms are given by the EOM as

$$\delta_n(\mathbf{k}) = \int \frac{d^3\mathbf{q}_1 \cdots d^3\mathbf{q}_n}{(2\pi)^{3n-3}} \delta_D \left(\mathbf{k} - \sum_{i=1}^n \mathbf{q}_i \right) F_n(\mathbf{q}_1, \dots, \mathbf{q}_n) \delta_1(\mathbf{q}_1, 0) \cdots \delta_1(\mathbf{q}_n, 0), \quad (2.60a)$$

$$\theta_n(\mathbf{k}) = \int \frac{d^3\mathbf{q}_1 \cdots d^3\mathbf{q}_n}{(2\pi)^{3n-3}} \delta_D \left(\mathbf{k} - \sum_{i=1}^n \mathbf{q}_i \right) G_n(\mathbf{q}_1, \dots, \mathbf{q}_n) \delta_1(\mathbf{q}_1, 0) \cdots \delta_1(\mathbf{q}_n, 0), \quad (2.60b)$$

where the integration kernels F_n and G_n can be obtained from the fundamental mode coupling functions of the fields δ and θ , α and β (Eqs. (2.53) and (2.57) respectively) according to the recursion relations valid for $n \geq 2$ (Bernardeau et al., 2002)

$$F_n(\mathbf{q}_1, \dots, \mathbf{q}_n) = \sum_{m=1}^{n-1} \frac{G_m(\mathbf{q}_1, \dots, \mathbf{q}_m)}{(2n+3)(n-1)} [(2n+1)\alpha(\mathbf{k}_1, \mathbf{k}_2)F_{n-m}(\mathbf{q}_{m+1}, \dots, \mathbf{q}_n) + 2\beta(\mathbf{k}_1, \mathbf{k}_2)G_{n-m}(\mathbf{q}_{m+1}, \dots, \mathbf{q}_n)], \quad (2.61a)$$

$$G_n(\mathbf{q}_1, \dots, \mathbf{q}_n) = \sum_{m=1}^{n-1} \frac{G_m(\mathbf{q}_1, \dots, \mathbf{q}_m)}{(2n+3)(n-1)} [3\alpha(\mathbf{k}_1, \mathbf{k}_2)F_{n-m}(\mathbf{q}_{m+1}, \dots, \mathbf{q}_n) + 2n\beta(\mathbf{k}_1, \mathbf{k}_2)G_{n-m}(\mathbf{q}_{m+1}, \dots, \mathbf{q}_n)]. \quad (2.61b)$$

On these recursion relations $\mathbf{k}_1 := \sum_{j=1}^m \mathbf{q}_j$ and $\mathbf{k}_2 := \sum_{j=m+1}^n \mathbf{q}_j$. These functions represent the coupling between Fourier modes of the fields δ and θ describing the non-linearity of their EOM. Note further that at linear order, i.e., for $n = 1$, these two kernels should reduce to unity, i.e., $F_1 = G_1 = 1$.

For the second-order solutions ($n = 2$), one has (Bernardeau et al., 2002)

$$F_2(\mathbf{q}_1, \mathbf{q}_2) = \frac{5}{7} + \frac{1}{2} \frac{\mathbf{q}_1 \cdot \mathbf{q}_2}{q_1 q_2} \left(\frac{q_1}{q_2} + \frac{q_2}{q_1} \right) + \frac{2}{7} \frac{(\mathbf{q}_1 \cdot \mathbf{q}_2)^2}{q_1^2 q_2^2}, \quad (2.62a)$$

$$G_2(\mathbf{q}_1, \mathbf{q}_2) = \frac{3}{7} + \frac{1}{2} \frac{\mathbf{q}_1 \cdot \mathbf{q}_2}{q_1 q_2} \left(\frac{q_1}{q_2} + \frac{q_2}{q_1} \right) + \frac{4}{7} \frac{(\mathbf{q}_1 \cdot \mathbf{q}_2)^2}{q_1^2 q_2^2}. \quad (2.62b)$$

The remarkable feature of the perturbative solutions for EdS cosmological models above is the fact that they are *separated* for the time and the wave-numbers, i.e., they are made of products of terms that depend only on these variables. However, in general, the universe should not be well described

always by an EdS solution. For more general Λ CDM-like cosmological models the mentioned property of separability can be approximatively maintained by allowing for the respective solutions for the linear growth factor G and its logarithmic derivative f (see §2.4.4 Bernardeau et al., 2002, for some discussion). In this sense, Eqs. (2.59) can be replaced by

$$\delta(\mathbf{k}, \eta) = \sum_{n=1}^{\infty} G^n(\eta) \delta_n(\mathbf{k}) \quad (2.63a)$$

$$\theta(\mathbf{k}, \eta) = -\mathcal{H}(\eta) f(\eta) \sum_{n=1}^{\infty} G^n(\eta) \theta_n(\mathbf{k}) \quad (2.63b)$$

and remain approximately valid for any Λ CDM cosmology maintaining the same solutions for the wave-number dependent perturbative coefficients, equations (2.60).

The most remarkable application of the PT formalism depicted above is on the construction of a perturbative expansion for the power spectrum of the total matter in the universe. The power spectrum is the two-point correlation of Fourier modes of the field of matter fluctuations or equivalently the Fourier transform of the two-point correlation function describing the probability of finding overdensities separated by a given distance scale in the universe. Considering two wave-numbers \mathbf{k}_1 and \mathbf{k}_2 , the power spectrum of matter $P(\mathbf{k}_1, \mathbf{k}_2, \eta)$ at conformal time η is defined via the relation (see § 2.4.2 for details)

$$\langle \delta(\mathbf{k}_1, \eta) \delta^*(\mathbf{k}_2, \eta) \rangle = (2\pi)^3 \delta_{\text{D}}(\mathbf{k}_1 - \mathbf{k}_2) P(|\mathbf{k}_1 - \mathbf{k}_2|, \eta). \quad (2.64)$$

Note that it depends only on the magnitude of the difference of the wave-vectors and also the appearance of the Dirac delta function. These are consequences of the assumption of statistical homogeneity and isotropy of the field of matter fluctuations. If we introduce the PT perturbative solutions of Eqs. (2.63) into this definition we end with the mentioned expansion for the power spectrum, which clearly should have the form $P(k, \eta) = \sum_{i,j} P_{ij}(k, \eta)$, where the perturbative terms P_{ij} are given by the two-point correlation of the fluctuation on the matter density field at different orders, i and j , in SPT scheme,

$$(2\pi)^3 \delta_{\text{D}}(\mathbf{k}_1 - \mathbf{k}_2) P_{ij}(|\mathbf{k}_1 - \mathbf{k}_2|, \eta) := \langle \delta_i(\mathbf{k}_1, \eta) \delta_j^*(\mathbf{k}_2, \eta) \rangle. \quad (2.65a)$$

Note then that at all orders the separation property of the PT expansions imply that the temporal part can be separated according to $P_{ij}(k, t) = G^{i+j}(t) P_{ij}(k)$.

At linear order the power spectrum is then given simply as the correlation of the linear fluctuations

$$P_{\text{PT}}^{(0)} = P_{11}(k, t) = G^2(t)P_{\text{Lin}}(k), \quad (2.66)$$

where $P_{\text{Lin}}(k)$ is the linear power spectrum today, also known as the *initial power spectrum*. In the context of the Λ CDM concordance model of cosmology, such spectrum is parametrized as $P_{\text{Lin}}(k) \propto k^{n_s}T^2(k)$, where n_s is the *primordial scalar spectral index* directly related to the initial conditions defined by inflation and $T^2(k)$ is the *transfer function*, which encodes the information of the linear evolution of matter fluctuations through the radiation domination era and the resulting recombination era of decoupling of matter and radiation (Peter & Uzan, 2013). Such transfer function should then be tracked by using the full dynamics of the mixture of the different species presented in the universe at these stages via the out of equilibrium formalism of the Einstein-Boltzmann system (see, e.g., Chap. 7 in Dodelson, 2003). In this work we use sophisticated numerical codes devoted to evolving these equations, specifically, we used the CAMB code (Lewis & Bridle, 2002).

The next order contribution to the power spectrum from PT expansion is the sum of two terms, each one of which mixes up two linear power spectra, $P_{\text{PT}}^{(1)} = P_{22} + P_{13}$ where (Bernardeau et al., 2002)

$$\begin{aligned} P_{22}(k, \eta) &= \frac{1}{4\pi^3} \int d^3\mathbf{q} F_2^2(\mathbf{k} - \mathbf{q}, \mathbf{q}) P(|\mathbf{k} - \mathbf{q}|, \eta) P(q, \eta) \\ &= \frac{G^4(\eta)}{4\pi^3} \int d^3\mathbf{q} F_2^2(\mathbf{k} - \mathbf{q}, \mathbf{q}) P_{\text{Lin}}(|\mathbf{k} - \mathbf{q}|) P_{\text{Lin}}(q), \end{aligned} \quad (2.67a)$$

$$\begin{aligned} P_{13}(k, \eta) &= \frac{3}{4\pi^3} P(k, \eta) \int d^3\mathbf{q} F_3(\mathbf{k}, \mathbf{q}, -\mathbf{q}) P(q, \eta) \\ &= \frac{3G^4(\eta)}{4\pi^3} P_{\text{Lin}}(k) \int d^3\mathbf{q} F_3(\mathbf{k}, \mathbf{q}, -\mathbf{q}) P_{\text{Lin}}(q). \end{aligned} \quad (2.67b)$$

This way one can continue up to any order desired.

The linear power spectrum and the first three perturbation terms as computed in the framework of PT just depicted above are shown in the left panel of Fig. 2.1 as a function of the wave-number. Solid and dashed lines denote positive and negative contributions. This figure shows the main problem of PT: except the linear power spectrum, each term has both positive and negative contributions. No tendency is seen for the different perturbative contributions to decrease in amplitude with increasing order. This leaves us with the impossibility to predict the sign and amplitude of any term before computing it explicitly and consequently decides where to truncate the

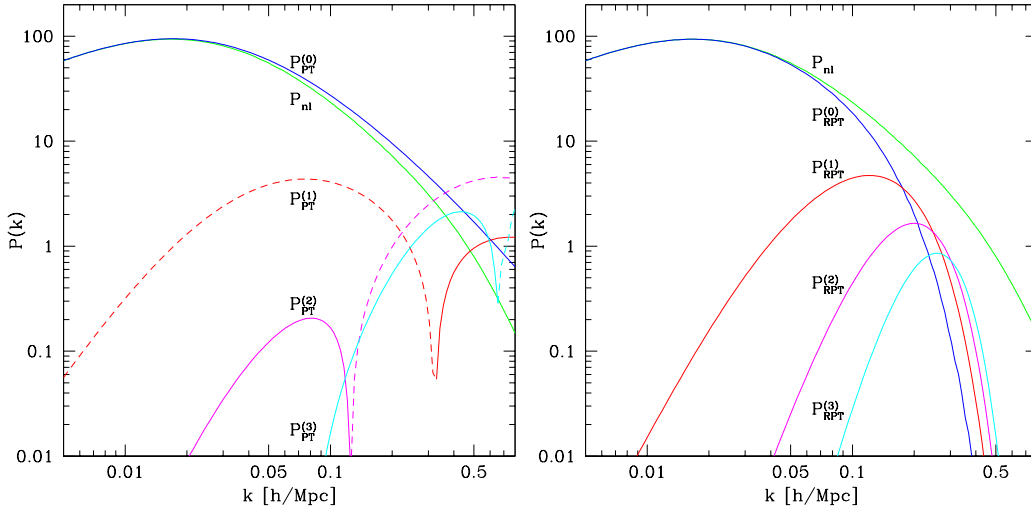


Figure 2.1: Comparison between PT and RPT nonlinear power spectrum. *Left panel:* PT nonlinear power spectrum, green line, decomposed according to perturbation theory as the sum of the linear term, blue line, and the first three perturbation terms, red, violet and cyan lines. Solid and dashed lines indicate positive and negative contributions, respectively. *Right panel:* Same nonlinear power spectrum decomposed according to RPT. The terms $P_{\text{RPT}}^{(0)}$ and $P_{\text{RPT}}^{(n)}$, for $n > 0$ in the figure are equivalent to $G^2(k, t_0)P(k, 0)$ and $P_{\text{MC}}^{(n)}(k, t_0)$ from Eq. (2.70). Figures from Crocce & Scoccimarro (2006).

PT expansion problematic. By this fundamental reason, one finds in the literature the statement that SPT can be used to describe only the mildly nonlinear regime but not the full nonlinear regime (see Crocce & Scoccimarro, 2006, 2008, and references therein).

Given the limitations of SPT, and the fact that the modeling of the two-point statistics requires proper account of nonlinear effects (e.g. Crocce et al., 2011; Sobreira et al., 2011), we now turn to the *Renormalized Perturbation Theory* (RPT) approach (Crocce & Scoccimarro, 2006, 2008) as an approach to improve SPT results. It is out of the scope of this work to do a detailed review of RPT, which requires a high level of technical developments and tools of field theory. Instead, we will mention the basis and main features of this approach. We closely follow the treatment presented in § 2.2 of Montesano (2011).

In a simple way, RPT can be understood as a reorganization of the terms in the PT expansion that remove the problems of this formalism mentioned above. The first idea is that all the terms in the SPT expansion for the power spectrum that are proportional to the initial power spectrum, here $P(k, t)$,

e.g. P_{13} (see Eq. 2.67b) and P_{15} (see e.g., Bernardeau et al., 2002; Crocce & Scoccimarro, 2006), are grouped together into a common factor $G(k, t)$, the so-called *renormalized propagator*, which can be interpreted as encoding the loss of information of the initial conditions due to nonlinear evolution. At very large scales, the low- k limit, the renormalized propagator should evolve as the growth factor, $G(k, t) \approx G(t)$, having no dependence on the initial conditions. Meanwhile, at small scales, the high- k limit, the behavior of the propagator was computed by Crocce & Scoccimarro (2006) to have approximatively the form of a Gaussian with zero mean and dispersion given by a characteristic scale determining where the linear theory breaks down. Here we refer to this scale as r_{NL} , following de Simoni et al. (2013)⁹

$$r_{\text{NL}}^2 = \frac{1}{3} \int dk \frac{P_{\text{Lin}}(k)}{k^2}. \quad (2.68)$$

That is, for small scales (Crocce & Scoccimarro, 2008)

$$G(k, \eta) \approx G(\eta) \exp \left[-\frac{1}{2} k^2 r_{\text{NL}}^2 (G(\eta) - 1)^2 \right], \quad (2.69)$$

with $G(\eta)$ the linear growth factor.

The remaining terms, those that are not proportional to $P(k, \eta)$, are organized according to the number n of initial modes coupled and grouped into the mode coupling power spectrum $P_{\text{MC}}^{(n)}(k, t)$. As an example, the lowest order term is the one that couples two initial power spectra, i.e., $P_{\text{MC}}^{(2)}(k, t)$. It is given by P_{22} of PT, Eq. (2.67b) (Crocce & Scoccimarro, 2008). Therefore, the full nonlinear power spectrum in the RPT formalism should have the following form

$$P(k, t) = G^2(k, t) P_{\text{Lin}}(k) + \sum_{n=2}^{\infty} P_{\text{MC}}^{(n)}(k, t) \quad (2.70)$$

The linear power spectrum and the first three perturbation terms as computed in the framework of RPT just depicted above are shown on the right panel of Fig. 2.1 as a function of the wave-number. Solid and dashed lines denote positive and negative contributions. This figure shows how the main problems of SPT are alleviated in the context of RPT, as each term has positive contributions and appears dominant over a restricted range of wave-numbers, which shows a tendency to increase in the values of k with increasing perturbative order. This shows the advantage of RPT over standard PT.

⁹Note that this quantity has different names in other works. Crocce & Scoccimarro (2008) originally call it σ_v and Crocce et al. (2011) call it s_{bao} .

In principle, it is simpler to decide where to truncate the series of Eq. (2.70) if a given precision at wave-number k is required.

As discussed in § 2.4.8, modern methods for BAO feature detection in galaxy surveys directly rely on the correct modeling for the linear two-point statistics of tracers at late times. As we will see, Eq. (2.69) is the starting point for the modeling strategy adopted to account for nonlinear structure formation effects in the detection of the BAO feature on the first year of observations of the DES results, presented in Chap. 5.

2.3 Halo-galaxy connection

Dark matter simulations have been well understood and modeled under the underlying assumption that matter is distributed on large scales in basic units of collapse called *dark matter halos*. Such objects can be schematically understood as gravitationally bound regions of matter in approximate virial equilibrium that have decoupled from the overall Hubble expansion and collapsed. In the context of numerical simulations, halos are generally defined by their masses M_Δ and radii r_Δ as specified by a given enclosed overdensity Δ relative to the mean background density $\bar{\rho}_m$,

$$M_\Delta = \frac{4\pi}{3} r_\Delta^3 \bar{\rho}_m \Delta. \quad (2.71)$$

The value of Δ is arbitrary and reflects in some sense the diversity of algorithms for identifying halos in simulations as well as the different observational proxies for detection of galaxy clusters. For the virial overdensity Δ_{vir} , this relation defines the halo virial mass M_{vir} and virial radius r_{vir} . For an Einstein-de Sitter universe ($\Omega_m = 1, \Omega_k = 0$), $\Delta_{\text{vir}} \approx 178$. The value $\Delta = 200$ is frequently employed in the literature, despite the fact that it does not reflect the virial density of halos at the current best-fit cosmology ($\Delta \approx 350$).

2.3.1 The halo model

The halo model (e.g. Cooray & Sheth, 2002) is an effective way to account for nonlinear effects, based on the properties of dark matter halos. The underlying assumption or approximation of the halo model is that all dark matter in the universe is contained within dark matter halos. Therefore to construct the halo-model correlations, we need prescriptions of halo properties: abundance, bias, and profile. Fortunately, simulations indicate that these properties are all close to universal.

Halo abundance

We start by introducing the *halo mass function*, which describes the abundance of halos as a function of halo mass M , as

$$\frac{dn}{d \ln M} = f(\sigma) \frac{\bar{\rho}_m}{M} \left| \frac{d \ln \sigma^{-1}}{d \ln M} \right|, \quad (2.72)$$

where σ^2 is the variance of the linear density field smoothed with a radial top-hat filter of radius R , corresponding to a mass scale of $M = 4\pi R^3 \bar{\rho}_m / 3$.

The multiplicity function $f(\sigma)$ has been found to be approximately universal for Λ CDM scenarios. The dependence of the mass function on the background cosmology, redshift and power spectrum enter via σ and $\bar{\rho}_m$. Frequently $f(\nu)$ is expressed as a function of the peak-height ν

$$\nu = \delta_c / \sigma \quad (2.73)$$

where $\delta_c = 1.686$ is the linear collapse density in spherical collapse.

The halo abundance is then described by a mass function characterized by an exponential high-mass suppression or cutoff. This exponential cutoff makes more massive halos, a.k.a. Rare halos, extremely sensitive to the amplitude of dark matter clustering signal, the power spectrum, and its growth rate, which in turn makes the abundance sensitive to both the expansion history and the growth of structures in the universe.

One important numerical study of dark matter halos is that of Tinker et al. (2008). In this work, a large number of N-body simulations were fitted giving rise to the functional form

$$f(\sigma) = A \left[\left(\frac{\sigma}{b} \right)^{-a} + 1 \right] e^{-c/\sigma^2}, \quad (2.74)$$

for spherical overdensity halos. Here the parameters A , a , b and c are functions of the interior spherical overdensity Δ defining halo sizes. Typically we take $\Delta = 200$ with respect to the cosmic mean density $\bar{\rho}_m$.

Under the halo model assumption, all matter is in halos. Therefore the mass-weighted integral of the mass function must be equal to the average background matter density $\bar{\rho}_m$. This imposes a normalization condition on the mass-function or similarly on the multiplicity function $f(\nu)$:

$$\int d \ln M \frac{M}{\bar{\rho}_m} \frac{dn}{d \ln M} = \int d \nu \frac{f(\nu)}{\nu} = 1 \quad (2.75)$$

where again $\nu = \delta_c / \sigma$.

Halo bias

To a first approximation, on large scales, halos of a given mass M are biased tracers of the underlying matter distribution with a bias factor $b_h(M)$. If $\delta_h(M)$ represents the overdensity of halos of mass M and δ_m the matter overdensity in a given region, we have

$$\delta_h(M) = b_h(M)\delta_m \quad (2.76)$$

It is found that $b_h(M)$ is approximately scale-independent on large scales and an increasing monotonic function of halo mass. Massive halos are expected to be more strongly clustered than the underlying matter distribution simply because schematically they form near high peaks of the initial density field, or deep gravitational potential wells, which arise more frequently in regions where the local background density is high.

As for the mass-function, the halo bias is also fit from N-body simulations. For instance, Tinker et al. (2010) provide the fit

$$b_h(\nu) = 1 - A \frac{\nu^a}{\nu^a + \delta_c^a} + B\nu^b + C\nu^c \quad (2.77)$$

where $\delta_c = 1.686$, and parameters A, B, C, a, b, c are again functions of the halo overdensity Δ .

Under the peak-background split, the halo bias can be derived from the halo mass-function, and the normalization of the mass-function implies a similar condition for the bias, namely:

$$\int d \ln M \frac{M}{\bar{\rho}_m} \frac{dn}{d \ln M} b_h(M) = \int d\nu b(M) \frac{f(\nu)}{\nu} = 1 \quad (2.78)$$

This condition means that the average bias from all halos is 1, so the rare, large-mass, highly biased halos are compensated by the abundant, low-mass halos of bias less than unity.

Halo profile

Numerical simulations indicate the existence of a universal profile for halos that is statistically isotropic, i.e., consistent with the assumption that halos are spherical on average. Fits to numerical simulations suggest the Navarro-Frenk-White (NFW, Navarro et al., 1996) as a good parametrical form for this profile, given for halos of mass M as

$$\rho(r|M) = \frac{\rho_s}{cr/r_{\text{vir}} (1 + cr/r_{\text{vir}})^2}, \quad (2.79)$$

where ρ_s is a normalization parameter directly related to the halo mass M , r_{vir} is the halo virial mass and c is the halo *concentration*, whose relation to M is also found from fits to simulations. For $cr \ll r_{\text{vir}}$, $\rho \propto (rc/r_{\text{vir}})^{-1}$ and for $cr \gg r_{\text{vir}}$, $\rho \propto (rc/r_{\text{vir}})^{-3}$, so NFW describes roughly a double power-law scaling relation.

If integrated to infinity, the halo mass diverges. The last issue is solved by imposing the halo boundary to be at a certain radius, e.g., the virial radius $r = r_{\text{vir}}$. In this case the halo virial mass is given by

$$M_{\text{vir}} = \int_0^{r_{\text{vir}}} dr 4\pi r^2 \rho(r|M) = 4\pi \rho_s \frac{r_{\text{vir}}}{c^2} \left[\ln(1+c) - \frac{c}{1+c} \right] \quad (2.80)$$

Matter power spectrum

Within the Halo Model framework, the nonlinear matter power spectrum can be decomposed in two terms. The first term comes from the clustering of halos on large scales, according mainly to the halo abundance and bias. This term is called 2-halo term and is given by

$$P_{2h}(k) = \left[\int d \ln M \frac{M}{\bar{\rho}_{m0}} \frac{dn}{d \ln M} b_h(M) u(k|M) \right]^2 P_L(k), \quad (2.81)$$

where $\bar{\rho}_{m0}$ is the mean background matter density today, $P_L(k)$ is the linear matter power spectrum and $u(k|M)$ is mass-normalized Fourier transform of the halo profile Eq. (2.79),

$$u(k|M) = 4\pi \int dr r^2 \frac{\sin(kr)}{kr} \frac{\rho(r|M)}{M}. \quad (2.82)$$

As $k \rightarrow 0$ on sufficiently large scales, $u(k|M) \rightarrow 1$ since the volume integral of the halo profile equals the halo mass M . In this case, the bias normalization condition Eq. (2.78) implies that the term under square brackets in Eq. (2.81) approaches unity and therefore $P^{2h}(k) \approx P_L(k)$, as expected.

The second term describes the matter clustering within the halo profile itself. It is therefore called the 1-halo term and given by

$$P_{1h}(k) = \int d \ln M \left(\frac{M}{\bar{\rho}_{m0}} \right)^2 \frac{dn}{d \ln M} |u(k|M)|^2. \quad (2.83)$$

Finally, the total matter power spectrum is the sum of the 1-halo and 2-halo terms:

$$P(k) = P^{1h}(k) + P^{2h}(k). \quad (2.84)$$

2.3.2 Halo occupation distribution

The halo model expressions from the last section provide an estimate for the *matter* nonlinear power spectrum. If we want to compute the *galaxy* power spectrum, we need an extra ingredient, which is the Halo Occupation Distribution (HOD) of these galaxies. An HOD tells us how galaxies of a given type populate halos of a given mass M .

Within the HOD, the fundamental quantity is $P(N|M)$, the conditional probability that a halo of mass M contains N galaxies. From this probability, we may compute two important quantities, which represent the first two moments of $P(N|M)$. These are the average number of galaxies populating halos of mass M :

$$\langle N(M) \rangle = \sum_N N P(N|M), \quad (2.85)$$

also, the average number of galaxy pairs

$$\langle N(N-1)(M) \rangle = \sum_N N(N-1) P(N|M). \quad (2.86)$$

The halo model prescriptions can be used for galaxies once we make the following replacements

$$\frac{M}{\bar{\rho}_m} \rightarrow \frac{\langle N \rangle}{\bar{n}_g} \quad \text{and} \quad \frac{M^2}{\bar{\rho}_m^2} \rightarrow \frac{\langle N(N-1) \rangle}{\bar{n}_g^2}, \quad (2.87)$$

where the average number density of galaxies \bar{n}_g is given by

$$\bar{n}_g = \int d \ln M \frac{dn}{d \ln M} \langle N \rangle. \quad (2.88)$$

The 1-halo term for the galaxy power spectrum becomes

$$P_g^{1h}(k) = \int d \ln M \frac{dn}{d \ln M} \frac{\langle N(N-1) \rangle}{\bar{n}_g^2} |u(k|M)|^2, \quad (2.89)$$

and the corresponding 2-halo term becomes

$$P_g^{2h}(k) = \left[\int d \ln M \frac{dn}{d \ln M} b_h(M) \frac{\langle N \rangle}{\bar{n}_g} u(k|M) \right]^2 P_L(k). \quad (2.90)$$

The galaxy power spectrum is then given by

$$P_g(k) = P_g^{1h}(k) + P_g^{2h}(k). \quad (2.91)$$

Again on large scales $u(k|M) \rightarrow 1$, the 2-halo term dominates, so we have

$$P_g(k) \approx P_g^{2h}(k) \approx b_g^2 P_L(k), \quad (2.92)$$

where the linear galaxy bias b_g is given by

$$b_g = \frac{1}{\bar{n}_g} \int d \ln M \frac{dn}{d \ln M} b_h(M) \langle N \rangle. \quad (2.93)$$

The only thing remaining is the specification of the HOD parametrization. As said earlier, the basic quantity is $P(N|M)$. However, most often the HOD parametrization is specified only for the first two moments, instead of the full $P(N|M)$. For example, we can model $\langle N \rangle$ by splitting it into one central galaxy and satellite galaxies:

$$\langle N(M) \rangle = \langle N_{\text{cen}}(M) \rangle + \langle N_{\text{sat}}(M) \rangle \quad (2.94)$$

In Zhai et al. (2017), we model these as

$$\langle N_{\text{cen}}(M) \rangle = \frac{1}{2} \left[1 + \text{erf} \left(\frac{\log M - \log M_{\text{min}}}{\sigma_{\log M}} \right) \right] \quad (2.95)$$

$$\langle N_{\text{sat}}(M) \rangle = \left(\frac{M}{M_{\text{sat}}} \right)^\alpha \exp \left(-\frac{M_{\text{cut}}}{M} \right) \langle N_{\text{cen}}(M) \rangle \quad (2.96)$$

Finally, assuming a nearest-integer distribution for the central galaxies (either 0 or 1 central) and a Poisson distribution for the satellites, we have

$$\langle N(N-1)(M) \rangle = 2\langle N_{\text{sat}}(M) \rangle + \langle N_{\text{sat}}(M) \rangle^2. \quad (2.97)$$

The equations above fully specify the HOD model for computing the galaxy power spectrum, for given HOD parameters M_{min} , M_{sat} , M_{cut} , $\sigma_{\log M}$ and α . Notice that from the basic prediction for the 3D galaxy power spectrum $P_g(k)$, we may predict all correlations of interest, e.g., the 3D correlation function, the angular correlation function, angular power spectrum, projected correlation function, etc.

In Chap. 4, we will show an application of the Halo Model + HOD formalism to predict the projected correlation function and fit for HOD parameters of LRGs from eBOSS (Zhai et al., 2017). The best-fit HOD parameters obtained are then used to predict the galaxy bias b_g from Eq. (2.93).

2.4 Galaxy clustering observables

In what follows, we present a review of the physical interpretation of galaxy clustering as a powerful window of information to be extracted from modern

galaxy surveys. We focus on the two-point function of the field describing the distribution of galaxies in the universe, as tracers of the total matter and then, ultimately, of the gravitational field as described on the first part of this chapter.

2.4.1 Galaxy correlation function

We have now depicted our current model for the large scale structure of the universe. The observed distribution of the universe matter/energy content results from the growth of primordial seed fluctuations. The possible scenarios of the generation of these primordial seeds are out of the scope of this thesis. Whatever this mechanism was, the resulting fluctuations were amplified by gravitational instability phenomena, which is formally described by cosmological perturbation theory.

Several interpretation issues for observations in cosmology emerge as we face two main difficulties: (a) we do not have access to the initial conditions of the evolution of perturbations, i.e., to the primordial fluctuations, and (b) the time-scale for cosmological evolution is too large, so it is not possible to follow the evolution of single systems or the growth of individual structures. These features imply that fluctuations around a perturbed FLRW background cannot be treated as deterministic variables; instead, they should be treated as random variables. The observable universe is thus modeled as a stochastic realization of a statistical ensemble of possibilities. In this context, observations should then be used to determine the statistical properties of such fluctuations.

A related problem is the issue of a unique observable universe, i.e., the fact that we have a single realization of the stochastic process we are interested in. It is then impossible to measure expectation values in a reproducible and controlled setup, as in experimental science. Having said this, we realize that we can, however, average observable quantities over many distinct regions of typical size r . Consequently, an ergodic-like hypothesis should be considered to replace the (desired) ensemble average by a (possible) spatial average over these regions. Such a hypothesis is known in the literature as the *fair sample hypothesis*, stating that the finite part of the universe accessible to observations is a fair sample of the whole universe (see, e.g., §6.3 of Bernardeau et al., 2002).

At this point we arrive at an important conclusion: in principle, the fair sample hypothesis is reasonable for scales much smaller than the observable universe ($r \ll D_H$), whereas for larger scales it is impossible to average over many volumes and thus the measured values could be far from the real ensemble average. This is known as the *cosmic variance* problem.

In the context of galaxy surveys, we observe a particular window of the universe, consisting of an angular mask of the observed area and a radial distribution of biased tracers (e.g., galaxies) of the matter density. From imaging surveys, it is possible to catalog positions, colors, and shapes of tracers. In order to correct for spatially varying selection effects, we do not make direct use of observed galaxy number density $n_g(\mathbf{x})$ but instead consider the dimensionless overdensity of galaxies $\delta_g(\mathbf{x}) = n_g(\mathbf{x})/\bar{n}_g - 1$, defined with respect to the mean number density \bar{n}_g .

In order to confront theoretical model predictions for the total mass distribution in the universe against observational data, a relationship between the fluctuation fields of galaxies and the total matter must be established. The problem resides in the fact that luminous astrophysical objects, such as galaxies and quasars, are not direct (but *biased*) tracers of mass in the universe. A difference of the spatial distribution between luminous astrophysical objects and the total matter in the universe has been indicated from a variety of observations. This difference is commonly referred to in the literature as the *biasing effect*. It is beyond the scope of this work to present a detailed discussion of galaxy bias modeling. Some related ideas are presented below and in § 2.4.4. For our purposes, it is enough to say that the galaxy bias b_g relates the galaxy density contrast δ_g to the matter density contrast δ via $\delta_g = b_g \delta$.

Beyond its average, the simplest statistical quantity one can consider for a random field is its two-point correlation function. The two-point correlation function of a random field δ is nothing but its second moment, $\langle \delta(\mathbf{x})\delta(\mathbf{x}') \rangle$, defined as the average over the ensemble (incorporating the probability distribution considered for δ). To have a physical insight into this quantity, consider the local number density of galaxies in the Universe $n_g(\mathbf{x})$. It can be expressed in terms of its fluctuation $\delta_g(\mathbf{x})$ around its spatial average \bar{n}_g . Therefore $n_g(\mathbf{x})$ can be considered a random field, as

$$n_g(\mathbf{x}) = \bar{n}_g (1 + \delta_g(\mathbf{x})). \quad (2.98)$$

Counting pairs

Now we can ask for the number of galaxy pairs separated by a *comoving* distance r on a direction specified by the unit vector $\hat{\mathbf{n}}$. Considering dV_1 and dV_2 volume elements around \mathbf{x} and $\mathbf{x} + r\hat{\mathbf{n}}$ respectively, we can write this number as

$$dN_{\text{pair}}(r, \hat{\mathbf{n}}) = n_g(\mathbf{x})dV_1 n_g(\mathbf{x} + r\hat{\mathbf{n}})dV_2, \quad (2.99)$$

or equivalently, by introducing the fluctuation field in Eq. (2.98)

$$dN_{\text{pair}}(r, \hat{\mathbf{n}}) = \bar{n}_g^2 [1 + \delta_g(\mathbf{x}) + \delta_g(\mathbf{x} + r\hat{\mathbf{n}}) + \delta_g(\mathbf{x})\delta_g(\mathbf{x} + r\hat{\mathbf{n}})] dV_1 dV_2. \quad (2.100)$$

Making use of the fair sample hypothesis, we average over all possible volume elements to predict the expected number of galaxy pairs separated by a distance r in the direction $\hat{\mathbf{n}}$ as

$$\langle dN_{\text{pairs}}(r, \hat{\mathbf{n}}) \rangle = \bar{n}_g^2 [1 + \langle \delta_g(\mathbf{x})\delta_g(\mathbf{x} + r\hat{\mathbf{n}}) \rangle] dV_1 dV_2, \quad (2.101)$$

where we made use of $\langle \delta_g(\mathbf{x}) \rangle = 0$ as expected by construction.

When there is no fluctuation in the number density of galaxies, $\delta_g(\mathbf{x}) = 0$, the expected number of pairs separated by a distance r in the direction $\hat{\mathbf{n}}$ is given by the squared spatially averaged number of galaxies, thus, independent of position.

When fluctuations are taken into account, the number of pairs is position dependent, and consequently, it appears an excess (or lack of) probability for finding pairs of galaxies depending on their separation, r , and $\hat{\mathbf{n}}$. This excess (lack of) probability is effectively quantified by the two-point correlation function, which is defined as

$$\xi_g(r, \hat{\mathbf{n}}) = \langle \delta_g(\mathbf{x})\delta_g(\mathbf{x} + r\hat{\mathbf{n}}) \rangle. \quad (2.102)$$

Correlation estimators

Exploiting the idea that the correlation function measures the excess (lack of) probability for finding a pair of objects separated by a distance r , different estimators are based on some average of the counts of galaxy neighbors at a given scale, or more precisely, within a narrow band of scales, commonly named as a *bin*. A fundamental problem that emerges is that *for galaxies close to the boundary of the window, the number of neighbors is underestimated*. Usually, an auxiliary random sample containing N_R points must be generated in W , i.e., a Poissonian point process with N_R points. The use of random samples in the estimators effectively constitutes a way to implement Monte Carlo integration of the volumes. So the number of random points must be much larger than the size of the data sample, as this is a basic requirement of Monte Carlo estimation techniques.

Given a catalog of N galaxies with their corresponding positions, we can think of a natural estimator for the probability of finding a pair of galaxies separated by a distance r on the $\hat{\mathbf{n}}$ direction. Given the probabilistic interpretation and Eqs. (2.101) and (2.102), it is *natural* to estimate ξ_g as the ratio between the number of pairs separated by a distance r on direction

$\hat{\mathbf{n}}$ in the catalog $DD(r, \hat{\mathbf{n}})$ (correctly normalized by the number of possible pairs $N(N-1)$) and the number of pairs with the same characteristics on a synthetic catalog of randomly distributed galaxies $RR(r, \hat{\mathbf{n}})$,

$$\frac{DD(r, \hat{\mathbf{n}})}{RR(r, \hat{\mathbf{n}})} = \frac{\langle dN_{\text{pair}}(r, \hat{\mathbf{n}}) \rangle}{\bar{n}_g^2 dV_1 dV_2} = 1 + \hat{\xi}_g(r, \hat{\mathbf{n}}). \quad (2.103)$$

The relation above defines the simplest pair counting-based estimator implementation, the *Peebles and Hauser estimator* (PH) (Peebles, 1973; Peebles & Hauser, 1974). The PH estimator $\hat{\xi}_{\text{PH}}$ is also known in the literature as the *natural estimator* $\hat{\xi}_{\text{N}}$ because of its straightforward interpretation as the excess probability of find pairs of galaxies as seen above.

$$\hat{\xi}_{\text{PH}} = \hat{\xi}_{\text{N}} = \frac{DD}{RR} - 1. \quad (2.104)$$

Despite its straightforward interpretation, the natural estimator is known to suffer from insufficient correction effects related with its biasing specially on large scales, where it can be of the same order of the uncertainties in the measurements (Hamilton, 1993).

Hamilton (1993) realized for the first time that as long as one is dealing with volume-limited samples, errors in the sample statistics of $\hat{\delta}$ using DD and RR pair counts only can be of the same order and can be larger than the uncertainty in $\hat{\xi}$, specially for small correlation amplitudes (on large scales), introducing a substantial bias in estimators. Hamilton (1993) then came up with a first strategy for correcting this bias using cross pair-counts between data and randoms DR , introducing a new estimator, the so-called *Hamilton estimator* (Ham),

$$\hat{\xi}_{\text{Ham}} = \frac{DD \cdot RR}{(DR)^2} - 1, \quad (2.105)$$

The main shortcoming of the Hamilton estimator, Eq. (2.105), is that the DR term may introduce numerical noise at small distances (Hamilton, 1993). Almost simultaneously, Landy & Szalay (1993) proposed another estimator having almost the same properties, the so-called *Landy-Szalay estimator* (LS),

$$\hat{\xi}_{\text{LS}} := \frac{DD - 2DR + RR}{RR}. \quad (2.106)$$

In addition to the bias reduction, Landy & Szalay (1993) showed that the LS estimator is effectively a maximum likelihood estimator when the galaxy counts statistics is Poissonian, a limit in which they provide expressions for the variance of the estimator.

The main shortcoming of LS estimator is that it had been shown to be optimal only for the particular case of Poisson-distributed points. Bernstein (1994) provided expressions for the variance of the estimator in a more general context, showing that this can significantly miss-estimate the covariance matrix when Poisson statistics is far from valid.

Throughout this work, we will make use of the LS estimator for the estimation of samples of Emission-Line Galaxies from eBOSS and DES in Chap. 3 and Luminous Red Galaxies from BOSS and eBOSS in Chap. 4, for which we do not expect to be far from its validity limits. Although it is out of the scope of this work, we refer the reader to Baxter & Rozo (2013) for a more detailed discussion of the extension of the LS estimator as a maximum likelihood estimator.

Correlation symmetries

Given the cosmological principle, perturbative quantities described as random fields are usually assumed to be *statistically homogeneous and isotropic*, i.e., invariant under translations and rotations. For the two-point correlation function the statistical homogeneity assumption translates into the condition

$$\langle \delta(\mathbf{x} - \mathbf{a})\delta(\mathbf{x} + r\hat{\mathbf{n}} - \mathbf{a}) \rangle = \langle \delta(\mathbf{x})\delta(\mathbf{x} + r\hat{\mathbf{n}}) \rangle$$

for all \mathbf{a} , which implies that the correlation function must depend only on the separation between points, $r\hat{\mathbf{n}}$, i.e. $\xi_\delta(r, \hat{\mathbf{n}}) = \xi_\delta(r\hat{\mathbf{n}})$. On the other hand, the statistical isotropy assumption translates into

$$\xi_\delta(rR[\hat{\mathbf{n}}]) = \xi_\delta(r\hat{\mathbf{n}}),$$

where R represents an arbitrary spatial rotation, which implies that the correlation function should depend only on the absolute value of the separation between the two points r , and therefore can be written as

$$\xi_\delta(r) = \langle \delta(\mathbf{x})\delta(\mathbf{x} + r\hat{\mathbf{n}}) \rangle, \quad (2.107)$$

so that ξ_δ does not depend on the position \mathbf{x} or the (unit) direction $\hat{\mathbf{n}}$.

Integral constraint

From Eq. (2.100), we may fix dV_1 such that it contains 1 galaxy i , i.e. $\bar{n}_g dV_1 = 1$. In this case, the number of pairs $dN_{\text{pairs}}(r)$ correspond simply to the number $dN(r)$ of galaxies at distance r from the given galaxy i and within volume $dV_2 = dV$

$$dN(r) = \bar{n}_g [1 + \xi_g(r)] dV \quad (2.108)$$

Dividing this number $dN(r)$ by the total number of galaxies in the observed volume V gives the fraction of galaxies or the probability $dP(r)$ of finding a galaxy at this separation r :

$$dP(r) = \frac{dN(r)}{\bar{n}_g V} = [1 + \xi_g(r)] \frac{dV}{V} \quad (2.109)$$

Since all galaxies are at some separation of i , this probability must be normalized to 1, i.e.

$$\int dP(r) = 1 \quad (2.110)$$

which implies that the correlation function must satisfy the so-called *integral constraint (IC)*

$$\int \xi_g(r) dV \propto \int dr r^2 \xi_g(r) = 0 \quad (2.111)$$

where we used $\int dV/V = 1$ and the fact that $\xi_g(r)$ depends only on the spherical coordinate r to trivially perform angular integrals.

Physically, we expect $\xi_g(r)$ to be positive for small separations (which are correlated by gravitational evolution) and to decrease for increasing values of r . Therefore, in order for the integral constraint to be satisfied, $\xi_g(r)$ must have negative values at large separations. Besides, it has the BAO feature, as an excess clustering at the scale of the drag sound horizon $r_d \approx 150$ Mpc (see § 2.4.8).

In Chap. 3, we will impose the integral constraint on a small sample of Emission-Line Galaxies (ELG's).

2.4.2 Correlation function and power spectrum

Consider a field $\delta(\mathbf{x}, z)$ at some instant t (and redshift z), i.e on the constant time hypersurface Σ_t . It can be any cosmological random field, but for our purposes here, we take it to represent fluctuations on the total matter density at some time on an FLRW model. Recall that $\delta = \delta_g/b_g$

The first task is to understand how to decompose this field in Fourier plane waves properly. This is simple when we are working on Cartesian coordinates and Σ_t is flat, in which case we decompose¹⁰,

$$\delta(\mathbf{x}, z) = \frac{1}{(2\pi)^3} \int d^3\mathbf{k} \delta(\mathbf{k}, z) e^{i\mathbf{k}\cdot\mathbf{x}}, \quad (2.112)$$

¹⁰Note we set here the convention on the Fourier transform normalization to be consistent with most of the cosmology literature, with the inverse Fourier transform having no factors of (2π) .

where

$$\delta(\mathbf{k}, z) = \int d\mathbf{k} \delta(\mathbf{x}, z) e^{-i\mathbf{k}\cdot\mathbf{x}}. \quad (2.113)$$

Notice that $\delta(\mathbf{x}, z)$ must be a real field, so $\delta(\mathbf{x}, z) = \delta^*(\mathbf{x}, z)$, where superscript $*$ refers to complex conjugation. The power spectrum $P(k, z)$ is then defined via

$$\langle \delta^*(\mathbf{k}, z) \delta(\mathbf{k}', z) \rangle = (2\pi)^3 \delta_D^3(\mathbf{k} - \mathbf{k}') P(k, z). \quad (2.114)$$

We can express the correlation function as

$$\begin{aligned} \xi(r, z) &= \langle \delta(\mathbf{x}, z) \delta(\mathbf{x} + \mathbf{r}, z) \rangle = \langle \delta^*(\mathbf{x}, z) \delta(\mathbf{x} + \mathbf{r}, z) \rangle \\ &= \left\langle \frac{1}{(2\pi)^3} \int d^3\mathbf{k} \delta^*(\mathbf{k}, z) e^{-i\mathbf{k}\cdot\mathbf{x}} \frac{1}{(2\pi)^3} \int d^3\mathbf{k}' \delta(\mathbf{k}', z) e^{i\mathbf{k}'\cdot(\mathbf{x}+\mathbf{r})} \right\rangle \\ &= \frac{1}{(2\pi)^6} \int d^3\mathbf{k} \int d^3\mathbf{k}' \langle \delta(\mathbf{k}, z) \delta^*(\mathbf{k}', z) \rangle e^{-i(\mathbf{k}-\mathbf{k}')\cdot\mathbf{x}} e^{i\mathbf{k}'\cdot\mathbf{r}} \\ &= \frac{1}{(2\pi)^3} \int d^3\mathbf{k} P(k, z) e^{i\mathbf{k}\cdot\mathbf{r}}, \end{aligned} \quad (2.115)$$

where we used Eqs. (2.112) and (2.114). Therefore $P(k, z)$ is the Fourier transform of $\xi(r, z)$. Since $P(k, z)$ depends only on the magnitude of \mathbf{k} , we may use spherical coordinates to trivially perform the angular integrals and find

$$\begin{aligned} \xi(r, z) &= \frac{1}{(2\pi)^3} \int d\phi \int dk k^2 P(k, z) \int d\cos\theta e^{-ikr\cos\theta} \\ &= \frac{1}{(2\pi)^2} \int dk k^2 P(k, z) \left[\frac{e^{ikr} - e^{-ikr}}{ikr} \right] \\ &= \int dk \frac{k^2}{2\pi^2} \frac{\sin(kr)}{kr} P(k, z). \end{aligned} \quad (2.116)$$

Spherical coordinates

As shown in § 2.1.1, spherical coordinates prove to be helpful when considering different distance measurements on the RW metric, which of course comes from its symmetries. Therefore it is desirable to perform the plane-wave decomposition in spherical coordinates for direct connection with distances. We will do that and recover the relation between $P(k)$ and $\xi(r)$ through a

different route. For that, we introduce the *Rayleigh plane wave expansion*

$$\begin{aligned} e^{i\mathbf{k}\cdot\mathbf{x}} &= 4\pi \sum_{\ell=0}^{\infty} \sum_{m=-\ell}^{\ell} i^{\ell} j_{\ell}(kr) Y_{\ell}^{m*}(\theta_{\mathbf{k}}, \varphi_{\mathbf{k}}) Y_{\ell}^m(\theta_{\mathbf{x}}, \varphi_{\mathbf{x}}) \\ &= 4\pi \sum_{\ell=0}^{\infty} \sum_{m=-\ell}^{\ell} i^{\ell} j_{\ell}(kr) Y_{\ell}^{m*}(\mathbf{n}_{\mathbf{k}}) Y_{\ell}^m(\mathbf{n}), \end{aligned} \quad (2.117)$$

where subscripts \mathbf{x}, \mathbf{k} refer to configuration and Fourier space coordinates respectively, $j_{\ell}(x)$ are the *spherical Bessel functions* of the first kind, Y_{ℓ}^m are *spherical harmonics* and we introduced $\mathbf{n} = (\theta, \varphi)$ to simplify the notation.

The Fourier transform of a field $\delta = \delta(z, r\mathbf{n})$ defined on the past light-cone in spherical coordinates results then in

$$\delta(z, r\mathbf{n}) = \sum_{\ell=0}^{\infty} \sum_{m=-\ell}^{\ell} \int_0^{\infty} dk \frac{k^2}{2\pi^2} \delta_{\ell m}(z, k) (-1)^{\ell} j_{\ell m}(kr) Y_{\ell}^m(\mathbf{n}), \quad (2.118)$$

where the inverse Fourier transform is

$$\delta_{\ell m}(z, k) = 4\pi \int dr r^2 \int d^2\Omega \delta(z, r\mathbf{n}) (-1)^{\ell} j_{\ell}(kr) Y_{\ell}^{m*}(\mathbf{n}). \quad (2.119)$$

In other words, and as it is known from electrodynamics, the radial mode of a plane Fourier wave is given by the Spherical Bessel functions $j_{\ell}(kr)$.

We can now consider the relation between the correlation function and the power spectrum again. Taking into account statistical homogeneity and isotropy, we know that on each time instant the two-point correlation function of matter depends only on the spatial separation of the two points considered. One can then compute $\xi(r)$ assuming two points located at the same angular position, i.e.,

$$\xi(z, r) = \langle \delta(z, 0\mathbf{n}) \delta(z, r\mathbf{n}) \rangle, \quad (2.120)$$

which, inserting Eq. (2.118) gives

$$\begin{aligned} \xi(z, r) &= \sum_{\ell, m, \ell', m'} \int dk \int dk' \frac{k^2 k'^2}{(2\pi^2)^2} j_{\ell}(kr) j_{\ell'}(k'r) Y_{\ell}^{m*}(\mathbf{n}) Y_{\ell'}^{m'}(\mathbf{n}) \\ &\quad \times \langle \delta_{\ell m}^*(z, k) \delta_{\ell' m'}(z, k') \rangle. \end{aligned} \quad (2.121)$$

Under the statistical homogeneity and isotropy condition, the correlation of Fourier spherical modes of a random field defines its *power spectrum*, $P(k)$, via

$$\langle \delta_{\ell m}^*(z, k) \delta_{\ell' m'}(z, k') \rangle = (2\pi)^3 \delta_{\ell\ell'} \delta_{mm'} \delta_D(k - k') k^{-2} P(z, k) \quad (2.122)$$

where $\delta_{\ell\ell'}$ and $\delta_{mm'}$ are Kronecker deltas and δ_D is the Dirac delta.

One can then find a relation between the correlation function and the power spectrum by inserting Eq. (2.122) into Eq. (2.121). The first thing one can do is to sum and integrate along with primed variables using the delta's and then take into account the fact that at $r = 0$ the only non-vanishing radial mode is the lowest one ($\ell = 0$), i.e., $j_\ell(0) = \delta_{\ell 0}$, to have

$$\begin{aligned}\xi(z, r) &= 4\pi \sum_{\ell m} \int dk \frac{k^2}{2\pi^2} \delta_{\ell 0} j_\ell(kr) Y_\ell^{m*}(\mathbf{n}) Y_\ell^{m'}(\mathbf{n}) P(z, k) \\ &= 4\pi \int dk \frac{k^2}{2\pi^2} j_0(kr) Y_0^{0*}(\mathbf{n}) Y_0^0(\mathbf{n}) P(z, k) \\ &= \int dk \frac{k^2}{2\pi^2} j_0(kr) P(z, k),\end{aligned}\tag{2.123}$$

where on the last line we use the property $Y_0^{0*}(\theta, \varphi) Y_0^0(\theta, \varphi) = |Y_0^0(\theta, \varphi)|^2 = (4\pi)^{-1}$ of spherical harmonics. Thus, again we find the Fourier transform relation between correlation and spectrum.

Growth

Finally, taking into account the results of § 2.2.1, we know that in linear theory the solution for the matter density contrast has the separated form $\delta(z, r\mathbf{n}) = G(z)\delta(z = 0, r\mathbf{n}) = G(z)\delta_0(r\mathbf{n})$. Thus, for the linear matter power spectrum $P(z, k)$ we also have a separated form

$$P(z, k) = G^2(z)P(k),\tag{2.124}$$

where from now on $P(k)$ represents the matter power spectrum today ($z = 0$).

One of the main complications when using correlations or spectra of galaxies in spectroscopic surveys resides in the fact that the peculiar velocity of a galaxy will cause it to appear shifted along the line-of-sight in redshift coordinates, an effect studied by Kaiser (1987) and Hamilton (1992). In other words, the peculiar velocities of galaxies on top of their background Hubble flow introduce a radial anisotropic distortion in *redshift-space* (RS), the space of measured positions of galaxies. That is, the redshift-inferred distance of an object will be altered from its actual distance, by its peculiar velocity radially oriented from the observer. This deviation alters the apparent clustering of galaxies and, collectively, the effect is said to be the result of *redshift space distortions* (see, e.g., Kaiser, 1987; Hamilton, 1992). We will describe this effect in § 2.4.5.

2.4.3 Angular clustering

The key concept on the theoretical interpretation of angular clustering of matter (or its tracers) is the field of *projected density fluctuation onto the sky*, which we will denote here by $\delta^{2D}(\mathbf{n})$, representing a random field on the sphere. Here $\mathbf{n} = (\theta, \varphi)$ denotes a particular direction (from the observer) on the sky.

It is convenient to define δ^{2D} as a properly weighted marginalization of its 3D counterpart, the total matter fluctuation on the observer's past light-cone, $\delta(r(z), r\mathbf{n})$, over its radial (redshift) dependence (see e.g., Sobreira et al., 2011; Crocce et al., 2011; Padmanabhan et al., 2007),

$$\delta^{2D}(\mathbf{n}) := \int dz F(z) \delta(z, r\mathbf{n}), \quad (2.125)$$

and should be interpreted as the total averaged fluctuation on a given direction on the sky. The marginalization kernel $F(z)$ represents a *redshift selection function*, as it describes the selection of matter (or tracers) in redshift and depends on the kind of observation considered. It should take into account the sky coverage for the definition of the field, the method used to estimate the redshift of galaxies, spatially varying magnitude limits, etc.

As long as δ^{2D} is a field properly defined on the sphere (full sky), one can consider its decomposition in spherical harmonics,

$$\delta^{2D}(\mathbf{n}) = \sum_{\ell=0}^{\infty} \sum_{m=-\ell}^{m=\ell} \delta_{\ell m}^{2D} Y_{\ell}^m(\mathbf{n}), \quad (2.126)$$

where

$$\delta_{\ell m}^{2D} = \int d^2\Omega \delta(\mathbf{n}) Y_{\ell}^m(\mathbf{n}). \quad (2.127)$$

As in the previous section, consider its two-point function,

$$w(\vartheta) = \langle \delta^{2D*}(\mathbf{n}) \delta^{2D}(\mathbf{n}') \rangle = \sum_{\ell m} \sum_{\ell' m'} Y_{\ell}^{m*}(\mathbf{n}) Y_{\ell'}^{m'}(\mathbf{n}') \langle \delta_{\ell m}^{2D*} \delta_{\ell' m'}^{2D} \rangle. \quad (2.128)$$

Statistical isotropy for δ^{2D} implies in configuration space that the *angular correlation function* (ACF) $w(\vartheta) = \langle \delta^{2D*}(\mathbf{n}) \delta^{2D}(\mathbf{n}') \rangle$ should be a function only of the angular separation on the sphere of the two-points ϑ ,

$$\cos \vartheta = \mathbf{n} \cdot \mathbf{n}'. \quad (2.129)$$

Similarly, in harmonic space an *angular power spectrum* (APS) C_{ℓ} can be defined via the relation

$$\langle \delta_{\ell m}^{2D*} \delta_{\ell m}^{2D} \rangle = \delta_{\ell\ell'} \delta_{mm'} C_{\ell}. \quad (2.130)$$

A relation between the ACF and the APS can be obtained using the addition theorem of spherical harmonics,

$$L_\ell(\mathbf{n} \cdot \mathbf{n}') = \frac{4\pi}{2\ell + 1} \sum_{m=-\ell}^{\ell} Y_\ell^{m*}(\mathbf{n}) Y_\ell^m(\mathbf{n}'), \quad (2.131)$$

where $L_\ell(x)$ are the Legendre Polynomials. Using Eqs. (2.130) and (2.131), Eq. (2.128) reduces to

$$w(\vartheta) = \sum_{\ell=0}^{\infty} \frac{2\ell + 1}{4\pi} C_\ell L_\ell(\cos \vartheta). \quad (2.132)$$

Now we look for the relation between two-point functions of $\delta^{2D}(\mathbf{n})$ and its three-dimensional counterpart $\delta(z, \mathbf{r}\mathbf{n})$. We begin by considering the harmonic expansion for δ , Eq. (2.118), and apply the radial projection, Eq. (2.125), to write

$$\delta^{2D}(\mathbf{n}) = \int dz F(z) \sum_{\ell m} \int dk \frac{k^2}{2\pi^2} \delta_{\ell m}(z, k) (-1)^\ell j_\ell(kr) Y_\ell^m(\mathbf{n}). \quad (2.133)$$

Then we consider the two-point correlation introducing the power spectrum $P(z, k)$, Eq. (2.122), to find

$$w(\vartheta) = \int dz F(z) \int dz' F(z') \frac{2}{\pi} \int dk k^2 \sum_{\ell} j_\ell(kr) j_\ell(kr') P(z, k) \times \sum_m Y_\ell^{m*}(\mathbf{n}) Y_\ell^m(\mathbf{n}').$$

Finally we use again the addition theorem for Spherical Harmonics, Eq. (2.131), to perform the sum over m and obtain

$$w(\vartheta) = \sum_{\ell} \frac{2\ell + 1}{4\pi} L_\ell(\cos \vartheta) \int dz F(z) \int dz' F(z') \times \left[\frac{2}{\pi} \int dk k^2 j_\ell(kr) j_\ell(kr') P(z, k) \right]. \quad (2.134)$$

Comparing Eqs. (2.132) and (2.134) we obtain the relation between the APS and the power spectrum,

$$C_\ell = \frac{2}{\pi} \int dz F(z) \int dz' F(z') \int dk k^2 j_\ell(kr) j_\ell(kr') P(z, k). \quad (2.135)$$

It is convenient to invert the order of the integrations and write this last relation as a projection over the Fourier modes k . Using the separated form for the matter power spectrum, Eq. (2.124), the APS results in a projection of the matter power spectrum today as

$$C_\ell = \frac{2}{\pi} \int dk k^2 P(k) [\Psi_\ell(k)]^2. \quad (2.136)$$

where

$$\Psi_\ell(k) = \int dz F(z) G(z) j_\ell(kr) \quad (2.137)$$

On the other hand, we can also obtain a relation between the ACF and the correlation function by simply considering the two-point function of the projection definition, Eq. (2.125),

$$\begin{aligned} w(\vartheta) &= \langle \delta^{2D*}(\mathbf{n}_1) \delta^{2D}(\mathbf{n}_2) \rangle \\ &= \int dz_1 F(z_1) \int dz_2 F(z_2) \langle \delta(z_1, \mathbf{n}_1) \delta(z_2, \mathbf{n}_2) \rangle \\ &= \int dz_1 F(z_1) \int dz_2 F(z_2) \xi(r_{12}), \end{aligned} \quad (2.138)$$

where $\cos \vartheta = \mathbf{n}_1 \cdot \mathbf{n}_2$ and r_{12} is the comoving distance between the two points $r_1 \mathbf{n}_1, r_2 \mathbf{n}_2$, which is given by the *cosines law* as

$$r_{12}^2 = r_1^2 + r_2^2 - 2r_1 r_2 \cos \vartheta. \quad (2.139)$$

The ACF $w(\vartheta)$ has been used successfully for a variety of cosmological analyses. In the context of cosmological information extraction, we have worked on the analysis of large-scale ACF of the CMASS luminous galaxies (LGs), a photometric-redshift catalog based on the Data Release 8 (DR8) of the Sloan Digital Sky Survey-III (SDSS-III) (de Simoni et al., 2013).

Limber approximation

The Limber approximation consists in approximating the integral

$$\frac{2}{\pi} \int dk k^2 P(k) j_\ell(kr) j_\ell(kr') \approx \frac{\delta_D(r - r')}{r^2} P \left(k = \frac{\ell + 1/2}{r} \right). \quad (2.140)$$

This can be seen as effectively replacing the highly oscillating Spherical Bessel functions by a Dirac delta function

$$j_\ell(x) \rightarrow \sqrt{\frac{\pi}{2x}} \delta_D \left[x - \left(\ell + \frac{1}{2} \right) \right],$$

which is accurate for sufficiently high- ℓ .

Under the Limber approximation, we may perform first the k integral in Eq. (2.135), to find

$$\begin{aligned} C_\ell &= \frac{2}{\pi} \int dz F(z) \int dz' F(z') \int dk k^2 j_\ell(kr) j_\ell(kr') P(z, k) \\ &= \int dz F(z) \int dz' F(z') \frac{\delta_D(r-r')}{r^2} P\left(z, k = \frac{\ell + 1/2}{r}\right), \\ &= \int dz \frac{F^2(z) H(z)}{r(z)^2} G^2(z) P\left(k = \frac{\ell + 1/2}{r(z)}\right). \end{aligned} \quad (2.141)$$

Therefore we reduce the original triple integral to a single redshift integral.

This is quite useful for numerical computations, as for small scales (high- ℓ), where the approximation is indeed valid, the oscillatory behavior of $j_\ell(kr)$ makes it challenging to perform the exact integral. However, the approximation is not accurate for the large-scale (low- ℓ) regime, in which case we must perform the exact integration.

For cases when the Limber approximation is inaccurate, faster integration algorithms become extremely useful. An example of such algorithm is `FFTLog` (see § 2.4.7 and Appendix E). Whereas the computation complexity of standard brute-force or even adaptative integration methods scale roughly as a power of N – the number of integrand evaluations – `FFTLog` relies on fast discrete Fourier transforms, and scales as $\sim N \log N$, frequently reducing the computation time by orders of magnitude. Moreover, this remains true for all the two-point correlations that can be constructed not only from positions of galaxies, but also from its shearing (from weak lensing), namely, shear, galaxy-galaxy lensing and the angular correlations presented here (see, e.g. DES Collaboration et al., 2018, and references therein). For a review of the extension of equations above to these cases, see App D

2.4.4 Galaxy bias

So far our description of clustering has referred mostly to the matter density field. Only in § 2.4.1 we briefly mentioned that overdensities of matter and galaxies do not coincide. The matter field is dominated by dark matter, which does not emit electromagnetic radiation. We want to relate the clustering of the matter field to that of galaxies, whose light is directly observed in photometric and spectroscopic surveys. Galaxies represent discrete and *biased* tracers of the matter field. That means that the density contrast of galaxies δ_g track those of matter δ , but must be corrected by a *bias* factor

b_g as

$$\delta_g = b_g \delta \quad (2.142)$$

As a result, all two-point statistics of galaxies are related to those of the matter field by a factor of b_g^2

$$\xi_g(r) = b_g^2 \xi(r) \quad (2.143)$$

$$P_g(k) = b_g^2 P(k) \quad (2.144)$$

$$w_g(\vartheta) = b_g^2 w(\vartheta) \quad (2.145)$$

$$(C_\ell)_g = b_g^2 C_\ell \quad (2.146)$$

On large scales, the galaxy bias in the linear regime is found to be fairly constant, i.e. independent of scale. In the nonlinear regime, the bias becomes scale dependent and there are approaches to account for these nonlinear effects (see e.g. § 2.2.2 and § 2.3).

2.4.5 Redshift space distortions

The observed redshift of an object in the universe is distorted by its peculiar movement with respect to the Hubble flow, i.e., its peculiar local movement with respect to the global gravitational free fall. If this peculiar velocity is non-relativistic, we can take into account this effect by correcting the gravitational redshift z with a non-relativistic redshift z_{pec} to compose the total observed redshift, z_{obs} ,

$$(1 + z_{\text{obs}}) = (1 + z)(1 + z_{\text{pec}}) \approx (1 + z) \left(1 + \frac{v_{\text{pec}}}{c}\right),$$

where we identify $z_{\text{pec}} = v_{\text{pec}}/c$, a non-relativistic Doppler effect due to a peculiar velocity that should be aligned with the Hubble flow, i.e. if the total peculiar velocity of the object is given by \mathbf{v}_{pec} , then $v_{\text{pec}} = \mathbf{v}_{\text{pec}} \cdot \mathbf{e}_x$, its radial component in the line-of-sight direction. Then, the observed redshift can be written as

$$z_{\text{obs}} = z + \frac{v_{\text{pec}}}{c}(1 + z) = z + \frac{\mathbf{v}_{\text{pec}} \cdot \mathbf{e}_x}{c}(1 + z)$$

Coordinates in redshift space

This change in observed redshift implies a correction on measured distances to objects on our past light cone. If we infer the position of such an object

according to our definition of the radial comoving distance, we have

$$\begin{aligned}
x_s(z) &= \int_0^{z_{\text{obs}}} \frac{c \, dz'}{H(z')} = \int_0^{z + \frac{v_{\text{pec}}}{c}(1+z)} \frac{c \, dz'}{H(z')} \\
&= \int_0^z \frac{c \, dz'}{H(z')} + \int_z^{z + \frac{v_{\text{pec}}}{c}(1+z)} \frac{c \, dz'}{H(z')} \\
&\approx x(z) + \frac{1+z}{H(z)} v_{\text{pec}} = x(z) + \frac{1+z}{H(z)} \mathbf{v}_{\text{pec}} \cdot \mathbf{e}_x
\end{aligned} \tag{2.147}$$

where in the last line $x(z)$ is the usual real-space radial comoving distance, and we approximate the second integral by its integrand evaluated at z times the integration interval $z_{\text{obs}} - z$ to write the contribution from the peculiar velocity to the redshift-space distance $x^s(z)$.

Jacobian

The natural question for clustering analyses is what the relation between the galaxy overdensities in real and redshift space coordinates is? The solution was proposed by Kaiser (1987) in the context of the linear theory of cosmological perturbations. The fundamental assumption is that the number of tracers of the matter distribution in the universe (e.g., galaxies) should be a locally conserved quantity, whether we are in real or redshift space, i.e.

$$n_g^{(s)}(\mathbf{x}_s) d^3 \mathbf{x}_s = n_g^{(r)}(\mathbf{x}) d^3 \mathbf{x},$$

where $n_g^{(r)}$ and $n_g^{(s)}$ are the number densities of objects in real and redshift space, and \mathbf{x} and \mathbf{x}_s are the spatial comoving coordinates in real and redshift space, respectively. Thus we can write the comoving volume in spherical coordinates as

$$d^3 \mathbf{x}_s = dx_s x_s^2 \sin(\theta) d\theta d\phi, \quad d^3 \mathbf{x} = dx x^2 \sin(\theta) d\theta d\phi$$

where we assume that photons travel on unperturbed null geodesics, so that the comoving angular coordinates are common in real and redshift space and only the radial coordinate is distorted in redshift space. This fact allows us to write the number density in redshift space as

$$n_g^{(s)}(\mathbf{x}_s) = n_g^{(r)}(\mathbf{x}) J,$$

where J is the Jacobian of the transformation of coordinates from redshift to real space,

$$J = \frac{dx}{dx_s} \frac{x^2}{x_s^2}.$$

Then, using the Eq. (2.147), the Jacobian can be written as

$$J = \left[1 + \frac{\partial}{\partial x} \left(\frac{1+z}{H(z)} \mathbf{v}_{\text{pec}} \cdot \mathbf{e}_x \right) \right]^{-1} \left[1 + \frac{1+z}{H(z)} \frac{\mathbf{v}_{\text{pec}} \cdot \mathbf{e}_x}{x} \right]^{-2}.$$

Kaiser (1987) realized that the correction term due to the derivative (first factor) of the velocity is much more important than the correction in the second factor. The argument goes as follows. For a plane wave perturbation, the term with the derivative is of order $\sim kv/H$, while the other correction is of the order $v/(Hx)$, i.e., the first correction is “larger” than the second one by a factor of kx . The reason why this factor is, in fact, $\gg 1$ is that in a survey of observed objects, x should be of the order of the size of the survey, while, for plane modes, k should be of the order of the Fourier modes we hope to measure in the observation (survey). Perturbations on the largest scale probed by such an observation, i.e., those with $k^{-1} \sim x$, should be very poorly determined since there are very few modes with a wavelength of the size of the survey. On the other hand, modes with wavelengths smaller than the size of the survey are much easier to probe as there are many such modes. Since we effectively average over all modes to estimate the power spectrum, we conclude that the most significant contribution should come from modes such that $kx \gg 1$. Expanding the leading contribution up to first order in v ,

$$J \simeq 1 - \frac{\partial}{\partial x} \left(\frac{1+z}{H(z)} \mathbf{v}_{\text{pec}} \cdot \mathbf{e}_x \right).$$

Density contrast in redshift space

For the fluctuations, we can write the number density of objects as $n_g^{(r)}(\mathbf{x}) = \bar{n}_g \left(1 + \delta_g^{(r)}(\mathbf{x}) \right)$ and $n_g^{(s)}(\mathbf{x}_s) = \bar{n}_g \left(1 + \delta_g^{(s)}(\mathbf{x}_s) \right)$ in real and redshift spaces respectively, with \bar{n}_g the background or average number density, to have

$$1 + \delta_g^{(s)} = (1 + \delta_g^{(r)}) \left[1 - \frac{\partial}{\partial x} \left(\frac{1+z}{H(z)} \mathbf{v}_{\text{pec}} \cdot \mathbf{e}_x \right) \right],$$

or, expanding up to first order in v and δ , i.e. in linear perturbation theory,

$$\delta_g^{(s)}(\mathbf{x}_s) = \delta_g^{(r)}(\mathbf{x}) - \frac{\partial}{\partial x} \left(\frac{1+z}{H(z)} \mathbf{v}_{\text{pec}} \cdot \mathbf{e}_x \right). \quad (2.148)$$

Power spectrum in redshift space

Now we would like to consider the redshift-space fluctuation in Fourier space. For that, we need to relate the peculiar linear velocity with the density contrast, which can be done using the evolution equations for matter in linear perturbation theory. From the solution for the velocity field in linear theory, Eq. (2.41), we have

$$\tilde{\mathbf{v}}(\mathbf{k}) = ifaH(a)\tilde{\delta}(\mathbf{k})\frac{\mathbf{k}}{k^2}, \quad (2.149)$$

where recall $f = d \ln(D_+)/d \ln(a)$ is the growth rate, with D_+ the linear growth mode of the perturbations. Notice that $\tilde{\mathbf{v}}(\mathbf{k})$ depends on the *matter* density contrast $\tilde{\delta}(\mathbf{k}) = \tilde{\delta}_g(\mathbf{k})/b_g$, where b_g is the linear galaxy bias. Then taking the Fourier transform of Eq. (2.148) and using the Fourier transform of the velocity field, Eq. (2.149), we can see that

$$\tilde{\delta}_g^{(s)}(\mathbf{k}) = (1 + \beta_g \mu_{\mathbf{k}}^2) \tilde{\delta}_g^{(r)}(\mathbf{k}), \quad (2.150)$$

where $\beta_g = f/b_g$ and $\mu_{\mathbf{k}} := \mathbf{e}_{\mathbf{k}} \cdot \mathbf{e}_x$, the cosine of the angle between the wave vector of the perturbation mode and the line of sight. This is the well known Kaiser relation, which is translated to the corresponding power spectrum as (Kaiser, 1987)

$$P_g^{(s)}(\mathbf{k}) = b_g^2 [1 + \beta_g \mu_{\mathbf{k}}^2]^2 P(k), \quad (2.151)$$

where $P(k)$ is the real-space *matter* power spectrum. We see that the redshift space distortion (RSD) to linear order is reflected in the power spectrum as an anisotropic dependence. Decomposing $\mathbf{k} = (k_{\parallel}, \mathbf{k}_{\perp})$ in components parallel and perpendicular to the line-of-sight, we have $\mu_{\mathbf{k}} = k_{\parallel}/k$ and $k^2 = k_{\parallel}^2 + k_{\perp}^2$.

Correlation function in redshift space and multipoles

Now, we can work the Fourier transform of this power spectrum to obtain the corresponding two-point correlation function in redshift space. The starting point is the plane wave decomposition, Eq. (2.117), which allows us to write

$$\begin{aligned} \xi_g^{(s)}(r) &= \int_{\mathbb{R}^3} \frac{d^3\mathbf{k}}{(2\pi)^3} P_g^{(s)}(\mathbf{k}) e^{i\hat{\mathbf{k}} \cdot \hat{\mathbf{n}} r} \\ &= \sum_{\ell=0}^{+\infty} \sum_{m=-\ell}^{+\ell} i^{\ell} \xi_{g\ell}(r) Y_{\ell}^{m*}(\hat{\mathbf{n}}) \int d^2\Omega_{\hat{\mathbf{k}}} [1 + \beta_g(z)\mu_{\mathbf{k}}^2]^2 Y_{\ell}^m(\hat{\mathbf{k}}), \end{aligned}$$

where we define

$$\xi_{g\ell}(r) := \int_0^\infty \frac{dk}{2\pi^2} k^2 j_\ell(kr) P_g(k). \quad (2.152)$$

Introducing the spherical harmonics Y_ℓ^m in terms of associate Legendre polynomials L_ℓ^m

$$Y_\ell^m(\theta, \phi) = \sqrt{\frac{2\ell + 1}{4\pi} \frac{(\ell - m)!}{(\ell + m)!}} L_\ell^m(\cos \theta) \exp(im\phi),$$

to evaluate the azimuthal integral as

$$\int_0^{2\pi} d\phi_{\hat{\mathbf{k}}} \exp[im(\phi_{\hat{\mathbf{k}}} - \phi_{\hat{\mathbf{n}}})] = 2\pi\delta_{m0},$$

we find

$$\xi_g^{(s)}(r) = \sum_{\ell=0}^{+\infty} i^\ell (2\ell + 1) \xi_{g\ell}(r) L_\ell(\mu_{\mathbf{n}}) \int_{-1}^1 \frac{d\mu_{\mathbf{k}}}{2} [1 + \beta_g(z)\mu_{\mathbf{k}}^2]^2 L_\ell(\mu_{\mathbf{k}}).$$

where L_ℓ are Legendre polynomials. Since the brackets within the last integral in $\mu_{\mathbf{k}}$ are polynomials of order 4, the integral is non-zero only for

$$\int_{-1}^{+1} \frac{dx}{2} [1 + \beta_g x^2]^2 L_\ell(x) = \begin{cases} \frac{1}{15} (3\beta_g^2 + 10\beta_g + 15) & \ell = 0, \\ \frac{1}{105} (\beta_g^2 + 28\beta_g) & \ell = 2, \\ \frac{8}{315} \beta_g^2 & \ell = 4. \end{cases}$$

So that we find

$$\begin{aligned} \xi_g^{(s)}(r) = & \left[1 + \frac{2}{3}\beta_g(z) + \frac{1}{5}\beta_g(z)^2 \right] \xi_{g0}(r) L_0(\mu_n) \\ & - \left[\frac{4}{3}\beta_g(z) + \frac{4}{7}\beta_g(z)^2 \right] \xi_{g2}(r) L_2(\mu_n) \\ & + \left[\frac{8}{35}\beta_g(z)^2 \right] \xi_{g4}(r) L_4(\mu_n), \quad (2.153) \end{aligned}$$

Note that the end result depends on $\mu_n := \mathbf{e}_x \cdot \hat{\mathbf{n}}$, the cosine of the angle between the line of sight (\mathbf{e}_x) and the line that connects the two points ($\hat{\mathbf{n}}$). We can also identify the monopole ($\ell = 0$ term) as the *Real Space Correlation Function*, $\xi_0(r) = \xi(r)$.

Angular clustering in redshift space

Let us begin by considering the harmonic modes of the redshift-space galaxy overdensity,

$$\begin{aligned}
\delta_{\ell m}^{(s)}(k) &= 4\pi \int dr r^2 \int d^2\Omega_{\mathbf{n}} \delta_g^{(s)}(r, \mathbf{n}) (-1)^\ell j_\ell(kr) Y_\ell^{m*}(\mathbf{n}) \\
&= 4\pi \int dr r^2 \int d^2\Omega_{\mathbf{n}} [1 + \beta_g(z) \partial_r^2 (\nabla^2)^{-1}] \delta_0(r\mathbf{n}) (-1)^\ell j_\ell(kr) Y_\ell^{m*}(\mathbf{n}) \\
&= \delta_{\ell m}(k) + \frac{\beta_g}{k^2} \left[4\pi \int dr r^2 \int d^2\Omega_{\mathbf{n}} (\partial_r^2) \delta_0(r\mathbf{n}) (-1)^\ell j_\ell(kr) Y_\ell^{m*}(\mathbf{n}) \right], \tag{2.154}
\end{aligned}$$

where in the last line we use integration by parts, showing the standard result that the Fourier representation of the inverse Laplace operator is nothing but k^{-2} . In order to evaluate the integrals, we can use recurrence relations of the radial modes. To simplify, let us call the radial mode $X_\ell(r, k) := (-1)^\ell j_\ell(kr)$. Recurrence relations for Spherical Bessel functions then give us,

$$(2\ell + 1)X'_\ell = (\ell + 1)X_{\ell+1} - \ell X_{\ell-1},$$

and allow us to write down the second derivative as

$$X''_\ell = -\frac{(2\ell^2 + 2\ell - 1)}{(2\ell + 3)(2\ell - 1)}X_\ell + \frac{\ell(\ell - 1)}{(2\ell - 1)(2\ell + 1)}X_{\ell-2} + \frac{(\ell + 1)(\ell + 2)}{(2\ell + 1)(2\ell + 3)}X_{\ell+2}. \tag{2.155}$$

By inserting Eq. (2.155) in (2.154) we arrive at the anisotropic harmonic modes,

$$\begin{aligned}
\delta_{\ell m}^{(s)}(k) &= \delta_{\ell m}(k) + \beta_g(z) \left[\frac{(2\ell^2 + 2\ell - 1)}{(2\ell + 3)(2\ell - 1)} \delta_{\ell m}(k) \right. \\
&\quad \left. - \frac{\ell(\ell - 1)}{(2\ell - 1)(2\ell + 1)} \delta_{\ell-2m}(k) - \frac{(\ell + 1)(\ell + 2)}{(2\ell + 1)(2\ell + 3)} \delta_{\ell+2m}(k) \right]. \tag{2.156}
\end{aligned}$$

This result is interesting, as it gives us the expansion of Fourier Spherical modes in redshift space over the past light-cone in terms of the Fourier Spherical modes for the total matter overdensity today $\delta_{\ell m}(k)$.

Finally, Eq. (2.156) also helps us find the redshift-space distorted APS. As in configuration space, Eq. (2.133), the projected overdensity in redshift-space can be written as

$$\delta^{(s)2D}(\mathbf{n}) = \int dz F(z) \sum_{\ell m} \int dk \frac{k^2}{2\pi^2} \delta_{\ell m}^{(s)}(z, k) (-1)^\ell j_\ell(kr) Y_\ell^m(\mathbf{n}), \tag{2.157}$$

so considering its two-point function, using the addition theorem for Spherical Harmonics (as in Eq. 2.134) and the relation between Fourier Spherical modes and the power spectrum, Eq. (2.122), we obtain the relation between the redshift-space APS and the real-space power spectrum,

$$C_\ell^{(s)} = \frac{2}{\pi} \int dk k^2 P(k) [\Psi_\ell(k) + \Psi_\ell^{\text{RSD}}(k)]^2, \quad (2.158)$$

where the projection kernels Ψ_ℓ are given by Eq. (2.137) and Ψ_ℓ^{RSD} by

$$\begin{aligned} \Psi_\ell^{\text{RSD}}(k) = \int dz \beta_g(z) G(z) F(z) \left\{ \frac{2\ell^2 + 2\ell - 1}{(2\ell + 3)(2\ell - 1)} j_\ell(kr) \right. \\ \left. - \frac{\ell(\ell - 1)}{(2\ell - 1)(2\ell + 1)} j_{\ell-2}(kr) - \frac{(\ell + 1)(\ell + 2)}{(2\ell + 1)(2\ell + 3)} j_{\ell+2}(kr) \right\}, \quad (2.159) \end{aligned}$$

This result generalizes the previous expressions from § 2.4.3, which did not account for RSD effects. These expressions are used in modeling the APS in our BAO analysis of the DES Y1 galaxy sample in Chap. 5.

2.4.6 Projected correlation function

Wide imaging and spectroscopic surveys offer the possibility of using more than one single tracer of the matter density to perform clustering analysis. This opens possibilities for LSS studies at different redshift ranges, as different astrophysical objects targeted appear preferably at different redshifts reflecting their particular evolution. One exciting window of opportunities is the combination of clustering measurements from different tracers which can help beat sample variance (see, e.g. Abramo & Leonard, 2013; Alarcon et al., 2018). However, this also brings the challenge of the correct targeting of samples. Such a non-trivial task is an excellent example of where a combination of efforts from imaging and spectroscopic surveys can be particularly useful. As an example, we have studied the detection properties of the emission line galaxies (ELG) population targeted from the Dark Energy Survey (DES) photometry, validating with spectra from the first test plates of the extended Baryon Oscillation Spectroscopic Survey (eBOSS), as presented in Jouvel et al. (2017). Here we present the clustering results of this sample in Chap. 3.

Clustering studies can also bring valuable information about galaxy formation, e.g., the statistical relationship between galaxies and halos and their evolution (see, e.g. Wechsler & Tinker, 2018, and references therein). For instance, we have worked on the very first scientific results from the luminous red galaxy (LRG) sample of the eBOSS, which measured small and

intermediate scale clustering of LRG's – where most of the information on the galaxy-halo connection is hoped to be encoded. These results were presented in Zhai et al. (2017), where we showed that the clustering of massive galaxies from BOSS-CMASS, BOSS-LOWZ, and SDSS is consistent with observations over the full redshift range that these samples cover and can be consistently interpreted in the context of the Halo Occupation Distribution (HOD) framework. We also described how the addition of eBOSS to previous surveys improves the investigation of the evolution of massive galaxies. Here we present some of these results in Chap. 4.

Both studies above made use of the *projected correlation function*, which we now describe. Under the distant-observer approximation, a plane-parallel decomposition of the comoving separation of pairs can be introduced in order to extract information contained on the anisotropic two-point correlation function. As long as there is only one line of sight, the following basic geometrical relations follow

$$\mathbf{r} = \mathbf{r}_2 - \mathbf{r}_1, \quad (2.160a)$$

$$\mathbf{l} = (\mathbf{r}_1 + \mathbf{r}_2) / 2, \quad (2.160b)$$

$$r_\pi = \mathbf{r} \cdot \mathbf{l} / l = \mu r, \quad (2.160c)$$

$$r_p = \sqrt{r^2 - r_\pi^2} = \sqrt{1 - \mu^2} r, \quad (2.160d)$$

where \mathbf{l} is the line of sight, $\mathbf{r}_1, \mathbf{r}_2$ are the given two-point positions, \mathbf{r} is their separation, μ is the cosine of the angle between \mathbf{l} and \mathbf{r} , and r_p and r_π are the perpendicular and parallel decomposition separation of \mathbf{r} with respect to the line of sight, see Fig. 2.2.

It is, therefore, possible to have two different parametrizations for the anisotropic correlation function,

$$\xi(r, \mu) = \xi(r_p, r_\pi). \quad (2.161)$$

The first one is useful to describe linear RSDs, as the Kaiser effect can be completely characterized by μ . The second parametrization in Eq. (2.161) is useful for introducing the *projected correlation function*, $w_p(r_p)$, which exhibits a set of nice mathematical properties as we explain below.

The projected correlation function is defined by the projection of the anisotropic correlation function over the parallel separations, r_π ,

$$w_p(r_p) = \int_{-\infty}^{\infty} dr_\pi \xi(r_p, r_\pi) = 2 \int_0^{\infty} dr_\pi \xi(r_p, r_\pi), \quad (2.162)$$

where the last equality follows from statistical isotropy.

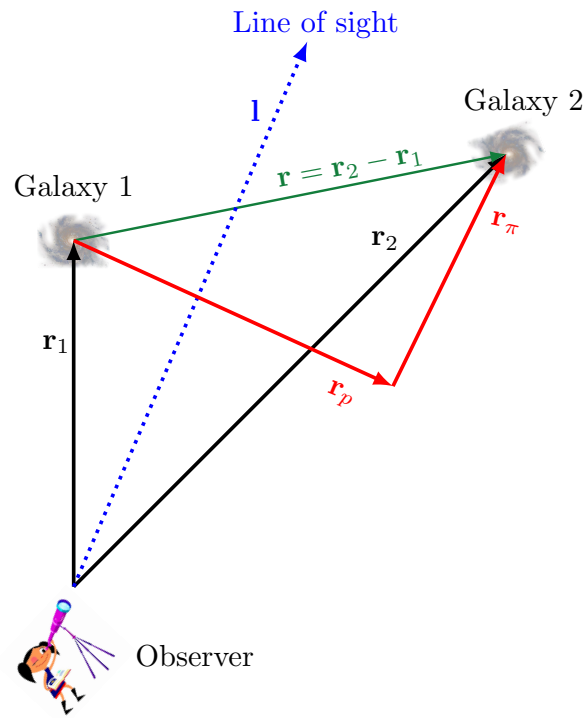


Figure 2.2: Geometry of two-point functions. Here \mathbf{r}_1 and \mathbf{r}_2 define the location of two galaxy positions with respect to the observer, $\mathbf{r} = \mathbf{r}_2 - \mathbf{r}_1$ is their separation and \mathbf{l} is the line-of-sight. Notice that for galaxies at similar redshifts and small angular separations, \mathbf{r}_1 , \mathbf{r}_2 and \mathbf{l} are nearly indistinguishable. The components r_p and r_π define the perpendicular and parallel decomposition of \mathbf{r} relative to the line of sight. [Clipart images credit. Observer: www.seekpng.com. Galaxies: www.cashadvance6online.com.]

For the purely isotropic case, i.e. when $\xi(\mathbf{r}) = \xi(r) = \xi(r_p, r_\pi)$, the 3D and the projected correlation function form an Abel transform pair,

$$w_p(r_p) = 2 \int_{r_p}^{\infty} dr \frac{r\xi(r)}{\sqrt{r^2 - r_p^2}}, \quad (2.163a)$$

$$\xi(r) = -\frac{1}{\pi} \int_r^{\infty} dr_p \frac{dw_p(r_p)}{dr_p} (r^2 - r_p^2)^{-1/2}. \quad (2.163b)$$

The advantage of using $w_p(r_p)$ is that the projection along the line of sight gets rid of the RSD effects. So if one is interested in studying galaxy properties, e.g., bias, but not RSD effects, this may be a good choice even for spectroscopic surveys. In Chaps. 3 and 4, we will employ the projected correlated function to measure the bias of eBOSS/DES Emission Line Galaxies and eBOSS Luminous Red Galaxies.

In Figs. 2.3, 2.4 and 2.5, we illustrate all two-point statistics defined so far, defined in 3D and 2D (angular), and in real/configuration/ and Fourier/Harmonic spaces. We also show effects of nonlinearities, RSD and Limber approximation.

2.4.7 Covariance matrices

The Gaussian covariance of the correlation function $\xi(r)$ is given by

$$\begin{aligned} \text{Cov}_\xi(r, r') &= \langle \xi(r)\xi(r') \rangle - \langle \xi(r) \rangle \langle \xi(r') \rangle \\ &= \frac{2}{V} \int_0^\infty dk \frac{k^2}{2\pi^2} j_0(kr) j_0(kr') \left[P(k) + \frac{1}{\bar{n}} \right]^2, \end{aligned} \quad (2.164)$$

where V is the volume of the sample and \bar{n} represents the mean number of galaxies per unit volume, accounting for the shot-noise.

In order to take into account the effect of binning on the estimates of the 2PTCF and its covariance, one can spherically average them inside each bin considered, following (Xu et al., 2012). Note that from Eq. (2.164), the pure shot-noise contribution (SN), i.e., that resulting from considering only the term proportional to \bar{n}^{-2} , is intrinsically diagonal and divergent. However, this property comes from the fact that Eq. (2.164) applies only in a continuous limit, i.e., for infinitesimal bin widths. For finite bins, we take the spherical average of such contribution to the covariance and find

$$\text{Cov}_\xi^{\text{SN}}(r_n, r_m) = \frac{2}{V} \frac{1}{4\pi} \left[\frac{3}{r_{n+1}^3 - r_n^3} \right] \frac{\delta_{mn}}{\bar{n}^2}. \quad (2.165)$$

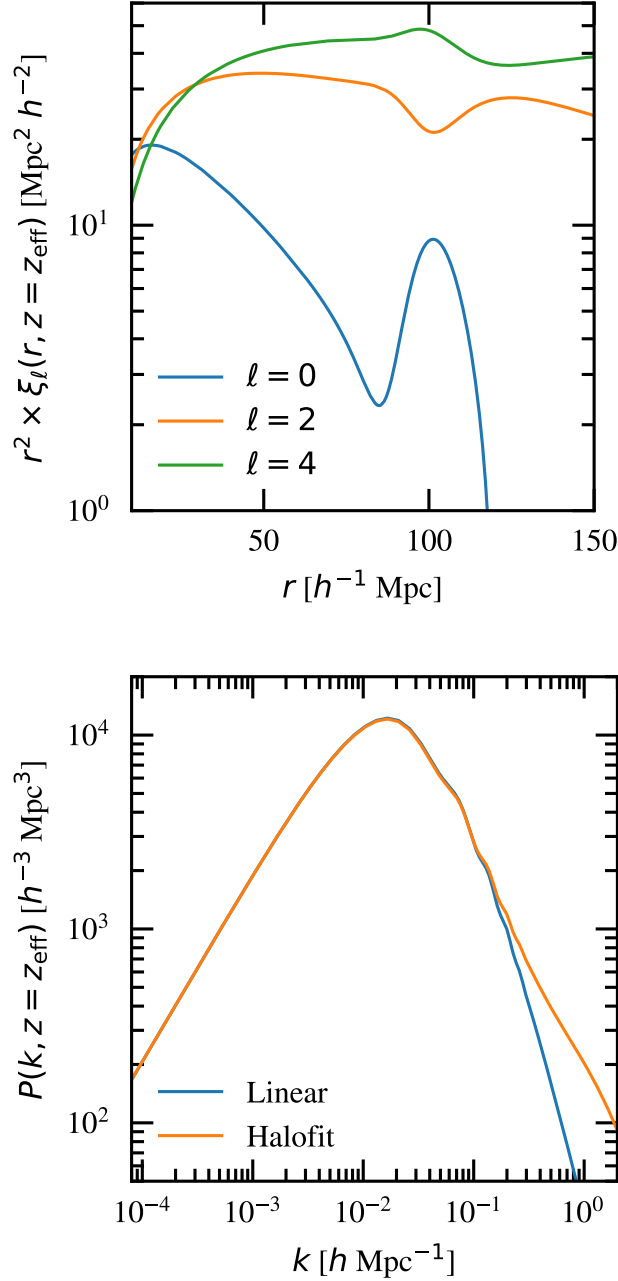


Figure 2.3: Three-dimensional 2-point statistics for the matter field in configuration and Fourier spaces, computed at $z_{\text{eff}} = 0.65$. (*Top*): Multipoles of the 3D correlation function $\xi(r)$ (see Eq. 2.152). Notice the presence of the BAO peak at $r_d \approx 100 \text{ Mpc}/h = 147 \text{ Mpc}$ (see § 2.4.8), which is emphasized by the multiplication by r^2 . (*Bottom*): 3D power spectrum $P(k)$ (Fourier transform of $\xi(r)$), as computed by CAMB (linear) and Halofit (nonlinear). The single BAO peak of the correlation gives rise to multiple peaks in Fourier space.

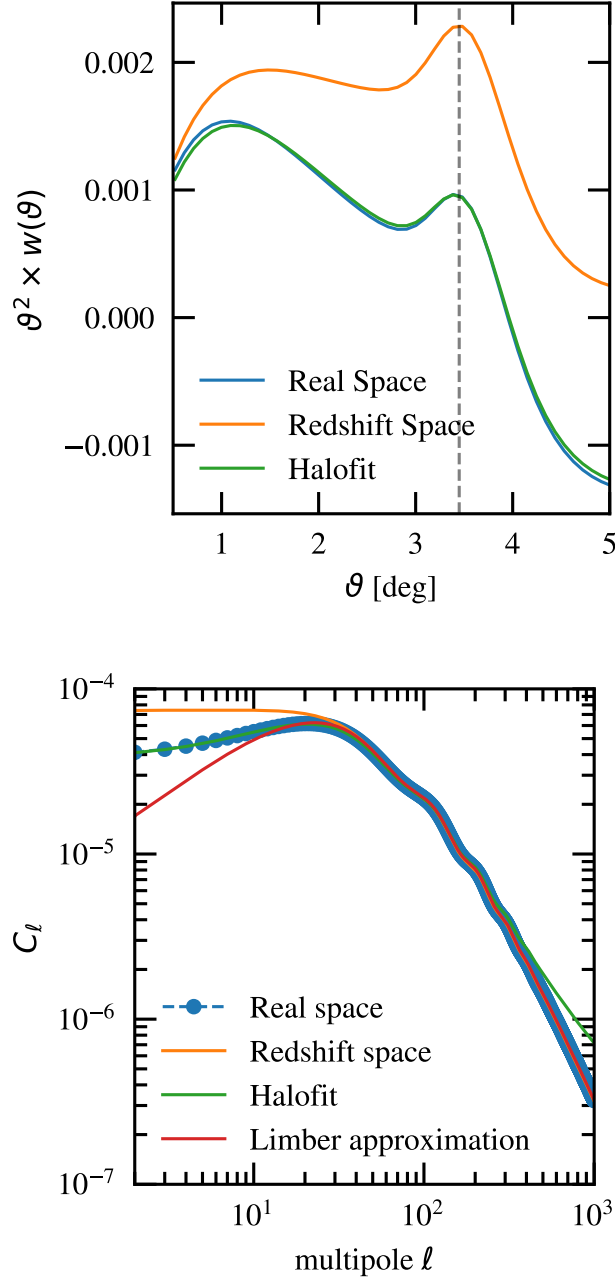


Figure 2.4: Two-dimensional (angular) 2-point statistics for the matter field in configuration and harmonic spaces, computed at $z = 0.65$. (*Top*): Angular correlation function $w(\vartheta)$ (see Eq. 2.138). The projection kernel $F(z)$ is the redshift selection function from the DES Y1 data for a photo- z bin in the range $z_{\text{phot}} \in [0.6, 0.7]$ (see Chap. 5). For the Planck 2018 cosmology we have $D_A(z) \approx 2443$ Mpc, so the peak location is $\vartheta_{\text{BAO}} = r_d/D_A = 147/2443 \approx 0.06$ rad ≈ 3.45 deg. (*Bottom*): Angular power spectrum C_ℓ . Again multiple peaks appear in harmonic space. Here we also show the effects of redshift-space distortions, Limber approximation and non-linear spectrum (Halofit).

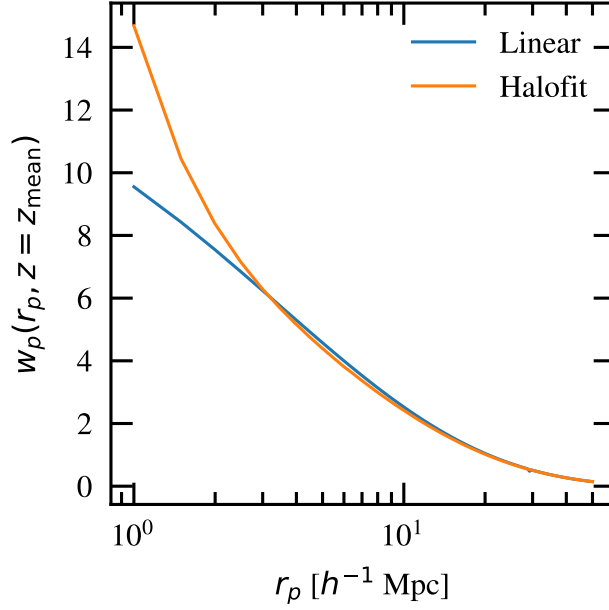


Figure 2.5: Projected correlation function $w_p(r_p)$ at $z_{\text{mean}} = 0.65$ (see Eq. 2.162) as a function of coordinate r_p perpendicular to the line of sight.

Similarly, the covariance of the projected correlation $w_p(r_p)$ is

$$\text{Cov}_{w_p}(r_p, r'_p) = 4 \int d\pi \int d\pi' \text{Cov}_\xi \left(\sqrt{\pi^2 + r_p^2}, \sqrt{\pi'^2 + r_p'^2} \right), \quad (2.166)$$

where Cov_ξ is given by Eq. (2.164).

The Gaussian covariance matrix of the APS at multipoles ℓ and ℓ' and redshift bins i and j is approximately given by

$$\begin{aligned} \text{Cov}[\text{APS}]_{\ell\ell'}^{ij} &= \langle C_\ell^i C_{\ell'}^j \rangle - \langle C_\ell^i \rangle \langle C_{\ell'}^j \rangle \\ &= \frac{2}{(2\ell + 1)f_{\text{sky}}} \left(C_\ell^{i,j} + \frac{\delta_{ij}}{\bar{n}_g^i} \right)^2 \delta_{\ell\ell'}, \end{aligned} \quad (2.167)$$

where f_{sky} denotes the observed sky fraction and \bar{n} the mean surface density of galaxies per unit solid angle accounting for shot noise.

The covariance matrix for the ACF can be constructed combining Eqs. (2.132) and (2.167). The cross-covariance between two redshift shells i and j and

two angular bins m and n can be written as

$$\begin{aligned} \text{Cov}(\text{ACF})_{mn}^{ij} &= \langle w^i(\vartheta_m)w^j(\vartheta_n) \rangle - \langle w^i(\vartheta_m) \rangle \langle w^j(\vartheta_n) \rangle \\ &= \sum_{\ell=0}^{\infty} \frac{2\ell+1}{(4\pi)^2} L_{\ell}(\cos \vartheta_m) L_{\ell}(\cos \vartheta_n) \left(C_{\ell}^{i,j} + \frac{\delta_{ij}}{\bar{n}_g^i} \right)^2. \end{aligned} \quad (2.168)$$

Notice that the purely shot-noise contribution from the ℓ -independent term $\delta_{ij}/(\bar{n}_g^i)^2$ in the parenthesis of the previous expression diverges when the sum is extended to $\ell = \infty$ due to the completeness relation for Legendre polynomials

$$\sum_{\ell=0}^{\infty} \frac{2\ell+1}{2} L_{\ell}(\mu_m) L_{\ell}(\mu_n) = \delta_D(\mu_m - \mu_n). \quad (2.169)$$

However, this is again an artifact from the fact that the above expression only applies in the continuous limit or for infinitely fine bins. In reality, $w(\vartheta)$ is estimated within angular bins $\Delta\vartheta = \vartheta_{n+1} - \vartheta_n$ as an average

$$w_{\Delta\vartheta}(\vartheta_n) = \frac{1}{\Delta\vartheta} \int_{\vartheta \in [\vartheta_n, \vartheta_{n+1}]} d\vartheta w(\vartheta). \quad (2.170)$$

Propagating this into the covariance, the Dirac delta function is regularized into a Kronecker delta, and the purely shot-noise (SN) contribution becomes finite. For small angles, we have

$$\text{Cov}[\text{ACF}]_{mn}^{ij} |^{\text{SN}} \propto \frac{\delta_{\vartheta_m, \vartheta_n}}{\bar{n}_i^2 2\pi \vartheta_n \Delta\vartheta^2} = \frac{\delta_{\vartheta_m, \vartheta_n}}{([\bar{N}_g]_n^i)^2} \quad (2.171)$$

where $[\bar{N}_g]_n^i$ is the average number of galaxies in the redshift shell given the angular binning around ϑ_n , and therefore the denominator in Eq. (2.171) is the number of galaxy pairs within the bin/shell.

For our purposes, we will simply write

$$\begin{aligned} \text{Cov}[\text{ACF}]_{mn}^{ij} &= \sum_{\ell=0}^{\infty} \frac{2\ell+1}{(4\pi)^2} L_{\ell}(\cos \vartheta_m) L_{\ell}(\cos \vartheta_n) \left[(C_{\ell}^{i,j})^2 + 2C_{\ell}^{i,j} \frac{\delta_{ij}}{\bar{n}_g^i} \right] \\ &\quad + \text{Cov}[\text{ACF}]_{mn}^{ij} |_{\text{SN}}. \end{aligned} \quad (2.172)$$

Since C_{ℓ}^{ij} goes to zero sufficiently fast as $\ell \rightarrow \infty$, the sum now correctly converges, and the finite SN contribution is added separately.

FFTL`og` method

As a result of the form of the harmonic modes on a flat space ($K = 0$), Eq. (2.117), in which the radial modes are given by Spherical Bessel functions $j_\ell(x)$, the different expressions relating two-point statistics in 3D and 2D (the sphere) results in particular forms of the same integral transform having as kernel $j_\ell(s)$'s. Such a kind of integral transforms belongs to the class of *Hankel* or *Fourier-Bessel transforms*, defined by the transform pair

$$\tilde{a}(k) = \int_0^\infty dr k(kr)^q J_\mu(kr) a(r), \quad (2.173a)$$

$$a(r) = \int_0^\infty dk r(kr)^{-q} J_\mu(kr) \tilde{a}(k), \quad (2.173b)$$

where the function \tilde{a} is the Hankel transform of a , q is a bias parameter and $J_\mu(x)$ are Bessel functions of the first kind. Recall the relation between J_μ and j_ℓ ,

$$j_\ell(x) = \sqrt{\frac{\pi}{2x}} J_{\ell+1/2}(x) \quad (2.174)$$

So one can always approach the problem of numerically computing such integrations as the problem of numerically evaluating Hankel transforms. On top of that, in cosmological applications, one usually requires transforming a function that extends over many orders of magnitude and is computed accurately in logarithmic space. For instance, that is the case of the matter power spectrum coming from Boltzmann codes, even in the linear regime, as the behavior of this function over at least 3 decades in k ($\sim 10^{-1} - 10^2 h \text{ Mpc}^{-1}$) is required to compute the multipoles $\xi_{\text{accurately}}$ on large scales (see e.g. Lesgourgues, 2011, for a discussion of this point).

The FFTL`og` algorithm, initially proposed in the cosmological context by Hamilton (2000), accomplishes the requirements above by computing the fast Hankel (Fourier-Bessel) transform of a periodic sequence of logarithmically spaced points. FFTL`og` can thus be regarded as a natural analog to the standard Fast Fourier Transform (FFT, e.g. Frigo & Johnson, 2005). Just like the usual FFT provides the exact (to machine precision) Fourier transform of a linearly spaced periodic sequence, representing the discretization of a function, FFTL`og` provides the exact Hankel transform of a logarithmically spaced periodic sequence, giving an appropriate discretization of a function for cosmological applications.

The FFTL`og` algorithm is reviewed in Appendix E. Based on the original set of Fortran routines developed by A. Hamilton¹¹, we have implemented our C-code version of FFTL`og`, which we used in this work.

¹¹<http://casa.colorado.edu/~ajsh/FFTLog/>

2.4.8 Baryon acoustic oscillations

BAO physics

Before formation of neutral atoms, at an energy of $E \sim 10^2$ KeV corresponding to a temperature of $T \sim 10^9$ K and time of $t \sim \text{min}$, $z \sim 10^{8-9}$ the ingredients of the matter-energy content of the universe were basically radiation, electrons, and protons (Hydrogen nuclei) and ionized Helium nuclei (He^{2+}), while other components were effectively negligible (Dodelson, 2003). As the universe cooled down, ionized Helium and Hydrogen nuclei started to capture free electrons and become neutral. Subsequently, on a short period of time, all free electrons and nuclei combined to form neutral atoms and the universe then become transparent to radiation. These events are known as *recombination* and *decoupling* respectively.

Before recombination, the dynamics of photons and baryons can be successfully described by kinetic theory. The primary thermalization mechanism for photons is *Compton scattering* by free electrons. Radiation is assumed to be non-polarized and furthermore is assumed to remain like that. The free electron density is considered to be non-relativistic and thermal around a bulk velocity \mathbf{v} , with a Maxwell-Boltzmann distribution given by

$$f_e(x, \mathbf{q}) = \left(\frac{2\pi}{m_e T_e} \right)^{3/2} \exp \left[-\frac{(\mathbf{q} - m_e \mathbf{v})^2}{2m_e T_e} \right], \quad (2.175)$$

where, m_e, T_e are the mass and temperature of free electrons and

$$n_e(x) = \int \frac{d^3 \mathbf{q}}{(2\pi)^3} f_e(x, \mathbf{q}) \quad (2.176)$$

is the electron number density. Electrons and protons are tightly coupled through Coulomb interaction, implying that their energy density contrasts and bulk velocities have common values,

$$\delta_p = \frac{n_p - \bar{n}_p}{\bar{n}_p} = \delta_e = \frac{n_e - \bar{n}_e}{\bar{n}_e} := \delta_b, \quad (2.177a)$$

$$\mathbf{v}_p = \mathbf{v}_e := \mathbf{v}. \quad (2.177b)$$

That is why they are collectively called *baryons*.

Before recombination baryons and photons are said to be tightly coupled via Compton scattering in the Thomson limit. That is to say that the mean path for photons scattered by free electrons, given by $\ell_C = (\sigma_T n_e)^{-1}$

(comoving), where $\sigma_T = 8\pi\alpha/(3m_e^2) = 6.65 \times 10^{-29} \text{ m}^2$ is the Thomson cross-section¹², is small compared to the causality scale of the universe, estimated by $D_H = H^{-1}$ (comoving).

In order to find an approximation for the epochs where recombination and decoupling take place, we follow the discussion in §3.3 of Dodelson (2003) and introduce the fraction of free electrons $X_e = n_e/n_b$, in terms of which $\ell_C = (X_e n_b \sigma_T)^{-1}$ to compare mean free path of electrons and the causality scale,

$$\frac{D_H(z)}{\ell_C(z)} = \frac{X_e n_b(z) \sigma_T}{H(z)}.$$

Now we can approximate $n_b(z) = (1+z)^3 \Omega_b \rho_c / m_p$, with m_p the proton mass and take $H(z)$ as the Hubble parameter for a universe with only matter and radiation, $H(z) = H_0 \Omega_m^{1/2} (1+z)^{3/2} [1 + (1+z)/(1+z_{\text{eq}})]^{1/2}$ where $z_{\text{eq}} = 2.4 \times 10^4 \Omega_m h^2$ is the redshift of matter-radiation equality (Eq. (2.88) from Dodelson, 2003). We then have (Eq. (3.46) from Dodelson, 2003),

$$\frac{D_H}{\ell_C} = 113 X_e \left(\frac{\Omega_b h^2}{0.02} \right) \left(\frac{0.15}{\Omega_m h^2} \right)^{1/2} \left(\frac{1+z}{1000} \right)^{3/2} \left[1 + \frac{1+z}{3600} \frac{0.15}{\Omega_m h^2} \right]^{-1/2}, \quad (2.178)$$

where all density parameter terms are normalized to typical values to simplify interpretation. The expression above tells us that the Compton mean free path is of the order of D_H when $z = z_d \sim 1000$ and X_e decreases from 1 to $\sim 10^{-2}$. Moreover, as X_e keeps decreasing, ℓ_C keeps growing relative to D_H , and we say that photons have effectively decoupled from baryons.

In the tight-coupling limit (before decoupling), we have two essential results governing the evolution of photons and baryons, i) the Boltzmann hierarchy for photons is complete up to the second moment, i.e., its fluid dynamics is determined by the evolution of its density and bulk velocity and ii) the bulk velocity of photons is shared by baryons.

As an illustration, consider the photon temperature fluctuation $\Theta = \Delta T_\gamma / T_\gamma$, which is directly related to the photon density perturbations $\delta_\gamma = \delta \rho_\gamma / \bar{\rho}_\gamma$. We can decompose Θ into multipoles Θ_ℓ representing the moments of the photon distribution function under the Boltzmann equation. The equation for $\ell = 0$ is given in Fourier space by (Eq. (8.18) from Dodelson, 2003)

$$\Theta_0'' + \frac{a'}{a} \frac{R}{1+R} \Theta_0' + k c_s(z) \Theta_0 = F(\Psi, \Phi, \eta) \quad (2.179)$$

¹²Here $\alpha \sim 1/137$ is the fine-structure constant of electrodynamics. Not to be confused with the *dilation* parameter introduced in Eq. (2.185).

where the forcing term F on the RHS depends on the gravitational potentials Ψ and Φ and conformal time η . This is the equation of a forced harmonic oscillator where the expansion plays the role of a dragging term and the sound speed $c_s(z)$ from pressure fluctuations in the baryon-photon fluid plays the role of the spring force. The gravitational potentials displace the equilibrium position of the oscillator. The speed of sound is given by

$$c_s(z) = \frac{c}{\sqrt{3(1+R)}} \quad (2.180)$$

where the baryon fraction R

$$R(a) = \frac{3a\Omega_b}{4\Omega_r} = \frac{3}{4} \frac{a}{a_{eq}} \frac{\Omega_b}{\Omega_m} \quad (2.181)$$

and $a_{eq} = \Omega_r/\Omega_m$. Deep into radiation domination, $a \ll a_{eq}$, we have $R \rightarrow 0$ and $c_s \rightarrow c/\sqrt{3} \approx 0.58c$. But the presence of baryons slows down the speed in which sound waves propagate. For instance at equality, for $\Omega_b \approx \Omega_m/6$, we have $R \approx 1/8$, and $c_s \rightarrow c\sqrt{8/27} \sim 0.54c$. Finally at the drag epoch $a_d \approx a_{eq}/3$ and $c_s \approx 0.49c$.

The solution to Eq. (2.179) is given by (Eq. (8.24) from Dodelson, 2003)

$$\begin{aligned} \Theta_0(\eta) = & - \Phi(\eta) + [\Theta_0(0) + \Phi(0)] \cos(kr_s) \\ & + \frac{k}{\sqrt{3}} \int_0^\eta d\tilde{\eta} [\Phi(\tilde{\eta}) - \Psi(\tilde{\eta})] \sin[kr_s(\eta) - kr_s(\tilde{\eta})] \end{aligned} \quad (2.182)$$

where the comoving *sound horizon* r_s at conformal time η is defined as

$$r_s(\eta) = \int_0^\eta d\tilde{\eta} c_s(\tilde{\eta}) = \int_z^\infty d\tilde{z} \frac{c_s(\tilde{z})}{H(\tilde{z})} \quad (2.183)$$

In particular, the comoving sound horizon r_s at the conformal drag time η_d or redshift z_d sets the scale for acoustic oscillations around the moment of decoupling. In Appendix C, we compute $r_d = r_s(z_d)$ at decoupling analytically for a flat universe with matter and radiation and find $r_d \approx 100 \text{ Mpc}/h \approx 150 \text{ Mpc}$. More precisely, for a Planck-like cosmology, we have $z_d \approx 1060$ and $r_d \approx 147 \text{ Mpc}$ (Abbott et al., 2019).

The BAO scale r_d becomes imprinted on both photon and baryon perturbations. Since baryons couple indirectly to the dark matter via gravity, this scale becomes impressed also (though with a smaller detectable signature) on the dark matter perturbations, and consequently on galaxy correlations.

The BAO feature has been measured on the temperature fluctuations of the Cosmic Microwave Background (CMB) photons and used to constrain

cosmological parameters. In Fig. 2.6 we show the BAO pattern in the angular power spectrum of temperature fluctuations of the CMB photons as measured by Abbott et al. (2019), where the BAO sound horizon $r_d \approx 150$ Mpc is imprinted in the position of the first acoustic peak $\ell \approx 200$.

Similarly, the BAO signature has also been detected on correlations of low-redshift Galaxies. In Fig. 2.7, we show the BAO peak in the monopole correlation function ξ_0 (see Eq. 2.152) of Luminous Red Galaxies (LRG's) from eBOSS DR14 as measured by Bautista et al. (2018). The BAO peak is found at comoving distance $r_d \approx 147$ Mpc, consistently with CMB measurements. A model with BAO peak is highly favored compared to a *no-peak* model. Our BAO analysis presented in Chap. 5 is closely related to this measurement. However, we work in harmonic space and with a photometric sample of DES galaxies.

BAO detection method

Because the prediction of the acoustic scale is based on the modeling of the early universe epoch, one may expect linear theory prediction to be sufficiently accurate for extracting the acoustic scale using two-point statistics, even for the late-time matter distribution. In other words, linear theory predictions of two-point correlations should be enough to extract the acoustic scale from low-redshift galaxies. Nonlinear matter effects mainly change the shape of the peak but barely alter its position.

Modern methods for detecting the BAO scale in galaxy surveys (for a review, see, e.g. Chap. 4 of Weinberg et al., 2013) adopt then the convenient strategy of using linear theory predictions on a fiducial cosmological model, necessary to translate angular and redshift separations into cosmological distances, as a template and then fit that template to the data over a convenient range of scales using the appropriate covariance matrix.

Such a template-fitting strategy allow for the location of the BAO feature itself to shift relative to the fiducial model expectation. The primary strategy is to sample the likelihood of obtaining the observed two-point statistics, the correlation function or power spectrum, as a function of the BAO scale shifts, while marginalizing over nuisance parameters. These nuisance parameters characterize “broad-band” physical or observational effects that smoothly change the shape or amplitude of the underlying two-point statistics. For such effects, we can enumerate at least four main categories: (i) nonlinear structure formation effects, (ii) tracer effects such as scale-dependent clustering bias and velocity bias, (iii) observational systematic effects as, e.g., errors in survey calibration, and (iv) non-Poissonian shot noise. The critical point is that none of these effects are contained in the linear prediction used

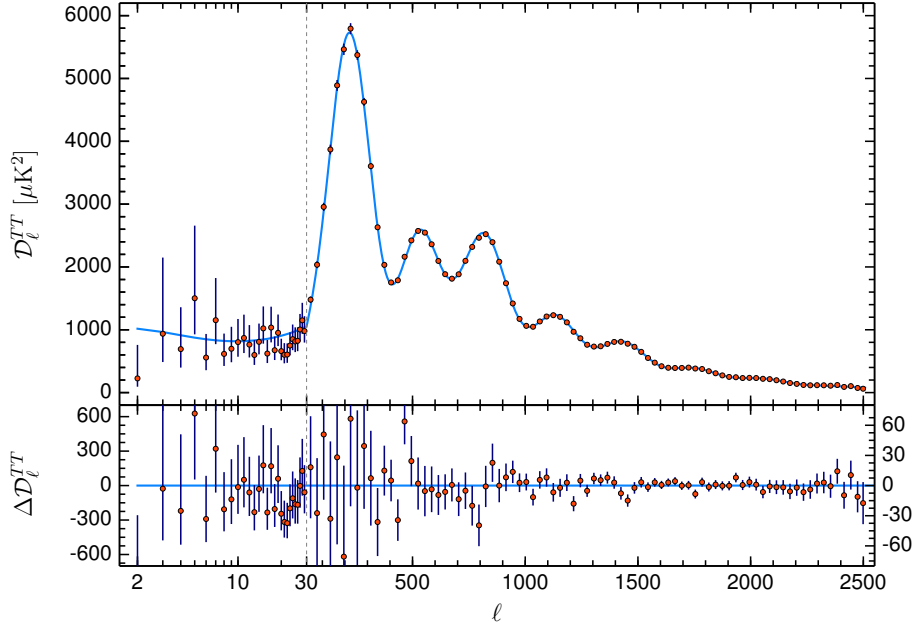


Figure 2.6: Temperature angular power spectrum of the CMB as measured by the Planck mission (Fig. 1 of Abbott et al., 2019). The oscillation pattern is directly related to sound waves in the primordial plasma as imprinted on the CMB photons at z_d according to Eqs. (2.179) and (2.182). At decoupling $z_d \approx 1090$, the angle projected on the sky by the sound horizon is $\vartheta_{\text{BAO}} = r_s(z_d)/D_A(z_d) \approx 144/13860 = 0.0104$ rad = 0.592 deg. This angle defines the acoustic multipole via $\vartheta_{\text{BAO}} = \pi/\ell_A$, so $\ell_A = \pi/0.0104 = 302.4$. Finally, ℓ_A is shifted relative to the multipole ℓ_1 of the first peak due to driving effects via $\ell_1 \approx \ell_A(1 - 0.27)$ (see e.g. Appendix in Hu et al., 2001). Therefore $\ell_1 \approx 302.4 \times 0.73 \approx 220.7$, which agrees with the observed position of the first peak.

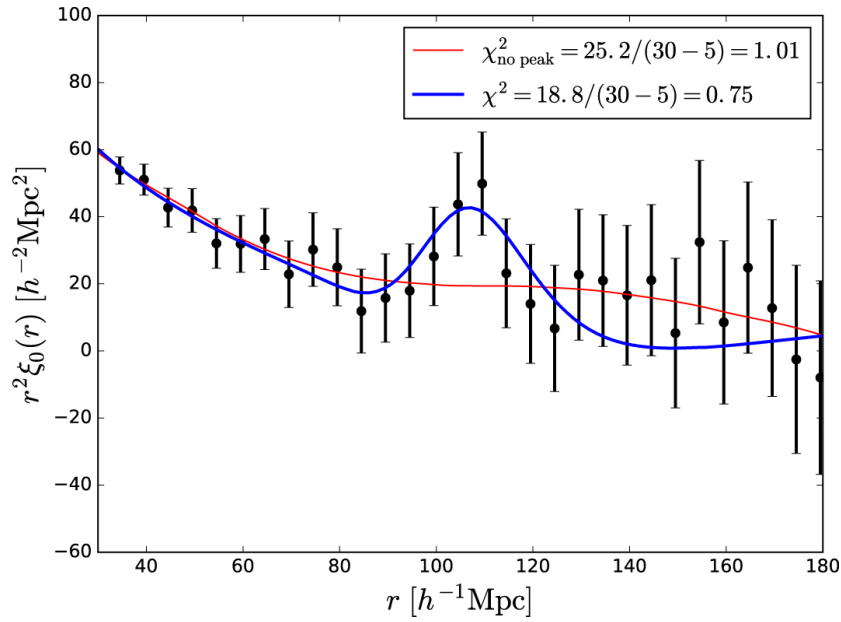


Figure 2.7: Monopole of the correlation function of Luminous Red Galaxies (LRG) from eBOSS DR14 as measured by Bautista et al. (2018). Notice the BAO peak is detected at $r_d \approx 102 \text{ Mpc}/h \approx 147 \text{ Mpc}$.

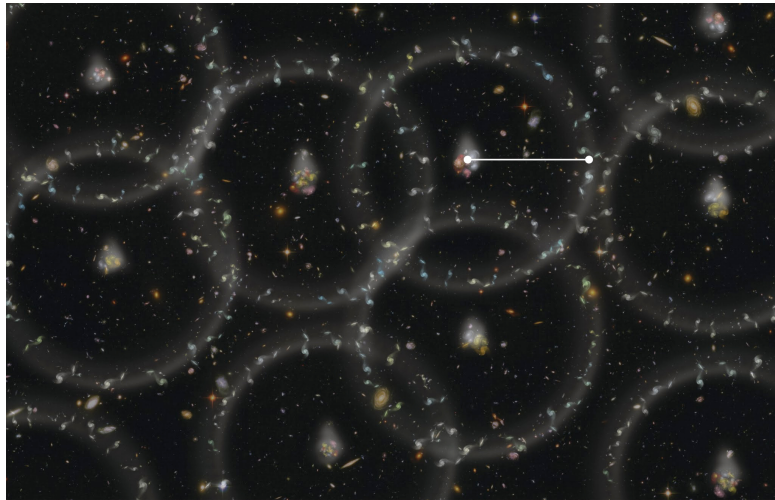


Figure 2.8: Representation of the observed pattern of BAO feature as a scale at which there is an enhancement in the probability of finding pairs of galaxies. If the plane of image represents the plane of sky at some z_{eff} , this scale subtends an angular separation directly related to the acoustic sound horizon r_d via the comoving angular diameter distance D_A following Eq. (2.186). [Image credit. www.bnl.gov]

for the template.

In order to account for (i) above, one can introduce theoretically motivated parametrizations. The one considered in this work accounts for the damping in clustering coming from nonlinear corrections to the linear growth of structure as predicted by RPT (see § 2.2.2, Eq. 2.69). Based on what RPT predicts, one can model clustering damping to have an approximated Gaussian form with zero mean and dispersion given by a characteristic scale directly related to the scale where the linear theory breaks down. However, this is desired only for the BAO feature, so the r_{NL} parameter from RPT will have its incarnation on BAO detection as a Σ_{NL} parameter accounting precisely for the same effect of clustering damping phenomenologically, but in the spirit of the template fit. Given $P_{\text{lin}}(k)$ the initial linear prediction for the power spectrum, one then wants to modify it as

$$P_m(k) = \exp(-k^2 \Sigma_{NL}) [P_{\text{lin}}(k) - P_{\text{nw}}(k)] + P_{\text{nw}}(k), \quad (2.184)$$

where Σ_{NL} is a constant that can be fitted from synthetic data and $P_{\text{nw}}(k)$ is the linear no-wiggle prediction for the power spectrum in which the BAO feature is effectively erased according to Eisenstein & Hu (1998).

This basic template for the power spectrum can be subsequently correctly projected to the desired two-point statistics $T_m(x)$ one is interested in, according to the formulae discussed in § 2.4. Finally, in order to account for (ii), (iii) and (iv), one can initially note that these are all related with scale-dependent clustering features and consequently can schematically be accounted for by introducing broad-band terms to the linear template over which one can marginalize in the end. Towards this end, and to be general, we will follow the notation from Abbott et al. (2019), and call $T(x)$ as a general two-point statistics, for which we introduce the following template for comparison with clustering measurements,

$$T^{\text{temp}}(x) = B_T(x)T_m(x\alpha') + A_T(x). \quad (2.185)$$

Here $T(x)$ is general in the sense that it can be (for our purposes) $\xi(r)$, $P(k)$, $w(\vartheta)$, C_ℓ , while $T_m(x)$ is the proper projection of $P_m(k)$ from Eq. (2.184), and $A_T(x)$, $B_T(x)$ are smooth functions describing broad-band terms. Also, x represents the specific separation defined by the corresponding two-point function, and parameter α' rescales this separation taking into account the conjugate nature of configuration and harmonic separations. In configuration space, it is simply a dilation parameter $\alpha' = \alpha$, so e.g., $x\alpha' = r\alpha$ for $\xi(r)$ and $x\alpha' = \vartheta\alpha$ for $w(\vartheta)$. In Fourier or harmonic space $\alpha' = \alpha^{-1}$ accordingly, so $x\alpha' = k/\alpha$ for $P(k)$ and $x\alpha' = \ell/\alpha$ for C_ℓ .

The main goal of fitting the template in Eq. (2.185) is to estimate α , also known in the literature as a *dilation parameter*, as its physical interpretation is that it dilates/contracts the scale of the predicted clustering, and fundamentally of the BAO feature in particular, relative to the actually observed clustering. Measurement of $\alpha = 1$, therefore, indicates that distance scales from the model and clustering measurements agree, in particular, the scale of the BAO feature. Measurement of $\alpha \neq 1$ could indicate one of two possibilities, (i) the BAO feature scale of the model is wrong, or (ii) the distance scale assumed for measuring clustering is incorrect.

In order to get physical insight on the purpose of α , let us consider the specific case of the ACF, $w(\vartheta)$. From the definition of comoving angular diameter distance Eq. (2.25), we know that the comoving acoustic scale r_d , Eq. (2.183), should subtend an angle ϑ_{BAO} on the sky is given by

$$\vartheta_{\text{BAO}} = \frac{r_d}{D_A(z_{\text{eff}})}, \quad (2.186)$$

such that a population of tracers with mean effective redshift of z_{eff} qualitatively defines the angular separation associated with the BAO peak location on a measurement of $w(\vartheta)$ for such a population. In other words, it should define a preferred separation for pairs of tracers, which corresponds to an excess clustering on that angular scale (see Fig. 2.8).

If one fits a $w(\vartheta)$ template from Eq. (2.185) using a fiducial cosmology (fid) that is moderately wrong, then one should estimate a dilation parameter $\alpha \neq 1$. However, this α is constructed to dilate/contract angular scales from the measured to the fiducial cosmology, in particular, the acoustic scale,

$$\vartheta_{\text{BAO}}^{\text{fid}} = \alpha \vartheta_{\text{BAO}}.$$

In other words, the dilation parameter should be proportional to the ratio of acoustic scale, as defined by the sound horizon (Eq. 2.186),

$$\alpha = \frac{r_d^{\text{fid}} D_A(z_{\text{eff}})}{r_d D_A^{\text{fid}}(z_{\text{eff}})}. \quad (2.187)$$

Note that the fitting procedure described above should break down if the recovered likelihood for α is not robust under different prescriptions for the *nuisance* parameters determining the corrections to the linear template in Eq. (2.185), i.e., the broad-band shape functions, $A_T(x)$, $B_T(x)$ and the non-linear Σ_{NL} . There is always a problem for when freedom in that prescription is too restricted, and we may introduce biases coming from scale-dependent clustering on the broad-band shape of clustering. Similarly, the other way around, when there is too much freedom, we may fall into a fit out of the

BAO feature, reducing the constraining power of data. Fortunately, we expect a clear difference between the signature of BAO feature and signatures from nonlinear clustering damping, scale-dependent biasing and noise contributions. However, this should always be tested and calibrated using, e.g., synthetic data in order to properly guarantee the constraining power of the template-fitting method. In Chap. 5 we present a series of robustness tests in the context of DES-Y1 data analysis, showing the stability of the recovered likelihood for α from the APS.

Finally, note that Eq. (2.187) can be re-arranged to

$$\frac{D_A(z_{\text{eff}})}{r_d} = \alpha \frac{D_A^{\text{fid}}(z_{\text{eff}})}{r_d^{\text{fid}}}, \quad (2.188)$$

so the recovered likelihood for α from template fitting method can easily be translated to a likelihood for the ratio $D_A(z_{\text{eff}})/r_d$ which can be directly used to constrain cosmological parameters.

Chapter 3

Emission Line Galaxies clustering at eBOSS and DES

In this chapter, we present our main contributions to the BOSS/eBOSS galaxy clustering analysis presented in Jouvel et al. (2017). In that work we presented results of the first test plates of the extended Baryon Oscillation Spectroscopic Survey (eBOSS) focusing on the emission-line galaxy (ELG) population, targeted from the Dark Energy Survey (DES) Science Verification data (SVA1). We studied how well the ELG redshifts can be estimated using the target selection photometry, validating with the spectroscopic redshifts measured by eBOSS. We also explored different techniques to reduce the photometric redshift outliers fraction, by comparison between template fitting and neural networks results.

In this chapter, we start in § 3.2 focusing on the study of the clustering properties of ELG samples from the DES SVA1, which represents our main contribution to Jouvel et al. (2017). For our clustering analysis, we select only the most secure spectroscopic redshift targets in the redshift range $0.6 < z < 1.2$, leading to a mean redshift for the so-called bright and faint samples of approximately 0.85 and 0.9 respectively. We measure the projected correlation function (defined in § 2.4.6) and obtain a galaxy bias by averaging on scales from 1 to $10 h^{-1}\text{Mpc}$, finding $b_g = 1.58 \pm 0.10$ for the bright sample and $b_g = 1.65 \pm 0.12$ for the faint sample. In § 3.3 we discuss our main results. In particular, we argue that the ELG bias values found in our analysis are representative of a galaxy population with $M_B - 5 \log h < -20.5$, in agreement with what we measure by fitting galaxy templates to the photometric data. We note that the galaxy biasing was derived in our analysis relative to a fixed theory model for the matter fluctuations, which led to relatively small error bars on the bias parameters.

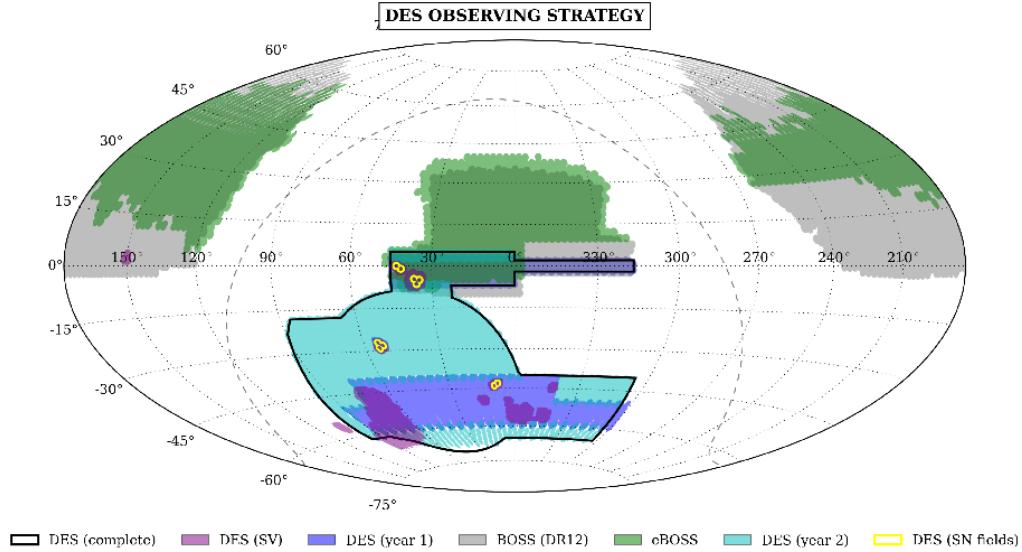


Figure 3.1: Footprints of DES, BOSS, and eBOSS. Coordinates are RA and Dec in degrees. Here we focus on the overlap between DES SV and eBOSS observations, concentrated on the DES SN deep fields and covering a total area of 9.2 deg^2 .

3.1 eBOSS ELG sample from DES photometry

The present work focuses on the eBOSS SVA1 ELG sample selected using an area of 9.2 deg^2 from the science verification data of DES (SVA1) which overlaps with eBOSS observations Fig 3.1. Three tiles from SVA1 data were used and observed in eight eBOSS plates, which allowed for obtaining a total of 5705 spectra.

These are part of the eBOSS ELG target selection definition effort, undergone in October 2014, and in a broader sense than presented here was used by Jouvel et al. (2017) to design three different target selections based on the SDSS (Ahn et al., 2014) the South Galactic Cap u -band Sky Survey (SCUSS Jia et al., 2014) and the DES. From those, the present work focuses on the study of the target selection defined with DES only.

The selection defined with DES data made use of grz imaging from DES and was divided into two main selections in Jouvel et al. (2017): i) A DES *bright selection* based on standard target selection for ELGs from DES imaging, and ii) A DES *faint selection* optimized to reach redshifts between 0.7 and 1.5 that has been designed for a DESI-like survey. For details on the target selection, see § 2 in Jouvel et al. (2017).

Photometric redshifts (photo- z s) for the samples were computed in Jouvel

et al. (2017) using two codes presented on a previous study of photo- z s of SVA1 galaxies by Sánchez et al. (2014): ANNz2 (Sadeh et al., 2016) and LePhare (Ilbert et al., 2006, 2009). ANNz2 is a machine learning code while LePhare is a template fitting method. Both produce single point estimates, as well as probability distributions for their photo- z s. This allowed for a comparison of the methods, with hopes of a photo- z estimation optimization. For the actual set up of the photo- z estimates and their comparison, we refer the reader to § 2.4 of Jouvel et al. (2017).

The outlier fraction in photo- z estimation is one of the primary sources of systematics in cosmic shear and large scale structure analyses (see, e.g., Bernstein & Huterer, 2010, and references therein). With a set of 4600 eBOSS spectroscopic redshifts (z_{sp}), possible techniques to identify photo- z (z_{ph}) outliers were studied in Jouvel et al. (2017). An implementation of comparison between LePhare and ANNz2 photo- z s as a possible strategy for decreasing the outlier fraction is also described in Jouvel et al. (2017)¹. The main conclusion from the comparison was that by reducing the galaxy sample by 15%, it is possible to decrease the outlier fraction by 30%.

For both samples, we have selected only those galaxies with secure and 1 line redshift to be in the redshift range $0.6 < z_{sp} < 1.2$ and that are within the DES footprint given by the angular mask, as detailed below. For the bright sample this represents 71.6% of the targeted sample and for the faint sample 68%. The number of ELGs in the final sample, the mean density and mean redshift for the bright and faint samples used in this chapter are shown in Table 3.1. The faint sample effectively selects a more distant galaxy set, with mean redshift at $z = 0.9$ (in comparison with the bright sample at $z = 0.855$) although with a worse efficiency.

3.2 eBOSS ELGs clustering properties

In this section, we present measurements of the monopole of the spatial correlation function (see discussion around Eq. 2.153), as well as the projected angular correlation function (see § 2.4.6) for the DES bright and DES faint ELG selections.

In addition to the spectroscopic bright and faint samples, we also estimate the monopole of the spatial correlation function for a photometrically selected bright and faint sample, using photo- z s given by ANNz2 and LePhare. Comparing these samples with the spectroscopic samples, we investigate how the ELG clustering signal will be seen in DES in comparison

¹Such comparison between a template fitting method and an empirical method had been previously suggested by, e.g. Abramo et al. (2012) and Newman et al. (2013)

bright			
	Number (purity)	mean density [gal/deg ²]	mean redshift
z_{sp}	2613 (100%)	284.02	0.855
ANNz2	2902 (86.66%)	315.43	0.866
LePhare	3038 (84.10%)	330.22	0.811
faint			
	Number (purity)	mean density	mean redshift
z_{sp}	2139 (100%)	232.50	0.901
ANNz2	2582 (79.43%)	280.65	0.928
LePhare	2662 (77.23%)	289.35	0.841

Table 3.1: Mean statistics for the bright and faint sample used in this section. The z_{sp} selection have been obtained selecting ELGs with secure and 1 line spectroscopic redshift $0.6 < z < 1.2$, while the ANNz2 and LePhare samples have been selected using their respective photometric redshift measurement in the same photometric redshift range. These numbers were obtained after the catalog was pruned by the angular mask, as detailed below.

with the spectroscopic counterpart. In Table 3.1, we show the number of ELGs, the mean density and mean redshift for these photometric selections. In these samples, we also look at the purity of ANNz2 and LePhare in selecting galaxies in the redshift range of interest. In this case, we define purity as the number of sources selected with a given photo- z code, with spectroscopic redshift in the range $0.6 < z_{sp} < 1.2$. For example, for the bright sample, 87% of the sources selected with ANNz2 in the range $0.6 < z_{ph} < 1.2$ are in $0.6 < z_{sp} < 1.2$. As can be seen in Table 3.1, the neural network redshift code ANNz2 seems to have a better performance than LePhare since it produces counts and number densities that more closely resemble those from the sample with spectroscopic redshifts. Also, both algorithms worked better for the bright than for the faint sample. It is important to note that in order to calculate the monopole for the photometric samples, we will use their spectroscopic redshifts to obtain distances and not their photometric redshifts.

The spectroscopic redshift distribution for the samples under analysis are shown in Fig. 3.2, along with the redshift distribution for the randoms used in the measurement of the correlation functions. The randoms have been computed considering the different depths of the DES survey, and the process is detailed next. Throughout this analysis we assume a flat Λ CDM+ ν (one massive neutrino) cosmological model based on Planck 2013 + WMAP

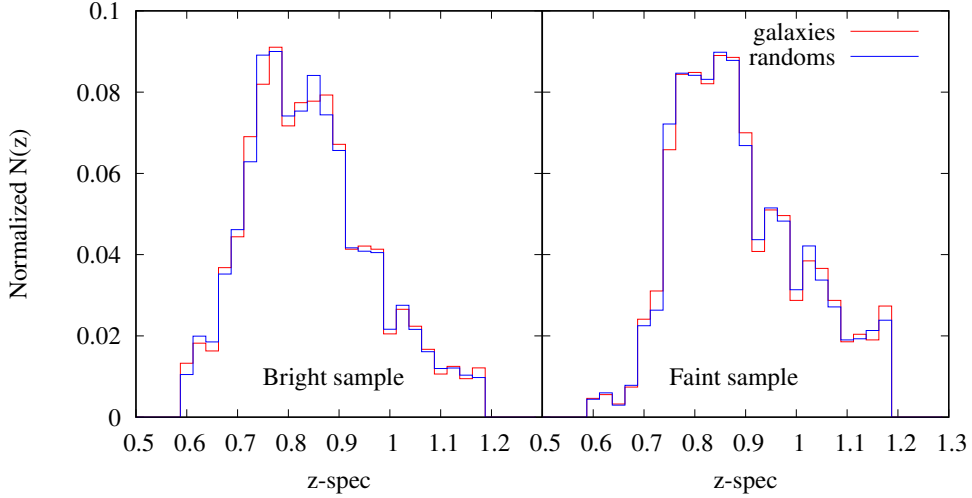


Figure 3.2: Redshift distribution for the ELG bright and faint samples, superimposed to their corresponding random samples used in the calculation of the correlation functions. The modelling of random samples is discussed in § 3.2.1.

polarisation + ACT/SPT + BAO, with a total matter density relative to critical $\Omega_m = 0.307$, $\sigma_8 = 0.8$ (Planck Collaboration et al., 2014).

3.2.1 Random fields

The DES observes at different depths, indicating that the measured density of galaxies in the catalog cannot be translated directly into the mean density of galaxies. In general, we will observe more (less) galaxies in regions where the survey is deeper (shallower). This information must be encoded into random catalogs to avoid misinterpretation of the galaxy clustering signal.

We use the Mangle mask of the SVA1 DES release in the observed field to create random catalogs, sampling the footprint with the same depth, angular distribution, and ELG selections. We use the g -band as the only detection band to which we define the magnitude limit, as imposed by the target selection. For a discussion on target selection see § 2 of Jouvel et al. (2017).

We first select regions inside the mask with limiting 2 arcsec aperture magnitude in g -band between $23.4 < \text{mag} < 25.8$. With this cut, we ensure a negligible loss of area. The final effective area continues to be 9.2 deg^2 . We then proceed to generate the random catalogs following the depth and

angular footprint of the mangle mask.

In order to generate non-uniform random catalogs corresponding to the variations in depth, we apply the following methodology:

1. Create a uniform random catalog following the angular footprint of the mask.
2. Associate the galaxy and random catalogs to the properties of the mask, polygon where they lay in. Retrieve information about the area and depth in band g , given in the mask for each source in both catalogs.
3. Study the distribution of galaxies as a function of mangle depth. Generate several galaxies binned in several ranges of g -band from 23.4 to 25.8.
4. Build the density distribution in each depth bin as the number of galaxies over the area (information given by mangle) and generate the density function, i.e., density as a function of depth.
5. Create the Probability Function according to:

$$P[i] = \left[\int_{m_{min}^{tot}}^{m_{max}^{tot}} dm \rho(m) \right]^{-1} \int_{m_{min}^i}^{m_{max}^i} dm \rho(m) \quad (3.1)$$

where m_{max}^i and m_{min}^i are the maximum and the minimum values of the magnitude depth in the i -th bin and m_{min}^{tot} and m_{max}^{tot} are the initial and final depth according to the binning used. In our case, $m_{max}^{tot} = 25.8$ and $m_{min}^{tot} = 23.4$;

6. Assign a probability to random points according to the magnitude limit.
7. Assign a random value in the interval $(0 - 1]$ for each random point and compare with the probability given in the previous step. We accept the random point if the random value is smaller than the probability and reject it otherwise.

Fig. 3.3 shows both the ELG density as a function of magnitude limit in g band, as well as the probability distribution as a function of magnitude limit in g band for the randoms, based on the steps above, both for the bright and faint sample. This measurement is very limited by sample variance. Nonetheless, we approximate the density distribution by a first-order polynomial to assign reject/acceptance probabilities as a function of

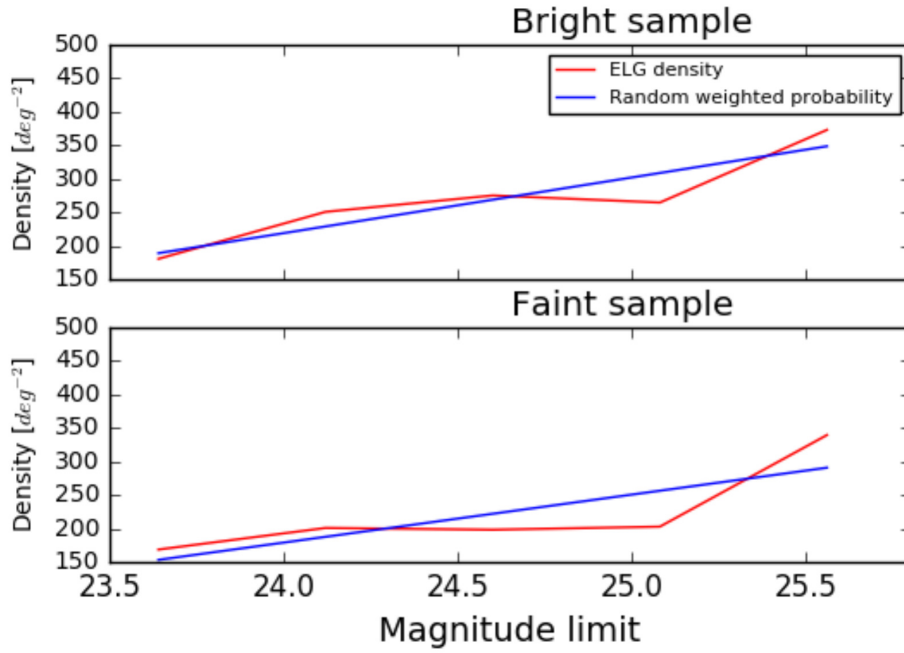


Figure 3.3: ELG density (blue lines) as a function of magnitude limit in g band for the bright (upper panel) and faint (bottom panel) samples. Red lines show the polynomial fit used to assign weights to the random catalogs, once we normalize it to 1 at its maximum = 25.8. For some intermediate magnitude limits, there is an apparent decrease in density. This is a variance effect, due to the small area observed in a very in-homogeneous footprint and the small number of ELG targets.

magnitude limit for the random samples. We find a mean error of 8% for each of the ELG probability densities estimated using the variance cookbook (Moster et al., 2011), with similar survey configurations as COSMOS. With the probability distribution as a function of depth and position in the footprint, we can now calculate the random sample used throughout the following analysis, after we model the ELG redshift distribution. In both samples, we calculate approximately 2.8×10^6 random points.

We model the line-of-sight redshift distribution of the bright and faint random samples based on the ELG distributions shown in Fig. 3.2. We transform the redshift distribution into a probability distribution function and use this to assign redshifts to the random sample. We do not consider the existing correlation between depth limit and redshift. As deeper regions reach higher redshifts, this might be a significant effect when we move to future larger data releases. For now, we ignore this effect since we are mostly limited by cosmic variance. The redshift distributions for galaxy data and randoms used in this analysis are shown in Fig. 3.2.

We have verified that a non-uniform random constructed from the mangle mask does not correlate with itself, whereas a random that is uniform in magnitude correlates with the data on small scales. This indicates that our random is appropriate for the clustering analysis, whereas uniform random is not. We have also applied our methodology for the generation of randoms to simulations of the DES and found that the correlations measured are consistent with theoretical results.

Another possible approach would be to perform a more conservative analysis and lower the magnitude limit such that field-to-field variations become negligible (see, e.g. Kim et al., 2014). Since this would decrease even further the size of our galaxy sample, we decided to account for the observed magnitude limit variations, as these were readily available from the mangle mask.

3.2.2 Two-point spatial correlation function

We estimate the two-point spatial correlation function (2PTCF) via the Landy & Szalay (1993) (LS) estimator under the fiducial cosmology on scales $1 < s < 50 \text{ Mpc } h^{-1}$ using the CUTE code² (Alonso, 2012) and compute the galaxy bias for the considered samples. Throughout this section, we use the letter s to refer to scales in redshift space for the 2PTCF monopole computation.

Poisson errors associated with LS estimator underestimate the actual uncertainty in the correlation function. Following Xu et al. (2012), we consider

²<https://github.com/damonge/CUTE>

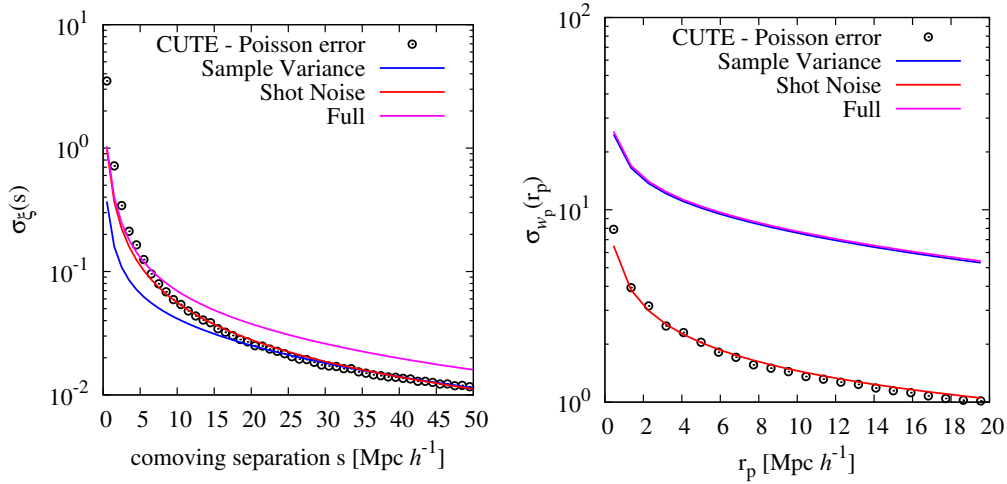


Figure 3.4: Contributions to the 2PTCF error estimates. Black circles represent the LS estimate for the pure Poisson error. Continuous curves show theoretical estimates of Gaussian and linear variance computed according to Eq. (2.164). The pure SN contribution has been isolated (red curve) from the Sample Variance-dependent part (Blue curve) in order to be compared with the LS Poisson error estimate. The agreement of SN and LS estimates is consistent with the interpretation of Poisson error as the number of data-data pairs estimated per bin. The full estimate from Eq. (2.164) (magenta curve) is the error estimate used in the analysis presented.

a theoretical estimation for the covariance of the spatial 2PTCF assuming Gaussianity and linear independent evolution of Fourier modes of the matter field over-density, given by Eq. (2.164)

A comparison of the contribution to the square root of the variance of the 2PTCF is shown on the left panel of Fig. 3.4, where the shot-noise contribution has been isolated in order to be compared with the Poisson error resulting from LS estimation according to the CUTE code (circle points). An agreement is observed between these two estimates; this is consistent with the interpretation of Poisson variance coming from the number of data-data pairs estimated per bin³. Note that the curves are shown under Sample Variance label in Fig. 3.4 represent all contributions to the 2PTCF variance except the pure SN one, Eq. (2.165).

³For the smallest scales, Fig. 3.4 shows that the estimate of SN contribution via Eq. (2.165) underestimates the Poisson contribution from LS. This is indeed expected given that here we are considering pure linear SN contribution (see, e.g., § 3.2 of Xu et al. (2012)).

The left panel of Fig. 3.4 shows that the effect of sample variance could have an impact on the error budget for our analysis even by assuming the simple case of Gaussian and linear covariance. Consequently, throughout the rest of our analysis, we consider its effect via the theoretical treatment described above. It is indeed important to mention that a more precise analysis of the clustering signal will require the creation of mock catalogs both for a more precise calculation of the covariance and in a bigger volume to have a significant clustering value.

Regarding the error estimates, in addition to the sample variance, we also account for the effects of the finite volume of the sample by estimating an integral constraint (IC) factor (see § 2.4.1). For this purpose, we measured random-random pairs from the random catalogs, $RR(s)$, up to the maximum separation allowed by the sample volume and, following Roche & Eales (1999), we estimate IC as

$$IC = \frac{\sum_i \xi(s_i) RR(s_i)}{\sum_i RR(s_i)}, \quad (3.2)$$

modelling the clustering signal on the spatial 2PTCF, $\xi(s)$, as a single power-law of the form

$$\xi(s) = \left(\frac{s}{s_0} \right)^{-\gamma}. \quad (3.3)$$

We consider two approaches to fit the power law, Eq. (3.3), to the data: (i) by subtracting the IC from the model and (ii) by allowing it to vary with the model parameters. We checked that these two approaches are consistent with each other given an iterative procedure for the first one, in which we first fit a model to the original data, then use this model to estimate a correction via Eq. (3.2), and apply this correction to the data. We repeat the process to the new data until convergence is achieved. In our case, convergence was always reached in less than 20 iterations. Note however that by using the second approach, fitting the model and IC correction simultaneously, we avoid the need for correcting the data.

This single power-law model represents reasonable approximation for comoving scales in the range $1 < s < 20 h^{-1}\text{Mpc}$. We considered different maximum scales between 10 and $50 h^{-1}\text{Mpc}$ to perform the fit and found that the results are insensitive to this scale. Nonetheless, $20 h^{-1}\text{Mpc}$ was chosen because: (i) at the redshifts of interest the linear regime extends up to this scale, and (ii) for scales below $20 h^{-1}\text{Mpc}$ the amplitude of measured $\xi(s)$ is always one order of magnitude larger than our estimates of the IC .

We apply the model above to the spectroscopically selected ELG bright and faint samples, to the photometrically selected catalogs using ANNz2 and

Sample	Redshift selection	s_0 [h^{-1} Mpc]	γ	IC	χ^2/dof
Faint	z_{sp}	$5.13^{+0.17}_{-0.17}$	$1.301^{+0.050}_{-0.054}$	0.014	0.594
	ANNz2	$5.42^{+0.14}_{-0.17}$	$1.260^{+0.043}_{-0.044}$	0.017	1.03
	LePhare	$5.35^{+0.16}_{-0.15}$	$1.244^{+0.044}_{-0.046}$	0.018	0.896
	ANNz2 $ \Delta_z < 0.24$	$5.64^{+0.14}_{-0.16}$	$1.272^{+0.041}_{-0.043}$	0.017	1.36
	LePhare $ \Delta_z < 0.24$	$5.54^{+0.15}_{-0.15}$	$1.252^{+0.043}_{-0.044}$	0.018	1.12
Bright	z_{sp}	$5.23^{+0.16}_{-0.15}$	$1.213^{+0.044}_{-0.044}$	0.019	0.741
	ANNz2	$5.74^{+0.13}_{-0.14}$	$1.212^{+0.036}_{-0.039}$	0.021	1.02
	LePhare	$5.66^{+0.13}_{-0.15}$	$1.211^{+0.034}_{-0.037}$	0.021	1.05
	ANNz2 $ \Delta_z < 0.24$	$5.80^{+0.14}_{-0.14}$	$1.208^{+0.038}_{-0.038}$	0.021	1.18
	LePhare $ \Delta_z < 0.24$	$5.82^{+0.15}_{-0.15}$	$1.174^{+0.035}_{-0.035}$	0.02	1.23

Table 3.2: 3D clustering properties of faint and bright with different redshift selections. Here $\Delta_z = z_{\text{LePhare}} - z_{\text{ANNz2}}$. Single power-law model for the 3D 2PTCF (Eq. (3.3)) parameters were constrained in the range $1 < s < 20 h^{-1}\text{Mpc}$. The integral constraint correction (IC) was modelled according to Eq. (3.2). For all cases presented and all scales considered, IC is one order of magnitude lower than the 2PTCF.

LePhare photo- z codes, and to some of the pruned catalogs. Our results are shown in Table 3.2. The z_{sp} samples are selected with spectroscopic redshifts between 0.6 and 1.2. ANNz2 and LePhare are samples selected in the same redshift range but using their photo- z value. For the bottom lines of Table 3.2 we use the photo- z values and a cut $|z_{\text{LePhare}} - z_{\text{ANNz2}}| < 0.24$. However, we use their true redshift, and not the photo- z , to compute distances and in $\xi(s)$. This way, we can study selection effects from the photo- z results.

A comparison of the clustering amplitudes for the bright and faint samples is shown in Fig. 3.5. The error bars were computed by propagating the uncertainties on the 2-point correlations. We see a statistical preference for the clustering amplitude of the bright sample to be higher than the one of the faint sample. This is consistent with the fitted power law parameters in Table 3.2. The bright sample has higher values for clustering length s_0 than the faint sample, while the slope γ seems more similar between samples.

Fig. 3.6 compares the amplitudes of $\xi(s)$ when z_{ph} are considered with respect to the spectroscopic selection. As we are limited by the sample size and large error bars, no significant comparison can be made between the clustering properties of the spectroscopic and photometric samples. There is a slight increase in the clustering correlation when photo- z s are used, which may be a result of competing scatter effects due to photo- z errors.

For the existing catalogs, the sample variance and the integral constraint

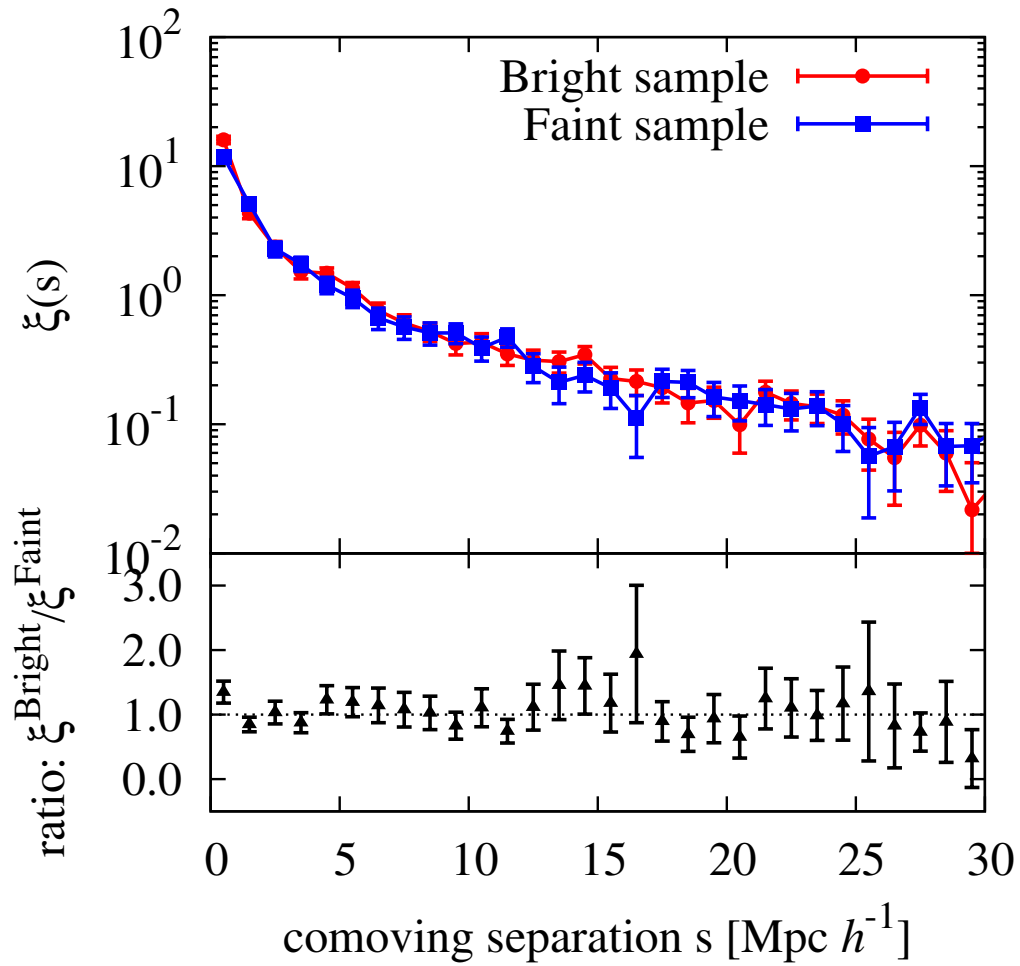


Figure 3.5: Comparison of the 3D 2PTCF $\xi(s)$ for the faint and bright samples. The top panel shows the measured correlations. The bottom panel displays the ratio between bright and faint samples.

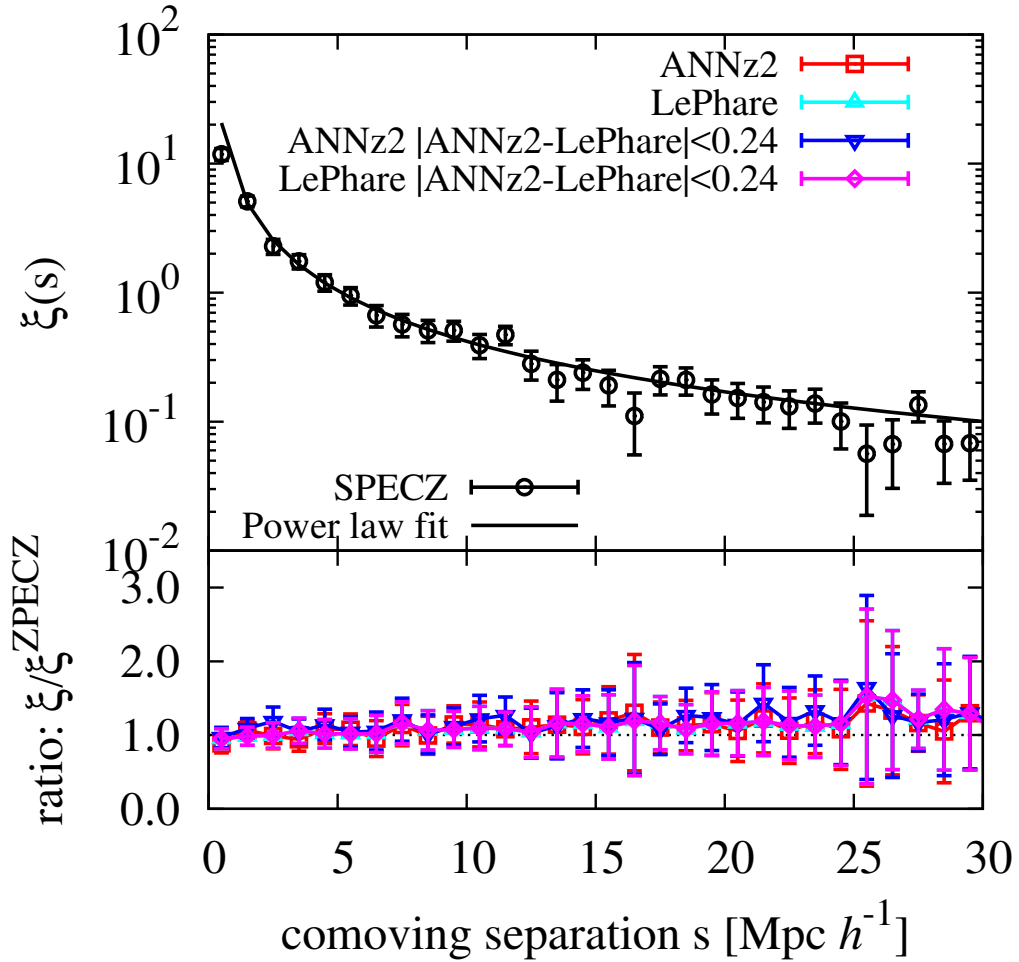


Figure 3.6: Comparison of $\xi(s)$ for different redshift selections for the faint sample only. The top panel shows the monopole for the clean photo- z sample between $0.6 < z < 1.2$. The bottom panel shows the ratio between different redshift selections and the clean sample. An apparent increase on the clustering at large scales is seen for the photometric redshifts selections.

contributions are significant sources of errors, but as the sample grows in size, it should be possible to investigate in detail the effects of photo-selection in the angular correlation function. We plan to assess the impact of propagating photo- z errors into angular correlations for future larger ELG catalogs from joint eBOSS/DES observations.

After investigating the monopole for these samples, beyond the spectroscopically selected ones, we focus again solely on the spectroscopic bright and faint ELG science samples, where we will measure the mean galaxy bias in the projected angular correlation function.

3.2.3 Galaxy bias

We measure a mean galaxy bias for the bright and faint samples separately. The samples span a large redshift range $0.6 < z < 1.2$. The meaning of the bias obtained must be taken with caution, as it is an average over a long cosmic time. We roughly assess the galaxy bias evolution by comparing the results for the bright and faint samples, which are at slightly different mean redshifts. As a result, we estimate the absolute magnitude limit that DES reaches when selecting ELGs.

In order to account for redshift space distortions, we follow the results from the VIPERS clustering analysis (Marulli et al., 2013) and estimate the galaxy bias for our samples using the projected real-space correlation function $w_p(r_p)$.

We first estimate the anisotropic 2PTCF, $\xi(r_p, \pi)$, in the spatial ranges $\pi \in [1, 40] h^{-1}\text{Mpc}$ and $r_p \in [1, 50] h^{-1}\text{Mpc}$ using the Landy & Szalay (LS) estimator (Landy & Szalay, 1993) under the fiducial cosmology using the CUTE code and integrate along the line of sight, π , to estimate $w_p(r_p)$ for all samples,

$$w_p(r_p) = 2 \int_0^\infty d\pi' \xi(r_p, \pi'), \quad (3.4)$$

where $\xi(r_p, \pi') = \xi(s = \sqrt{\pi'^2 + r_p^2})$ and in practice the line of sight integration is taken up to $\pi_{\text{max}} = 30 h^{-1}\text{Mpc}$ as in Marulli et al. (2013).

Then, the galaxy bias is defined as

$$b(r_p) = \sqrt{\frac{w_p(r_p)}{w_p^m(r_p)}}, \quad (3.5)$$

where $w_p(r_p)$ is given by Eq. (3.4) and is obtained from the galaxy sample, while $w_p^m(r_p)$ is the projected correlation function of matter.

Throughout the analysis, we assume a passive bias model. Even though the sample is not passively evolved, once the sample increases a more robust

bias analysis will be necessary, but considering the small statistics, a passive model is sufficient. We compute $w_p^m(r_p)$ from the theoretical power spectrum obtained using CAMB (Lewis & Bridle, 2002), with the `Halofit` routine (Smith et al., 2003) for non-linear corrections.

As for the case of the 3D 2PTCF, the sample variance impact on the error for the estimates of the projected 2PTCF is considered using a Gaussian and linear theoretical prediction given in Eq. (2.166)

A comparison of the contribution to the square root of the variance of the projected 2PTCF is shown in the right panel of Fig. 3.4, where, as in the previous section, the pure shot-noise contribution had been isolated in order to be compared with the pure Poisson error resulting from LS estimation according to CUTE code (circle points). As in the 3D 2PTCF, we confirm an agreement between these two estimates. As for the 3D 2PTCF, throughout the rest of our analysis, we consider its effect via the theoretical treatment described above.

For comparison with VIPERS (Marulli et al., 2013), the bias is first estimated as the average of $b(r_p)$ in the range of $[1 - 10] h^{-1}\text{Mpc}$, where the bias is reasonably constant, as claimed in VIPERS and shown in Figure 3.7. In order to account for a small scale-dependency on the smallest scales, we also fit a relation $b(r_p) = b_0 + b_1/r_p$, such that b_0 can be taken as an estimate of the linear large-scale bias.

For both the averaged bias and the fit, the results depend on the scales used, as can be seen in Table 3.3. The smallest scales bring in non-linearities whereas the largest scales are subject to sample variance, lower signal-to-noise and the largest possible effects from the *IC*. We note that we find the constant *IC* (0.01 – 0.02) to be an order of magnitude lower than the correlation (0.1 – 0.2) around $20 h^{-1}\text{Mpc}$. This 10% effect on the correlation could in principle affect the bias estimation. This effect is smaller around $10 h^{-1}\text{Mpc}$, where the correlation is a factor of 2-3 larger.

The values for the bias change significantly between the average bias and the fit to the scale-dependent bias, even when the same maximum scale is used in both procedures, indicating a measurable effect of the non-linearity on the smallest scales.

The errors have been obtained propagating the uncertainties in r_0 and γ shown in the table, after fitting to Marulli et al. (2013).

$$w_p(r_p) = r_p \left(\frac{r_0}{r_p} \right)^\gamma \frac{\Gamma(\frac{1}{2})\Gamma(\frac{\gamma-1}{2})}{\Gamma(\frac{\gamma}{2})} \quad (3.6)$$

In Fig. 3.8, we compare our measurements to those published for VIPERS (Marulli et al., 2013). For this comparison, we use our averaged bias as

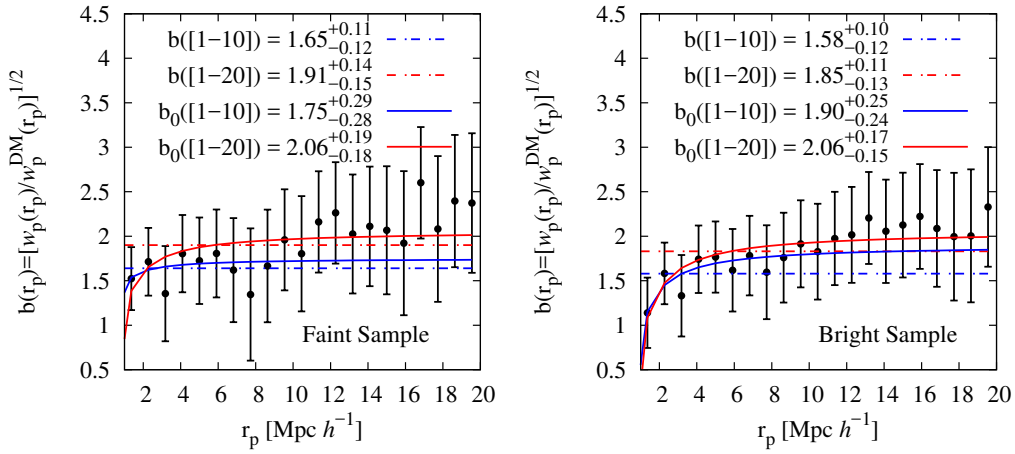


Figure 3.7: The galaxy bias calculated using a constant and a scale dependent relation for the faint (*left*) and bright (*right*) sample, measured from projected correlation function. The straight dashed lines show the bias value calculated as the average between 1 and 10 h^{-1} Mpc (blue) and between 1 and 20 h^{-1} Mpc (red). The solid lines are a scale dependent bias fitting to $b(r_p) = b_0 + b_1/r_p$, such that b_0 represents a large scale bias. The results depend on the range of scales used in the average and the limiting value of the fit. For comparison to previous studies, we select the averaged bias between 1 and 10 h^{-1} Mpc (dashed blue) as our bias proxy, but we note that different definitions give different results.

Sample	Bright	Faint
s_0 [h^{-1} Mpc]	$4.04^{+0.64}_{-0.95}$	$4.26^{+0.68}_{-1.02}$
γ	$1.47^{+0.11}_{-0.12}$	$1.50^{+0.11}_{-0.15}$
mean z	0.855	0.901
$\langle b \rangle$ up to $10 h^{-1}$ Mpc	$1.58^{+0.10}_{-0.12}$	$1.65^{+0.11}_{-0.12}$
$\langle b \rangle$ up to $20 h^{-1}$ Mpc	$1.85^{+0.11}_{-0.13}$	$1.91^{+0.14}_{-0.15}$
b_0 up to $10 h^{-1}$ Mpc	$1.90^{+0.25}_{-0.24}$	$1.75^{+0.29}_{-0.28}$
b_0 up to $20 h^{-1}$ Mpc	$2.06^{+0.17}_{-0.15}$	$2.06^{+0.19}_{-0.18}$

Table 3.3: Clustering properties and bias for the faint and bright samples selected with spectroscopic redshifts. The clustering length and slope were obtained by fitting a power law for $w_p(r_p)$ for $0.5 < r_p < 20 h^{-1}$ Mpc. The averaged bias value was obtained by averaging the scale dependent bias $b(r_p) = [w_p(r_p)/w_p^m(r_p)]^{1/2}$, while b_0 comes from a fit to the scale-dependent bias $b(r_p) = b_0 + b_1/r$. Both the average and the fit bias are obtained over scales $1 < r_p < 10 h^{-1}$ Mpc as well as $1 < r_p < 20 h^{-1}$ Mpc.

a reference to reflect the VIPERS procedure. Our bias agrees with that from VIPERS for a population brighter than $M_B - \log(h) < -20.5$. To confirm this result, we calculated the absolute magnitude for the faint and bright samples together (there is a substantial overlap between both samples) to directly measure the absolute limiting magnitude of our sample. We calculate the absolute magnitude for the B band using the template fitting code `LePhare`, fixing the redshift to its spectroscopic value. We show the B-band absolute magnitude density distribution in Fig. 3.9 as a function of redshift for the bright and faint sample. The result agrees well with what it is expected from the galaxy bias of the sample. The luminosity-dependent clustering will be analyzed in further detail in future studies.

3.3 Discussion

This chapter presents the use of 9.2 deg^2 of eBOSS test plates data to study the clustering properties of different possible ELG target selections. For that, a set of three different target selections were designed using SDSS, SCUSS, and DES-SVA1 data from whom present work focuses on DES-based only. The DES based selection was divided into two samples designated as bright and faint selections, with the latter optimized for reaching higher redshifts following target selection designed for a DESI like survey. The two samples have a mean redshift of 0.8 and 0.87 for bright and faint, respectively.

The clustering properties of samples considered here were studied esti-

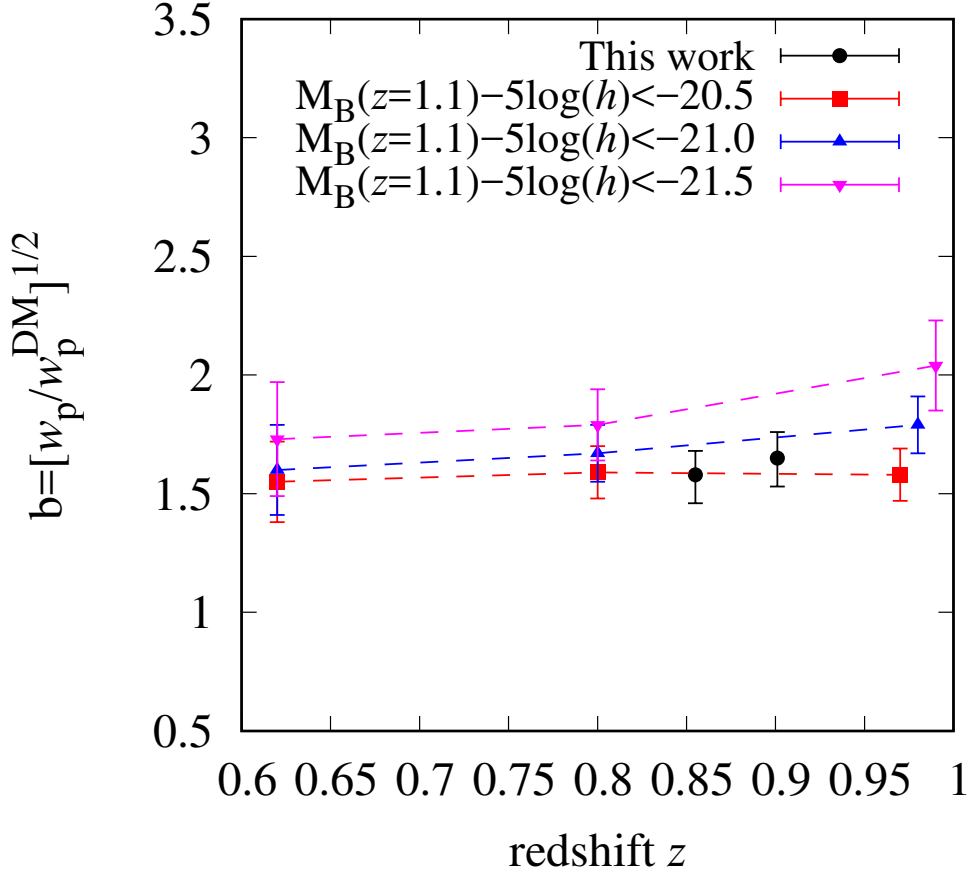


Figure 3.8: In black, the galaxy bias for our target selection samples in the range $0.6 < z < 1.2$ for the faint and bright. The reference values come from Table 1 of Marulli et al. (2013) from the VIPERS survey. In both cases, biases have been measured as the average in $[1 - 10] h^{-1} \text{Mpc}$. Our bias agrees within one sigma with a galaxy population brighter than $M_B - 5 \log(h) < -20.5$.

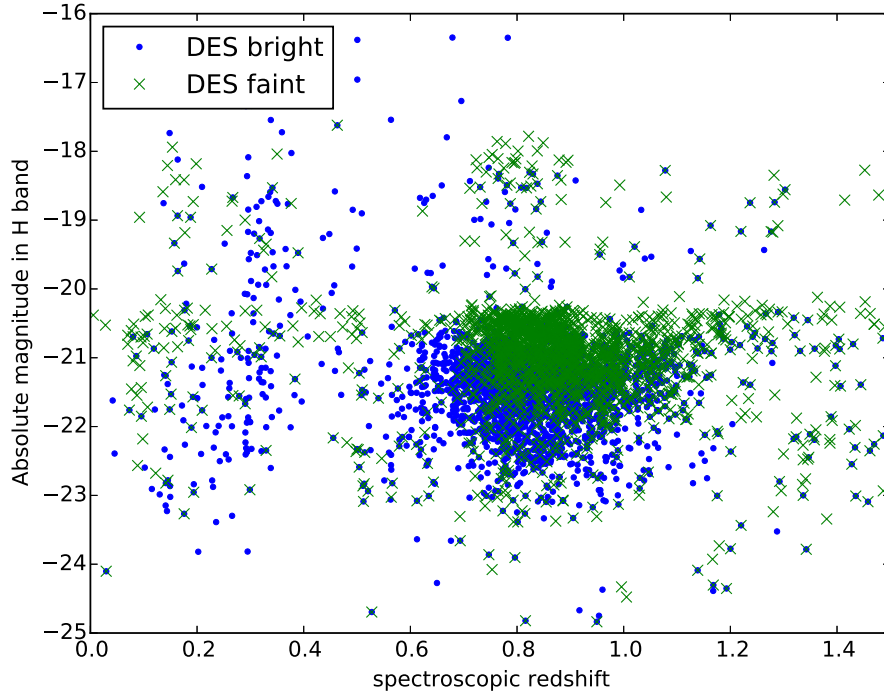


Figure 3.9: Absolute magnitude in the B-band for the ELG spectroscopic sample as a function of spectroscopic redshift. Magnitudes were calculated using `LePhare` with the same configuration as in the photo- z calculation, but using the galaxy spectroscopic redshifts. The population is consistent with a selection $M_B - \log(h) < -20.5$ in the redshift interval $0.6 < z < 1.2$, in agreement with the bias measurement from Figure 3.8. This corresponds to 84% and 72% in respectively the bright and faint sample.

mating the 3D two-point correlation function monopole $\xi(s)$ and the projected real space correlation function $w_p(r_p)$. We used these measurements to compute the large-scale galaxy bias and found it to be consistent with previous ELG measurements. The galaxy bias between the DES bright and faint sample are within 1σ of each other. We find a slightly higher bias for the faint sample compared to the bright which is expected due to redshift evolution. We also looked at the binning effect in clustering analysis when having to define a redshift window with photometric redshifts. Considering that DES will have a good photometric redshifts calibration, we used spectroscopic redshifts to compute correlation functions and use the photo- z to define the 0.6 to 1.2 redshift window. We do not find significant differences when using spectroscopic and photometric redshifts. Finally, we compare the mean value of the galaxy bias to the deep spectroscopic survey VIPERS and find that the ELG sample agrees with that from VIPERS for a population brighter than $M_B - \log(h) < -20.5$.

Chapter 4

Luminous Red Galaxies clustering at eBOSS

This chapter describes results presented in Zhai et al. (2017), where the first scientific results from the Luminous Red Galaxy (LRG) sample of the extended Baryon Oscillation Spectroscopic Survey (eBOSS) were presented studying the definition and clustering properties of a combined sample from BOSS and eBOSS. Our main contribution to this work was to independently measure the small and intermediate scale clustering from a sample of more than 61,000 galaxies in the redshift range $0.6 < z < 0.9$, which were subsequently interpreted in the framework of the Halo Occupation Distribution and shown to be in agreement with the clustering of massive galaxies from BOSS, demonstrating that eBOSS galaxies would be reliable tracers of large scale structure at $z \sim 0.7$.

4.1 The eBOSS-BOSS LRG sample

The present work focuses on the eBOSS LRG sample, designed to extend the BOSS LRG sample deeper in redshift to survey galaxies with $0.6 < z < 1.0$ with an expected target density of 60 deg^{-2} . The LRG sample selection is based on the *ugriz* imaging of the SDSS (Fukugita et al., 1996) in combination with infrared photometry from the Wide-Field Infrared Survey Explorer (WISE) (Wright et al., 2010) for two primary purposes: i) select fainter objects at higher redshifts and ii) Optimize the minimization of stellar contamination of the sample. A full description of the target selection for the eBOSS LRGs is presented in (Prakash et al., 2016).

Here we highlight that this selection was designed to allow for the combination with the high-redshift tail of the CMASS sample, a BOSS sample

targeted by SDSS imaging to probe $0.4 < z < 0.7$. Such a combination is desired as first, cosmological analysis planned with eBOSS data were likely to increase the density of the sample in order to reduce statistical uncertainties, and second, such a combination goes in the direction of making the sample complete in the sense of including all galaxies above some mass or luminosity threshold. The latter point is fundamental for part of the analysis presented by Zhai et al. (2017), as an HOD analysis was carried on and such kind of analysis typically assumes this kind of completeness. In order to achieve such a combination, the eBOSS LRG target selection imposed a bright limit of $i = 19.9$ optimizing the complementarity of the samples.

The present work used eBOSS DR14 (Abolfathi et al., 2018) LRG data taken before May 2016. This LRG sample has a total of 110000 spectra and area coverage of 1591 deg^2 . After applying specific quality criteria (see Prakash et al., 2016; Zhai et al., 2017), eBOSS LRG sample ended with a total of 61000 galaxies. The BOSS-CMASS sample was restricted to the same footprint of eBOSS and combined with the latter to define the *eBOSS-BOSS* sample, basis of this work. The eBOSS-BOSS sample ended up with a total of 97000 galaxies.

On top of that, an additional mask to account for *knockouts* was applied to data. There is an intrinsic physical limit for fibers on a given SDSS plate not allowed to be closer than a given *collision radius*, this phenomenon is known in the literature as *fiber collisions* and is basically an experimental restriction, the impossibility of drill and plug two holes on a given plate when two objects are close enough together. In SDSS-I/II, the collision radius was $55''$. In BOSS and eBOSS, the collision radius is $62''$. Additionally, fiber allocation strategy (see Dawson et al., 2016) dictates that LRGs went to fiber allocation process only after all other targets. This implies that there is a significant amount of area in some sense prohibited to LRGs coming from the fiber collisions. LRG targets that are within the collision radius of a higher priority target are designed as *knockouts*. Although some knockouts can be recovered in plate overlaps, approximately 10% of the total LRG footprint have to be masked due to this effect.

Another important effect that can impact angular selection is the contamination by bright stars. The fiducial analysis presented here, corresponding to the same one in (Zhai et al., 2017), did not use the Bright star mask from WISE. Fortunately, although we did not conduct such analysis, Zhai et al. (2017) (see App A) demonstrated that the impact of such a mask has negligible effects for the clustering analysis conducted, less than 5% for the scales considered.

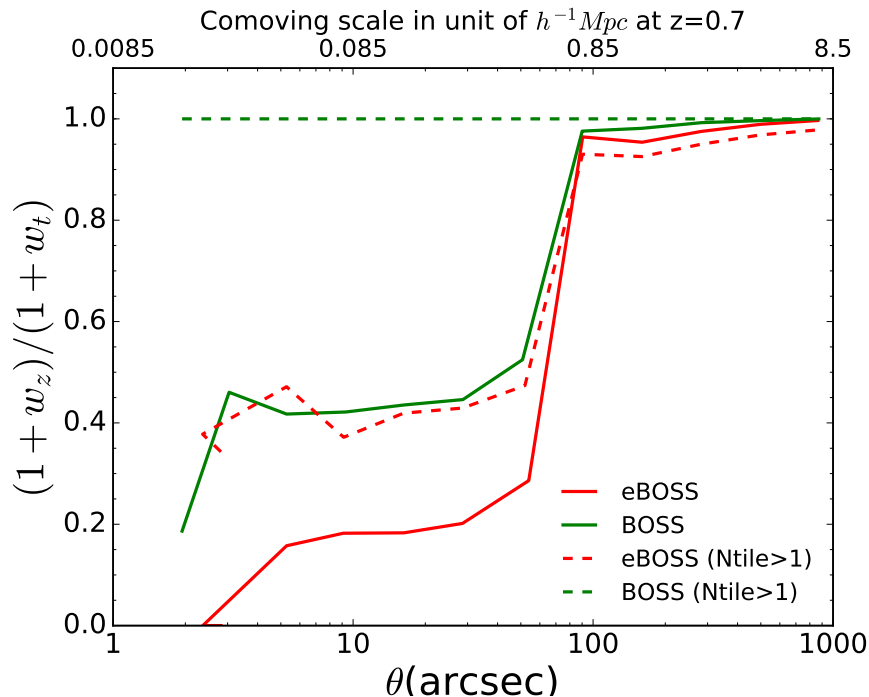


Figure 4.1: The angular correction (Eq. 4.1) for eBOSS (red) and BOSS (green) samples building up the eBOSS-BOSS sample (§4.1) (Zhai et al., 2017, Fig 4). $N_{\text{tile}} > 1$ refers to “more than one tile”, i.e., the sectors that are observed more than once. This quantity is used to weight the galaxy pairs to account for the loss of pairs due to collisions. The top x -axis scale relates angular separations with comoving separations at the sample effective redshift by using the comoving angular diameter distance Eq. (2.25).

4.2 LRG clustering measurements

We performed measurements of the projected correlation function (see §2.4.6) eBOSS-BOSS sample of LRG galaxies using 10 logarithmic bins in the perpendicular to the line of sight separation r_p (see Fig. 2.2 and surrounding text) on the range $0.2h^{-1}\text{Mpc} < r_p < 60h^{-1}\text{Mpc}$. In order to translate angular positions and redshift to two-point separations, we assume a fiducial spatially flat ΛCDM model with parameters $(\Omega_m, h, \Omega_b, \sigma_8, n_s) = (0.29, 0.7, 0.04, 0.8, 0.95)$. The correlation function measurements were done via the (Landy & Szalay, 1993, (LS) estimator) using the CUTE¹ code (Alonso, 2012).

As discussed in the previous section, a known problem of spectroscopic

¹<https://github.com/damonge/CUTE>

redshifts using fibers is that the finite size of the fiber plugs prohibit two fibers from being placed too close on the same plate resulting in having a significant fraction of imaging targeted galaxies with no assigned fibers and consequently without spectroscopic redshifts. We highlight this effect is different from the knockouts, as in the latter a given target cannot have assigned fiber due to collision with other, high priority, and more important *uncorrelated* target. The fiber collision effect then refers to a collision between two targets of the same kind.

The two main effects of fiber collision are i) a reduction in the spectroscopic completeness, that for LRGs of eBOSS is estimated as $\sim 5\%$, and ii) an impact on the observed clustering of tracers, that effectively impacts all the scales of interest, i.e., both, the measured large-scale bias and the small scale clustering (see, e.g., Guo et al., 2012, and references therein).

In order to address this effect on our w_p measurements, we follow the strategy of combining two different weighting schemes: i) up-weighting galaxies which have a fiber assigned in the collided-pairs, and ii) reconstructing the correct galaxy pair counts in scales smaller than $62''$. The first weighting scheme is similar to the “nearest-neighbor method” (Zehavi et al., 2002, 2005) and corrects for the impact of collisions on the large scales, i.e., allow for an unbiased determination of large-scale bias of the population. The second one is designed to correct the clustering signal at small scales by using the ratio of angular correlation functions (Hawkins et al., 2003) to build up the correction factor

$$F(\vartheta) = \frac{1 + w_z(\vartheta)}{1 + w_t(\vartheta)}, \quad (4.1)$$

where $w_{z,t}$ refer to the angular correlation function of galaxies (§2.4.3) drawn from the spectroscopic and the photometric sample respectively. Note that the former is effectively constructed from targets which had fibers assigned whereas the latter is the entire imaging-based targeted sample.

In order to gain insight on Eq. (4.1), we begin by noting that the quantity $1 + w(\vartheta)$ can be interpreted as the number of pairs of targets separated by an angle ϑ (see Eq. (2.103) and surrounding text), so in order to account for the loss of pairs due to fiber collisions, one can weight each DD pair in LS estimator (Eq. 2.106) by the factor $1/F(\theta)$.

Fig. 4.2 (see Fig. 4 in Zhai et al., 2017) presents the correction factor of Eq. (4.1) for both eBOSS and BOSS galaxy samples used to build the eBOSS-BOSS sample used for the analysis presented in this chapter. The correction factor for pair counts is close to unity for scales above the fiber collision scale and decreases significantly at angular separations below this scale.

An interpretation for such behavior can be drawn from the results from BOSS. Fiber allocation strategy for BOSS was based on the requirement of achieving 100% completeness in the “decollided” set, the one containing all targets that are not within collision groups (groups of targets that lie within $62''$ of one another), combined with the subset of collided targets that can be assigned fibers on a single plate (Dawson et al., 2016). Therefore, in areas of the survey covered by more than one tile, all collisions were resolved by observing one galaxy on each plate. However, only 40% of BOSS footprint was covered by more than one tile, which should result in $F \approx 0.4$ for $\vartheta < 62''$, validating the result in Fig. 4.2. For eBOSS, F is substantially smaller below the collision scale. The reason may reside in the fiber allocation priorities. In BOSS, the goal of 100% completeness in the decollided set was met at the expense of some unused fibers, which totaled 7%. To maximize fiber usage in eBOSS, the goal of 100% decollided completeness was relaxed *only* for the LRGs, which implies variations in the number of LRG assigned fibers from plate to plate due to fluctuations in the density of higher priority targets.

In practice, the additional weights to account for fiber collisions were applied differentially for pair counts at $\vartheta < 62''$ correlating different samples: BOSS-BOSS pairs were up-weighted by 2.64, eBOSS-eBOSS pairs by 5.1, and eBOSS-BOSS cross pairs were not up-weighted as there are no collisions between surveys.

Our measurement of $w_p(r_p)$ for the eBOSS-BOSS sample is shown on the top panel of Fig. 4.2. From our clustering estimates, we performed a determination of the large-scale bias of the sample. Similar to the analysis presented in Chap. 3, the galaxy bias is defined through Eq. (3.5),

$$b(r_p) = \sqrt{\frac{w_p(r_p)}{w_p^m(r_p)}},$$

where $w_p(r_p)$ is given by Eq. (3.4) and is obtained from the galaxy sample, while $w_p^m(r_p)$ is the projected correlation function of matter. For the latter, we compute the predicted linear matter power spectrum using CAMB (Lewis & Bridle, 2002) on the mean redshift of the sample, $z_{\text{eff}} = 0.7$ and the fiducial cosmology (see § 4.1) and project it according to Eqs. (2.162) and (2.116) by using the FFTLog algorithm (Appendix E) to compute the corresponding Hankel transforms.

For the galaxy bias determination, we restrict the analysis to scales where the clustering signal is well represented by the two halo term contribution, Fig. 4.3. Effectively we used the last 5 bins in r_p , $3.7h^{-1} \text{ Mpc} < r_p < 60h^{-1} \text{ Mpc}$. We found a galaxy bias for the eBOSS-BOSS LRG sample given

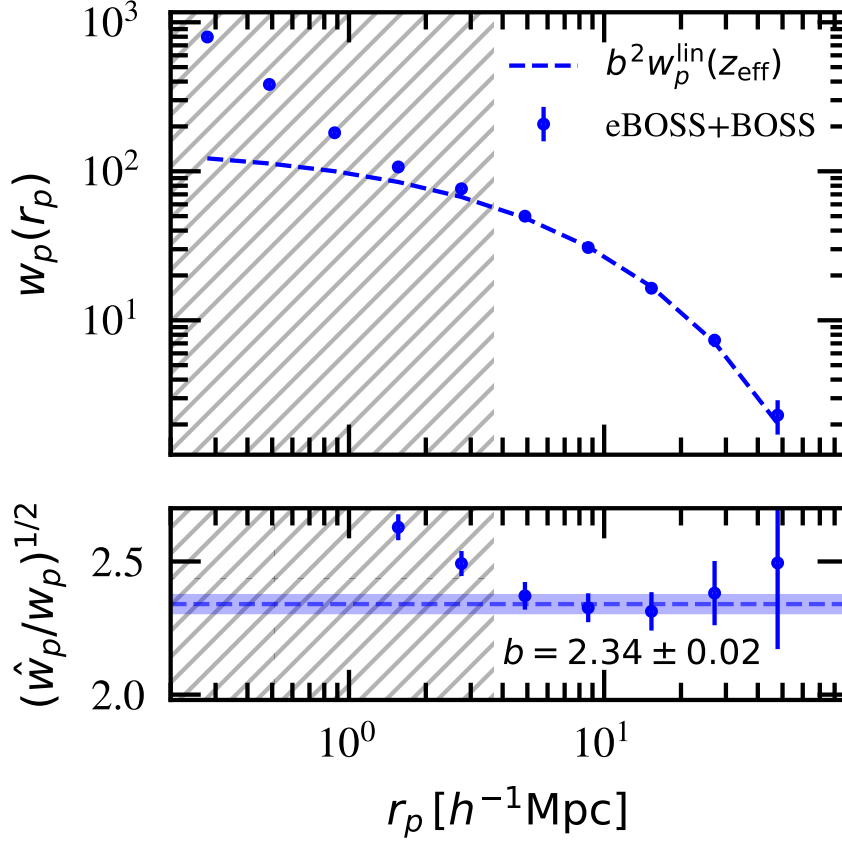


Figure 4.2: (*Top*): Measurements of w_p for the eBOSS-BOSS sample (points) compared to the linear theory predicted following Eq. (2.162) corrected by the fitted large-scale bias (see text). (*Bottom*): Bias measured from the projected two-point w_p correlation function of the eBOSS-BOSS LRG sample as a function of coordinate r_p perpendicular to the line of sight. Blue points represent the measurements, scaled adequately by the total matter prediction to give the bias and blue horizontal region shows the 1σ confidence region for the bias fits. The non-hatch region shows the range of scales used for the fit, representing scales well described by the two-halo term, see Fig. 4.3.

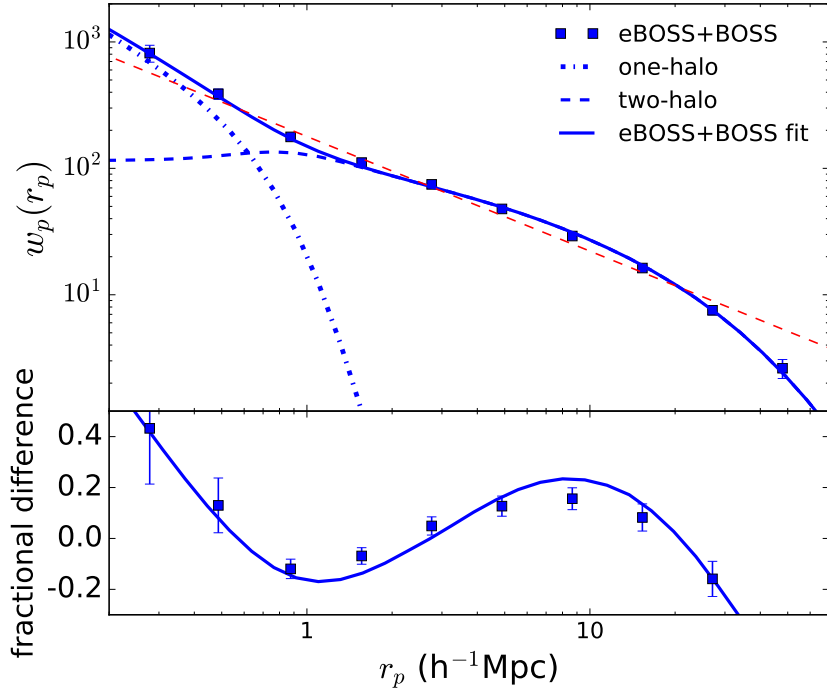


Figure 4.3: Projected correlation function $w_p(r_p)$ of the eBOSS-BOSS LRG sample. (*Top*): Blue dashed lines represent the one- and two-halo term contributions from the Halo model, Eqs. (2.83) and (2.81) and their combined best-fit. Red dashed line shows the best-fit power law model, Eq. (3.6), for which $\gamma = 1.95$. (*Bottom*): Fractional difference and residuals of HOD best-fit (line) and measurements (points), respectively, with respect to the best-fit power law model. The χ^2 for fit was $\chi_{\text{red}}^2 = \chi^2/\text{dof} = 13.6/6 = 2.3$.

by

$$b_{\text{LRG}}(z_{\text{eff}}) = 2.34 \pm 0.02, \quad (4.2)$$

with a $\chi^2 = 4.8$ for 4 degrees of freedom (dof).

A Halo Occupation Distribution model (HOD) to describe the small and intermediate clustering of the eBOSS-BOSS LRG sample was also fitted on (Zhai et al., 2017). The model used in the analysis was presented in § 2.3.2 (see also § 4.1 of Zhai et al., 2017). Table 4.1 displays the recovered constraints for the main HOD parameters (top) and two recovered parameters, namely the bias b and the satellite fraction f_{sky} of the population. Here we focus on the galaxy bias. It was computed using Eq. (2.93) according to the parameters and uncertainties are shown at the top of Table 4.1. We find

HOD parameter	eBOSS-BOSS
$\log M_{\min}$	$13.68^{+0.06}_{-0.05}$
$\log M_{\text{sat}}$	$14.87^{+0.60}_{-0.32}$
α	$0.41^{+0.20}_{-0.16}$
$\log M_{\text{cut}}$	$12.32^{+0.76}_{-0.88}$
$\sigma_{\log M}$	0.82 ± 0.05
b	2.30 ± 0.03

Table 4.1: Constraints on an HOD model parameters (see § 2.3.2) for the eBOSS-BOSS sample as obtained by Zhai et al. (2017) (see Table 2). The fit has a $\chi^2 = 13.6$ for 6 degrees of freedom. The top panel displays the constraints on the HOD intrinsic parameters. The bottom panel displays the galaxy bias as a derived parameter of the HOD model. The galaxy bias was obtained following Eq. (2.93) and shows excellent agreement with the one obtained from a direct comparison of measurements and the total matter prediction, Fig. 4.2 and Eq. (4.2).

an excellent agreement between the values of the bias as recovered by the two methods.

We highlight the somehow large value found for the reduced $\chi^2_{\text{red}} = \chi^2/\text{dof} = 13.6/6 = 2.3$ of the best-fit HOD model, Table 4.1 and Fig. 4.3, when compared with the direct fit to large-scale clustering, Eq. (4.2), of $\chi^2_{\text{red}} = 4.8/4 = 1.2$. It can be explained by the relatively poor agreement of the HOD fit with the data at $1 < r_p < 3 h^{-1}$ Mpc, do not taken into account in the direct measurement of the large-scale bias, which in turns is advocated by Zhai et al. (2017) to be likely a failure of the scale-dependent bias model used, namely, Eq. (2.77) as fitted by Tinker et al. (2010) feeding Eq. (2.93), which is calibrated on lower-mass halos and lower-redshift samples, and had been found to be responsible for uncertainty in HOD fitting (see, e.g., Tinker et al. 2012). With that, more flexible modeling of the scale-dependent galaxy bias is likely to account for the differences in the mentioned scales and consequently lowering the χ^2 . However, the characteristics of the galaxy sample, namely its HOD parameters, are unlikely to change, as there is an intrinsic consistency between them and the large-scale bias.

4.3 Discussion

This chapter presents some of the results described in Zhai et al. (2017), which defines the first scientific results from the eBOSS LRG program by analyzing for the first time the clustering properties of a combined sample

from BOSS and eBOSS.

Our main contribution was to provide an independent measurement of the large-scale bias for a combined sample of eBOSS-BOSS LRGs galaxies which is in perfect agreement with the one coming from an HOD model fitted to the same population of galaxies. In our measurements, we properly account for all the standard observational systematics managed by the SDSS pipeline and also for the fiber collision effect via an up-weight of the galaxy pair counts based on the angular clustering of spectroscopic and photometric targets as described in Zhai et al. (2017).

Measurements of large-scale bias coming directly from the large-scale clustering signal and the fit of an HOD model are in perfect agreement offering validation for the HOD fit, and a robustness test to all the methodology presented in Zhai et al. (2017).

Chapter 5

Measurement of the angular power spectrum BAO feature in DES Y1 galaxies

This chapter presents results from Camacho et al. (2018), where we present measurements of the galaxy angular power spectrum (APS) from the first-year observations (Y1) of the DES collaboration. Such measurements were subsequently used in (Abbott et al., 2019) in combination with other two-point statistics to offer the first BAO feature determination on DES data.

The results of this chapter are contained in a series of papers dedicated to the detection of the BAO features in Y1 data. It relies on the construction of a catalog suitable for the study of clustering of galaxies, especially concerning the BAO feature (Crocce et al., 2019), the mock catalogs used to validate the analysis and results (Avila et al., 2017) and the computation of galaxy photo- z s (Gaztanaga et al. in prep). Other papers detail methods to study the BAO feature in configuration space with the angular correlation function $w(\theta)$ (Chan et al., 2018), and using the comoving transverse separation (Ross et al., 2017), while the present work details the use of the angular power spectrum. The joint results applied to the Y1 data are described in the BAO main paper (Abbott et al., 2019).

We test our methodology in a sample of 1800 DES Y1-like mock catalogs. We use the pseudo- C_ℓ method to estimate the APS and the mock catalogs to estimate its covariance matrix. We use templates to model the measured spectra and estimate template parameters firstly from the C_ℓ 's of the mocks using two different methods, a maximum likelihood estimator and a MCMC, finding consistent results with a good reduced χ^2 . Robustness tests are performed to estimate the impact of different choices of settings used in our analysis. Finally, we apply our method to a galaxy sample constructed from

DES Y1 data specifically for LSS studies. This catalog comprises galaxies within an effective area of 1318 deg^2 and $0.6 < z < 1.0$. We find that the DES Y1 data favors a model with BAO at the 2.6σ C.L.

However, the goodness-of-fit is somewhat poor, with $\chi^2/(\text{dof}) = 1.49$. We identify a possible cause showing that using a theoretical covariance matrix obtained from C_ℓ 's that are better adjusted to data results in an improved value of $\chi^2/(\text{dof}) = 1.36$ which is similar to the value obtained with the real-space analysis. Our results correspond to a distance measurement of $D_A(z_{\text{eff}} = 0.81)/r_d = 10.65 \pm 0.49$, consistent with the main DES BAO findings. These results are part of a to the main DES BAO article and focus on details of the harmonic-space analysis.

In this work we use a template-based method to study the BAO feature in the angular power spectra from the DES Y1 data. We describe our method and test it on realistic survey mocks. These mocks were also used to measure the covariance matrix of the C_ℓ 's. The covariance matrix was then used to find the likelihood corresponding to the template adopted to model the data. We estimate the significance of the detection of the BAO feature for a baseline template using two independent methods: a maximum likelihood estimator (MLE) and a Markov Chain Monte Carlo (MCMC) method. We also present the reduced χ^2 values for the mocks to demonstrate the goodness-of-fit. We explore the robustness of our baseline model to the estimation of parameters testing different choices of settings and assumptions in the analysis. After the validation of our methodology, we apply it to Y1 data with the intent to search for BAO features. We find that the DES Y1 data favors a model with BAO wiggles at the 2.6σ confidence level with a best-fit shift parameter of $\alpha = 1.023 \pm 0.047$ with a somewhat large value of $\chi^2/(\text{dof}) = 1.49$. We investigate this issue substituting the covariance matrix obtained from the mocks by a gaussian theoretical covariance matrix taking into account the Y1 mask with input C_ℓ 's that are better adjusted to data obtaining an improved value of $\chi^2/(\text{dof}) = 1.36$ which is similar to the value obtained with the real-space analysis.

This chapter is organized as follow. We start by describing the theoretical modeling of the angular power spectrum in § 5.1, including the template, used to study the BAO feature. In § 5.2 we describe the DES Y1 galaxy catalog constructed for BAO studies, focusing on the redshift binning, pixelization and masking. The 1800 mock catalogs used for the verification of our measurements, for the covariance matrix estimation and for testing our parameter estimation from the template method are briefly presented in § 5.3. In § 5.4 the measurement of the APS using the pixelized maps is described. The methodology we adopt is tested on the mocks in § 5.5 where

we also study the impact of different choices of templates and settings on the parameter estimation as robustness checks. Having validated our methodology, we apply it for Y1 data in § 5.6 where we concentrate on finding BAO features in the angular power spectrum. Finally, in § 5.7 we present our chapter conclusions.

5.1 Theory

Most of the theoretical development used here have been developed in detail in § 2.4. In this section, we reproduce the equations that are most relevant to our work in this chapter.

We detect the BAO feature from measurements of the angular power spectrum of DES galaxies. Recall that the angular cross-spectrum C_ℓ^{ij} at z bins i and j is given by

$$C_\ell^{ij} = \frac{2}{\pi} \int dk k^2 P_{\text{gal}}(k) \left[\Psi_\ell^i + \tilde{\Psi}_\ell^i \right] \left[\Psi_\ell^j + \tilde{\Psi}_\ell^j \right], \quad (5.1)$$

where $P_{\text{gal}}(k) = b^2 P_m(k)$ is the 3D galaxy power spectrum, b is the galaxy bias, $P_m(k)$ is the matter power spectrum. The kernels are given by

$$\Psi_\ell^i = \int dz G(z) \phi^i(z) j_\ell[k\chi(z)]. \quad (5.2)$$

and

$$\tilde{\Psi}_\ell^i = \int dz \beta(z) G(z) \phi^i(z) \left\{ \frac{2\ell^2 + 2\ell - 1}{(2\ell + 3)(2\ell - 1)} j_\ell[k\chi] - \frac{\ell(\ell - 1) j_{\ell-2}[k\chi]}{(2\ell - 1)(2\ell + 1)} - \frac{(\ell + 1)(\ell + 2)}{(2\ell + 1)(2\ell + 3)} j_{\ell+2}[k\chi] \right\}, \quad (5.3)$$

where $G(z)$ is linear growth function (normalized such that $G(z = 0) = 1$), $\phi^i(z)$ is the redshift selection function, j_ℓ are Spherical Bessel functions and

$$\beta(z) = \frac{1}{b(z)} \frac{d \ln G}{d \ln a}. \quad (5.4)$$

Notice that $\tilde{\Psi}_\ell^i$ carries information on RSD's. The angular power spectrum at z bin i is defined by $C_\ell^i \equiv C_\ell^{ii}$. The Gaussian covariance matrix for C_ℓ^i 's measured at photo- z bins i and j can be theoretically modeled in the so-called f_{sky} approximation as:

$$\text{Cov}[\text{APS}]_{\ell\ell'}^{ij} \equiv \langle C_\ell^i C_{\ell'}^j \rangle - \langle C_\ell^i \rangle \langle C_{\ell'}^j \rangle = \frac{2}{f_{\text{sky}} \Delta\ell (2\ell + 1)} \left(C_\ell^{ij} + \frac{\delta_{ij}}{\bar{n}_i} \right)^2 \delta_{\ell\ell'}, \quad (5.5)$$

where $\Delta\ell$ is the ℓ bin size, f_{sky} is the sky fraction covered by the survey, \bar{n}_i is the mean galaxy number density at bin i and δ_{ij} is a Kronecker delta.

5.1.1 APS template

Our goal is to extract from mocks and DES Y1 observations the scale associated with the BAO feature, namely the angular distance scale $D_A(z)$. In order to be as insensitive as possible to nonlinear effects such as bias and redshift space distortions, we will use a template method (Seo et al., 2012; Anderson et al., 2014; Gil-Marín et al., 2016; Ata et al., 2018a; Ross et al., 2017; Chan et al., 2018).

Since the selection function for the simulations and data is fully specified, the C_ℓ template may be defined by first settling on a template for $P(k)$ and projecting onto C_ℓ 's using Eq. (5.1). We start with

$$P^{\text{temp}}(k) = [P(k)^{\text{lin}} - P^{\text{nw}}(k)]e^{-k^2\Sigma_{nl}^2} + P^{\text{nw}}(k), \quad (5.6)$$

where $P(k)^{\text{lin}}$ is the linear power spectrum and the no-wiggle power spectrum $P(k)^{\text{nw}}$ is obtained from the Eisenstein-Hu parametrization (Eisenstein & Hu, 1998). The nonlinear damping scale is fixed at $\Sigma_{nl} = 5.2$ Mpc/h, which was determined from a fit to the mean of mocks (Chan et al., 2018). Recall this exponential damping is inspired by nonlinear effects in RPT (see § 2.2.2).

We chose our template by optimizing the BAO signal in the mock catalogs. Tests of different templates will be shown below. Our default template for C_ℓ is given by:

$$C_\ell \equiv C(\ell) = B_0 C^{\text{temp}}(\ell/\alpha) + A_0 + A_1\ell + A_2/\ell^2, \quad (5.7)$$

where $C^{\text{temp}}(\ell)$ is the projection of $P^{\text{temp}}(k)$ as described above. The amplitude B_0 is related to the linear bias squared and the parameters A_i take into account scale-dependent bias, shot noise, uncertainties in redshift-space distortions, etc. We allow these parameters to change with redshift. Therefore, for 4 redshift bins, we will have 16 of these parameters to adjust. We will marginalize over them in MCMC analysis and keep them fixed at the values that maximize the likelihood in the MLE analysis as will be described in § 5.5.

The most important parameter in our analysis is the so-called shift parameter α , which measures the shift of the BAO peak positions with respect to a fiducial cosmology. We will assume that it does not change significantly with respect to its value at the “effective redshift” of the sample used ($z_{\text{eff}} = 0.81$ in the BAO Y1 sample) (Abbott et al., 2019). If the fiducial cosmology used to compute $P(k)^{\text{lin}}$ and $P(k)^{\text{nw}}$ turns out to be the correct one then one should find $\alpha = 1$. The shift parameter is related to the change in the BAO location, given by the ratio of the angular diameter distance

$D_A(z)$ to the sound horizon scale at the drag epoch (r_d):

$$\alpha = \frac{(D_A(z)/r_d)}{(D_A(z)/r_d)_{\text{fid}}}. \quad (5.8)$$

For example, for a fiducial cosmology given by the MICE simulations ($h = 0.7$, $\Omega_m = 0.25$, $\Omega_\Lambda = 0.75$) (Crocce et al., 2010; Fosalba et al., 2015b) we find that, with respect to the cosmology found by DES combined with other observations ($h = 0.678$, $\Omega_m = 0.30$, $\Omega_\Lambda = 0.70$) (Abbott et al., 2018), $\alpha \approx 1.03$.

We will test this parametrization with the mocks below and show that it results in biases below 1% for parameter estimation. We study the impact of other templates as robustness tests in § 5.5.

5.2 DES Y1 BAO galaxy sample

The catalog for LSS analyses using DES Y1 data was created from the so-called Y1 Gold catalog (Drlica-Wagner et al., 2018) which in turn was built from the data reduction performed by the Dark Energy Survey Data Management (DESDM) system on DECam images. The LSS sample selection is based on color, magnitude and redshift cuts designed to provide an optimal balance between the density of objects and the photometric redshift uncertainty for $z > 0.6$, minimizing the forecasted BAO error (Crocce et al., 2019). We will use the LSS catalog with photometric redshifts obtained with a Multi-Object Fitting (MOF) photometry (Drlica-Wagner et al., 2018) and the Directional Neighborhood Fitting (DNF) algorithm (De Vicente et al., 2016). After proper masking described in Crocce et al. (2019) the catalog has approximately 1.3 million galaxies in an area of 1317 deg² comprised on a footprint covering two compact regions of the sky: one in the southern hemisphere covering 1203 deg² and overlapping South Pole Telescope observations (SPT, Carlstrom et al., 2011), and one near Equator with 115 deg² and overlapping the *Stripe 82* (S82, Annis et al., 2014), Fig. 5.1.

We divide the catalog into 4 tomographic photo- z bins with width $\Delta z_{\text{phot}} = 0.1$ in the range $0.6 < z_{\text{phot}} < 1.0$. In Fig. 5.2 we show the redshift distribution for each bin obtained by stacking a Monte Carlo sampled value of the photo- z from the estimated probability distribution function for each object. The tomographic bins are defined using a point-estimate of the photo- z given by the maximum likelihood redshift produced by DNF.

Regarding observational systematic effects mitigation, present work follows the methodology developed from early DES Science Verification (SV)

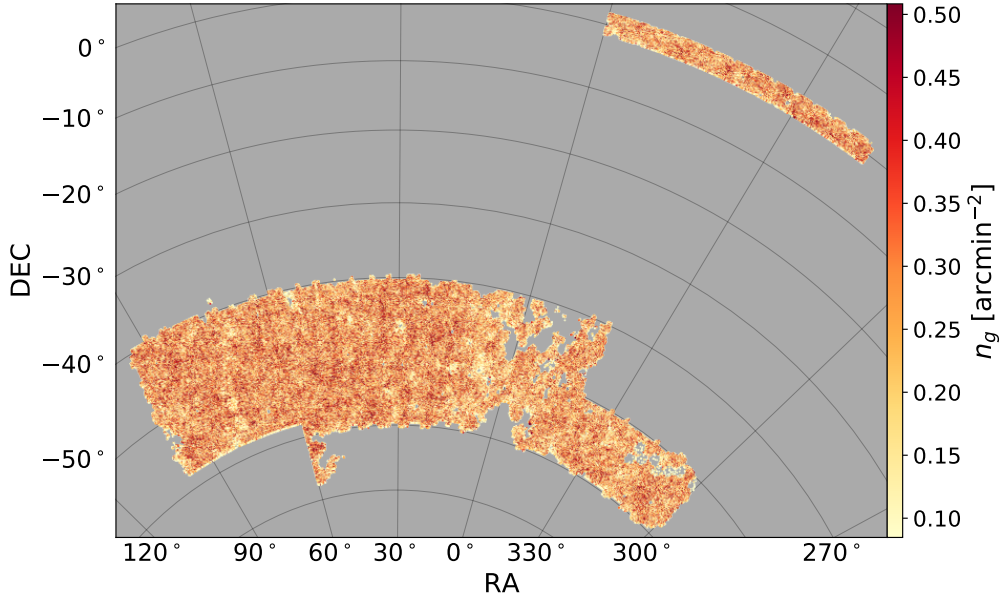


Figure 5.1: Angular distribution and projected density of the DES-Y1 BAO galaxy sample (Fig. 1 in Crocce et al., 2019). DES-Y1 observations cover two compact sky regions: one in the southern hemisphere covering 1203 deg^2 overlapping South Pole Telescope observations (SPT, Carlstrom et al., 2011), and one near the Equator with 115 deg^2 overlapping the *Stripe 82* (S82, Annis et al., 2014). The DES-Y1 BAO sample contains about 1.3 million galaxies with photometric redshifts in the range $[0.6 - 1.0]$ and constitutes the baseline for our DES Y1 BAO analysis.

z_{phot}	N_{gal}	\bar{z}
0.6 – 0.7	386057	0.652
0.7 – 0.8	353789	0.739
0.8 – 0.9	330959	0.844
0.9 – 1.0	229395	0.936

Table 5.1: Characteristics of the tomographic bins of DES-Y1 BAO sample used in the present work (Table 3 in Crocce et al., 2019) \bar{z} represents the mean redshift of the true-redshift distribution in tomographic bin, the *selection function*, Fig. 5.2. For further details on validation of this and other characteristics of the sample we refer the reader to (Crocce et al., 2019).

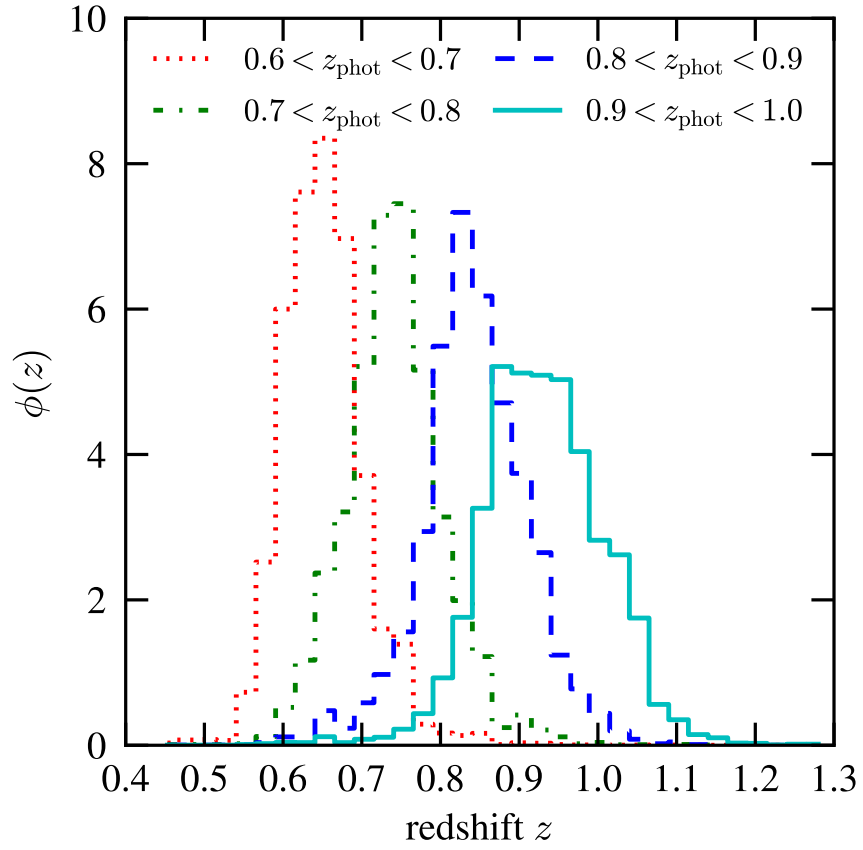


Figure 5.2: Redshift selection function $\phi(z) \propto dN/dz$ in the four photo- z bins considered in this work.

data (Crocce et al., 2016) and detailed for DES Y1 data clustering analysis in Elvin-Poole et al. (2018). The bottom line is that fluctuations in the number density of observed galaxies dependent on imaging quality are expected due to intrinsic limitations of observing pipeline. Such fluctuations can contaminate the galaxy field used for clustering analysis by imprinting the structure of certain survey properties resulting in a non-cosmological clustering signal. In order to account for that, maps of DES imaging properties were produced as described in Leistedt et al. (2016). From such maps, the set of survey properties that are correlated with fluctuations in the galaxy density field at a given significance is identified and used to produce a set of weights to be applied to the galaxy catalog built to correct for the contamination at the two-point function level. For the details on the definition and validation of the weight, we refer the reader to Elvin-Poole et al. (2018).

The DES Y1 BAO catalog was endorsed with systematic weights for three main survey properties: local stellar density, mean i -band PSF (FWHM) and detection limit (g -band depth) (Crocce et al., 2019). In the present work, we use these weights on top of the angular mask to generate our pixelized galaxy density field as described in § 5.2.1.

5.2.1 Pixelized map generation

Each redshift bin is pixelized using HEALPix (Gorski et al., 2005) at a resolution of $N_{\text{side}} = 1024$, with N_I galaxies in each pixel I . A pixelized angular mask described in Crocce et al. (2019) is used to find the density contrast maps. Each pixel in the mask comes with its fractional coverage which we denote w_I such that

$$\frac{\sum_I w_I}{N_{\text{pix}}} = f_{\text{sky}}, \quad (5.9)$$

where $N_{\text{pix}} = 12N_{\text{side}}^2$ is the total number of pixels for a given resolution and again f_{sky} is the survey sky fraction.

We degrade the mask resolution from $N_{\text{side}} = 4096$ to $N_{\text{side}} = 1024$ keeping the fractional coverage as an average of the smaller pixels contained in the large (smaller resolution) pixel. The number density of galaxies n_I in each pixel inside the footprint is computed as:

$$n_I = \frac{N_I}{w_I \Omega}, \quad (5.10)$$

where Ω is the (common) area of one pixel. The average number density of galaxies is

$$\bar{n} = \frac{\sum_I N_I}{(\sum_I w_I) \Omega}, \quad (5.11)$$

and finally the density contrast δ_I in each pixel is given by:

$$\delta_I = \frac{n_I}{\bar{n}} - 1. \quad (5.12)$$

These maps generated for each redshift bin are used to measure the APS as explained in § 5.4.

5.3 DES mock simulations

In addition to the DES Y1 galaxy catalog, we use a set of 1800 mock galaxy simulations, specially made for studies of large-scale structure in DES, including the present BAO analysis (Avila et al., 2017).

These mocks serve a dual purpose in our study. First, we use them to test our codes for estimating C_ℓ 's, covariances and the BAO feature extraction in a DES-like survey. Second, we make direct use of the covariance matrices estimated from them in the BAO analysis of the DES Y1 data.

These simulations match all aspects of the DES Y1 data, including its footprint, abundance, and clustering of galaxies and redshift distribution. One starts with halo catalogs that are constructed with the HALOGEN method (Avila et al., 2015), such that they satisfy halo mass-functions and bias appropriately from N-body simulations. Next, galaxies are assigned to these halos according to a hybrid Halo Occupation Distribution (HOD)/Halo Abundance Matching (HAM) prescription. The methodology is much faster than using full N-body simulations and allows for the construction of thousands of simulations. These mock catalogs were constructed using the MICE Grand Challenge N-body simulations (Crocce et al., 2010; Fosalba et al., 2015b; Crocce et al., 2015; Fosalba et al., 2015a), with cosmological parameters close but not equal to those of the Planck mission. We refer the reader to Avila et al. (2017) for details of the construction of these DES galaxy mocks.

5.4 Angular power spectrum measurement in cut sky

For data collected over the whole sky, an unbiased estimator of the APS is simply the average of the $a_{\ell m}$ coefficients over all m values (Hivon et al., 2002):

$$\hat{C}_\ell = \frac{1}{2\ell + 1} \sum_{m=-\ell}^{m=\ell} |a_{\ell m}|^2. \quad (5.13)$$

When performing full-sky estimations, we compute the coefficients $a_{\ell m}$ from the pixelized density contrast maps using the `anafast` routine within HEALPIX.

As the DES measurements are not made over the full-sky, the previous estimator is not appropriate, since spherical harmonics no longer provide a complete orthonormal basis to expand angular overdensities. In this case, we use the so-called pseudo- C_ℓ method to relate the APS measured in a masked sky \hat{C}_ℓ to the “true” APS C_ℓ (Hivon et al., 2002). The pseudo- C_ℓ estimator relies on the assumption:

$$\langle \hat{C}_\ell(\tilde{\delta}_{\text{gal}}(\hat{\mathbf{n}})) \rangle = \sum_{\ell'} \mathcal{M}_{\ell\ell'} C_{\ell'}(\delta_{\text{gal}}(\hat{\mathbf{n}})), \quad (5.14)$$

where \mathcal{M} is called the coupling matrix. In the equation above the masked density contrast field $\tilde{\delta}_{\text{gal}}$ is related to the full-sky one δ_{gal} by a mask function M :

$$\tilde{\delta}_{\text{gal}}(\hat{\mathbf{n}}) = M(\hat{\mathbf{n}})\delta_{\text{gal}}(\hat{\mathbf{n}}). \quad (5.15)$$

It can be shown that the coupling matrix in terms of Wigner $3 - j$ symbols is given by:

$$\mathcal{M}_{\ell_1\ell_2} = (2\ell_2 + 1) \sum_{\ell_3} \frac{2\ell_3 + 1}{4\pi} C_{\ell_3}(M) \begin{pmatrix} \ell_1 & \ell_2 & \ell_3 \\ 0 & 0 & 0 \end{pmatrix}^2, \quad (5.16)$$

where $C_\ell(M)$ is the angular power spectrum of the pixelized mask. Notice that for full sky measurements, $\mathcal{M}_{\ell\ell'}$ is simply the identity matrix, and in general, it carries information about the survey geometry and mask. The true C_ℓ can then be estimated from the pseudo- C_ℓ by solving the linear system defined by Eq. (5.14).

We use two independent codes to measure C_ℓ 's via the pseudo- C_ℓ method without shot-noise subtraction. The first code is our own implementation of the pseudo- C_ℓ method in python. The second is the publicly available code `NaMaster`¹, which is implemented in C. We compared the C_ℓ 's estimated from the two codes when applied to a single DES mock simulation. The two codes agree at better than 5% for all ℓ values considered here, and better than 1% for $\ell > 100$, indicating our measurements are robust. All results presented in the remainder of this chapter will make use only of the `NaMaster` code.

We consider in our default analysis multipoles in the range $30 < \ell < 330$, corresponding roughly to the angular scales used in the $w(\theta)$ analysis (Chan et al., 2018), and we then bin using a bin width of $\Delta\ell = 15$ in order to

¹<https://github.com/damonge/NaMaster>

make the reduced covariance matrix more diagonal and amenable to algebraic manipulations. Effects of different ranges and binnings will be studied as robustness tests in § 5.5.4.

Finally, the covariance matrix is estimated from the $N_m = 1800$ mocks as:

$$\text{Cov}[\text{APS}]_{\ell\ell'}^{ij} = \frac{1}{N_m - 1} \sum_{k=1}^{N_m} \left(C_\ell^{i(k)} - \bar{C}_\ell^i \right) \left(C_{\ell'}^{j(k)} - \bar{C}_{\ell'}^j \right), \quad (5.17)$$

where the average \bar{C}_ℓ^i at photo- z bin i is given by

$$\bar{C}_\ell^i = \frac{1}{N_m} \sum_{k=1}^{N_m} C_\ell^{i(k)}. \quad (5.18)$$

5.5 Tests of methodology on mocks

We now apply our full methodology on the 1800 DES Y1 HALOGEN mock simulations with known cosmology and perform robustness tests to estimate the impact of changing our default settings on parameter estimation.

5.5.1 Measurements of the APS

In Fig. 5.3 we show the results of our C_ℓ measurements in the four photo- z bins for 1800 mocks together with the mean of the mocks. We also show theoretical predictions from C_ℓ 's computed with a linear matter spectrum at the same cosmology as the mocks. In each photo- z bin, we multiply the theoretical matter C_ℓ 's by a galaxy bias factor squared determined by Avila et al. (2017) and add a shot-noise determined by the number density of Y1 galaxies in that photo- z bin.

The measured C_ℓ 's from the mocks are in good agreement with the theoretical prediction. However, when compared to data there is some discrepancy in the second and third redshift bins, reflected in the somewhat high value of $\chi^2 = 1.92$ and 1.57 respectively. In these bins, the C_ℓ 's from data exceed the ones from the mocks at large ℓ 's. We will discuss some consequences of this behaviour below.

5.5.2 Covariance matrix

In order to quantify the correlation between bandpowers in our analysis, we show the correlation matrix,

$$\text{Corr}_{ab} = \frac{\text{Cov}_{ab}}{\sqrt{\text{Var}_{aa} \times \text{Var}_{bb}}}, \quad (5.19)$$

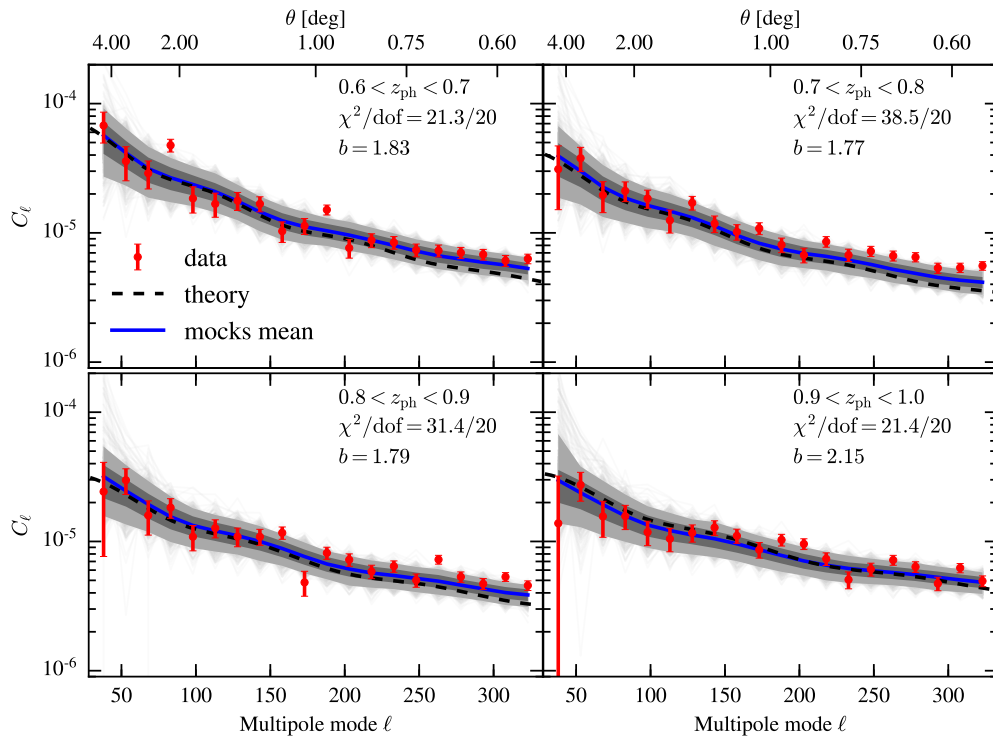


Figure 5.3: Measurements of C_ℓ in four photo- z bins for the 1800 mocks (gray lines) and the Y1 data (red circles). The dashed line shows the theoretical prediction from a linear spectrum with MICE cosmology multiplied by a bias factor (shown in the panels) and including shot-noise and shaded regions show 68% and 95% C.L. from mocks measurements. The blue line is the average of the mocks. The χ^2 values show reasonable agreement between average measurements of the mocks and measurements on data.

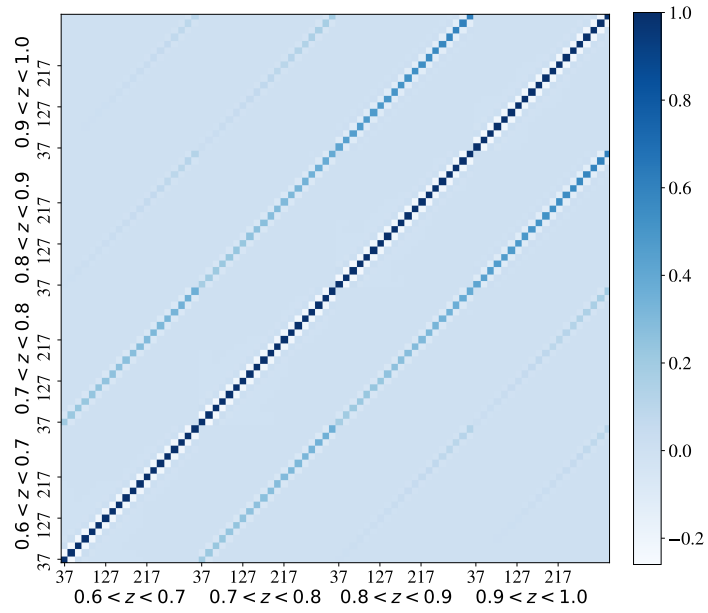
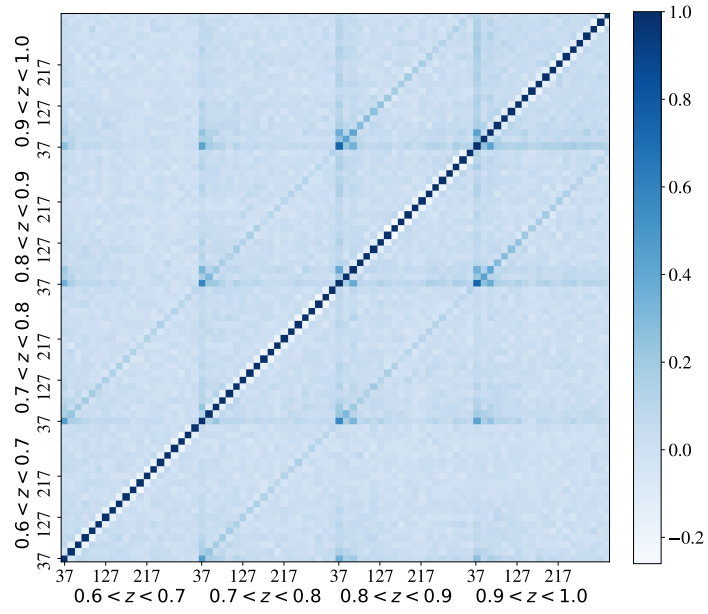


Figure 5.4: C_ℓ 's correlation matrix for the 4 photo- z bins. (*Top*): measured from the 1800 mock simulations mimicking the DES Y1 data. (*Bottom*): Theoretical estimation computed at the mock cosmology, accounting for binning and mask effects.

where the a, b indexes label bandpowers, as measured from the mocks in the top panel of Fig. 5.4 for the four redshift bins and using our fiducial $\Delta\ell = 15$ binning. We see it is close to block-diagonal with structure similar to the one found in Chan et al. (2018) for the covariance matrix for $w(\theta)$. The bottom panel of Fig. 5.4 shows the theoretical estimation for the covariance computed at the mock cosmology, using the mock bias, adding the data shot-noise and correcting for binning and mask effects (Efstathiou, 2004). The theoretical covariance is much less noisy, as expected.

In Fig. 5.5, we compare the diagonal errors of the C_ℓ 's estimated from the mock simulations and the Gaussian prediction of the fiducial cosmology using two approximations: the naive f_{sky} approximation Eq. (5.5) and the prediction of the covariance matrix of the pseudo- C_ℓ estimator (Efstathiou, 2004; Brown et al., 2005). We find good agreement between the errors coming from the simulation covariance matrix and from the pseudo- C_ℓ estimator. However, for the f_{sky} approximation we find that a ‘‘boost factor’’ of 1.35 is necessary to match the measured errors. This was also the case for a similar analysis in SDSS (Ho et al., 2012).

We will use the full covariance matrix estimated from the mocks. It is well known that statistical noise on the estimation of the covariance matrix from mock realizations translates into a bias on its inverse, the precision matrix, which is the actual fundamental piece on the likelihood estimation. We included this correction factor in our analysis (Hartlap et al., 2007; Dodelson & Schneider, 2013; Percival et al., 2014). Given the number of mocks used, we have checked that the correction factor for the precision matrix is always less than 5%, having no impact on the recovered value of α .

5.5.3 Parameter estimation

We use two independent methods for the parameter estimation: a Markov Chain Monte Carlo (MCMC) implemented with `emcee` (Foreman-Mackey et al., 2013) and a maximum likelihood estimator (MLE) with analytical least square fit of the nuisance parameters (Cowan, 1998). We used our default BAO template described in § 5.1.1 with the covariance matrix estimated from the mocks. We performed a joint fit for the 4 photo- z bins with 17 parameters in our default template.

In Fig. 5.6 we show the distribution of α values resulting from fits of our C_ℓ measurements in four photo- z bins for the 1800 mocks. The remaining 16 parameters are marginalized over for the MCMC analysis and fixed to the values that maximize the likelihood for the MLE analysis as described in Chan et al. (2018). For the MLE method we find the best fit analytically over the 12 parameters A_0, A_1, A_2 in each redshift bin and numerically over

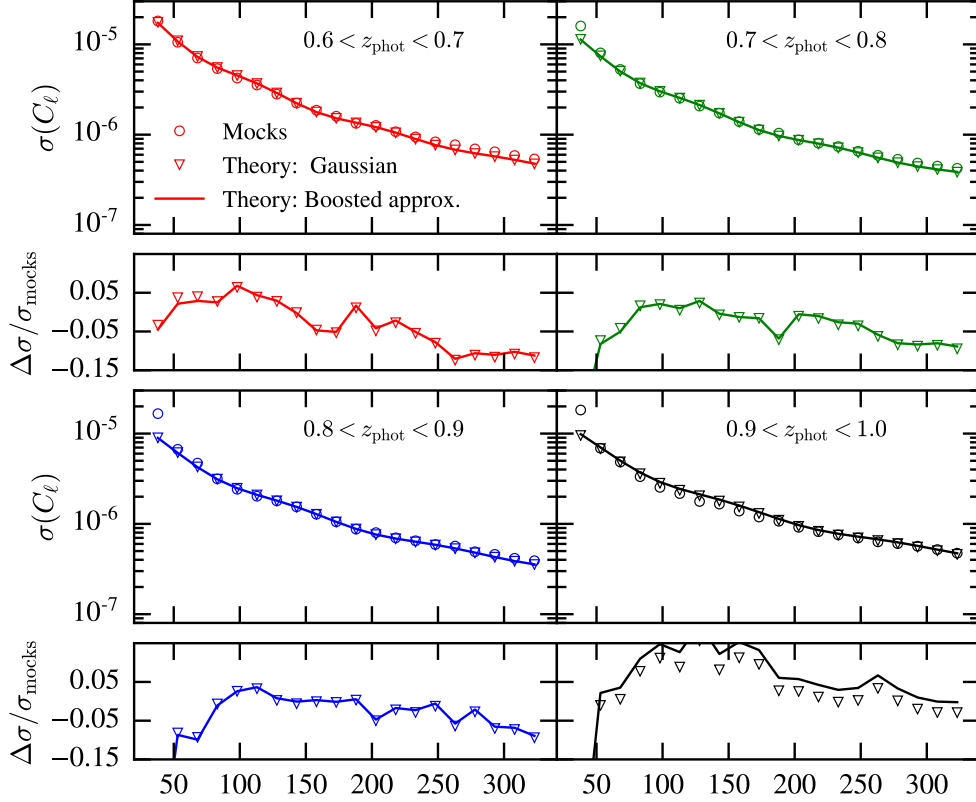


Figure 5.5: Comparison of the C_ℓ 's diagonal errors in 4 photo- z bins. For each bin, the top panel shows the standard deviation estimated from the 1800 DES mock simulations (open circles) the Gaussian prediction on the fiducial cosmology (solid lines) after rescaled by an empirical boost factor of 1.35 and the Gaussian prediction from the pseudo- C_ℓ method (open triangles). The bottom panels show the relative differences with respect to the mocks standard deviation.

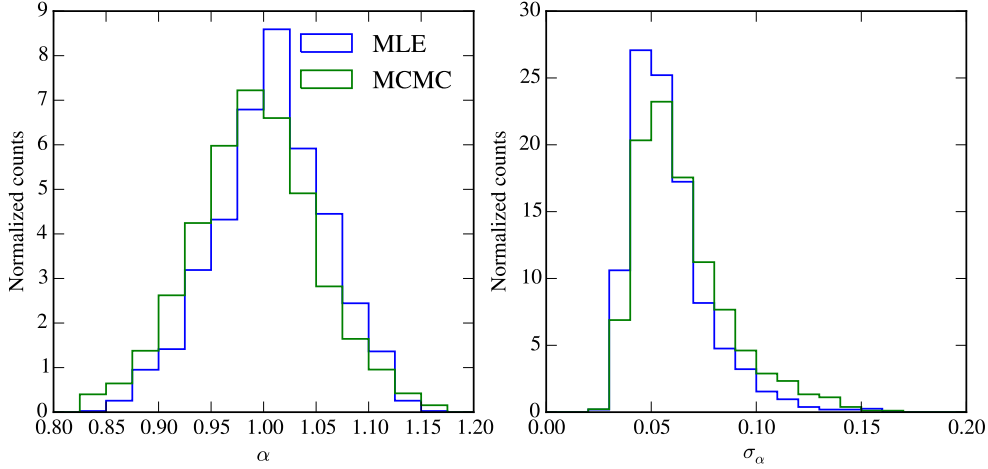


Figure 5.6: (*Left*): distribution of the recovered α for the detected mocks. (*Right*): distribution of the estimated error on α . Results from different methods are presented.

the 4 B_0 's requiring $B_0 > 0$ for each value of α , following Chan et al. (2018).

For the MCMC we used the flat priors $\alpha \in [0.8, 1.2]$, $A_1 \in [-800, 800] \times 10^{10}$, $A_2 \in [-50, 50] \times 10^6$, $A_3 \in [-200, 200] \times 10^3$ and $B_0 \in (0, 6]$.

We exclude outliers defined as mocks whose 1σ values for α lie outside the range $0.8 < \alpha < 1.2$ (see Chan et al. (2018)) using the MLE method. For our fiducial analysis, 86.4% of the mocks are kept.

Since our fiducial model has the same cosmology as the mocks, we expect to find $\alpha = 1$. In fact we find that the mean value in the mocks is $\bar{\alpha} = 1.006$ for MLE and $\bar{\alpha} = 0.992$ for MCMC. Therefore both our methods recover α with bias at the sub-percent level.

In Fig. 5.7 we show the results from the MCMC chains when fitting the BAO template to the averaged C_ℓ measured in the mock simulations for our fiducial template. In this case, we find for the shift parameter $\alpha = 0.988 \pm 0.060$ and it can be seen that it does not show strong correlations with the *nuisance* parameters. In fact, the *nuisance* parameters are poorly constrained, having broad distributions. The best-fit values for B_0 and A_0 are found to be roughly consistent with the squared bias and the shot-noise in each bin, respectively. Moreover, they present intrinsic degeneracies. For the MLE method, we find $\alpha = 1.009 \pm 0.056$ from a fit to the average of the mocks.

It is important to recall from the discussion in § 2.4.8 the primary goal of the template fitting technique for BAO feature extraction is the determina-

tion of α . First, the poor constraints on nuisance parameters do not affect the recovering of α as it shows to be robust over a wide range of choices for the broadband terms shape (see Table 5.2) and second, it is not observed any clear degeneracy of nuisance parameters with α . This indicates robustness for the BAO feature detection from APS measurements. Such robustness will be discussed in details on § 5.5.4.

In Fig. 5.8 we show C_ℓ 's measured in four photo- z bins for the DES mock simulations. The errors are computed from the mock covariance matrix. The solid line displays the best-fit theoretical prediction using the BAO template described in § 5.1.1. We see that our BAO template is able to accurately capture the behaviour of the C_ℓ 's from the mocks.

The compatibility between the two independent methods (MCMC and MLE) is shown in Fig. 5.9 where we plot the normalized likelihood for the α parameter determined from the average of the mocks for both methods.

In Fig. 5.10 we show the distribution of χ^2 for the 1800 mocks demonstrating the good fit of our template. Also shown in the plot as a dashed line is the χ^2 obtained from the data using the covariance matrix estimated from the mocks (discussed in § 5.6).

We estimate the significance of recovering α (or detecting the BAO feature) by measuring the difference in χ^2 as a function of α between a model with no BAO feature (a no-wiggle model), which is independent of α , and our BAO template. In Fig. 5.11 we show $\Delta\chi^2 = \chi^2(\alpha) - \chi^2_{\min}$ for fits of the average C_ℓ 's from the mocks as a function of the α parameter. The best-fit value is $\alpha_{\min} = 1.009$. From Fig. 5.11 we see that for the average of the mocks a BAO signal would be detected at 2.3σ with respect to a no-wiggle model.

We will use the methods described in this section to study the BAO signal in Y1 data. However, before doing so, we use the mocks to perform some robustness tests related to choices made in our analysis.

5.5.4 Robustness tests

The bottom line of BAO detection (see discussion in § 2.4.8) is that the recovered likelihood for α should be robust under different prescriptions for the *nuisance* parameters determining the corrections to the linear template in Eq. (2.185), i.e., the broad-band shape functions, $A(x), B(x)$. In other words, all the information for the BAO feature is well contained in the linear model for the two-point correlation, in our case here, the APS.

For our default analysis above, a number of choices were made: the binning of harmonics in $\Delta\ell = 15$, adopting $\ell_{\min} = 30$ and $\ell_{\max} = 330$, and the fiducial template used. We recall that we include linear RSD in the

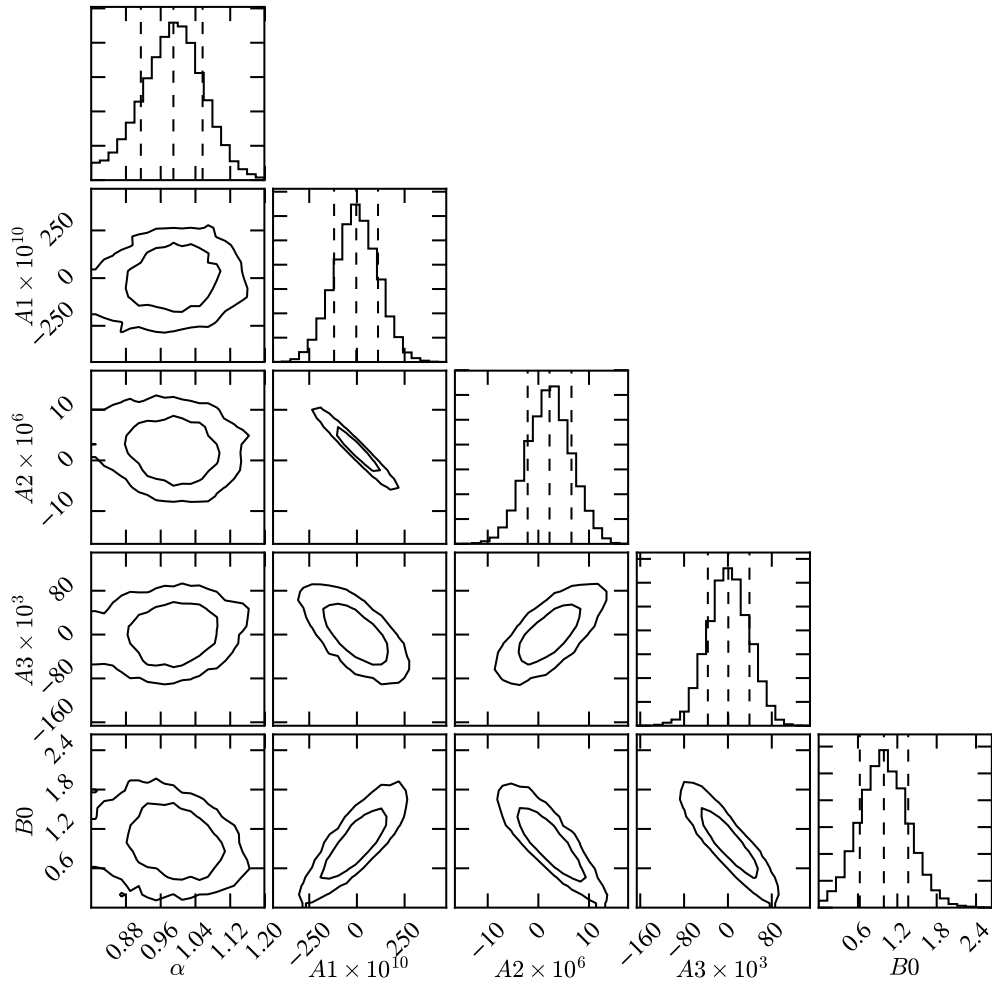


Figure 5.7: Fit results for α and template parameters B_0 , A_0 , A_1 and A_2 in the first photo- z bin for a BAO template fitted to the average of the 1800 DES mock simulations. The plots for the parameters in other bins are similar.

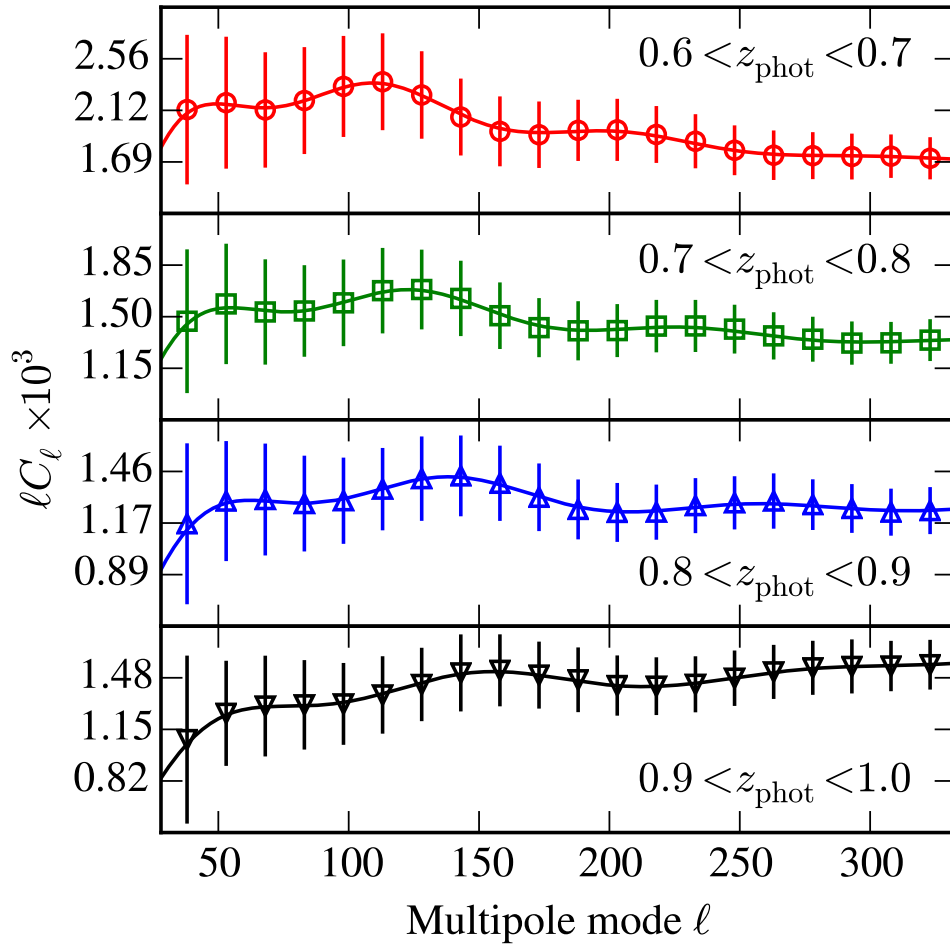


Figure 5.8: Measured C_ℓ 's from DES mock simulations in four photo- z bins. The points show the average C_ℓ 's from 1800 simulations, and the error bars represent the diagonal of the covariance matrix of these measurements. The line shows a theoretical prediction estimated at the simulation cosmology and best-fit template parameters.

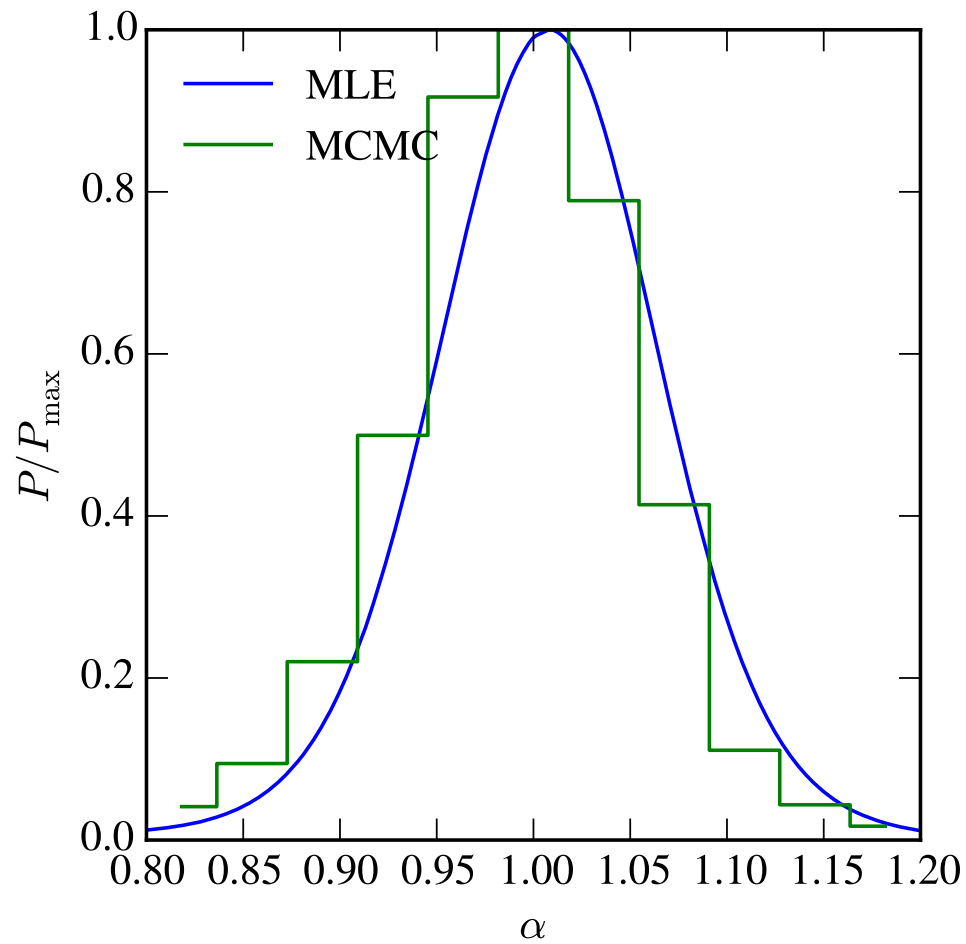


Figure 5.9: Normalized likelihoods from the MLE (solid line) and MCMC (histogram) methods for the α parameter determined from the average of the mock C_ℓ 's.

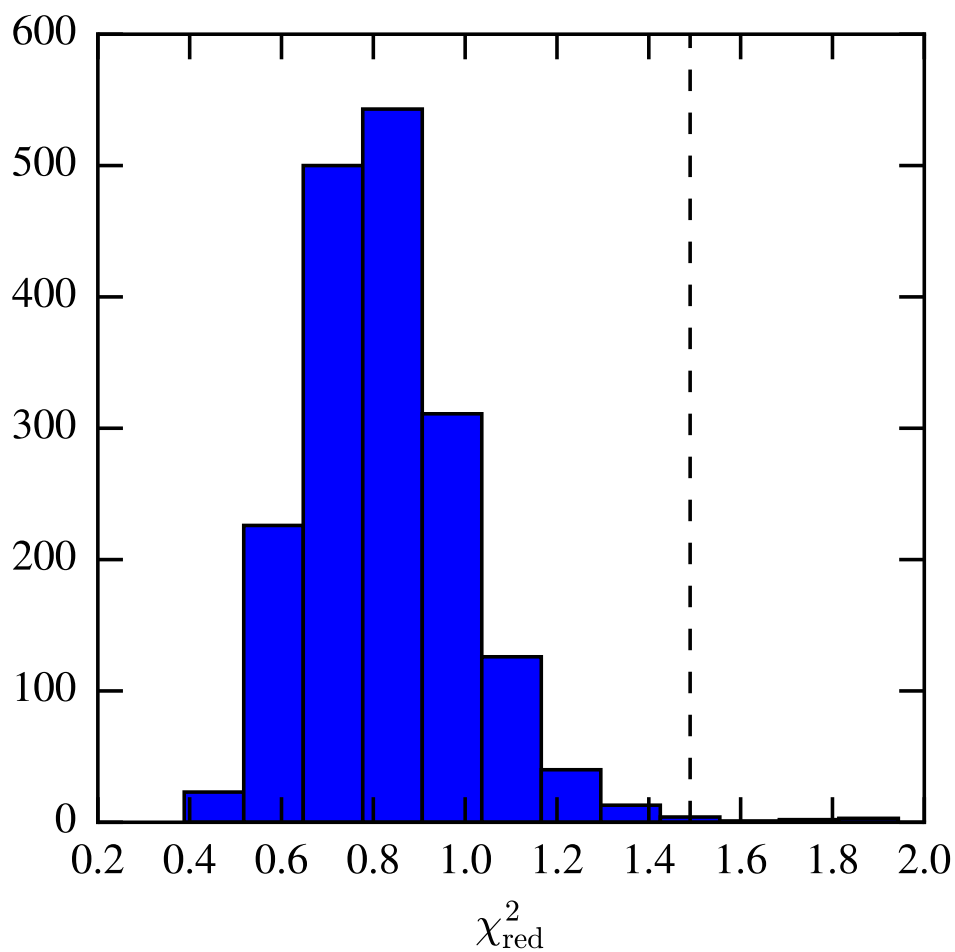


Figure 5.10: Distribution of the reduced χ^2 values for the 1800 mocks. The dashed line shows the value of χ^2 obtained from the data using the covariance matrix estimated from the mocks (§ 5.6).

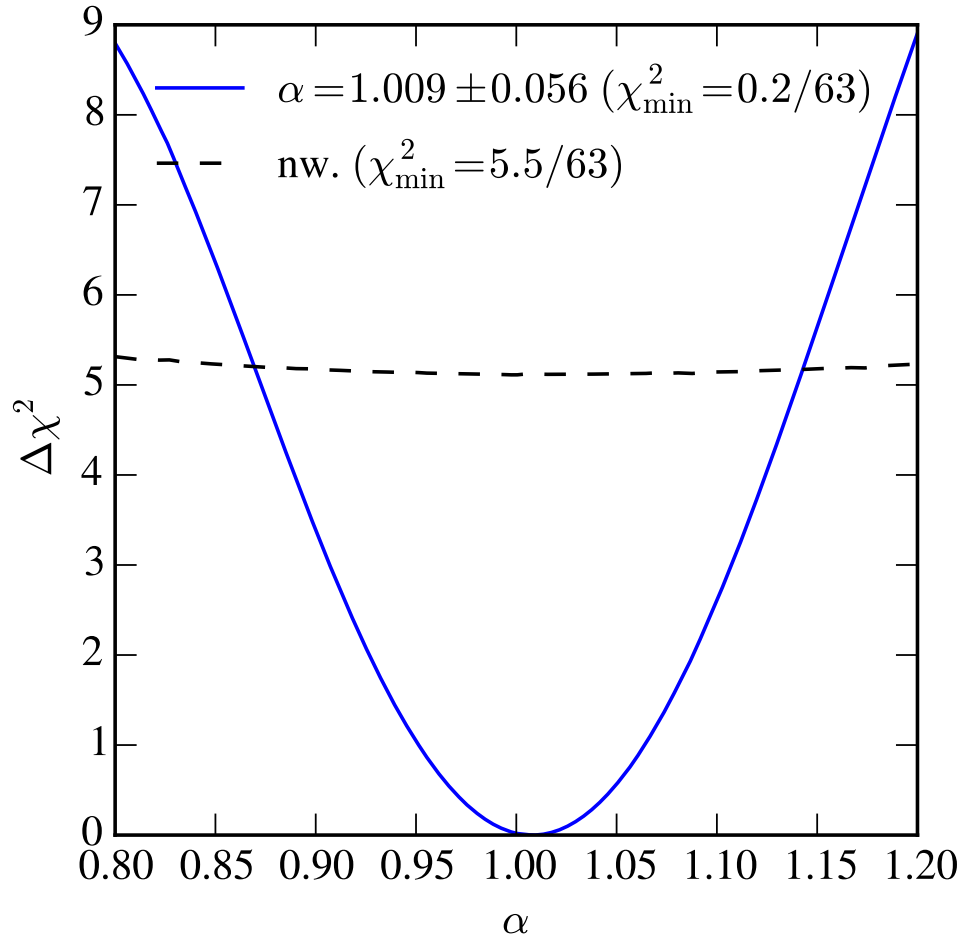


Figure 5.11: $\Delta\chi^2 = \chi^2(\alpha) - \chi^2_{\min}$ as a function of α for the BAO template fitted on the mean of mocks. For each value of α we subtract from χ^2 the value of $\chi^2_{\min} = \chi^2(\alpha_{\min})$. Dashed line is the approximately constant χ^2 for the non-wiggle template subtracted from the minimum of the template.

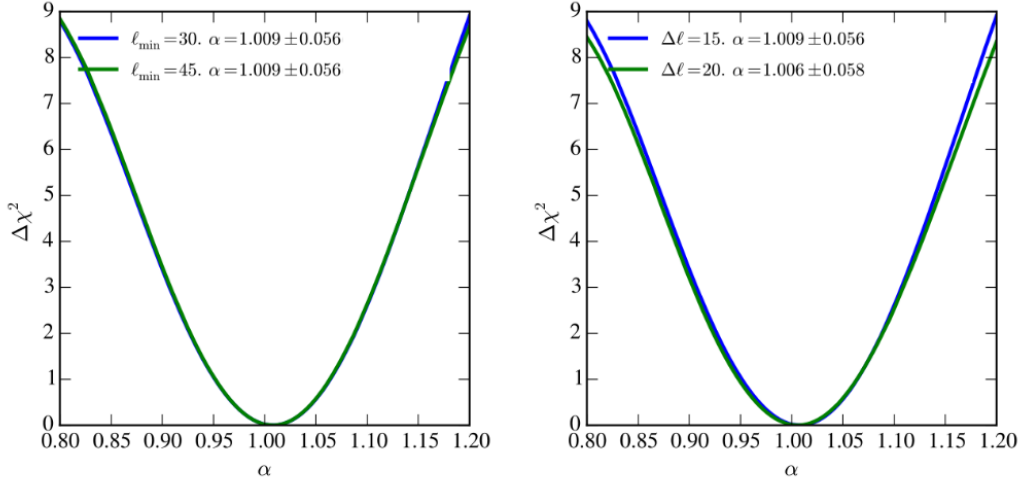


Figure 5.12: $\Delta\chi^2$ profile for different band-widths on the binning schemes, keeping the range of multipoles fixed $\ell \in [30, 330]$. Different choices of $\Delta\ell$ produce very similar results for the dilation parameter.

modelling and we are using the full covariance matrix with redshift bin cross-correlations. We have examined the impact on the parameter estimation and on the fraction of detection of the mocks (the fraction of mocks remaining when excluding outliers) for some other choices. Fig. 5.12 shows the impact of choosing different sizes for the bandwidth for measurements on the recovered χ^2 profiles for the dilation parameter. A summary of some of our tests is shown in Table 5.2, for choices of binning and range of ℓ as well as C_ℓ templates. We conclude that our choice of the template gives an unbiased result for α at the percent level and a reasonable detection fraction. Although different choices produce small changes in the fits, they do not affect the BAO detection significantly, showing that our analysis is robust.

In addition to the tests in Table 5.2, we have also investigated other choices made. Let us elaborate about them below.

From the model to the linear APS at the heart of BAO fitting, we investigate the impact of using the Limber approximation, Eq. (2.141), instead of the full integral calculation in Eqs. (5.1) and (2.137) without taking into account RSD effects, and also fully taking them into account using Eq. (2.158) and Eq. (5.3). The impact of such approximations was discussed in § 2.4.5 and around Fig. 2.4. Recall the Limber approximation, § 2.4.3, is valid only for small scales and underestimate the real clustering amplitude on large scales, low- ℓ s. On the other hand, RSD corrects for the enhancement in clustering predicted by the Kaiser effect and impacts only large scales,

case	$\langle\alpha\rangle$	$\langle\sigma\rangle$	S_α	$f(N_{\text{det}})$	mean of mocks
$\Delta\ell = 15, 30 < \ell < 330 :$					
$A_0 + A_1\ell + A_2\ell^{-1}$	1.003	0.051	0.058	0.752	1.008 ± 0.056
$A_0 + A_1\ell + A_2\ell^{-2}$	1.007	0.058	0.053	0.864	1.009 ± 0.056
$A_0 + A_1\ell + A_2\ell^2$	1.011	0.056	0.055	0.851	1.013 ± 0.056
$\Delta\ell = 20, 40 < \ell < 300 :$					
$A_0 + A_1\ell + A_2\ell^{-1}$	1.003	0.051	0.060	0.734	1.006 ± 0.058
$A_0 + A_1\ell + A_2\ell^{-2}$	1.006	0.059	0.056	0.812	1.006 ± 0.058
$A_0 + A_1\ell + A_2\ell^2$	1.009	0.057	0.057	0.790	1.012 ± 0.057
$\Delta\ell = 15, 45 < \ell < 330 :$					
$A_0 + A_1\ell + A_2\ell^{-1}$	1.004	0.050	0.059	0.736	1.009 ± 0.056
$A_0 + A_1\ell + A_2\ell^{-2}$	1.007	0.057	0.054	0.841	1.009 ± 0.056
$A_0 + A_1\ell + A_2\ell^2$	1.011	0.056	0.055	0.839	1.013 ± 0.056
$\Delta\ell = 20, 40 < \ell < 320 :$					
$A_0 + A_1\ell + A_2\ell^{-1}$	1.004	0.050	0.060	0.731	1.008 ± 0.056
$A_0 + A_1\ell + A_2\ell^{-2}$	1.007	0.058	0.055	0.833	1.008 ± 0.057
$A_0 + A_1\ell + A_2\ell^2$	1.011	0.056	0.057	0.831	1.014 ± 0.057

Table 5.2: Summary of the robustness tests performed on the 1800 mocks using MLE. We show the average values of α and its 1σ standard deviation for all the mocks, the standard deviation of α obtained only for the detected mocks S_α and the fraction of detected mocks. The fiducial case we adopt has a template $A_0 + A_1\ell + A_2\ell^{-2}$ and $\Delta\ell = 15, 30 < \ell < 330$ shown in boldface.

low- ℓ s. So both affect large scales in opposite directions, see Fig. 2.4. We highlight that all predictions mentioned were computed using the FFTLog algorithm (see Appendix E).

Fig. 5.13 shows the impact of the different assumptions below on the determination of the BAO feature. It indicates that the choice for the fiducial range in ℓ in combination with the signal to noise for the measurements leaves the determination of α insensitive to subtleties at large scales, where no-RSD and Limber approximations should break down. However, the use of FFTLog algorithm leaves the computation times for all of the cases almost equal, so we choose for our analysis to work with the full computation including RSD's.

Exclusion of cross-correlations between photo- z bins in the covariance matrix was also tested in real and harmonic space showing no impact on the recovered likelihood for α . Contributions from cross-correlations are nothing but the nondiagonal blocks of the covariance matrix as depicted in Fig. 5.5. Fig. 5.14 shows how the recovered likelihood for α is insensitive to the contribution of such cross-correlations to the covariance matrix.

5.6 BAO in DES Y1 data

We now apply the methods described and tested above to study the BAO feature in the angular power spectrum in the DES Y1 data. In Fig. 5.15 we show C_ℓ 's measured in four photo- z bins for the DES Y1 data. The errors are computed from the variance of the 1800 mock simulations. The solid line displays the best-fit theoretical prediction using the BAO template described in § 5.1.

In Fig. 5.16 we show the $\Delta\chi^2 = \chi^2(\alpha) - \chi_{\min}^2$ of the fits as a function of α for the DES Y1 data from the MLE described above and also used in Chan et al. (2018). We find $\alpha = 1.023 \pm 0.047$ with $\chi_{\min}^2/\text{dof} = 93.7/63 = 1.49$. This somewhat large value of χ^2 seems to indicate that the covariance matrix obtained from the mocks may underestimate the errors. We will discuss this possibility below.

The small deviation of α from unity can be traced to the fact that the template cosmology has been fixed to reflect that of the mock simulations (to be consistent with the fact that we also use the covariance from the mock simulations). The mocks have a cosmology slightly different from, e.g., the Planck cosmology, and the latter has been shown to be consistent with clustering measurements of the DES Y1 data (Gruen et al., 2018; Abbott et al., 2018). A difference of a few percents in α from unity is expected and is also found in a similar analysis in configuration space (Chan et al., 2018; Ab-

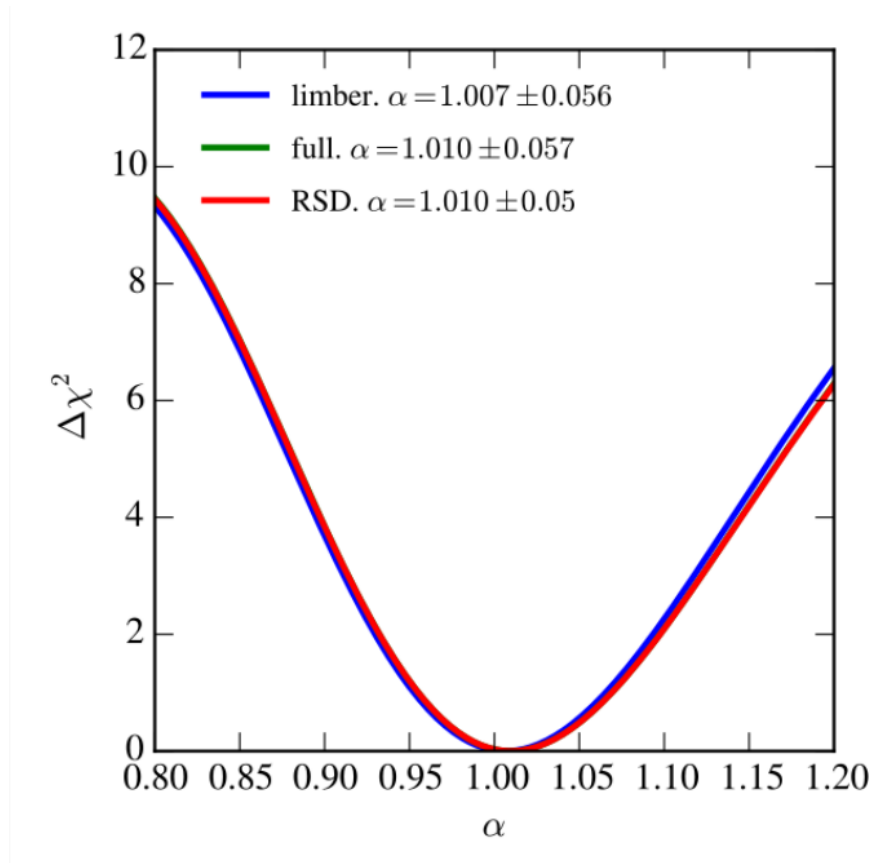


Figure 5.13: χ^2 profiles for different assumptions for linear prediction of the APS. Blue line, *limber*: Limber approximation Eq. (2.141), green line, *full*: full computation (non-Limber) discarding RSDs, Eqs. (5.1) and 2.137, and red line, *RSD*: full computation (non-Limber) taking into account linear RSDs. The different recovered profiles show no dependence on the recovered likelihood for α .

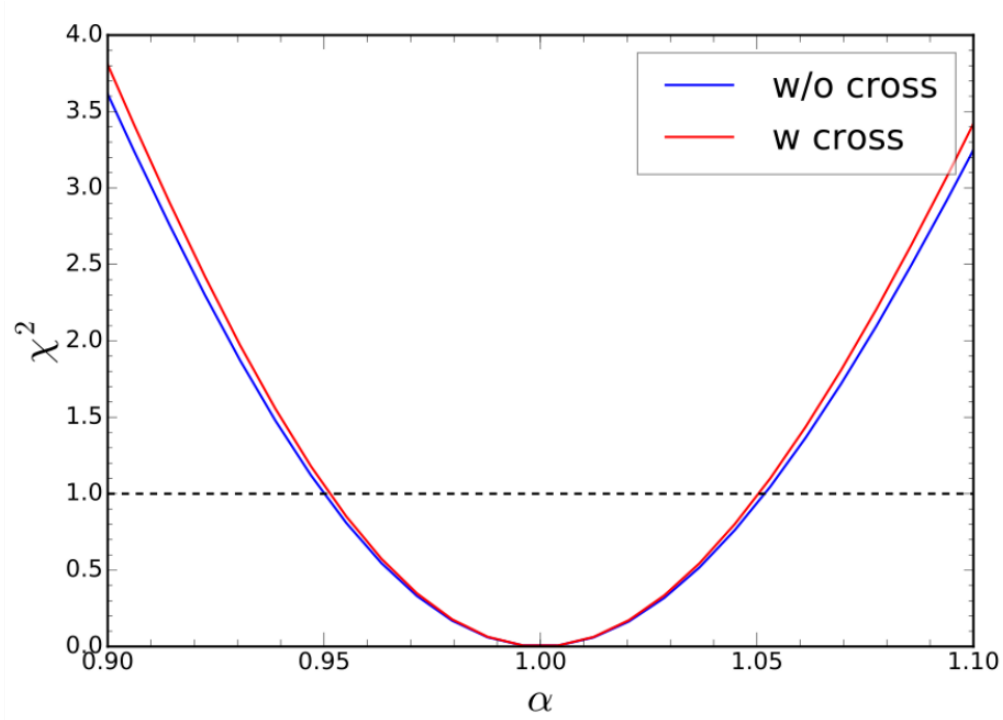


Figure 5.14: χ^2 profile as determined from the angular correlation function analysis (Chan et al., 2018, Fig. 12) for the constraint on α for the case of considering cross-correlations between different tomographic bins in the covariance matrix (red line) and without considering them (blue line). The recovery of BAO feature is insensitive to the cross-correlation impact on the covariance matrix.

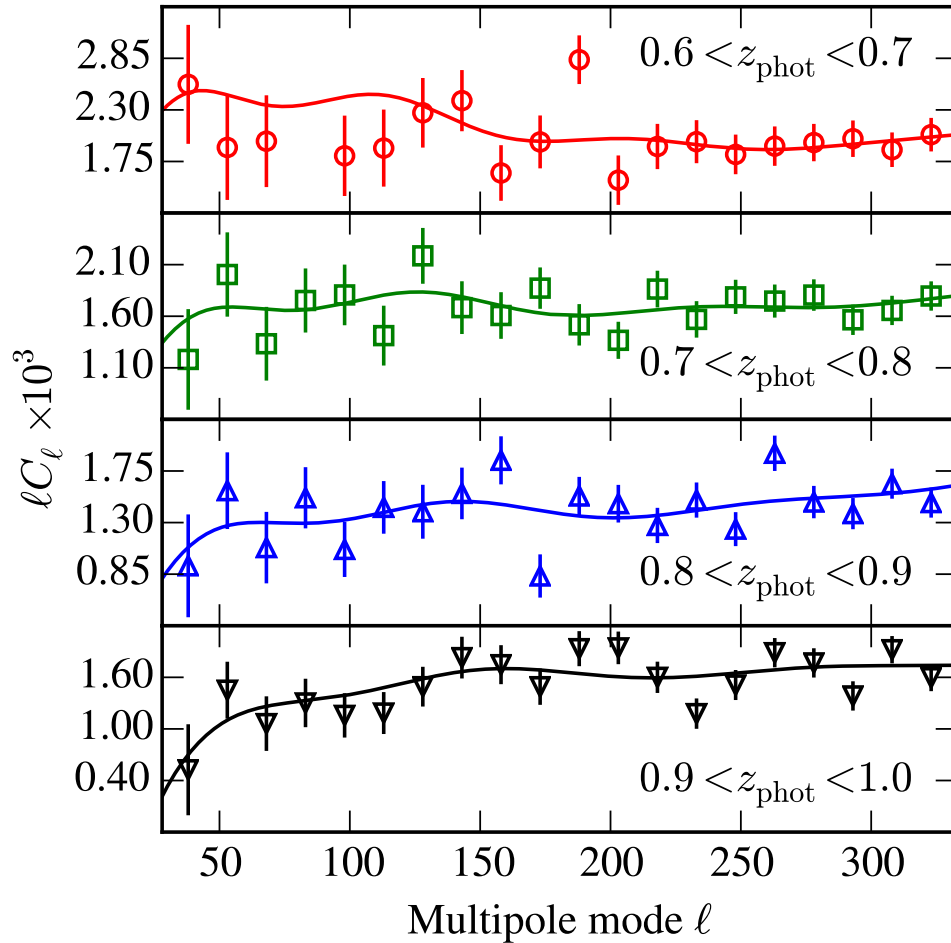


Figure 5.15: Measured C_ℓ 's from DES Y1 data in four photo- z bins. The errors represent the diagonal of the covariance of 1800 mock simulations. The line shows our best fits from the fiducial analysis.

bott et al., 2019). We have repeated our analysis with the covariance matrix re-calculated at the best fit cosmology and we have not found significant changes in our results, which was also the case for Abbott et al. (2019).

Finally, we also show the difference in χ^2 from our best-fit template and a no-wiggle model. Assuming Gaussian statistics for the likelihood, we find that the angular power spectrum measured from DES Y1 data finds the BAO feature at a significance of 2.6σ level with respect to a no-wiggle template.

In order to address the issue of the large value of χ^2 obtained above we study the changes that arise from using a theoretical covariance matrix better adjusted to the data. We use a power spectrum predicted by `Halofit` (Takahashi et al., 2012) with MICE cosmological parameters, supplemented by the galaxy bias and shot-noise measured on the Halogen mocks and taking into account linear redshift space distortions. In the resulting angular power spectrum, we added a term proportional to ℓ with a coefficient that was allowed to vary for each redshift bin. These 4 coefficients were fitted using the DES Y1 data. This theoretical C_ℓ was then inputted into `NaMaster` to compute a new Gaussian covariance matrix that accounts for the Y1 mask and the binning in ℓ . When this new covariance matrix is used the minimum χ^2 is indeed reduced to $\chi_{\min}^2/\text{dof} = 85.8/63 = 1.36$ without a significant change in the estimated value of α , which is found to be $\alpha = 1.039 \pm 0.053$ in this case.

In Fig. 5.17 we show the result of the significance using this new theoretical covariance matrix. The value of α changed by a third of the standard deviation and the error increased by 13%. Although the changes are small, they point to the uncertainties inherent in this analysis.

We also studied the impact of the systematic errors following Crocce et al. (2019). We compute a χ^2 for the corrections induced by including the associated weights, $\chi_{\text{sys}}^2 = \Delta C_\ell^T \cdot \Psi \cdot \Delta C_\ell$, where $\Delta C_\ell = (C_\ell^{\text{weighted}} - C_\ell)$ and Ψ the precision matrix. The square root of this quantity offers an upper bound for the ‘‘number of σ ’s’’ that weights could bias the determination of any model parameter. For the fiducial scale-cuts of the analysis we find $\chi_{\text{sys}}^2 = 0.62, 0.24, 0.29$ and 0.95 respectively for each photo- z bin individually and $\chi_{\text{sys}}^2 = 0.43$. This implies that by considering each photo- z individually, an extreme case for the last bin appears in which if weights are not properly considered, results can be shifted by almost one σ . But by combining information on all bins, the impact is reduced to 0.66σ . We also perform the analysis without correcting by the weights, obtaining a fit $\alpha = 1.019 \pm 0.058$ with goodness-of-fit of $\chi^2 = 98/63$, with no apparent implication on the error estimation and goodness-of-fit, but leaving a shift in the dilation parameter of 0.085σ , well below the upper bound from χ_{sys}^2 . This can be understood

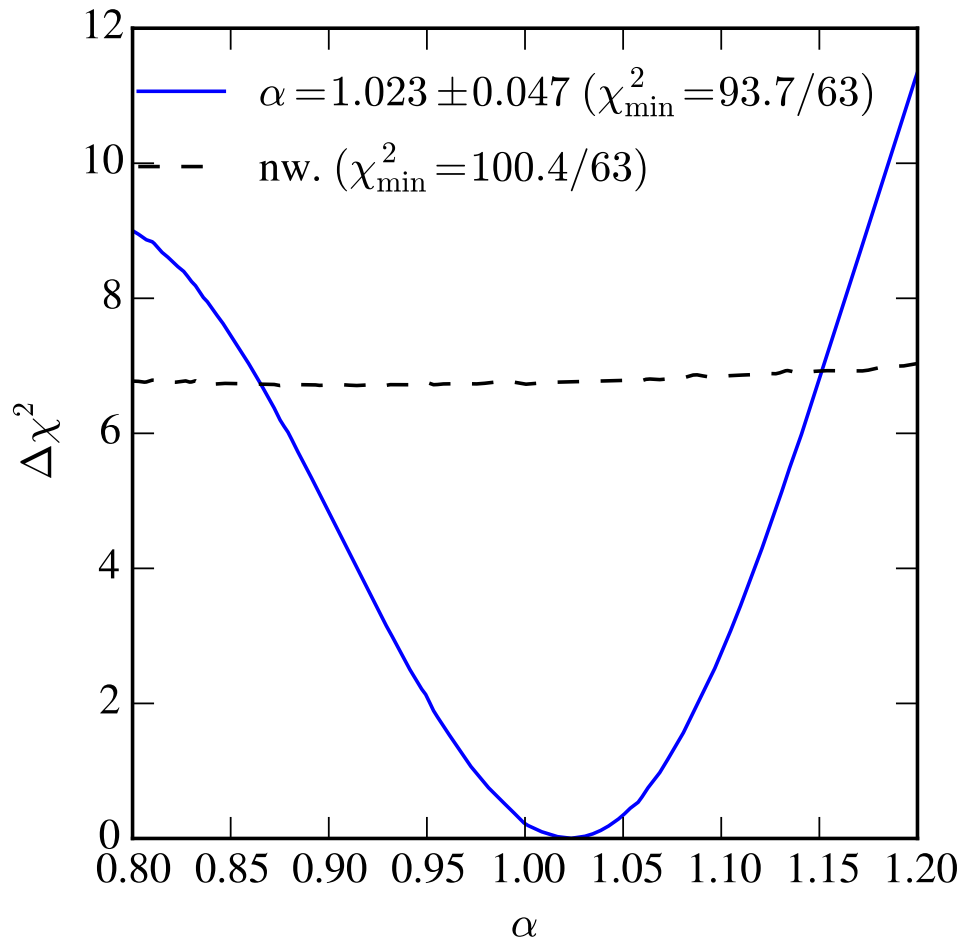


Figure 5.16: $\Delta\chi^2$ as a function of α for the DES Y1 galaxy data, when fitted to a BAO templates (solid blue curve) and to a no-wiggle template (dashed black curve).

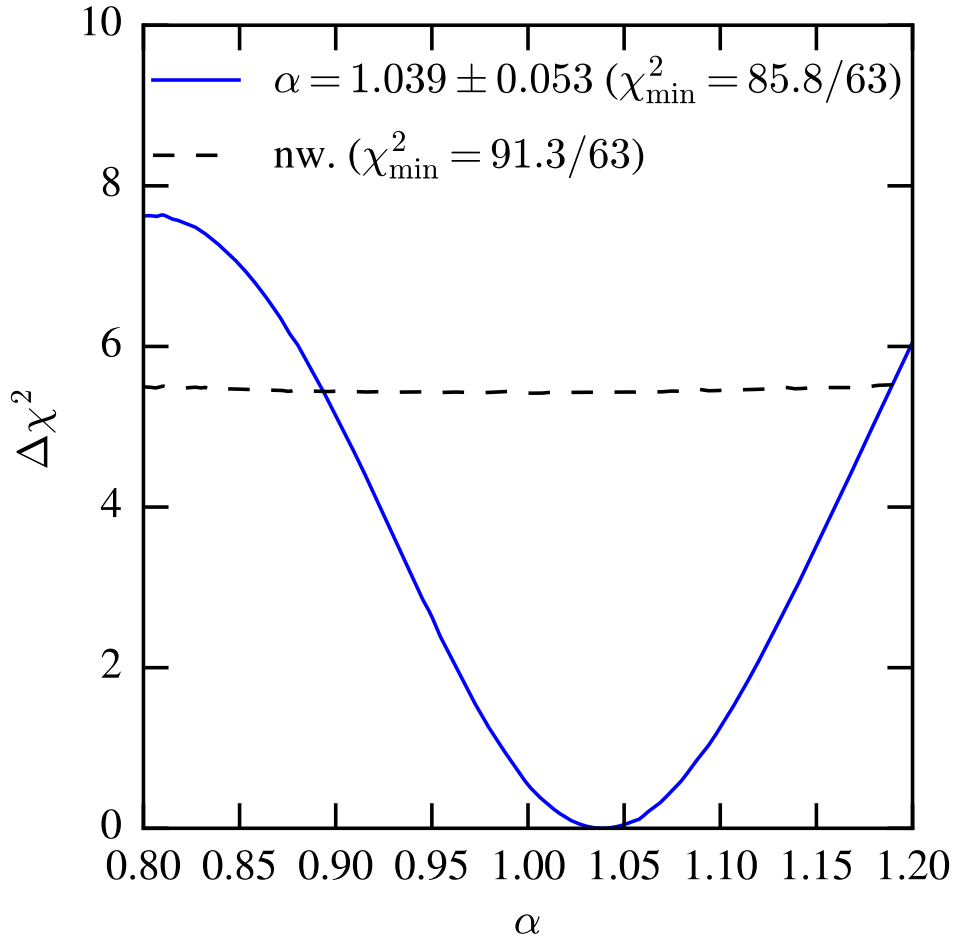


Figure 5.17: $\Delta\chi^2$ as a function of α for the DES Y1 galaxy data, when fitted using a new theoretical covariance matrix (see text) to a BAO template (solid blue curve) and to a no-wiggle template (dashed black curve).

as an indication of the BAO feature not being easily reproducible by contaminants and insensitive to its corrections in agreement with configuration space analysis (Crocce et al., 2019).

5.7 Discussion

The DES is on its way to produce the largest survey to date, projected to map 300 million galaxies using photometric techniques in an area of 5000 deg² up to a redshift $z \approx 1.3$ (see § 1.3.2). The Y1 data has been recently analysed resulting in a key paper combining three correlations: weak gravitational lensing, galaxy clustering, and their cross-correlation or galaxy-galaxy lensing (Abbott et al., 2018). Several papers dealing with the essential developments that led to the key paper were also produced (Cawthon et al., 2017; Avila et al., 2017; Davis et al., 2017; Gatti et al., 2017; Hoyle et al., 2018; Drlica-Wagner et al., 2018; Krause et al., 2017). Scientific analyses on Y3 are underway, and data from Y4 and Y5 have been collected and are being processed.

Fig. 5.18 shows the recovered likelihoods for α obtained from the three different methods presented in (Abbott et al., 2019), from which the C_ℓ case was presented in this chapter. All likelihoods diverge only at high ($\xi(s_\perp)$) or low (C_ℓ) α values, but present good agreement for the maximum likelihood, leaving the recovered value for α in good agreement.

The likelihood for α , Fig. 5.18, the fiducial cosmology, and the effective redshift of measurement can be combined to effectively constrain cosmological model parameters (see discussion in § 2.4.8). The fiducial cosmology used during the analysis was the one used for mock generation (Avila et al., 2017), for which $D_A^{\text{fid}}(z_{\text{eff}})/r_d^{\text{fid}} = 10.41$. All one needs to do to translate α to a distance constraint is to follow Eq. (2.188). The official DES Y1 result is the one obtained using the ACF, $w(\theta)$, for which we obtained a Y1 measurement of $D_A(z_{\text{eff}})/r_d = 10.75 \pm 0.43$ at $z_{\text{eff}} = 0.81$.

Fig. 5.20 shows the DES Y1 BAO feature measurement for the angular diameter distance and compares it with detections from independent determinations by other recent surveys and the Planck Λ CDM prediction (with fixed minimal neutrino mass). The measurements shown came from Beutler et al. (2011, 6dFGS), Ross et al. (2015a, SDSS MGS), Alam et al. (2017, BOSS), Kazin et al. (2014, WiggleZ), Ata et al. (2018b, eBOSS quasars), and the combination of Bautista et al. (2017); du Mas des Bourboux et al. (2017, BOSS Ly α). Some of the measurements presented were made in terms of the spherically averaged distance, namely the comoving volume distance, Eq. (2.26), which is a combination of the angular diameter distance

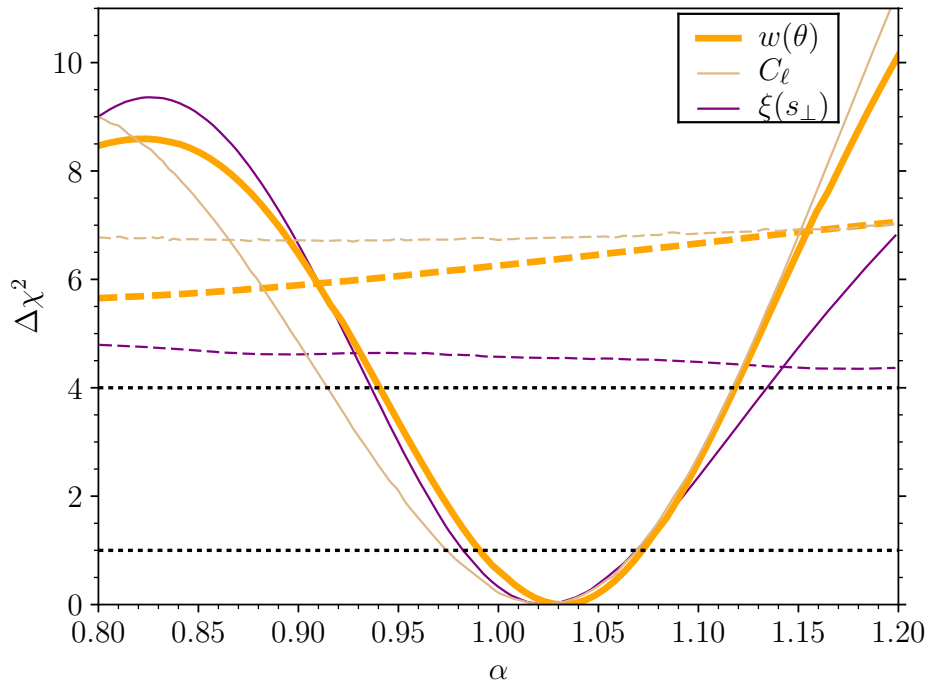


Figure 5.18: Recovered likelihoods for α determined with the three different two-point clustering statistics (Abbott et al., 2019, Fig. 7). Dotted black lines denote 1 and 2 σ levels, and dashed lines show the results obtained assuming a model with no BAO feature. Results for the BAO feature from the different clustering estimates are consistent and seem to indicate the data prefer a BAO feature with more than 2 σ significance.

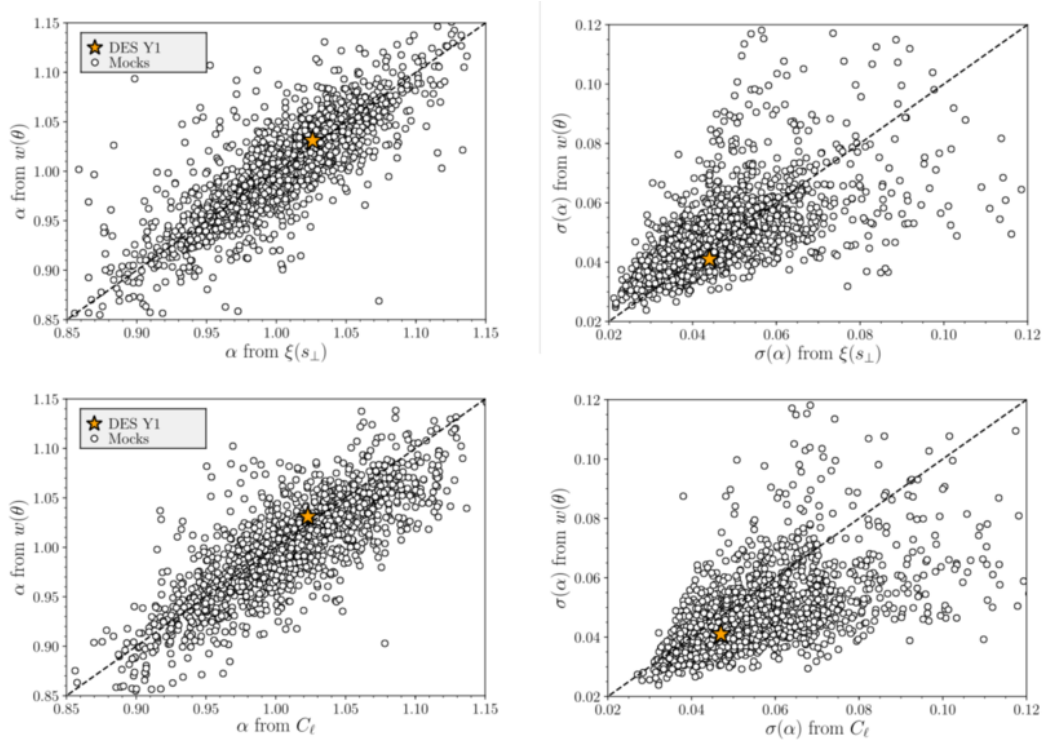


Figure 5.19: Comparison of the performance of the BAO feature determination from two methods in configuration space (left panels) and between the ACF and the APS (right panels) (Abbott et al., 2019, Figs. 2 and 3). Top panels compare the best fit value recovered for α and bottom panels its uncertainty from mock realizations.

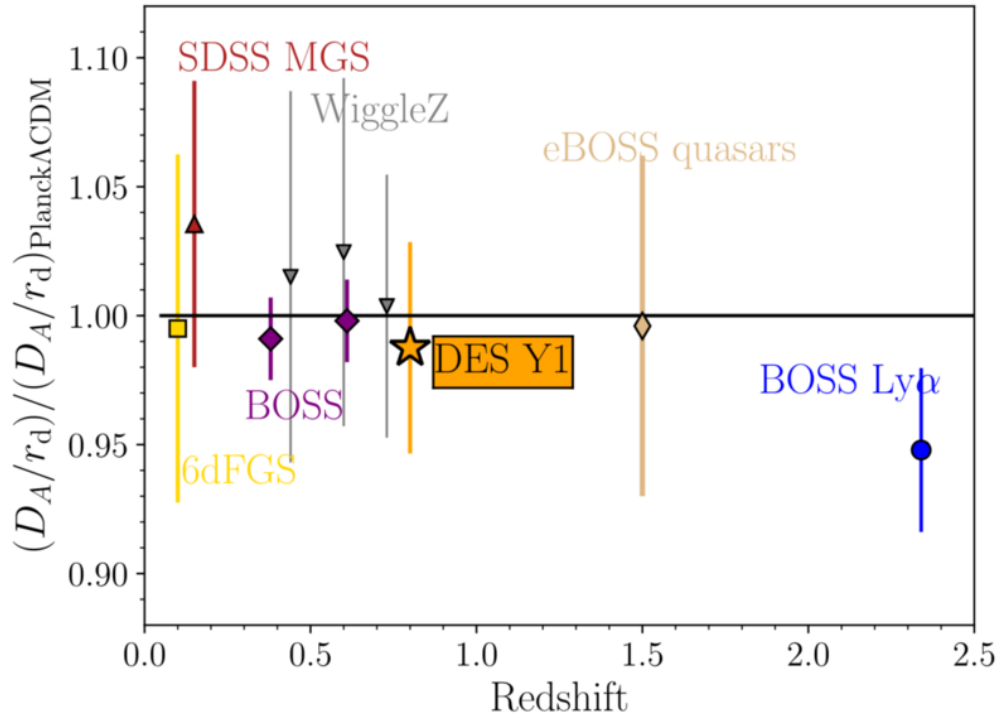


Figure 5.20: Ratio of angular diameter distance and sound horizon compared to Planck Λ CDM prediction measured using the BAO feature in late-time clustering of different tracers of the matter distribution in the universe by different surveys (Abbott et al., 2019, Fig. 8). The official DES Y1 measurement is shown using a gold star. For the studies that have reported spherically averaged distances only, 6dFGS, SDSS MGS and eBOSS QSOs, uncertainties are corrected by a factor of 1.5 (see text).

and $H(z)$. Assuming spherical symmetry, Ross et al. (2015b) showed that constraints on $D_A(z)$ are 50 per cent less precise. So for a fair comparison, the error-bars have been corrected by a 1.5 factor fixing the relative $(D_A/r_d)/(D_A/r_d)_{\text{Planck}\Lambda\text{CDM}}$ spherically averaged measurement.

The results shown in this chapter are part of an effort for the detection of the BAO feature in Y1 data. It relies on the construction of a catalog suitable for the study of clustering of galaxies, especially concerning the BAO feature (Croce et al., 2019), the mock catalogs used to validate the analysis and results (Avila et al., 2017) and the computation of galaxy photo- z s (Gaztanaga et al. in prep). Other papers detail methods to study the BAO feature in configuration space with the angular correlation function $w(\theta)$ (Chan et al., 2018), and using the comoving transverse separation (Ross et al., 2017), while the present work details the use of the angular power spectrum. The joint results applied to the Y1 data are described in the BAO main paper (Abbott et al., 2019).

The main goal of this work was to provide a harmonic-space counterpart to the analysis made in configuration space (Abbott et al., 2019). We did not attempt to fully optimize the catalog and strategy for mitigating systematic errors in our harmonic-space analysis. Instead, we used the catalog and systematic tools that were optimized for the configuration-space analysis. It is possible that systematic errors absent or unimportant for the analysis in configuration space may be relevant in some range of ℓ 's in harmonic space, and we hope to investigate this in further detail on DES Y3 data. However, our final results were all comparable to those of configuration space, which indicates that further optimization would have a small effect on our results.

We developed a methodology based on template-fitting (see § 2.4.8) and tested it on realistic DES Y1 galaxy mocks. First, we tested two independent codes for pseudo- C_ℓ estimators and found agreement between codes to better than 1% in nearly all scales of interest. We then measured the APS in four photo- z bins for 1800 mock catalogs, checking their consistency with theoretical expectations. We measured the covariance matrix from the mocks and compared it with a theoretical prediction, finding good agreement again. We then used two independent methods, a maximum likelihood estimator (MLE) and a Markov Chain Monte Carlo (MCMC) analysis to estimate the shift parameter for the average of the mocks and found the two methods to be compatible. Comparing the values of χ^2 for our BAO template to a no-wiggle model we find a 2.3σ signal for BAO in the mocks.

Several choices were made for our fiducial analysis, and we performed a number of robustness tests to assess their impact on the results. We find that our results on the mocks were not significantly sensitive to changing the

binning $\Delta\ell$ from 10 to 20, changing the smallest scales of our analysis from $\ell_{\max} = 300$ to $\ell_{\max} = 330$, neglecting the redshift cross-covariance, using the Limber approximation, neglecting linear RSD's, including a non-linear matter power spectrum and modifying the C_ℓ template used.

We then applied the fiducial analysis to measure the APS of a galaxy sample obtained from DES Y1 data also split into four photo- z bins up to $z = 1$ (Crocce et al., 2019). We obtain a best-fit $\alpha = 1.023 \pm 0.047$. This corresponds to a measurement of the ratio of the angular diameter distance to the effective redshift of our sample ($z_{\text{eff}} = 0.81$) and the BAO physical scale r_d of $D_A(z_{\text{eff}} = 0.81)/r_d = 10.65 \pm 0.49$. Comparing to the best-fit no-wiggle template we find a significance of 2.6σ for BAO detection.

This best fit has a somewhat large $\chi^2/(\text{dof})=1.49$ value. We could trace the reason to the covariance matrix computed from the mocks since the C_ℓ 's measured from them seem to underestimate the data at high ℓ 's in two redshift bins. We investigate this issue with a new Gaussian theoretical covariance matrix obtained from C_ℓ 's that are better adjusted to the data, taking into account the mask and the binning. With this new covariance matrix, we obtain a reduced value of $\chi^2 = 1.36$ without significant changes in the recovered value of α .

Our results are consistent with those from the real-space BAO analysis of Y1 data (Abbott et al., 2019), but the methodological uncertainties we found, despite being small, must be understood in more detail in future DES analyses.

The use of photometric data such as that from DES allows us to extend the BAO detection to high-redshift galaxies. The consistency of the BAO scale inferred from CMB and galaxies is an essential test of the standard cosmological model over most of the cosmic history. As DES continues to collect and analyze more data, the significance of the BAO feature detection will continue to improve. Data collected over three years of observations (Y3) covers nearly the whole DES footprint. In combination with additional probes of geometry and structure growth, the BAO feature detected in this extended area of DES will be an important element for constraining and distinguishing models of cosmic acceleration in the near future.

Chapter 6

Conclusion and outlook

The recent confluence of data from different complementary cosmological probes points out to the validity of a Standard Cosmological Model (the concordance Λ CDM model) which displays a late-time accelerated expansion driven by an unknown sector of the matter-energy content of the universe consistent with a cosmological constant. There are a series of exciting questions we can ask to help to illuminate our understanding of cosmic acceleration, e.g., are probes of early and late time expansion of the universe consistent within the same theoretical framework ? Are probes of late-time structure formation consistent with probes of expansion history ? Are observations of those probes consistent with a cosmological constant, or do they point to some kind of time evolution ?

The self-consistent combination of complementary observational probes constitutes a powerful way to approach these questions in the context of modern large galaxy surveys. In this context, the present thesis presents a set of analyses of the late-time clustering of galaxies in the context of three large galaxy surveys, namely the SDSS and the DES.

In Chap. 1 we present a general overview of the framework for the thesis. We provide motivations for using the information content of the large-scale structure of the universe as observed by modern wide-area galaxy surveys and present an overview of the current status of the SDSS and the DES.

Chap. 2 is devoted to present a review of the theoretical tools used to study and physically interpret the large-scale structure of the universe. We review the standard Λ CDM scenario starting from the expansion history, as described by the RW metric as a formal solution to the Einstein Field Equations. We then proceed to present the connection between expansion and structure formation, by discussing the evolution of perturbations. We provide a detailed discussion of the evolution of the linear regime for matter perturbations and consider some approaches to study the nonlinear regime

used on our latter analyses. We also provide a review for the physical interpretation of galaxy clustering in § 2.4 as the fundamental probe from which we extract information from galaxy surveys data in the remaining of the thesis. We focus on the two-point correlation of the field of galaxies as tracers of the total matter field and gravitational potentials at large-scales. We also provide a deeper theoretical discussion of perturbations of the RW metric in Appendix B. Finally, we review the theoretical foundations of the BAO and modern approaches for extracting its feature as imprinted in the observed late-time clustering of galaxies.

Chaps. 3, 4 and 5 present three analyses of the information content in the clustering of galaxies as observed by large modern galaxy surveys and represent the main contributions of the present thesis. These works are contained in Jouvel et al. (2017); Zhai et al. (2017); Camacho et al. (2018); Avila et al. (2018); Abbott et al. (2019); DES Collaboration et al. (2018)

In Chap. 3 we present a study of the clustering of ELGs targeted from eBOSS by using *grz* imaging from the SV data from DES. We present measurements of the two-point monopole (angular average) and the projected correlation function of a sample of two DES-based target selections, namely bright and faint, based on standard eBOSS and a DESI-like targeting. The latter was proposed in Jouvel et al. (2017) as a way to reach higher redshifts and fainter objects. For each sample, the clustering for selections based on z_{spec} was compared with selections based on z_{phot} as estimated from a neural network method and a template-based method in Jouvel et al. (2017), based on DES imaging. No differences in the clustering of samples were observed by any of the different selections probed, we argue, because of the small area of overlap between the experiments, 9.2 deg^2 . On top of systematics accounted by eBOSS observations pipeline, we also present the way variations in depth along the survey footprint and a small area of observations were taken into account for not biasing the clustering measurements.

Measurements of the projected correlation function of ELGs were used to constrain their large-scale bias and compared with previous spectroscopic studies of the evolution of the clustering of ELGs with magnitude limit of the sample. Although we could not find a difference in the clustering of the different samples proposed, we do find consistency for the complete set of ELGs to be brighter than $M_B - \log h < 20.5$. These results tested the first plates of eBOSS observations, prior to May 2016, showing the project was doing well.

In Chap. 4 we present our contribution to the first scientific results from the LRG sample of eBOSS. A definition of a combined sample from BOSS and eBOSS was presented by Zhai et al. (2017), along with a study of the

sample clustering properties. We show how, on top of standard observational systematics carefully considered by the SDSS pipeline, the effect of fiber collisions was addressed for the measurements of the projected correlation function of LRGs and how these measurements were subsequently used to obtain a constraint on the large-scale bias of LRGs from BOSS and eBOSS. Such a direct measurement was compared with its counterpart in the framework of HOD and shown to be consistent.

The primary scientific goal of eBOSS is to probe the growth and expansion history from the BAO feature and the evolution of RSDs on the clustering signal of different tracers of the matter field of the universe. Our results showed that after one year of observations, with a sample of 34000 LRGs at $z_{\text{eff}} \approx 0.7$, clustering statistics from eBOSS are consistent with previous stages of the SDSS project, showing that the project is progressing well.

Wide imaging and spectroscopic surveys as the DES and the SDSS offer the possibility of using more than one single tracer of the matter density to perform clustering analyses. This opens possibilities for LSS studies at different redshift ranges, as different astrophysical objects targeted appear preferably at different redshifts reflecting their particular evolution. From them, we presented in Chap. 3 an analysis using the synergy between DES and eBOSS for characterizing target selections of ELGs. One other exciting window of opportunities is the combination of clustering measurements from different tracers which can help beat sample variance (see e.g. Abramo & Leonard, 2013; Alarcon et al., 2018). However, this also brings the challenge of the correct targeting of samples. Such a non-trivial task is an excellent example of where a combination of efforts from imaging and spectroscopic surveys can be particularly useful.

In Chap. 5 we present what we consider to be the major contribution of the present thesis, namely the measurements and analyses in harmonic space of two-point statistics of DES Y1 data for a first robust and precise determination of the BAO feature from DES galaxies.

Measurements of the BAO scale have proven to be a robust and precise means for measuring cosmological distances when using spectroscopic redshift estimations (e.g. Alam et al., 2017, and references therein). Likewise, BAO measurements from photometric surveys have started to be made with good accuracy and precision. The DES 4 percent angular diameter distance measurement of $D_A(z_{\text{eff}} = 0.81)/r_d = 10.75 \pm 0.043$ is summarized in Abbott et al. (2019). This measurement is the result of efforts presented in a set of 5 companion papers. Crocce et al. (2019) presents the selection of our DES Y1 sample, optimized for $z > 0.6$ BAO measurements, and tests of its basic

properties. Avila et al. (2018) describes how 1800 realizations approximating the spatial properties of the DES Y1 data sample were produced and validated. Using these mock Y1 realizations, validation and optimization of the methodology for measuring BAO using three different individual 2-point statistics in terms of the angular separation, the co-moving transverse separation, and angular power spectrum are presented in Chan et al. (2018), Ross et al. (2017) and Camacho et al. (2018), respectively.

The BAO method probes the expansion history of the late-time universe directly by measuring absolute distances assuming a calibration with the sound horizon. In this way, part of its beauty relies on the fact that such calibration depends on physical modeling of the early universe and mainly the linear evolution of perturbations, as long as they successfully describe the sound horizon. Moreover, as long as SN measure also distance ratios but relative to local (late) calibrators they are expected to be complementary (Weinberg et al., 2013). The DES has now presented its first independent cosmological analysis in DES Collaboration et al. (2018). Such analysis is summarized here in Fig. 6.1 and represents a major advance for our efforts to understand the nature of cosmic acceleration. Besides the combination with SN, DES Collaboration et al. (2018) presents the self-consistent combination of our BAO results with measurements of cosmic shear and galaxy-galaxy lensing, all from DES data alone (black contours) and compares with external (non-DES) datasets only (green contours) and the combination of DES dataset with external Low- z SN (blue contours). In all cases, constraints are consistent with a cosmological constant ($w = 1$). Interestingly, DES data constrains w to within a factor of ~ 2 of that obtained when combining multiple major external data sets. This then illustrates the bright prospects for multiple independent, precise low-redshift constraints on dark energy from upcoming large-scale photometric experiments.

We are currently leading the DES-Y3 BAO analysis in harmonic space, which will contain nearly the whole DES footprint. The analysis on DES-Y3 and beyond will not only improve the Y1 BAO detection precision but, in combination with other probes within DES (lensing, full shape clustering, clusters, and Supernovae) as well as with CMB data, will provide the most stringent cosmological constraints to date. Similar improvements are expected for the future BAO analysis of eBOSS using multiple probes such as LRGs, ELGs, and Quasars.

Within the parameter inference problem in cosmology, the estimation of covariance matrices is a vibrant and active field of research. The relevant quantity to be considered is the inverse of the covariance or precision matrix. Currently, there are mainly three methods to tackle this problem: es-

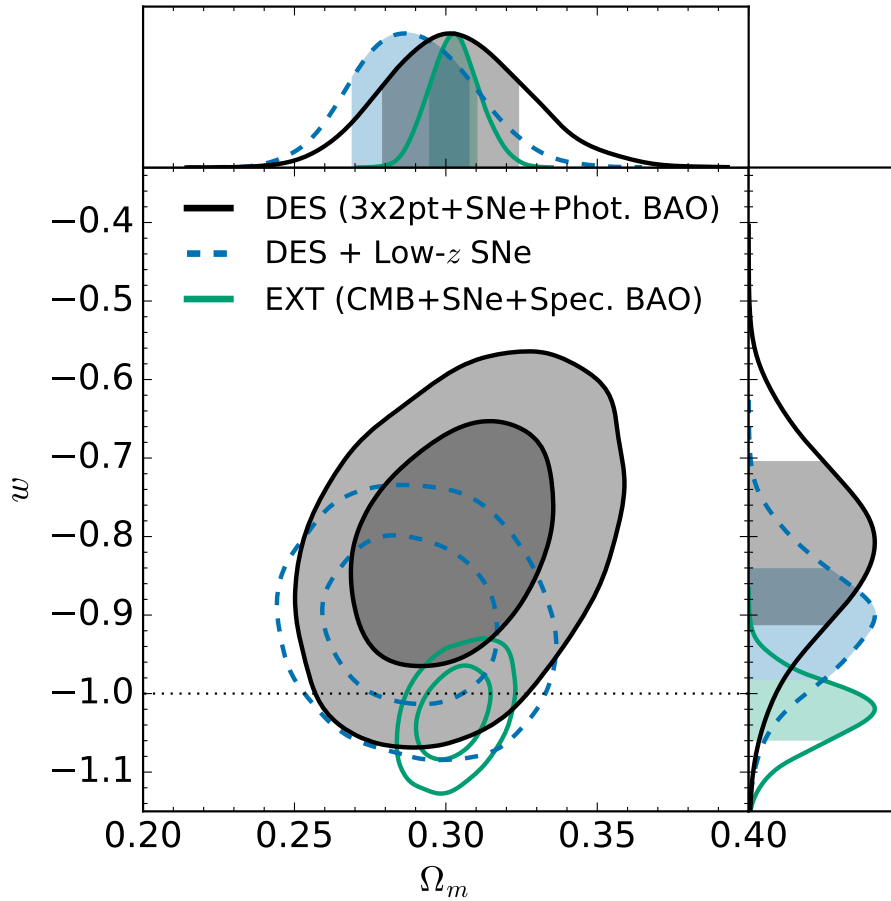


Figure 6.1: DES Y1 data combined constraints on Ω_m and w for a w CDM model, governed at background level by Eq. (2.20) (DES Collaboration et al., 2018, Fig 2). Contours represent the 68% and 95% C.L. for model parameters from the combination of BAO measurements presented in Chap. 5 with cosmic shear and galaxy-galaxy lensing (3×2 pt DES analysis) and SN from DES data only (black contours) and compares with external (non-DES) datasets only (green contours) and the combination of DES dataset with external Low- z SN (blue contours).

estimation from simulations, directly from real data, and analytical modeling. Estimation from simulations is computationally expensive mainly because of intrinsic noise in sample covariance estimators (Friedrich & Eifler, 2018). Estimation from data – bootstrap or Jackknife methods – does not rely on any assumption for the model parameters. However, limited survey area makes it challenging to reach the optimal large number of sky regions, and it is unclear if these regions can be treated as independent (Norberg et al., 2009). Estimation from analytical modeling minimizes the noise in the estimation process. However, the modeling of non-linear/non-Gaussian contributions is yet less precise than sophisticated numerical simulations (Krause & Eifler, 2017). In previous studies, we dealt with these issues. In de Simoni et al. (2013) and Jouvel et al. (2017), a comparison of Jackknife and analytical modeling was made for validating the optimal method for covariance estimation on clustering analyses. In Camacho et al. (2018) a suite of 1800 realizations was specially produced (Avila et al., 2018) for approximating the spatial characteristics of the galaxy sample and optimizing the covariance for analysis methodology by comparing with analytical computations. Based on our experience, we believe that the inter-relation between the success points of these three different approaches should offer valuable information for the best practices in covariance/precision matrix optimal estimation. That will be one of our primary strategies for future analyses.

One of the main topics of research we would like to explore in the future is the self-consistent combination of information from galaxy clustering and weak lensing, using the galaxy and shear auto-correlations as well as the galaxy-shear cross-correlation, i.e., the three possible 2-point statistics from δ_g and κ/γ . Such a combination contains a significant amount of valuable complementary information for uncovering and characterizing cosmological models. Tensions between individual probes can give insights into new physical concepts or significant neglected systematic effects. On the other hand, the consistency between individual probes provides a substantial gain of information in the joint parameter space for cosmology and systematic effects (nuisance parameters).

For photometric surveys, efforts for combining 2-point statistics have started to be developed, which is the case of the DES-Y1 3 \times 2pt key project summarized in Abbott et al. (2018). The methodology for such an effort was developed entirely for configuration-space 2-point statistics (Krause et al., 2017). We plan to use our experience in harmonic-space analyses (Camacho et al., 2018) to join this effort by developing a parallel methodology for harmonic space 2-point statistics. Any tension between these analyses can give insights to relevant systematic effects and peculiarities of each method.

The South Pole Telescope (SPT, Carlstrom et al., 2011) and the Planck mission (Planck Collaboration et al., 2011) have recently enabled high signal-to-noise mapping of gravitational lensing of the CMB, typically quantified via the lensing convergence, κ_{CMB} . One important characteristic of these observations is the overlap with the DES survey, as it opens the possibility for the joint measurement of all 2-point statistics that can be formed from δ_g , γ and κ_{CMB} . Baxter et al. (2018) recently introduced a methodology for the self-consistent combination of all six 2-point statistics allowed by the mentioned fields ($6 \times 2\text{pt}$), and the same excluding $\langle \kappa_{\text{CMB}} \kappa_{\text{CMB}} \rangle$ ($5 \times 2\text{pt}$). This exclusion is supported by the negligible cross-covariance between $\langle \kappa_{\text{CMB}} \kappa_{\text{CMB}} \rangle$ and other 2-point statistics coming from full-sky high-resolution κ_{CMB} maps from Planck, which allows decomposition of the final posterior as the product of $\langle \kappa_{\text{CMB}} \kappa_{\text{CMB}} \rangle$ and $5 \times 2\text{pt}$ posteriors.

Such $5 \times 2\text{pt}$ methodology in harmonic space represents a relevant extension for the proposed project. One major conclusion of Baxter et al. (2018) is the primary importance of the characterization and impact of bias in CMB lensing maps induced by the thermal Sunyaev-Zel'dovich effect, which appears quite large at small scales for the case of DES-Y1 like data-vector, and reduces the improvement in cosmological constraints given the fiducial priors of the $3 \times 2\text{pt}$ analysis. A harmonic-space counterpart of this analysis will help on the characterization of the impact of this bias, and we propose to perform this study.

Appendices

Appendix A

Alternative metric, curvature and distance definitions

In this appendix we present alternative definitions for the metric with curvature and related distance definitions.

Recall we defined the space-time FRW metric tensor as

$$\bar{g} = -dt \otimes dt + a^2(t) \gamma_{ij} dx^i \otimes dx^j, \quad (\text{A.1})$$

or similarly in terms of the *conformal time* η

$$\bar{g} = a^2(\eta) [-d\eta \otimes d\eta + \gamma_{ij} dx^i \otimes dx^j]. \quad (\text{A.2})$$

For the constant time hypersurfaces one can always choose spherical coordinates $x^i = (\chi, \theta, \varphi)$, where χ is a radial coordinate and (θ, φ) are the usual polar and azimuthal angles of spherical coordinates on the unit sphere \mathbb{S}_2 . The components of the spatial metric for this coordinates choice are given in the (comoving) spatial line element as

$$d\ell^2 = \gamma_{ij} dx^i dx^j = \begin{cases} -K^{-1} [d\chi^2 + \sinh^2(\chi) d\Omega^2] & K < 0, \\ d\chi^2 + \chi^2 d\Omega^2 & K = 0, \\ K^{-1} [d\chi^2 + \sin^2(\chi) d\Omega^2] & K > 0; \end{cases} \quad (\text{A.3})$$

where $\chi \in [0, \infty)$ for $K \leq 0$, $\chi \in [0, \pi]$ for $K > 0$ and $\theta \in [0, \pi]$ and $\varphi \in [0, 2\pi)$ for all cases in order to cover the spacetime and $d\Omega^2$ is the unit area element on the sphere. This choice of coordinates is particularly useful because it leaves all the spatial coordinates with the same dimensionality. Note that here $K^{-1/2}$ can be interpreted as determining a radius of curvature of constant time hypersurfaces. Notice the radius is imaginary for $K < 0$. In fact, 3D spaces of constant curvature can be constructed by embedding a

3D hyperboloid, plane and sphere on a 4D flat space for the $K < 0$, $K = 0$ and $K > 0$ cases, respectively. The radius of each one of these hypersurfaces defined as $|K|^{-1/2}$ imply the embedded metric to be given by Eq. (A.3) (see e.g., Peter & Uzan, 2013).

One can also choose a fully dimensional radial coordinate (a more frequent choice in the literature) by defining the radial comoving distance,

$$r = \begin{cases} |K|^{-1/2}\chi & K \neq 0, \\ \chi & K = 0. \end{cases} \quad (\text{A.4})$$

Thus for coordinates $x^i = (r, \theta, \varphi)$ the comoving spatial line element reads:

$$d\ell^2 = \gamma_{ij}dx^i dx^j = dr^2 + f_K^2(r)d\Omega^2, \quad (\text{A.5})$$

where the function $D_A = f_K(r)$ defines the *comoving* angular diameter distance and depends on the sign of the curvature as

$$f_K(r) = \begin{cases} (-K)^{-1/2} \sinh(\sqrt{-K}r) & K < 0, \\ r & K = 0, \\ K^{-1/2} \sin(\sqrt{K}r) & K > 0. \end{cases} \quad (\text{A.6})$$

There are other common choices for the spatial coordinates, as e.g., taking the function $f_K(r)$ itself as the radial coordinate. Setting $x^i = (R, \theta, \varphi)$ with $R = D_A := f_K(r)$ the spatial metric reads

$$\gamma_{ij}dx^i dx^j = \frac{dR^2}{1 - KR^2} + R^2 d\Omega^2. \quad (\text{A.7})$$

When the forms of Eqs. (A.3) and (A.5) are considered on the full RW metric Eq. (A.2), for each value of η the curvature of spatial sections Σ_t is given by $K a^{-2}(\eta)$, so that it is possible to rescale the scale factor in order to make K to have only three discrete values $-1, 0, +1$. In that case, choosing a radial coordinate adimensional/dimensional is equivalent to choosing the scale factor dimensional/adimensional. This kind of choice has the disadvantage of inhibiting the choice of an arbitrary value for the scale factor today, say $a_0 = 1$, which proves to be very useful for cosmological analyses. In fact, Universe models based on the RW metric have as degrees of freedom the function $a(\eta)$, determining the evolution in time of spatial scales, and the constant K , determining the curvature of spatial sections of spacetime. When the rescaling of $a(\eta)$ is done, the degree of freedom in K can be thought to be translated to the value of a_0 plus the sign of K .

The gravitational effects of spatial curvature can be characterized by comparing the curvature radius $|K|^{-1/2}$ and the radial comoving scales considered r . From Eqs. (A.3) or (A.6) one can see that the spatial metric γ for the $K \neq 0$ cases reduces to the flat case when $r|K|^{1/2} = \chi \rightarrow 0$, and according to the equivalence principle, this should be independent of the coordinates used. Therefore, when $r|K|^{1/2} = \chi \gg 1$ the effects of curvature should be important, in contrast to situations in which $r|K|^{1/2} = \chi \ll 1$ where they should become negligible.

Recall the *line-of-sight or radial comoving distance* at a given redshift z , is given by

$$r(z) = \int_0^z \frac{dz'}{H(z')} = D_{\text{H0}} \int_0^z \frac{dz'}{E(z')} \quad (\text{A.8})$$

where

$$E(z) = \frac{H(z)}{H_0} \quad \text{and} \quad D_{\text{H0}} = \frac{1}{H_0} \quad (\text{A.9})$$

On the past light-cone, $r(z)$ is related to the adimensional radial comoving coordinate according to

$$\chi(z) = \begin{cases} |K|^{1/2} r(z), & K \neq 0, \\ r(z), & K = 0. \end{cases} \quad (\text{A.10})$$

Note that, according to this relation, on the light-cone surface the variable z and the coordinates t and χ are equivalent. That is because of the physical interpretation of $r(z)$ as the comoving distance travelled by a photon propagating in a radial null geodesic from a point of radial coordinate χ to the observer (assumed at $\chi = 0$ without loss of generality). One can say that $r(z)$ is the fundamental distance measure in cosmology/cosmography, as all cosmological relevant distance measures can be expressed in terms of it (for a recent review see e.g., Hogg, 1999).

We defined in the text the comoving angular diameter distance D_A as the ratio of an object's comoving angular or transverse size to its angular size. Directly from RW metric, we see that it is given by $D_A(r) = f_K(r)$, or in terms of D_{H0} , r and $\Omega_K = -K/H_0^2$

$$D_A = f_K(r) = \begin{cases} D_{\text{H0}} \Omega_K^{-1/2} \sinh \left(\Omega_K^{1/2} r / D_{\text{H0}} \right) & K < 0 \\ r & K = 0 \\ D_{\text{H0}} |\Omega_K|^{-1/2} \sin \left(|\Omega_K|^{1/2} r / D_{\text{H0}} \right) & K > 0 \end{cases} \quad (\text{A.11})$$

Similarly, the ratio of an object's *physical* transverse size to its angular size in radians is the *physical* angular diameter distance d_A , given by

$$d_A = \frac{D_A}{1+z} \quad (\text{A.12})$$

In the literature, we find another distance measure definition directly related to the angular diameter distance, the so-called *transverse comoving distance* D_M between two events at the same constant time hypersurface, i.e. at same time or redshift, but observed separated on the sky by an angle $\Delta\theta$ is given by $D_M\Delta\theta$. Clearly, this is simply our comoving angular diameter distance

$$D_M = D_A. \quad (\text{A.13})$$

In the literature D_M is also known as the *proper motion distance*, as it can be also defined as the ratio of the actual transverse velocity of an object to its proper motion on the sky in rad/sec (see §5 of Hogg, 1999, for details).

Finally, recall the *comoving volume* element dV_C is given by

$$dV_C = (D_A^2 d^2\Omega) dr = D_{H0} \frac{D_A^2}{E(z)} d^2\Omega dz = D_V^3 d^2\Omega dz, \quad (\text{A.14})$$

whereas the *physical* volume element dV is given using physical distances:

$$dV = \frac{dV_C}{(1+z)^3} \quad (\text{A.15})$$

Appendix B

Cosmological perturbations

In this Appendix we review cosmological perturbation theory in some detail. We begin by reviewing results for the background FLRW spacetime needed for some developments presented in the thesis. Then, the gauge problem is discussed and gauge invariant first order EFE for a pure dust fluid under scalar perturbations are considered. The latter constitutes the basic theoretical basis to understand the large scale structure of the Universe within GR in the linear regime.

B.1 Background geometry

In this section we present some geometrical quantities for the background FLRW Universe relevant for the development of the present work. In particular we are interested on the connection coefficients (Christoffel symbols) for different choices of comoving spatial system of coordinates considered in § 2.1.

Starting from the RW metric, Eq. (A.2), one can derive the Christoffel symbols of the metric connection from the definition (Weinberg, 1972; Peter & Uzan, 2013),

$$\bar{\Gamma}^{\mu}_{\nu\sigma} = \frac{1}{2}\bar{g}^{\mu\tau}(-\partial_{\tau}\bar{g}_{\nu\sigma} + \partial_{\nu}\bar{g}_{\tau\sigma} + \partial_{\sigma}\bar{g}_{\nu\tau}), \quad (\text{B.1})$$

as

$$\bar{\Gamma}^0_{00} = \mathcal{H}, \quad \bar{\Gamma}^0_{ij} = \mathcal{H}\gamma_{ij}, \quad \bar{\Gamma}^i_{0j} = \bar{\Gamma}^i_{j0} = \mathcal{H}\gamma^i_j, \quad \bar{\Gamma}^i_{jk} = {}^3\Gamma^i_{jk}, \quad (\text{B.2})$$

where ${}^3\Gamma^i_{jk}$ denotes the Christoffel symbols associated to the spatial metric γ_{ij} . In this work the forms from Eqs. (A.3) and (A.5) are considered. The

non-null symbols for this chooses of coordinates are

$$\bar{\Gamma}^2_{12} = \bar{\Gamma}^3_{13} = \begin{cases} \cosh(\chi)/\sinh(\chi) & K < 0, \\ \chi^{-1} & K = 0, \\ \cos(\chi)/\sin(\chi) & K > 0, \end{cases} \quad \bar{\Gamma}^2_{33} = -\cos(\theta)\sin(\theta), \quad (\text{B.3a})$$

$$\bar{\Gamma}^1_{33} = \begin{cases} -\cosh(\chi)\sinh(\chi)\sin^2(\theta) & K < 0, \\ -\chi\sin^2(\theta) & K = 0, \\ -\cos(\chi)\sin(\chi)\sin^2(\theta) & K > 0, \end{cases} \quad \bar{\Gamma}^3_{23} = \frac{\cos(\theta)}{\sin(\theta)}, \quad (\text{B.3b})$$

$$\bar{\Gamma}^1_{22} = \begin{cases} -\cosh(\chi)\sinh(\chi) & K < 0, \\ -\chi & K = 0, \\ -\cos(\chi)\sin(\chi) & K > 0, \end{cases} \quad (\text{B.3c})$$

for $x^i = (\chi, \theta, \varphi)$, the spatia metric in Eq. (A.3), and

$$\bar{\Gamma}^2_{12} = \bar{\Gamma}^3_{13} = f'_K(r)/f_K(r), \quad \bar{\Gamma}^1_{22} = -f_K(r)f'_K(r), \quad (\text{B.4a})$$

$$\bar{\Gamma}^1_{33} = -f_K(r)f'_K(r)\sin^2(\theta), \quad \bar{\Gamma}^3_{23} = \cos(\theta)/\sin(\theta), \quad (\text{B.4b})$$

$$\bar{\Gamma}^2_{33} = -\cos(\theta)\sin(\theta), \quad (\text{B.4c})$$

where the f_K is given by Eq. (A.6), for $x^i = (r, \theta, \varphi)$, Eq. (A.5).

B.2 Perturbation theory and the gauge problem

In perturbation theory the main goal is to find approximated solutions to Einstein field equations which can be considered as small deviations from a known exact solution, the background spacetime solution. The perturbation of any tensorial field \mathbb{T} should then be given by the difference between its value in the physical spacetime \mathbb{T} and its corresponding value on the background spacetime $\bar{\mathbb{T}}$. However, its a basic fact of in differential geometry that in order to perform comparisons of such quantities one should consider them at the same point on a manifold. Since the manifolds representing the physical and background spacetimes are different the necessity for a prescription to identify events between them emerges. Such a prescription is what should be understood as a *gauge choice*, see (see Bardeen, 1980; Bruni et al., 1997; Peter & Uzan, 2013, and references therein).

One then ends with a definition of gauge choice as a diffeomorphism between the background and physical spacetimes. Different choses for this

diffeomorphism and its relations should define *gauge transformations* and the freedom to choose it is equivalent to the freedom to choose the functional forms for the perturbation of any tensor field. This statement constitutes a framework to specify the *gauge problem*.

A way to put on formal grounds the previous ideas is to introduce a family of differential manifolds as models of the spacetime $\{(M_\lambda, \mathfrak{g}_\lambda) | \lambda \in \Lambda\}$, here M_λ defines its topological structure and \mathfrak{g}_λ represents its associated metric, see §7.5 of Wald (1984). There is a natural way to treat this situation, by introducing a (4+1)-dimensional manifold N defined as the product manifold $N = M \times \mathbb{R}$, where each M_λ is a 4-dimensional manifold, $M_\lambda = M \times \lambda$, so that N can be interpreted as a foliation, $N = \cup_{\lambda \in \mathbb{R}} M_\lambda$. This formulation is clearly explained in Bruni et al. (1997). Here we provide a review of the main concepts and ideas presented there, in order to obtain the perturbed EFE in first order gauge invariant variables.

Since the natural differential structure over \mathbb{R} consist of charts $(U, id)^1$, there is a natural form for the chart over N formed by charts (U, h_U) around $q = (p, \lambda) \in N^2$ such that $h(q) = (x^0, x^1, x^2, x^3, \lambda) \in \mathbb{R}^5$, where the coordinates x^a with $a = 0, 1, 2, 3$ are the ones associated to the local chart on M around p .

If a tensorial field \mathbb{T}_λ is defined on each model of spacetime M_λ a tensorial field is defined on N . In fact,

$$\forall q = (p, \lambda) \in N, \quad \mathbb{T}_q = \mathbb{T}_{(p,\lambda)} := \mathbb{T}_\lambda(p) \quad (p \in M_\lambda). \quad (\text{B.5})$$

Particularly, on each spacetime model a metric tensor and a set of matter and radiation fields exist satisfying the Einstein field equations.

In order to formally define a perturbation of a tensorial field, as was previously discussed, the basic requirement is a way to compare \mathbb{T}_λ with $\mathbb{T}_0 := \bar{\mathbb{T}}$ for every λ . This is equivalent to define a diffeomorphism between each model M_λ and the background spacetime $\bar{M} := M_0$. Therefore, one can consider all the diffeomorphisms $\varphi_\lambda : N \rightarrow N$ such that its restriction to M_0 cover M_λ , i.e., $\varphi_\lambda|_{M_0} : M_0 \rightarrow M_\lambda$ is a diffeomorphism. By choosing each φ_λ as a member of the group of diffeomorphisms associated to the flux of a vectorial field over N one can instead to deal with the diffeomorphism itself to deal with the field whose flux over N is given by φ_λ . The condition $\varphi_\lambda|_{M_0} : M_0 \rightarrow M_\lambda$ for the diffeomorphism translates to the field as the condition that on the natural charts for N discussed above the fifth component of the field should be the unity.

¹Here U is an open set on \mathbb{R} and id represents the identity application.

²Here $p \in M$ and $\lambda \in \mathbb{R}$.

Summarizing, one can define a *gauge vector field* as a vector field \mathbf{X} over $N = M \times \mathbb{R}$ such that on the differential structure induced by the natural differential structure on \mathbb{R} have the property $X^4 = 1$ for each $q \in N$. That is because such fields define through its fluxes over N the way to identify events on the spacetime models M_λ and M_0 diffeomorphically.

B.2.1 Taylor expansion of a tensor field

A Taylor expansion is a convenient way to write the value of a function on some given point of its domain in terms of its value and the value of all its derivatives on some other near point. This is impossible for a tensor field defined on a manifold just because its value at different points on the manifold, \mathbb{T}_q and $\mathbb{T}_{q'}$ for $q \neq q' \in N$, are objects belonging to different spaces by definition. However, a Taylor-like expansion can be defined when an application between tensors on different points of a manifold is given, and in particular, when this application is viewed as induced by the flux of a vector field on the manifold.

Given $\varphi^{\mathbf{X}} : \mathbb{R} \times N \rightarrow N$, the flux of a vector field \mathbf{X} over N , $q \in N$ and \mathbb{T} a tensor field on N . Since for every $\lambda \in \mathbb{R}$, $\varphi_\lambda^{\mathbf{X}}$ defines a diffeomorphism of N onto N , the pull-back of $\mathbb{T}_{\varphi_\lambda^{\mathbf{X}}(q)}$ through $\varphi_\lambda^{\mathbf{X}}$ (the tensor field \mathbb{T} evaluated at $\varphi_\lambda^{\mathbf{X}}(q) \in N$), $\varphi_\lambda^{\mathbf{X}*} \left(\mathbb{T}_{\varphi_\lambda^{\mathbf{X}}(q)} \right)^3$, defines a tensor evaluated at $q \in N$. Such a tensor admits the following Taylor expansion around $\lambda = 0$, lemma 1 in Bruni et al. (1997):

$$\varphi_\lambda^{\mathbf{X}*} \left(\mathbb{T}_{\varphi_\lambda^{\mathbf{X}}(q)} \right) = \sum_{n=0}^{\infty} \frac{\lambda^n}{n!} (\mathcal{L}_{\mathbf{X}}^n \mathbb{T})_q, \quad (\text{B.6})$$

where $(\mathcal{L}_{\mathbf{X}} \mathbb{T})_q$ denotes the tensor over N given by the Lie derivative of \mathbb{T}_q both at $q \in N$ and $(\mathcal{L}_{\mathbf{X}}^n \mathbb{T})_q$ denotes the n -th Lie derivative under the same of \mathbb{T} at q . For a good review of induced maps (pull-back and push-forward maps) and Lie derivatives see e.g. Chap. 5 of Nakahara (2003).

The general Taylor expansion in Eq. (B.6) allows us to define the perturbation of a tensor field. Let \mathbf{X} be a gauge field on the family of spacetime models $N = \mathbb{R} \times M$ and \mathbb{T} a tensor field defined on each model and extended to N according to Eq. (B.5), then the perturbation of \mathbb{T} can be defined as a tensor field on the background spacetime \bar{M} as

$$\delta_{\mathbf{X}}^{(n)} [\mathbb{T}] := \mathcal{L}_{\mathbf{X}}^n \mathbb{T}|_{\bar{M}}, \quad (\text{B.7})$$

³Here the superscript * denotes the pull-back induced mapping.

in such a way that, according to Eq. (B.6), the tensor field associated with the tensor in any model of spacetime, since is given in the background by the pullback of $\varphi_\lambda^{\mathbf{X}}$, can be written as

$$\varphi_\lambda^{\mathbf{X}*}(\mathbb{T}) = \bar{\mathbb{T}} + \sum_{n=1}^{\infty} \frac{\lambda^n}{n!} \delta_{\mathbf{X}}^{(n)}[\mathbb{T}]. \quad (\text{B.8})$$

Note that the perturbations of \mathbb{T} , $\delta_{\mathbf{X}}^{(n)}[\mathbb{T}]$, are tensor fields on the background, this formalizes the common statement in the literature that perturbations are tensor fields defined on the background. The parameter λ used to label different models of spacetime also works as perturbative parameter according to the gauge field definition.

B.2.2 Gauge transformations and gauge invariance

The natural question that remains from the previous construction is how the perturbation of a tensor fields changes under a change of gauge.

Consider two gauge fields \mathbf{X} and \mathbf{Y} generating fluxes $\varphi_\lambda^{\mathbf{X}}$ and $\psi_\lambda^{\mathbf{Y}}$ over N , respectively. This two fields, through the pullback of its fluxes, allow to define two background representations of the same tensor field \mathbb{T} , $\varphi_\lambda^{\mathbf{X}*}(\mathbb{T})$ and $\psi_\lambda^{\mathbf{Y}*}(\mathbb{T})$, and thus two perturbative expansions of the form of (B.8).

Define a family of diffeomorphisms

$$\Psi_\lambda := \varphi_\lambda^{\mathbf{X}} \circ \psi_\lambda^{\mathbf{Y}} : N \rightarrow N \quad (\forall \lambda \in \mathbb{R}). \quad (\text{B.9})$$

Then this family satisfies the following properties: (a) for each $\lambda \in \mathbb{R}$ $\Psi_\lambda|_{\bar{M}}$ defines a diffeomorphism of \bar{M} onto itself, (b) $\{\Psi_\lambda|\lambda \in \mathbb{R}\}$ is not an uniparametric group and (c) for each tensor field \mathbb{T}

$$\psi_\lambda^{\mathbf{Y}*}(\mathbb{T}) = \Psi_\lambda^*(\varphi_\lambda^{\mathbf{X}*}(\mathbb{T})). \quad (\text{B.10})$$

Properties (a) and (b) follow from the construction of family (B.9), while property (c) follows from the property of pullbacks $(\varphi \circ \psi)^* = \psi^* \circ \varphi^*$, and allow to formally connect the two background representations of any tensor field, thus defining a gauge transformation from \mathbf{X} to \mathbf{Y} .

Having formalized the idea of gauge transformation is convenient to introduce the concept of gauge invariant tensor field. Given \mathbf{X} and \mathbf{Y} gauge fields, a tensor field \mathbb{T} is said to be *totally invariant* if its background representations on both gauges coincide, i.e., if $\varphi_\lambda^{\mathbf{X}*}(\mathbb{T}) = \psi_\lambda^{\mathbf{Y}*}(\mathbb{T})$.

On any practical application one is interested on perturbations up to some given order, so that it is convenient to have a more relax definition of gauge invariance up to some order. A tensor field \mathbb{T} is said to be *gauge*

invariant up to order n if all its perturbations on both gauges, up to order n coincide, i.e., if

$$(\forall k \leq n) \quad \delta_{\mathbf{X}}^{(k)} [\mathbb{T}] = \delta_{\mathbf{Y}}^{(k)} [\mathbb{T}]. \quad (\text{B.11})$$

For $n \geq 1$ the condition for a tensor field to be gauge invariant up to order n , Eq. (B.11), is equivalent to say that for every vector field \mathbf{V} on \bar{M} and for all $k \leq n$,

$$\mathcal{L}_{\mathbf{V}} \delta_{\mathbf{X}}^{(k)} [\mathbb{T}] = 0. \quad (\text{B.12})$$

This result can be probed by induction over n . For $n = 1$, follows from the definition of the perturbations, Eq. (B.7), that

$$\delta_{\mathbf{X}}^{(1)} [\mathbb{T}] = \delta_{\mathbf{Y}}^{(1)} [\mathbb{T}] \quad \Leftrightarrow \quad \mathcal{L}_{\mathbf{V}} \mathbb{T}|_{\bar{M}} = 0, \quad (\text{B.13})$$

so that, since \mathbf{X} and \mathbf{Y} define arbitrary vector fields on \bar{M} the field $\mathbf{V} := \mathbf{X} - \mathbf{Y}$ is an arbitrary vector field on \bar{M} . By supposing (B.12) is true for some $n > 1$ then from the definition of perturbations,

$$\delta_{\mathbf{X}}^{(n+1)} [\mathbb{T}] = \delta_{\mathbf{Y}}^{(n+1)} [\mathbb{T}] \quad \Leftrightarrow \quad \mathcal{L}_{\mathbf{V}} \delta_{\mathbf{X}}^{(n)} [\mathbb{T}]|_{\bar{M}} = 0. \quad (\text{B.14})$$

This probes the result.

The result in Eq. (B.12) is a generalization of the Stewart–Walker lemma Stewart & Walker (1974). probe for a tensor degree of freedom to be gauge invariant.

Although the result in Eq. (B.12) answers the question of how to determine whether a tensor field is gauge invariant up to some order, the question of how do change this perturbations under gauge transformations, Eq. (B.10), remains open.

In order to consider this problem, one have to introduce the concept of *Knight diffeomorphism* Bruni et al. (1997). Let $\{\mathbf{V}_{(n)} | n \in \mathbb{N}\}$ a non-numerable family of vector fields over N and

$$\left\{ \phi_{\lambda}^{(n)} := \varphi_{\lambda}^{\mathbf{V}_{(n)}} : \mathbb{R} \times N \rightarrow N | n \in \mathbb{N} \right\}$$

the family of its corresponding generated fluxes. A *uniparametric family of Knight diffeomorphisms* is defined to be formed by the applications

$$\begin{aligned} \Psi_{\lambda} : \mathbb{R} \times N &\rightarrow N \\ (\lambda, p) &\mapsto \Psi_{\lambda}(p) := \phi_{\lambda}^{(1)} \circ \phi_{\frac{\lambda}{2}}^{(2)} \circ \cdots \circ \phi_{\frac{\lambda}{n!}}^{(n)} \circ \cdots (q). \end{aligned} \quad (\text{B.15})$$

That is, a Knight diffeomorphism over N is a suitable composition of the fluxes of a non-numerable family of vector fields over N . The vector fields $\mathbf{V}_{(1)}, \mathbf{V}_{(2)}, \dots$ are called *generators of the Knight diffeomorphism* Ψ_{λ} . It can

be proved that in general a family of Knight diffeomorphisms Eq. (B.15) does not form a uniparametric group of diffeomorphisms.

Knight diffeomorphisms has two important properties: (a) the pullback of a tensor field \mathbb{T} on N induced by a uniparametric family of Knight diffeomorphisms with gererators $\{\mathbf{V}_{(n)}|n \in \mathbb{N}\}$ can be expanded around $\lambda = 0$ as, lemma 2 in Bruni et al. (1997):

$$\Psi_\lambda^* (\mathbb{T}_{\Psi_\lambda(q)}) = \sum_{\ell_1=0}^{\infty} \sum_{\ell_2=0}^{\infty} \cdots \sum_{\ell_n=0}^{\infty} \cdots \left[\prod_{n=1}^{\infty} \frac{1}{\ell_n!} \left(\frac{\lambda^n}{n!} \right)^{\ell_n} \right] \left(\cdots \mathcal{L}_{\mathbf{V}_{(n)}}^{\ell_n} \cdots \mathcal{L}_{\mathbf{V}_{(2)}}^{\ell_2} \mathcal{L}_{\mathbf{V}_{(1)}}^{\ell_1} \mathbb{T}_q \right), \quad (\text{B.16})$$

$\forall q \in N$. The proof of this property follows from the expansion for the pullback of the flux of a vector field on a tensor \mathbb{T} , equation (B.6). In fact, given $q \in N$

$$\begin{aligned} \Psi_\lambda^* (\mathbb{T}_{\Psi_\lambda(q)}) &= \left(\cdots \phi_{\frac{\lambda^n}{n!}}^{(n)*} \circ \cdots \circ \phi_{\frac{\lambda^2}{2!}}^{(2)*} \circ \phi_{\lambda}^{(1)*} \right) \left(\mathbb{T} \left[\phi_{\lambda}^{(1)} \circ \phi_{\frac{\lambda^2}{2}}^{(2)} \circ \cdots \circ \phi_{\frac{\lambda^n}{n!}}^{(n)} \circ \cdots \right] (q) \right) \\ &= \left(\cdots \phi_{\frac{\lambda^n}{n!}}^{(n)*} \circ \cdots \circ \phi_{\frac{\lambda^3}{3!}}^{(3)*} \circ \phi_{\frac{\lambda^2}{2!}}^{(2)*} \right) \sum_{\ell_1=0}^{\infty} \frac{\lambda^{\ell_1}}{\ell_1!} \left(\mathcal{L}_{\mathbf{V}_{(1)}}^{\ell_1} \mathbb{T} \right) \left[\phi_{\frac{\lambda^2}{2!}}^{(2)} \circ \phi_{\frac{\lambda^3}{3!}}^{(3)} \circ \cdots \circ \phi_{\frac{\lambda^n}{n!}}^{(n)} \circ \cdots \right] (q) \\ &= \left(\cdots \phi_{\frac{\lambda^n}{n!}}^{(n)*} \circ \cdots \circ \phi_{\frac{\lambda^4}{4!}}^{(4)*} \circ \phi_{\frac{\lambda^3}{3!}}^{(3)*} \right) \sum_{\ell_2=0}^{\infty} \frac{\lambda^{2\ell_2}}{(2!)^{\ell_2} \ell_2!} \\ &\quad \times \sum_{\ell_1=0}^{\infty} \frac{\lambda^{\ell_1}}{\ell_1!} \left(\mathcal{L}_{\mathbf{V}_{(2)}}^{\ell_2} \mathcal{L}_{\mathbf{V}_{(1)}}^{\ell_1} \mathbb{T} \right) \left[\phi_{\frac{\lambda^3}{3!}}^{(3)} \circ \phi_{\frac{\lambda^4}{4!}}^{(4)} \circ \cdots \circ \phi_{\frac{\lambda^n}{n!}}^{(n)} \circ \cdots \right] (q) \\ &= \sum_{\ell_1=0}^{\infty} \sum_{\ell_2=0}^{\infty} \cdots \sum_{\ell_n=0}^{\infty} \cdots \left[\frac{\lambda^{\ell_1} \lambda^{2\ell_2} \cdots \lambda^{n\ell_n} \cdots}{(2!)^{\ell_2} (3!)^{\ell_3} \cdots (n!)^{\ell_n} \cdots \ell_1 \ell_2 \cdots \ell_n \cdots} \right] \\ &\quad \times \left(\cdots \mathcal{L}_{\mathbf{V}_{(n)}}^{\ell_n} \cdots \mathcal{L}_{\mathbf{V}_{(2)}}^{\ell_2} \mathcal{L}_{\mathbf{V}_{(1)}}^{\ell_1} \right)_q, \end{aligned}$$

which reduces to Eq. (B.16); and (b) given $\Psi : \mathbb{R} \times N \rightarrow N$ an uniparametric family of diffeomorphisms over N , exist $\phi^{(1)}, \dots, \phi^{(2)}, \dots, \phi^{(n)}, \dots$ uniparametric groups of diffeomorphisms over N , such that each diffeomorphism Ψ_λ can be written as the composition

$$\Psi_\lambda = \phi_{\lambda}^{(1)} \circ \phi_{\frac{\lambda^2}{2}}^{(2)} \circ \cdots \circ \phi_{\frac{\lambda^n}{n!}}^{(n)} \circ \cdots, \quad (\text{B.17})$$

in other words, every uniparametric family of diffeomorphisms Ψ_λ can always be written as a family of Knight diffeomorphisms, theorem 2 in Bruni et al. (1997).

To see a little bit better how the expansion in Eq. (B.16) works, one can consider it explicitly up to second order,

$$\Psi_\lambda^* (\mathbb{T}_{\Psi_\lambda(q)}) \approx \mathbb{T}_q + \lambda \left(\mathcal{L}_{\mathbf{V}_{(1)}} \mathbb{T} \right)_q + \frac{\lambda^2}{2!} \left(\mathcal{L}_{\mathbf{V}_{(1)}}^2 \mathbb{T} + \mathcal{L}_{\mathbf{V}_{(2)}} \mathbb{T} \right)_q + \dots \quad (\text{B.18})$$

Properties (a) and (b) combined allow to treat the gauge transformation law $\mathbf{X} \rightarrow \mathbf{Y}$ given by the uniparametric family of diffeomorphisms

$$\Psi_\lambda = \varphi_{-\lambda}^{\mathbf{X}} \circ \psi_\lambda^{\mathbf{Y}} : \bar{M} \rightarrow \bar{M}, \quad (\text{B.19})$$

according to Eq. (B.10) as a Knight diffeomorphism. Therefore, given \mathbb{T} a tensor field on M , by comparing the expansions of the expression in Eq. (B.10) using Eq. (B.6) and (B.16) (or Eq. (B.18) to go up to second order only) one can determine the relations between its perturbation on two different gauges (\mathbf{X} and \mathbf{Y}) up to second order as

$$\delta_{\mathbf{Y}}^{(1)} [\mathbb{T}] - \delta_{\mathbf{X}}^{(1)} [\mathbb{T}] = \mathcal{L}_{\mathbf{V}_{(1)}} \mathbb{T}, \quad (\text{B.20a})$$

$$\delta_{\mathbf{Y}}^{(2)} [\mathbb{T}] - \delta_{\mathbf{X}}^{(2)} [\mathbb{T}] = \mathcal{L}_{\mathbf{V}_{(2)}} \mathbb{T} + \mathcal{L}_{\mathbf{V}_{(2)}}^2 \mathbb{T} + 2\mathcal{L}_{\mathbf{V}_{(1)}} \delta_{\mathbf{X}}^{(1)} [\mathbb{T}], \quad (\text{B.20b})$$

where the $\mathbf{V}_{(n)}$ are the vector generators of Ψ_λ seen as a Knight diffeomorphism given according to the perturbation definition, equation (B.7), by (proposition 3 in Bruni et al. (1997))

$$\mathbf{V}_{(1)} = \mathbf{Y} - \mathbf{X}, \quad (\text{B.21a})$$

$$\mathbf{V}_{(2)} = [\mathbf{Y}, \mathbf{X}]. \quad (\text{B.21b})$$

B.3 First order perturbations

B.3.1 Scalar–vector–tensor decomposition

Scalar–vector–tensor decomposition principle establish that for a three–dimensional differential manifold equipped with a metric tensor γ , and a covariant derivative D , every vector field \mathbf{X} can be decomposed in a *unique* manner on a scalar mode S and one transverse vector mode \mathbf{V} , that is, the components of \mathbf{X} are given as

$$X^i = D^i S + V^i; \quad D^i V_i = 0. \quad (\text{B.22})$$

Here, \mathbf{X} has three degrees of freedom (its three components) which are distributed as one on the scalar mode, and two on the vector mode, because of the transversal condition.

Analogously, every second rank symmetric tensor \mathbb{X} can be decomposed in a unique manner on two scalar modes S_1 and S_2 , one transverse vector mode \mathbf{V} and a symmetric, transverse and trace-free tensor mode \mathbb{T} as

$$X_{ij} = D_i D_j S_1 + S_2 \gamma_{ij} + D_{(i} V_{j)} + T_{ij}; \quad D^i V_i = 0, \quad D^i T_{ij} = \gamma_{ij} T^{ij} = 0. \quad (\text{B.23})$$

Here the six \mathbb{T} degrees of freedom are distributed in one on each scalar mode, two on the vector mode, because of the transverse condition, and the remaining four on the tensor mode, because of the transverse and trace-free conditions.

A very common practice in the literature is to redistribute the scalar degrees of freedom into the trace of \mathbb{X} and S_1 , i.e., to change S_2 for the trace

$$X = \gamma_{ij} X^{ij} = \nabla^2 S_1 + 3S_2, \quad (\text{B.24})$$

where ∇^2 is the Laplace operator on the three-dimensional manifold, $\nabla^2 := \gamma_{ij} D^i D^j$. In terms of the trace X the decomposition of a symmetric second rank tensor, equation (B.23), is given by

$$X_{ij} = \frac{1}{3} \gamma_{ij} X + \Delta_{ij} S_1 + D_{(i} V_{j)} + T_{ij}; \quad D^i V_i = 0, \quad D^i T_{ij} = \gamma_{ij} T^{ij} = 0, \quad (\text{B.25})$$

where the trace-free differential operator Δ was introduced as

$$\Delta_{ij} = D_i D_j - \frac{1}{3} \gamma_{ij} \nabla^2 \quad (\text{B.26})$$

The most important property of the decomposition in Eqs. (B.22) and (B.23) or (B.25) is its uniqueness. It is not our purpose here to discuss the conditions for this property to be satisfied, the interested reader can see e.g. Bardeen (1980).

B.3.2 Metric perturbations

Consider a gauge field \mathbf{X} . The most general way to parametrize the n -th order perturbation of the metric tensor around an FLRW background (in conformal time), on the light of scalar-vector-tensor decomposition for fields over the constant time hypersurfaces, is given by

$$\begin{aligned} \delta_{\mathbf{X}}^{(n)}[\mathfrak{g}] = a^2(\eta) & \left[-2_{\mathbf{X}} \Phi^{(n)} d\eta \otimes d\eta + \left(D_{i\mathbf{X}} B^{(n)} + {}_{\mathbf{X}} B_i^{(n)} \right) (d\eta \otimes dx^i + dx^i \otimes d\eta) \right. \\ & \left. + \left(-2_{\mathbf{X}} \Psi^{(n)} \gamma_{ij} + D_i D_{j\mathbf{X}} E^{(n)} + D_{(i\mathbf{X}} E_{j)}^{(n)} + 2_{\mathbf{X}} E_{ij}^{(n)} \right) dx^i \otimes dx^j \right], \quad (\text{B.27}) \end{aligned}$$

where the notation $\mathbf{x}\mathbb{T}^{(n)} := \delta_{\mathbf{X}}^{(n)}[\mathbb{T}]$ was introduced for simplicity. On the metric perturbation Eq. (B.27) the temporal component (00) defines a scalar mode parametrized as $-2\mathbf{x}\Phi^{(n)}$, the mixed components (0*i*) and (*i*0) defines a vectorial field on the constant time hypersurfaces expanded according to Eq. (B.22) into a scalar mode $\mathbf{x}B^{(n)}$ and a transverse vector mode $\mathbf{x}B_i^{(n)}$, finally, the spatial components (*ij*) define a symmetric tensor on the constant time hypersurfaces decomposed according to Eq. (B.23) into two scalar modes $\mathbf{x}\Psi^{(n)}$ and $\mathbf{x}E^{(n)}$, one transverse vector mode $\mathbf{x}E_i^{(n)}$ and one symmetric, transverse and trace-free tensor mode $\mathbf{x}E_{ij}^{(n)}$.

B.3.3 First order scalar perturbations

During this work only linear perturbation scalar modes are considered. Let \mathbf{X}_S represents the vector gauge field in which the perturbations are purely scalar. The first order perturbation for the metric tensor according to Eq. (B.27) is given by

$$\delta_{\mathbf{X}_S}^{(1)}[\mathbb{g}] = a^2 \left[-2\Phi d\eta \otimes d\eta + D_i B d\eta \otimes dx^i + D_i B dx^i \otimes d\eta \right. \\ \left. + 2(D_i D_j E - \Psi \gamma_{ij}) dx^i \otimes dx^j \right], \quad (\text{B.28})$$

where for all the scalar modes S the notation is relaxed via $S := \mathbf{x}_S S^{(1)} = \delta_{\mathbf{X}_S}^{(1)}[S]$.

The contravariant components of the first order perturbation to the metric tensor can be computed by considering the identity $g^{\mu\nu} = \bar{g}^{\mu\nu} - \bar{g}^{\mu\lambda} (g_{\lambda\sigma} - \bar{g}_{\lambda\sigma}) g^{\sigma\nu}$. By perturbing this relation up to first order one can find for a general gauge specified by \mathbf{X} the relation

$$\delta_{\mathbf{X}}^{(1)}[g^{\mu\nu}] = -\bar{g}^{\nu\rho} \bar{g}^{\mu\sigma} \delta_{\mathbf{X}}^{(1)}[g_{\sigma\rho}]. \quad (\text{B.29})$$

Choosing \mathbf{X}_S gauge, one finds

$$a^2 \delta_{\mathbf{X}_S}^{(1)}[g^{00}] = 2\Phi, \quad (\text{B.30a})$$

$$a^2 \delta_{\mathbf{X}_S}^{(1)}[g^{0i}] = a^2 \delta_{\mathbf{X}_S}^{(1)}[g^{i0}] = D^i B, \quad (\text{B.30b})$$

$$a^2 \delta_{\mathbf{X}_S}^{(1)}[g^{ij}] = 2(\gamma^{ij} \Psi - D^i D^j E). \quad (\text{B.30c})$$

The perturbations to the Christoffel symbols of second kind, Eq. (B.1), can be obtained by perturbing its definition directly,

$$\delta_{\mathbf{X}}^{(1)}[\Gamma^{\alpha}_{\mu\nu}] = \frac{1}{2} \bar{g}^{\alpha\beta} \left(-\partial_\beta \delta_{\mathbf{X}}^{(1)}[g_{\mu\nu}] + \partial_\nu \delta_{\mathbf{X}}^{(1)}[g_{\beta\mu}] + \partial_\beta \delta_{\mathbf{X}}^{(1)}[g_{\beta\nu}] \right) \\ + \frac{1}{2} \delta_{\mathbf{X}}^{(1)}[g^{\alpha\beta}] (-\partial_\beta \bar{g}_{\mu\nu} + \partial_\nu \bar{g}_{\beta\mu} + \partial_\beta \bar{g}_{\beta\nu}), \quad (\text{B.31})$$

so that, on the \mathbf{X}_S gauge

$$\delta_{\mathbf{X}_S}^{(1)} [\Gamma^0_{00}] = \Phi', \quad (\text{B.32a})$$

$$\delta_{\mathbf{X}_S}^{(1)} [\Gamma^0_{0i}] = \delta_{\mathbf{X}_S}^{(1)} [\Gamma^0_{i0}] = D_i (\Phi + \mathcal{H}B), \quad (\text{B.32b})$$

$$\delta_{\mathbf{X}_S}^{(1)} [\Gamma^0_{ij}] = -[2\mathcal{H}(\Phi + \Psi) + \Psi'] \gamma_{ij} - D_i D_j (B - 2\mathcal{H}E - E'), \quad (\text{B.32c})$$

$$\delta_{\mathbf{X}_S}^{(1)} [\Gamma^i_{00}] = D^i (\Phi + B' + \mathcal{H}B), \quad (\text{B.32d})$$

$$\delta_{\mathbf{X}_S}^{(1)} [\Gamma^i_{0j}] = \delta_{\mathbf{X}_S}^{(1)} [\Gamma^i_{j0}] = -\Psi' \delta^i_j + D^i D_j E', \quad (\text{B.32e})$$

$$\delta_{\mathbf{X}_S}^{(1)} [\Gamma^i_{jk}] = \gamma_{jk} D^i \Psi - \gamma^i_k D_j \Psi - \gamma^i_j D_k \Psi - \gamma_{jk} \mathcal{H} D^i B + D^i D_j D_k E. \quad (\text{B.32f})$$

In analogous way one can compute the perturbation of the mixed components of the Ricci tensor as

$$a^2 \delta_{\mathbf{X}_S}^{(1)} [R^0_0] = -6\mathcal{H}'\Phi - 3\mathcal{H}(\Phi + \Psi) - 3\Psi'' + \nabla^2 [-\Phi - \mathcal{H}(B - E') - B' + E'], \quad (\text{B.33a})$$

$$a^2 \delta_{\mathbf{X}_S}^{(1)} [R^0_i] = 2D_i (-\mathcal{H}\Phi - \Psi' + KB), \quad (\text{B.33b})$$

$$a^2 \delta_{\mathbf{X}_S}^{(1)} [R^i_0] = 2D^i [\mathcal{H}\Phi + \Psi' + (\mathcal{H}^2 - \mathcal{H}')B], \quad (\text{B.33c})$$

$$a^2 \delta_{\mathbf{X}_S}^{(1)} [R^i_j] = \gamma^i_j \left\{ -2\Phi (2\mathcal{H}^2 + \mathcal{H}') + 4K\Psi - \mathcal{H}(\Phi' + 5\Psi') + \nabla^2 [\Psi - \mathcal{H}(B - E')] \right\} + D^i D_j [-\Phi + \Psi - 2\mathcal{H}(B - E') - (B' - E'') - 4KE], \quad (\text{B.33d})$$

and of the Ricci curvature scalar

$$a^2 \delta_{\mathbf{X}_S}^{(1)} [R] = -12(\mathcal{H}^2 - \mathcal{H}')\Phi - 6\mathcal{H}(\Phi' + 3\Psi') + 12K\Psi - 6\Psi'' + \nabla^2 [2(-\Phi + 2\Psi) - 3\mathcal{H}(2B - E') - 2(B' - E'') - 4KE]. \quad (\text{B.34})$$

With this results the mixed components of the first order perturbation

for the Einstein tensor are given by

$$a^2 \delta_{\mathbf{X}_S}^{(1)} [G^0_0] = 6\mathcal{H}^2 \Phi - 6K\Psi + 6\mathcal{H}\Psi' + \nabla^2 [-2\Psi + 2\mathcal{H}(B - E') + 2KE], \quad (\text{B.35a})$$

$$a^2 \delta_{\mathbf{X}_S}^{(1)} [G^0_i] = 2D_i (-\mathcal{H}\Phi - \Psi' + KB), \quad (\text{B.35b})$$

$$a^2 \delta_{\mathbf{X}_S}^{(1)} [G^i_0] = 2D^i [\mathcal{H}\Phi + \Psi' + (\mathcal{H}^2 - \mathcal{H}')B], \quad (\text{B.35c})$$

$$a^2 \delta_{\mathbf{X}_S}^{(1)} [G^i_j] = \frac{1}{3} \gamma^i_j \tilde{G}_{\mathbf{X}_S}^{(1)} + \Delta^i_j [-(\Phi - \Psi) - 2\mathcal{H}(B - E') - (B' - E'') - 2KE]; \quad (\text{B.35d})$$

where the trace-free part had been separated from the trace-full part given by:

$$\tilde{G}_{\mathbf{X}_S}^{(1)} = 6(\mathcal{H}^2 + 2\mathcal{H}')\Phi + 6\mathcal{H}(\Phi' + 2\Psi') - 6K\Psi + 6\Psi'' + 2\nabla^2 [(\Phi - \Psi) + 2\mathcal{H}(B - E') + (B' - E'')]. \quad (\text{B.35e})$$

Gauge invariant variables

The gauge transformation law for first order perturbations of a tensor, Eq. (B.20a), can be used to determine the transformation properties of the scalar fields $\mathbf{x}_S \Phi^{(1)}, \mathbf{x}_S \Psi^{(1)}, \mathbf{x}_S B^{(1)}, \mathbf{x}_S E^{(1)}$, defining the metric perturbations. Consider a second gauge field \mathbf{Y}_S parametrized as Eq. (B.28) but with scalar fields $\mathbf{Y}_S \Phi^{(1)}, \mathbf{Y}_S \Psi^{(1)}, \mathbf{Y}_S B^{(1)}, \mathbf{Y}_S E^{(1)}$ and consider the vector field generator of the Knight diffeomorphism of the gauge transformation $\mathbf{X}_S \rightarrow \mathbf{Y}_S$ given by

$$\mathbf{V}_{(1)} = \mathbf{Y}_S - \mathbf{X}_S = T^{(1)} \partial_0 + (D^i L^{(1)} + L^{(1)i}) \partial_i; \quad D^i L_i^{(1)} = 0, \quad (\text{B.36})$$

according to the scalar-vector-tensor decomposition Eq. (B.22).

Thus, by computing the Lie derivative of \bar{g} along \mathbf{V}_1 $\mathcal{L}_{\mathbf{V}_{(1)}} \bar{g}$ and separating the scalar modes for each component one can find

$$\mathbf{Y}_S \Phi^{(1)} - \mathbf{x}_S \Phi^{(1)} = \mathcal{H}T^{(1)} + T^{(1)'}, \quad (\text{B.37a})$$

$$\mathbf{Y}_S \Psi^{(1)} - \mathbf{x}_S \Psi^{(1)} = -\mathcal{H}T^{(1)}, \quad (\text{B.37b})$$

$$\mathbf{Y}_S B^{(1)} - \mathbf{x}_S B^{(1)} = L^{(1)'} - T^{(1)}, \quad (\text{B.37c})$$

$$\mathbf{Y}_S E^{(1)} - \mathbf{x}_S E^{(1)} = L^{(1)}. \quad (\text{B.37d})$$

Therefore, it is not so difficult to see that the combinations

$$\hat{\Phi}^{(1)} = \mathbf{x}_S \Phi^{(1)} + (\mathbf{x}_S B^{(1)} - \mathbf{x}_S E^{(1)'})' + \mathcal{H}(\mathbf{x}_S B^{(1)} - \mathbf{x}_S E^{(1)'}) \quad (\text{B.38a})$$

$$\hat{\Psi}^{(1)} = \mathbf{x}_S \Psi^{(1)} - \mathcal{H}(\mathbf{x}_S B^{(1)} - \mathbf{x}_S E^{(1)'}) \quad (\text{B.38b})$$

are gauge invariant scalar modes for the metric perturbations. However it is important to remark that there are other possible choices for these two variables, this is, another kind of combinations giving rise to gauge invariant quantities (see e.g. § 5.2 in Peter & Uzan, 2013).

B.3.4 Matter–energy perturbations

The energy–momentum tensor at background level on a FLRW model is given by a perfect fluid one, see the discussion in § 2.1.

$$\bar{T}_{\mu\nu} = (\bar{\rho} + \bar{p}) \bar{u}_\mu \bar{u}_\nu + \bar{p} \bar{g}_{\mu\nu}, \quad (\text{B.39})$$

where \bar{u}^μ is the 4–velocity of fundamental observers, $\bar{\rho}$ the energy density and \bar{p} the pressure of the fluid. On a perturbed model, it can be generalized to have the form

$$T_{\mu\nu} = (\rho + p) u_\mu u_\nu + p g_{\mu\nu} + \pi_{\mu\nu}, \quad (\text{B.40})$$

where $\pi_{\mu\nu}$ accounts for anisotropic stress and therefore is a symmetric trace–free second rank tensor on the constant time hypersurfaces.

The up to first order four velocity is given by

$$u^\mu = \frac{dx^\mu}{dt} = \frac{1}{a} \frac{dx^\mu}{d\eta} = \bar{u}^\mu + \delta u^\mu, \quad (\text{B.41})$$

where $\bar{u}^\mu = a^{-1} \delta_0^\mu$ and should be a time–like four–vector, $g_{\mu\nu} u^\mu u^\nu = -1$. This normalization condition allows to derive the actual expressions for the components of the four velocity (covariant and contravariant) as

$$\begin{aligned} u^\mu &= \frac{1}{a} (1 - \Phi, D^i v), \\ u_\mu &= a (-1 - \Phi, D_i v + D_i B). \end{aligned} \quad (\text{B.42})$$

Therefore, the mixed components of the first order perturbations of the energy–momentum tensor should be found to be

$$\delta T^0_0 = -\delta\rho, \quad (\text{B.43a})$$

$$\delta T^0_i = (\bar{\rho} + \bar{p}) (D_i v + D_i B), \quad (\text{B.43b})$$

$$\delta T^i_j = \delta p \gamma^i_j + a^2 \delta \pi^i_j. \quad (\text{B.43c})$$

Here the anisotropic stress perturbation $\delta \pi_{ij}$ can be decomposed according to scalar–vector–tensor decomposition Eq. (B.25) as

$$\delta \pi^i_j = \Delta^i_j \Pi + D^{(i} \Pi_{j)} + \Pi^i_j; \quad D^i \Pi_i = D^i \Pi_{ij} = \gamma_{ij} \Pi^{ij} = 0, \quad (\text{B.44})$$

because the anisotropic stress is trace-free by construction.

Here the interest is on the scalar modes of first order perturbations. One can define a gauge fixing only scalar perturbations to the energy-momentum tensor by writing

$$\delta_{\mathbf{x}_S}^{(1)} [T^0_0] = -\delta\rho, \quad (\text{B.45a})$$

$$\delta_{\mathbf{x}_S}^{(1)} [T^0_i] = (\bar{\rho} + \bar{p}) (D_i v + D_i B), \quad (\text{B.45b})$$

$$\delta_{\mathbf{x}_S}^{(1)} [T^i_j] = \delta p \gamma^i_j + a^2 \Delta^i_j \Pi. \quad (\text{B.45c})$$

Gauge invariant variables

As for the metric perturbations, the gauge transformation law for first order perturbations of a tensor field, Eq. (B.20a), can be used to determine the transformation laws of the scalar modes of the components of the first order perturbation of the energy-momentum tensor, $\delta\rho$, v , δp and Π . By computing the Lie derivative of the background energy-momentum tensor along the vector field generator of the Knight diffeomorphism of gauge transformation $\mathbf{V}_{(1)}$ (Eq. (B.36)) $\mathcal{L}_{\mathbf{V}_{(1)}} \bar{T}$ one can find

$$\mathbf{y}_S \delta\rho - \mathbf{x}_S \delta\rho = \bar{\rho}' T^{(1)}, \quad (\text{B.46a})$$

$$\mathbf{y}_S v - \mathbf{x}_S v = -L^{(1)'}, \quad (\text{B.46b})$$

$$\mathbf{y}_S \delta p - \mathbf{x}_S \delta p = \bar{p}' T^{(1)}, \quad (\text{B.46c})$$

$$\mathbf{y}_S \Pi - \mathbf{x}_S \Pi = 0. \quad (\text{B.46d})$$

Therefore, by also using the transformation laws for the metric scalar modes, Eqs. (B.37), one can verify that the combinations

$$\hat{\delta\rho} = \mathbf{x}_S \delta\rho + \bar{\rho}' (\mathbf{x}_S v + \mathbf{x}_S B^{(1)}), \quad (\text{B.47a})$$

$$\hat{\delta p} = \mathbf{x}_S \delta p + \bar{p}' (\mathbf{x}_S v + \mathbf{x}_S B^{(1)}), \quad (\text{B.47b})$$

$$\hat{v} = \mathbf{x}_S v + \mathbf{x}_S E^{(1)'}, \quad (\text{B.47c})$$

$$\hat{\Pi} = \mathbf{x}_S \Pi, \quad (\text{B.47d})$$

are gauge invariant quantities. Again, these are just one possible set of combinations giving rise to gauge invariant quantities, there are other that we do not mention here because they are outside of the scope of the present work (see e.g. § 5.2 in Peter & Uzan, 2013).

B.3.5 First order Einstein field equations

The first order Einstein field equations,

$$\delta_{\mathbf{X}_s}^{(1)} [G^\mu{}_\nu] = \kappa \delta_{\mathbf{X}_s}^{(1)} [T^\mu{}_\nu] \quad (\text{B.48})$$

determine the evolution of the scalar modes of perturbations. Four independent scalar equations can be found from Eq. (B.48), given by the (00) and (i0) components and the trace and trace free part of (ij) components. According to Eqs. (B.35) and (B.43) one ends up with the system

$$(\nabla^2 + 3K) \Psi - 3\mathcal{H}(\Psi' + \mathcal{H}\Phi) + \mathcal{H}\nabla^2(E' - B) = a^2 \frac{\kappa}{2} \delta\rho, \quad (\text{B.49a})$$

$$\mathcal{H}\Phi + \Psi' - KB = -a^2 \frac{\kappa}{2} (\bar{\rho} + \bar{p})(v + B), \quad (\text{B.49b})$$

$$\Phi'' + 2\mathcal{H}\Phi' - K\Phi + \mathcal{H}\Psi' + (2\mathcal{H}' + \mathcal{H}^2) \Psi = a^2 \frac{\kappa}{2} \delta p, \quad (\text{B.49c})$$

$$(E' - B)' + 2\mathcal{H}(E' - B) + (\Phi - \Psi) = a^2 \kappa \Pi. \quad (\text{B.49d})$$

Total matter (pure dust) fluid

For a pure dust-like energy-momentum tensor, pressure-less fluid, $p = \pi_{ij} = 0$ so the system Eqs. (B.49) can be reduced to

$$(\nabla^2 + 3K) \Psi - 3\mathcal{H}(\Psi' + \mathcal{H}\Phi) + \mathcal{H}\nabla^2(E' - B) = a^2 \frac{\kappa}{2} \delta\rho, \quad (\text{B.50a})$$

$$\mathcal{H}\Phi + \Psi' - KB = -a^2 \frac{\kappa}{2} \bar{\rho}(v + B), \quad (\text{B.50b})$$

$$\Phi'' + 2\mathcal{H}\Phi' - K\Phi + \mathcal{H}\Psi' + (2\mathcal{H}' + \mathcal{H}^2) \Psi = 0, \quad (\text{B.50c})$$

$$(E' - B)' + 2\mathcal{H}(E' - B) + (\Phi - \Psi) = 0. \quad (\text{B.50d})$$

This is a system of four equations for six degrees of freedom, four metric perturbations and two fluid quantities, the perturbation to the energy density $\delta\rho$ and the peculiar velocity potential v . However, taking into account the gauge freedom to choose these potentials, one knows from § B.3.3 and § B.3.4 that from the four metric degrees of freedom it can be constructed two gauge invariant quantities given by Eqs. (B.38) and the two fluid ones can be combined to give the gauge invariant quantities Eqs. (B.47).

Therefore, introducing the gauge invariant scalar modes of Eqs. (B.38) and (B.47) and the gauge invariant fluctuation of matter, $\hat{\delta} := \hat{\delta}\rho/\bar{\rho}$, the system Eqs. (B.50) is equivalent to

$$(\nabla^2 + 3K) \hat{\Phi} - 3\mathcal{H} (\hat{\Phi}' + \mathcal{H}\hat{\Phi}) = a^2 \frac{\kappa}{2} \bar{\rho} (\hat{\delta} - 3\mathcal{H}\hat{v}), \quad (\text{B.51a})$$

$$\hat{\Phi}' + \mathcal{H}\hat{\Phi} = -a^2 \frac{\kappa}{2} \bar{\rho} \hat{v}, \quad (\text{B.51b})$$

$$\hat{\Phi}'' + 3\mathcal{H}\hat{\Phi}' + (2\mathcal{H}' + \mathcal{H}^2 - K) \hat{\Phi} = 0. \quad (\text{B.51c})$$

This system of equations along with the background EFE, Eqs. (2.14),

$$2\mathcal{H}' + \mathcal{H}^2 + K = -a^2 \kappa \bar{p} = 0, \quad (\text{B.52a})$$

$$\mathcal{H}^2 + K = a^2 \frac{\kappa}{3} \bar{\rho}, \quad (\text{B.52b})$$

can be combined to eliminate terms with explicit dependence on conformal time derivatives of \mathcal{H} and Φ , this is, to obtain evolution equations for δ , v and Φ ,

$$\hat{\delta}' + (\nabla^2 + 3K) \hat{v} = 0, \quad (\text{B.53a})$$

$$\hat{v}' + \mathcal{H}\hat{v} + \hat{\Phi} = 0, \quad (\text{B.53b})$$

$$(\nabla^2 + 3K) \hat{\Phi} = a^2 \frac{\kappa}{2} \bar{\rho} \hat{\delta}. \quad (\text{B.53c})$$

Since GR was assumed on top of the derivation of the system Eqs. (B.53) the first two equations can be shown to be equivalent to the first order perturbations to the local conservation of energy–momentum tensor $\nabla_\mu T^\mu{}_\nu = 0$. That is because the EFE formally contain this equations according to the Bianchi identities.

The evolution Eqs. (B.53) are equivalent in form to fluid equations obtained via the Poisson–Vlasov system in Newtonian theory. However, as long as they are a relativistic result according to the treatment presented, they have another interpretation. The system Eqs. (B.53) accounts for evolution equations to gauge invariant, then physically observable degrees of freedom, first order perturbations of matter fluid around a FLRW background model.

Appendix C

Comoving sound horizon

Let us compute the comoving sound horizon r_s at decoupling, which sets the BAO scale and is therefore a key ingredient of BAO analyses.

For simplicity, in this appendix we will assume the following values:

$$z_{eq} \approx 3200 \quad (a_{eq} = \frac{\Omega_r}{\Omega_m} \approx 3 \times 10^{-4}) \quad (\text{C.1})$$

$$z_d \approx 1100 \quad (a_d \approx 9.0 \times 10^{-4} = 3a_{eq}) \quad (\text{C.2})$$

$$\Omega_m \approx 0.3 \quad (\text{C.3})$$

$$\Omega_b \approx 0.05 = \Omega_m/6 \quad (\text{C.4})$$

$$h \approx 0.68 \quad (\text{C.5})$$

The sound horizon at decoupling is given by

$$r_s = \int_{z_d}^{\infty} dz \frac{c_s(z)}{H(z)} = \int_0^{a_d} \frac{c_s(z) da}{a^2 H(a)} \quad (\text{C.6})$$

where the sound speed is given by

$$c_s(a) = \frac{c}{\sqrt{3[1 + R(a)]}} \quad (\text{C.7})$$

and

$$R(a) = \frac{3\Omega_b a^{-3}}{4\Omega_r a^{-4}} = \frac{3a(\Omega_m/6)}{4\Omega_r} = \frac{a}{8a_{eq}} \quad (\text{C.8})$$

Therefore, the sound speed can be written as

$$c_s(z) = \frac{c}{\sqrt{3}} \sqrt{\frac{8a_{eq}}{8a_{eq} + a}}. \quad (\text{C.9})$$

The sound horizon then becomes

$$\begin{aligned}
r_s &= \frac{1}{H_0} \int_0^{a_d} \frac{c_s(z) da}{a^2 \sqrt{\Omega_m a^{-3} + \Omega_r a^{-4}}} \\
&= \frac{c \sqrt{8a_{eq}}}{H_0 \sqrt{3}} \int_0^{a_d} \frac{da}{\sqrt{(\Omega_m a + \Omega_r)(8a_{eq} + a)}}
\end{aligned} \tag{C.10}$$

Using $a_{eq} = \Omega_r/\Omega_m$, we find

$$\begin{aligned}
r_s &= \frac{c \sqrt{8a_{eq}}}{H_0 \sqrt{3} \sqrt{\Omega_m}} \int_0^{a_d} \frac{da}{\sqrt{a^2 + 9a_{eq}a + 8a_{eq}^2}} \\
&= \frac{c \sqrt{8a_{eq}}}{H_0 \sqrt{3} \sqrt{\Omega_m}} \log \left[2\sqrt{a^2 + 9a_{eq}a + 8a_{eq}^2} + 9a_{eq} + 2a \right]_0^{a_d}
\end{aligned} \tag{C.11}$$

Finally, setting $a_d = 3a_{eq}$ and using $c/H_0 = 2997 \text{ Mpc}/h$, we find

$$\begin{aligned}
r_s &= \frac{c \sqrt{8a_{eq}}}{H_0 \sqrt{3} \sqrt{\Omega_m}} \log \left[\frac{(2\sqrt{44} + 15)}{(2\sqrt{8} + 9)} \right] \\
&= \frac{0.58 \times 2997 \text{ Mpc}/h \sqrt{8 \times 3 \times 10^{-4}}}{\sqrt{0.3}} \log \left[\frac{(2\sqrt{44} + 15)}{(2\sqrt{8} + 9)} \right] \\
&= 102 \text{ Mpc}/h = 150 \text{ Mpc}
\end{aligned} \tag{C.12}$$

Appendix D

Two-point functions on the sphere

Consider two random fields $A(z, \mathbf{x})$ and $B(z, \mathbf{x})$ in the universe with Fourier transforms defined according to

$$A(z, \mathbf{k}) := \int d^3\mathbf{x} e^{-i\mathbf{k}\cdot\mathbf{x}} A(z, \mathbf{x}). \quad (\text{D.1})$$

As long as fields respect statistical homogeneity, its three-dimensional cross-correlation power spectrum, $P_{AB}(\mathbf{k}, z_1, z_2)$ is given by

$$\langle A(z_1, \mathbf{k}_1) B^*(z_2, \mathbf{k}_2) \rangle = (2\pi)^3 \delta^3(\mathbf{k}_1 - \mathbf{k}_2) P_{AB}(\mathbf{k}_1, z_1, z_2). \quad (\text{D.2})$$

If the projection on the sky of A, B can be defined by specific projection kernels, F_A, F_B as

$$A^{2D}(\hat{\mathbf{n}}) = \int dr F_A(r) A(z, r\hat{\mathbf{n}}), \quad (\text{D.3})$$

projections can then be decomposed in spherical harmonics to allow to obtain the angular cross-power spectrum, $C_{AB}(\ell)$, in terms of the corresponding three-dimensional power spectrum (Loverde & Afshordi, 2008),

$$\begin{aligned} C_{AB}(\ell) &:= \langle A_{\ell m}^{2D} B_{\ell m}^{2D*} \rangle \\ &= \int dr_1 f_A(r_1) J_{\ell+1/2}(kr_1) \int dr_2 f_B(r_2) J_{\ell+1/2}(kr_2) \\ &\quad \times \int dk k P_{AB}(k, z(r_1), z(r_2)), \end{aligned} \quad (\text{D.4})$$

where J_μ 's are the Bessel functions of the first kind and new projection kernels were defined as

$$f_A(r) := r^{-1/2} F_A(r). \quad (\text{D.5})$$

On configuration space, a correlation function, $\zeta_{AB}(\vartheta)$, can be associated with this angular power spectrum, $C_{AB}(\ell)$, via Stebbins (1996)

$$\zeta_{AB}(\vartheta) = \langle A^{2D}(\hat{\mathbf{n}})B^{2D*}(\hat{\mathbf{n}}') \rangle = \sum_{\ell=0}^{\infty} \frac{2\ell+1}{4\pi} C_{AB}(\ell) d_{mn}^{\ell}(\vartheta), \quad (\text{D.6})$$

where $\cos \vartheta = \hat{\mathbf{n}} \cdot \hat{\mathbf{n}}'$ gives the angular separation on the sky and $d_{mn}^{\ell}(\vartheta)$ are Wigner D-matrix elements. The properties of fields A, B on the sphere fix the indices m, n .

On the small-angle limit, typically where $\cos \theta \sim 1$, can be approximated with the Limber approximation (Limber, 1953; Loverde & Afshordi, 2008),

$$C_{AB}(\ell) = \int dr f_A(r) f_B(r) P_{AB} \left(k = \frac{\ell + 1/2}{r}, z(r) \right) \quad (\text{D.7})$$

and a Hankel transform, in the flat-sky approximation (Stebbins, 1996),

$$\zeta_{AB}(\vartheta) = \int d\ell \ell C_{AB}(\ell) J_{\mu}(\vartheta), \quad (\text{D.8})$$

respectively, where the index μ , coming from m, n , is determined by the properties of fields A, B .

Appendix E

Hankel transforms and FFTlog

This appendix reviews the construction of the FFTLog algorithm used to compute discrete Hankel transforms, which appear in different two-point statistics in cosmology.

Consider a well behaved function $a : \mathbb{R} \rightarrow \mathbb{R}$ periodic in logarithmic space with period L , i.e.,

$$a(re^L) = a(r),$$

where r_0 , the central point of the interval, is a free parameter. The periodicity of the function imply that its continuous Fourier transform should contain only discrete Fourier modes,

$$a(r) = \sum_m c_m \exp \left[2\pi i m \frac{\ln(r/r_0)}{L} \right], \quad (\text{E.1})$$

where the coefficients c_m satisfy

$$\begin{aligned} c_m &= \frac{1}{N} a_n \exp \left[-2\pi i m \frac{n}{N} \right]; \\ a_n &:= a(r_n), \quad r_n := r_0 \exp \left[L \frac{n}{N} \right]. \end{aligned} \quad (\text{E.2})$$

Consider now the Hankel transform, Eq. (2.173), of $a(r)$, $\tilde{a}(k)$,

$$\begin{aligned} \tilde{a}(k) &= \sum_m c_m \int_0^\infty dr k(kr)^q J_\mu(kr) \exp \left[2\pi i m \frac{\ln(r/r_0)}{L} \right] \\ &= \sum_m c_m (kr_0)^{-2\pi i m/L} \left[\int_0^\infty dt t^{(q+2\pi i m/L)} J_\mu(t) \right] \\ &= \sum_m c_m u_m \exp \left[-2\pi i m \frac{\ln(k/k_0)}{L} \right], \end{aligned} \quad (\text{E.3})$$

where the extra coefficients u_m were introduced as

$$u_m(\mu, q) = (k_0 r_0)^{-2\pi i m/L} U_\mu(q + 2\pi i m/L) \quad (\text{E.4})$$

with

$$U_\mu(x) = \int_0^\infty dt t^x J_\mu(t). \quad (\text{E.5})$$

Therefore the problem is reduced to computing $U_\mu(x)$, which is formally a *Mellin transform* of the Bessel function of the first kind.

The key point of the FFTLog method is that such a Mellin transform, Eq. (E.5), can be computed analytically in terms of Gamma functions only,

$$U_\mu(x) = 2^x \frac{\Gamma[(1 + \mu + x)/2]}{\Gamma[(1 + \mu - x)/2]}, \quad (\text{E.6})$$

and therefore, one ends up with an expansion for the Hankel transform of $a(r)$ in the form of a Fourier expansion. Note that the functions $u_m(\mu, q)$ satisfy $u_m^* = u_{-m}$, which guarantees that if $a(r)$ is real-valued, its Hankel transform is also real-valued. Note further that the variable k_0 as introduced in Eq. (E.3) can be understood as the center of the fundamental interval where the Hankel transform defined, $[\ln(k_0) - L/2, \ln(k_0) + L/2]$.

Finally, in order to derive a sequence of discrete samples for $\tilde{a}(k)$ at the discrete points $k_0 e^{Ln/N}$, analogue to the discrete Fourier transform, the *Sampling theorem* (see e.g., Press et al., 2002) requires $c_{-N/2} u_{-N/2} = c_{N/2} u_{N/2}$. As by construction, $c_{-N/2} = c_{N/2}$, condition reduces to $u_{-N/2} = u_{N/2}$, which is not trivially satisfied, see Eqs. (E.4) and (E.6). Fortunately, Hamilton (2000) noted that the sum of the terms with $m = -N/2$ and $m = N/2$ evaluated at the discrete points $k_n = k_0 e^{Ln/N}$ is given

$$\begin{aligned} (-1)^n c_{N/2} (u_{N/2} - u_{-N/2}) &= (-1)^n c_{N/2} (u_{N/2} + u_{N/2}^*) \\ &= (-1)^n c_{N/2} 2\Re [u_{N/2}], \end{aligned}$$

so condition is indeed guaranteed by further requiring

$$u_{\pm N/2} \rightarrow \Re [u_{N/2}]. \quad (\text{E.7})$$

Therefore, one can write a *discrete Hankel transform pair* of the form

$$a_n = \sum_m \tilde{a}_m \left\{ \frac{1}{N} \sum_k \frac{1}{u_k} \exp \left[2\pi i k \frac{n+m}{N} \right] \right\}, \quad (\text{E.8a})$$

$$\tilde{a}_m = \sum_n a_n \left\{ \frac{1}{N} \sum_k u_k \exp \left[2\pi i k \frac{n+m}{N} \right] \right\}, \quad (\text{E.8b})$$

which constitutes the basis of the FFTLog algorithm summarized in the following steps as pseudo-code:

1. FFT $\{a_n\}$ to obtain $\{c_m\}$ (Eq. E.2).
2. Construct the sequence $\{c_m u_m\}$ using the analytic expressions (E.4) and (E.6).
3. FFT back the sequence $\{c_m u_m\}$ to get $\{\tilde{a}_n\}$, the discrete Hankel transform (Eq. E.8).

Finally, we point out that since there exists good numerical approximations for the Gamma function, e.g. the Lanczos approximation (§ 6 in Press et al., 2002), the `FFTLog` algorithm can be constructed on the basis of a Fast Fourier Transform (e.g. `FFTW`, Frigo & Johnson, 2005) as depicted by the pseudo-code above. As such, it has a numerical complexity of $N \log N$ and does not rely on special recipes for dealing with the highly oscillating Spherical Bessel functions, which represents a major advantage for cosmological applications.

Bibliography

- Abbott T. M. C., et al., 2018, *Phys. Rev. D*, 98, 043526
- Abbott T. M. C., et al., 2019, *MNRAS*, 483, 4866
- Abolfathi B., et al., 2018, *ApJS*, 235, 42
- Abramo L. R., Leonard K. E., 2013, *MNRAS*, 432, 318
- Abramo L. R., et al., 2012, *MNRAS*, 423, 3251
- Agrawal A., Makiya R., Chiang C.-T., Jeong D., Saito S., Komatsu E., 2017, *Journal of Cosmology and Astro-Particle Physics*, 2017, 003
- Ahn C. P., et al., 2014, *The Astrophysical Journal Supplement Series*, 211, 17
- Alam S., et al., 2017, *MNRAS*, 470, 2617
- Alarcon A., Eriksen M., Gaztanaga E., 2018, *MNRAS*, 473, 1444
- Albrecht A., et al., 2006, preprint, pp astro-ph/0609591 ([arXiv:astro-ph/0609591](https://arxiv.org/abs/astro-ph/0609591))
- Alonso D., 2012, preprint, ([arXiv:1210.1833](https://arxiv.org/abs/1210.1833))
- Amendola L., Tsujikawa S., 2010, *Dark Energy: Theory and Observations*. Cambridge University Press
- Amendola L., et al., 2013, *Living Reviews in Relativity*, 16, 6
- Anderson L., et al., 2014, *MNRAS*, 441, 24
- Annis J., et al., 2014, *ApJ*, 794, 120
- Ata M., et al., 2018a, *Mon. Not. Roy. Astron. Soc.*, 473, 4773
- Ata M., et al., 2018b, *MNRAS*, 473, 4773

- Avila S., Murray S. G., Knebe A., Power C., Robotham A. S. G., Garcia-Bellido J., 2015, *MNRAS*, 450, 1856
- Avila S., et al., 2017, Submitted to: *Mon. Not. Roy. Astron. Soc.*
- Avila S., et al., 2018, *MNRAS*, 479, 94
- Bardeen J. M., 1980, *Phys. Rev. D*, 22, 1882
- Bautista J. E., et al., 2017, *A&A*, 603, A12
- Bautista J. E., et al., 2018, *ApJ*, 863, 110
- Baxter E. J., Rozo E., 2013, *ApJ*, 779, 62
- Baxter E. J., et al., 2018, preprint, p. arXiv:1802.05257 ([arXiv:1802.05257](https://arxiv.org/abs/1802.05257))
- Bernardeau F., Colombi S., Gaztañaga E., Scoccimarro R., 2002, *Phys. Rep.*, 367, 1
- Bernstein G. M., 1994, *ApJ*, 424, 569
- Bernstein G., Huterer D., 2010, *MNRAS*, 401, 1399
- Beutler F., et al., 2011, *MNRAS*, 416, 3017
- Blot L., et al., 2019, *MNRAS*, 485, 2806
- Bond J. R., Myers S. T., 1996, *The Astrophysical Journal Supplement Series*, 103, 1
- Brown M. L., Castro P. G., Taylor A. N., 2005, *Mon. Not. Roy. Astron. Soc.*, 360, 1262
- Bruni M., Matarrese S., Mollerach S., Sonogo S., 1997, *Classical and Quantum Gravity*, 14, 2585
- Camacho H., et al., 2018, preprint, p. arXiv:1807.10163 ([arXiv:1807.10163](https://arxiv.org/abs/1807.10163))
- Carlstrom J. E., et al., 2011, *Publications of the Astronomical Society of the Pacific*, 123, 568
- Cawthon R., et al., 2017, Submitted to: *Mon. Not. Roy. Astron. Soc.*
- Chan K. C., et al., 2018, *MNRAS*, 480, 3031
- Clifton T., Ferreira P. G., Padilla A., Skordis C., 2012, *Phys. Rep.*, 513, 1

- Colavincenzo M., et al., 2019, MNRAS, 482, 4883
- Cooray A., Sheth R. K., 2002, Phys. Rept., 372, 1
- Copeland E. J., Sami M., Tsujikawa S., 2006, International Journal of Modern Physics D, 15, 1753
- Cowan G., 1998, Statistical data analysis. Oxford University Press, UK
- Crocce M., Scoccimarro R., 2006, Phys. Rev. D, 73, 063519
- Crocce M., Scoccimarro R., 2008, Phys. Rev. D, 77, 023533
- Crocce M., Fosalba P., Castander F. J., Gaztañaga E., 2010, MNRAS, 403, 1353
- Crocce M., Cabré A., Gaztañaga E., 2011, MNRAS, 414, 329
- Crocce M., Castander F. J., Gaztañaga E., Fosalba P., Carretero J., 2015, Mon. Not. Roy. Astron. Soc., 453, 1513
- Crocce M., et al., 2016, MNRAS, 455, 4301
- Crocce M., et al., 2019, MNRAS, 482, 2807
- DES Collaboration et al., 2018, arXiv e-prints, p. arXiv:1811.02375
- DESI Collaboration et al., 2016a, preprint, p. arXiv:1611.00036 (arXiv:1611.00036)
- DESI Collaboration et al., 2016b, preprint, p. arXiv:1611.00037 (arXiv:1611.00037)
- Davis C., et al., 2017, Submitted to: Mon. Not. Roy. Astron. Soc.
- Dawson K. S., et al., 2016, AJ, 151, 44
- De Vicente J., Sánchez E., Sevilla-Noarbe I., 2016, Mon. Not. Roy. Astron. Soc., 459, 3078
- Dodelson S., 2003, Modern cosmology. Academic Press
- Dodelson S., Schneider M. D., 2013, Phys. Rev. D, 88, 063537
- Drlica-Wagner A., et al., 2018, ApJS, 235, 33
- Efstathiou G., 2004, Mon. Not. Roy. Astron. Soc., 349, 603

- Eisenstein D. J., Hu W., 1998, *ApJ*, 496, 605
- Ellis G. F. R., van Elst H., 1999, in Lachièze-Rey M., ed., *NATO ASIC Proc. 541: Theoretical and Observational Cosmology*. pp 1–116 ([arXiv:gr-qc/9812046](https://arxiv.org/abs/gr-qc/9812046))
- Elvin-Poole J., et al., 2018, *Phys. Rev. D*, 98, 042006
- Flaugher B., 2005, *International Journal of Modern Physics A*, 20, 3121
- Foreman-Mackey D., Hogg D. W., Lang D., Goodman J., 2013, *PASP*, 125, 306
- Fosalba P., Gaztañaga E., Castander F. J., Crocce M., 2015a, *Mon. Not. Roy. Astron. Soc.*, 447, 1319
- Fosalba P., Crocce M., Gaztañaga E., Castander F. J., 2015b, *Mon. Not. Roy. Astron. Soc.*, 448, 2987
- Friedrich O., Eifler T., 2018, *MNRAS*, 473, 4150
- Frigo M., Johnson S. G., 2005, *Proceedings of the IEEE*, 93, 216
- Fukugita M., Ichikawa T., Gunn J. E., Doi M., Shimasaku K., Schneider D. P., 1996, *AJ*, 111, 1748
- Gatti M., et al., 2017, Submitted to: *Mon. Not. Roy. Astron. Soc.*
- Gil-Marín H., et al., 2016, *MNRAS*, 460, 4210
- Gorski K. M., Hivon E., Banday A. J., Wandelt B. D., Hansen F. K., Reinecke M., Bartelman M., 2005, *Astrophys. J.*, 622, 759
- Grieb J. N., Sánchez A. G., Salazar-Albornoz S., Dalla Vecchia C., 2016, *MNRAS*, 457, 1577
- Gruen D., et al., 2018, *Phys. Rev. D*, 98, 023507
- Gunn J. E., et al., 2006, *AJ*, 131, 2332
- Guo H., Zehavi I., Zheng Z., 2012, *ApJ*, 756, 127
- Hamilton A. J. S., 1992, *ApJ*, 385, L5
- Hamilton A. J. S., 1993, *ApJ*, 417, 19
- Hamilton A. J. S., 2000, *MNRAS*, 312, 257

- Hartlap J., Simon P., Schneider P., 2007, *A&A*, 464, 399
- Hawkins E., et al., 2003, *MNRAS*, 346, 78
- Hivon E., Gorski K. M., Netterfield C. B., Crill B. P., Prunet S., Hansen F., 2002, *Astrophys. J.*, 567, 2
- Ho S., et al., 2012, *ApJ*, 761, 14
- Hogg D. W., 1999, arXiv e-prints, pp astro-ph/9905116
- Hoyle B., et al., 2018, *MNRAS*, 478, 592
- Hu W., Fukugita M., Zaldarriaga M., Tegmark M., 2001, *Astrophys. J.*, 549, 669
- Ilbert O., et al., 2006, *A&A*, 457, 841
- Ilbert O., et al., 2009, *ApJ*, 690, 1236
- Izard A., Crocce M., Fosalba P., 2016, *MNRAS*, 459, 2327
- Jia Y., et al., 2014, *MNRAS*, 441, 503
- Jouvel S., et al., 2017, *MNRAS*, 469, 2771
- Kaiser N., 1987, *MNRAS*, 227, 1
- Kazin E. A., et al., 2014, *MNRAS*, 441, 3524
- Kim J.-W., et al., 2014, *MNRAS*, 438, 825
- Kitaura F. S., Yepes G., Prada F., 2014, *MNRAS*, 439, L21
- Klypin A., Yepes G., Gottlöber S., Prada F., Heß S., 2016, *MNRAS*, 457, 4340
- Krause E., Eifler T., 2017, *MNRAS*, 470, 2100
- Krause E., et al., 2017, preprint, p. arXiv:1706.09359 ([arXiv:1706.09359](https://arxiv.org/abs/1706.09359))
- Landy S. D., Szalay A. S., 1993, *ApJ*, 412, 64
- Leistedt B., et al., 2016, *ApJS*, 226, 24
- Lesgourgues J., 2011, arXiv e-prints, p. arXiv:1104.2932
- Lewis A., Bridle S., 2002, *Phys. Rev. D*, 66, 103511

- Limber D. N., 1953, *ApJ*, 117, 134
- Lippich M., et al., 2019, *MNRAS*, 482, 1786
- Loverde M., Afshordi N., 2008, *Phys. Rev. D*, 78, 123506
- Lyth D. H., Liddle A. R., 2009, *The primordial density perturbation: Cosmology, inflation and the origin of structure*. Cambridge University Press, UK, <http://www.cambridge.org/uk/catalogue/catalogue.asp?isbn=9780521828499>
- Ma C.-P., Bertschinger E., 1995, *ApJ*, 455, 7
- Marulli F., et al., 2013, *A&A*, 557, A17
- Montesano F., 2011, PhD thesis, Ludwig-Maximilians-Universität
- Moster B. P., Somerville R. S., Newman J. A., Rix H.-W., 2011, *ApJ*, 731, 113
- Munari E., Monaco P., Koda J., Kitaura F.-S., Sefusatti E., Borgani S., 2017, *Journal of Cosmology and Astro-Particle Physics*, 2017, 050
- Nakahara M., 2003, *Geometry, Topology and Physics*, Second Edition. Graduate student series in physics, Taylor & Francis, <http://books.google.com.br/books?id=cH-XQB0Ex5wC>
- Navarro J. F., Frenk C. S., White S. D. M., 1996, *ApJ*, 462, 563
- Newman J. A., et al., 2013, *The Astrophysical Journal Supplement Series*, 208, 5
- Norberg P., Baugh C. M., Gaztañaga E., Croton D. J., 2009, *MNRAS*, 396, 19
- Padmanabhan N., et al., 2007, *MNRAS*, 378, 852
- Peebles P. J. E., 1973, *ApJ*, 185, 413
- Peebles P. J. E., 1980, *The large-scale structure of the universe*. Princeton University Press
- Peebles P. J. E., Hauser M. G., 1974, *The Astrophysical Journal Supplement Series*, 28, 19
- Peebles P. J., Ratra B., 2003, *Reviews of Modern Physics*, 75, 559

- Percival W. J., et al., 2014, MNRAS, 439, 2531
- Perlmutter S., et al., 1999, ApJ, 517, 565
- Peter P., Uzan J.-P., 2013, Primordial Cosmology. Oxford University Press
- Planck Collaboration et al., 2011, A&A, 536, A1
- Planck Collaboration et al., 2013, preprint, ([arXiv:1303.5076](#))
- Planck Collaboration et al., 2014, A&A, 571, A16
- Planck Collaboration et al., 2018, preprint, p. [arXiv:1807.06209](#)
([arXiv:1807.06209](#))
- Prakash A., et al., 2016, ApJS, 224, 34
- Press W. H., Teukolsky S. A., Vetterling W. T., Flannery B. P., 2002, Numerical recipes in C++ : the art of scientific computing. Cambridge university press
- Riess A. G., et al., 1998, AJ, 116, 1009
- Roche N., Eales S. A., 1999, MNRAS, 307, 703
- Ross A. J., Samushia L., Howlett C., Percival W. J., Burden A., Manera M., 2015a, MNRAS, 449, 835
- Ross A. J., Percival W. J., Manera M., 2015b, MNRAS, 451, 1331
- Ross A. J., et al., 2017, MNRAS, 472, 4456
- Sadeh I., Abdalla F. B., Lahav O., 2016, Publications of the Astronomical Society of the Pacific, 128, 104502
- Sánchez C., et al., 2014, MNRAS, 445, 1482
- Seo H.-J., et al., 2012, Astrophys. J., 761, 13
- Smith R. E., et al., 2003, MNRAS, 341, 1311
- Sobreira F., de Simoni F., Rosenfeld R., da Costa L. A. N., Maia M. A. G., Makler M., 2011, Phys. Rev. D, 84, 103001
- Stebbins A., 1996, ArXiv Astrophysics e-prints,

- Stewart J. M., Walker M., 1974, *Proceedings of the Royal Society of London Series A*, 341, 49
- Takahashi R., Sato M., Nishimichi T., Taruya A., Oguri M., 2012, *ApJ*, 761, 152
- Tinker J., Kravtsov A. V., Klypin A., Abazajian K., Warren M., Yepes G., Gottlöber S., Holz D. E., 2008, *ApJ*, 688, 709
- Tinker J. L., Robertson B. E., Kravtsov A. V., Klypin A., Warren M. S., Yepes G., Gottlöber S., 2010, *ApJ*, 724, 878
- Tinker J. L., et al., 2012, *ApJ*, 745, 16
- Tsujikawa S., 2010, in Wolschin G., ed., *Lecture Notes in Physics*, Berlin Springer Verlag Vol. 800, *Lecture Notes in Physics*, Berlin Springer Verlag. pp 99–145 ([arXiv:1101.0191](https://arxiv.org/abs/1101.0191)), doi:10.1007/978-3-642-10598-2_3
- Wald R. M., 1984, *General relativity*. University of Chicago Press
- Wechsler R. H., Tinker J. L., 2018, preprint, p. [arXiv:1804.03097](https://arxiv.org/abs/1804.03097) ([arXiv:1804.03097](https://arxiv.org/abs/1804.03097))
- Weinberg S., 1972, *Gravitation and Cosmology: Principles and Applications of the General Theory of Relativity*. John Wiley & Sons
- Weinberg D. H., Mortonson M. J., Eisenstein D. J., Hirata C., Riess A. G., Rozo E., 2013, *Phys. Rep.*, 530, 87
- Wright E. L., et al., 2010, *AJ*, 140, 1868
- Xavier H. S., Abdalla F. B., Joachimi B., 2016, *MNRAS*, 459, 3693
- Xu X., Padmanabhan N., Eisenstein D. J., Mehta K. T., Cuesta A. J., 2012, *MNRAS*, 427, 2146
- Zehavi I., et al., 2002, *ApJ*, 571, 172
- Zehavi I., et al., 2005, *ApJ*, 630, 1
- Zhai Z., et al., 2017, *ApJ*, 848, 76
- Zhao G.-B., et al., 2016, *MNRAS*, 457, 2377
- de Simoni F., et al., 2013, *MNRAS*, 435, 3017
- du Mas des Bourboux H., et al., 2017, *A&A*, 608, A130